

# Numerical investigations of transport and chemistry modeling for lean premixed hydrogen combustion

Thesis by  
Jason R. Schlup

In Partial Fulfillment of the Requirements for the  
Degree of  
Doctor of Philosophy

CALIFORNIA INSTITUTE OF TECHNOLOGY  
Pasadena, California

2018  
Defended May 23, 2018

© 2018

Jason R. Schlup

ORCID: 0000-0002-3121-3477

All rights reserved

## ACKNOWLEDGEMENTS

I would first like to thank my research advisor, Professor Guillaume Blanquart, for his passion of this research project and desire to see results, leading to numerous publications, presentations, conferences, and collaborations. I would also like to thank my committee members, Professors Dan Meiron, Dale Pullin, and Joseph Shepherd for their willingness to serve on both my dissertation and candidacy committees, read the dissertation, and provide valuable feedback throughout the project.

I would also like to acknowledge my research group members. Previous group members, especially Simon Lapointe, Bruno Savard, and Brock Bobbitt, were instrumental in connecting me within the group, Caltech, and Pasadena. Many group members were also critical in my research success, providing support by reading drafts of papers and sitting through practice presentations, as well as making conferences a great place to relax.

The GALCIT and Mechanical and Civil Engineering departments also provided necessary support during my time at Caltech. Whether it was my first interaction with the administrative staff during my campus visit, the first year of courses, financial support of my research, or even the scheduling of my defense, both departments were invaluable to my research success. I would also like to thank all of my friends on campus and in Pasadena, who provided countless numbers of stress-free days and nights away from school and work.

Finally, I would like to thank my family for their unending support. My parents fostered in me a love of learning and encouraged me through 24 years of school. My brother and sister also supported me in their own unique ways. And my wife, Susie, allowed me to pursue this passion of learning, with nothing but encouragement and patience. I am deeply thankful for her unwavering support.

## ABSTRACT

The use of hydrogen as a fuel for power generation applications has been suggested as an additive to, or replacement of, hydrocarbon fuels. The safety of hydrogen combustion has also received recent attention due to nuclear power plant disasters and the rise of hydrogen refuelling stations. In these uses and scenarios, lean hydrogen–air flames are prone to thermo-diffusive instabilities which can be dangerous to equipment and personnel. These instabilities are heavily influenced by two mechanisms: transport properties (e.g., diffusion) and chemical species production rates. This thesis investigates lean premixed hydrogen combustion using direct numerical simulations. A wide range of flame configurations are considered, spanning one-dimensional steady configurations to three-dimensional unsteady laminar and turbulent flames with high curvature. In particular, the two controlling mechanisms of thermo-diffusive instabilities are carefully investigated.

The effects of transport properties, in particular the importance of thermal diffusion in these mixtures, are quantified through global and local evaluations. Thermal diffusion is found to change flame speeds in one-dimensional flat flames, and also modify species profiles due to the increased diffusivity of light reactants. The impact of thermal diffusion is greatly enhanced in the presence of flame curvature, resulting in higher flame speeds (20% to 30% for two- and three-dimensional laminar and turbulent flames), fuel consumption, and flame surface area relative to simulations neglecting thermal diffusion. The mixture-averaged thermal diffusion model proposed by Chapman and Cowling (1970) is found to accurately reproduce global and local flame statistics (including enhanced burning and local extinction) computed using multicomponent transport at significantly reduced costs. Further cost reductions of the mixture-averaged thermal diffusion method are undertaken, and a new model is developed with constant computational requirements for large (~100 species) chemical models. The resulting reduced thermal diffusion model additionally improves upon the accuracy of the mixture-averaged thermal diffusion technique.

The effects of fluctuating chemical source terms on flame instabilities are then investigated using tabulated chemistry. One-dimensional unstretched flames including non-equal diffusion and thermal diffusion are incorporated into a chemistry table. This table successfully captures the interaction of differential diffusion and flame curvature. The chemistry tabulation approach is applied to a similar set of flame

configurations, and accurate predictions of global and local statistics are found. The tabulated chemistry method reproduces flame curvature, local enhanced burning, and local extinction of unstable flames using one-dimensional, flat, burning flames in its construction. The proposed reduced-order thermal diffusion and chemistry tabulation models significantly reduce computational costs while simultaneously including physical properties necessary to predict lean premixed hydrogen–air flame instabilities.

## PUBLISHED CONTENT AND CONTRIBUTIONS

- [1] J. Schlup and G. Blanquart. “A reduced thermal diffusion model for H and H<sub>2</sub>”. In: *Combust. Flame* 191 (2018), pp. 1–8. DOI: [10.1016/j.combustflame.2017.12.022](https://doi.org/10.1016/j.combustflame.2017.12.022).

The author of this thesis developed the reduced-order thermal diffusion model, performed all simulations, analyzed the data, made the figures, and wrote the manuscript.

- [2] J. Schlup and G. Blanquart. “Validation of a mixture-averaged thermal diffusion model for premixed lean hydrogen flames”. In: *Combust. Theor. Model.* 22.2 (2018), pp. 264–290. DOI: [10.1080/13647830.2017.1398350](https://doi.org/10.1080/13647830.2017.1398350).

The author of this thesis performed all simulations, analyzed the data, made the figures, and wrote the manuscript.

- [3] J. Schlup and G. Blanquart. “Reproducing curvature effects due to differential diffusion in tabulated chemistry”. In: *Proc. Combust. Inst.* (Under review).

This manuscript has been accepted for presentation and is under review for publication. The author of this thesis developed the chemistry model, performed all simulations, analyzed the data, made the figures, and wrote the manuscript.

## TABLE OF CONTENTS

Acknowledgements . . . . .	iii
Abstract . . . . .	iv
Published Content and Contributions . . . . .	vi
Table of Contents . . . . .	vii
List of Illustrations . . . . .	x
List of Tables . . . . .	xix
Chapter I: Introduction . . . . .	1
1.1 Background and motivation . . . . .	1
1.2 Premixed hydrogen combustion . . . . .	2
1.3 Thermo-diffusive instabilities . . . . .	3
1.4 Mass and thermal diffusion models . . . . .	4
1.5 Importance and inclusion of thermal diffusion . . . . .	6
1.6 Chemistry models . . . . .	7
1.6.1 Brief overview of finite-rate chemistry . . . . .	7
1.6.2 Tabulated chemistry . . . . .	8
1.7 Objectives and outline . . . . .	10
Chapter II: Governing equations and simulation methodology . . . . .	12
2.1 Governing equations . . . . .	12
2.2 Transport property definitions . . . . .	14
2.2.1 Conductivity and viscosity models . . . . .	14
2.2.2 Mixture-averaged mass diffusion model . . . . .	15
2.2.3 Thermal diffusion models . . . . .	16
2.3 Chemistry models . . . . .	19
2.3.1 Finite-rate chemistry . . . . .	19
2.3.2 Tabulated chemistry . . . . .	20
2.4 Numerics of the NGA flow solver . . . . .	21
2.4.1 Semi-implicit time integration . . . . .	21
2.4.2 Preconditioner for the chemical source terms . . . . .	25
2.4.3 Finite difference scheme for velocity discretization . . . . .	25
2.4.4 Finite volume scheme for scalar transport . . . . .	27
2.5 Special case: Governing equations for tubular flames . . . . .	29
2.6 Computational configurations . . . . .	32
2.6.1 One-dimensional flat unstretched flames . . . . .	33
2.6.2 One-dimensional cylindrical flames . . . . .	35
2.6.3 Two-dimensional tubular flames . . . . .	36
2.6.4 Two-dimensional freely-propagating flames . . . . .	38
2.6.5 Three-dimensional laminar flames . . . . .	39
2.6.6 Three-dimensional turbulent flames . . . . .	40
Chapter III: Validation of a mixture-averaged thermal diffusion model . . . . .	43

3.1	One-dimensional unstretched (flat) laminar flames . . . . .	43
3.2	One-dimensional stretched laminar flames . . . . .	45
3.3	Two-dimensional tubular flame . . . . .	46
3.4	Two-dimensional freely propagating flame . . . . .	48
3.5	Three-dimensional, laminar, freely propagating flame . . . . .	52
3.6	Three-dimensional, turbulent, freely propagating flame . . . . .	54
3.7	Discussion . . . . .	57
3.7.1	Size of the Cartesian computational domains . . . . .	57
3.7.2	Thermal diffusion effects . . . . .	61
3.7.3	Computational cost . . . . .	61
Chapter IV: A reduced thermal diffusion model . . . . .		64
4.1	Review of mixture-averaged thermal diffusion . . . . .	64
4.2	Model development . . . . .	66
4.3	Model evaluation . . . . .	70
4.3.1	One-dimensional unstretched laminar flame evaluation . . . . .	70
4.3.2	Three-dimensional turbulent flame evaluation . . . . .	73
4.3.3	Computational cost . . . . .	74
Chapter V: Tabulated chemistry model development including curvature effects		77
5.1	Proposed chemistry tabulation method . . . . .	77
5.1.1	Derivation of the mixture fraction transport equation . . . . .	78
5.1.2	Analysis of the proposed mixture fraction equation . . . . .	86
5.2	Implementation of the mixture fraction transport equation into NGA . . . . .	88
5.2.1	Chemistry tabulation . . . . .	88
5.2.2	Treatment of regions outside the chemistry table . . . . .	89
5.3	Verification of the tabulated chemistry model . . . . .	91
5.3.1	Analytical verification of the mixture fraction transport equation . . . . .	91
5.3.2	Comparison with optimal estimations from detailed chemistry . . . . .	92
Chapter VI: Validation of the tabulated chemistry model including curvature effects . . . . .		95
6.1	One-dimensional unstretched flames . . . . .	95
6.2	Cylindrical, outwardly-propagating flame . . . . .	97
6.3	Two-dimensional cellular tubular flame . . . . .	99
6.4	Two-dimensional freely propagating flame . . . . .	102
6.4.1	A priori analysis . . . . .	102
6.4.2	A posteriori analysis . . . . .	103
6.5	Three-dimensional turbulent flame . . . . .	106
6.6	Summary of results . . . . .	111
6.7	Reduction in computational cost . . . . .	113
6.7.1	Wall time reduction . . . . .	113
6.7.2	Stiff chemistry removal . . . . .	114
6.7.3	Summary of computational cost reductions . . . . .	117
Chapter VII: Conclusion . . . . .		118
7.1	Mixture-averaged thermal diffusion . . . . .	118
7.2	Development of a reduced thermal diffusion model . . . . .	119

7.3	Incorporating differential and thermal diffusion in tabulated chemistry	119
7.4	Future Work . . . . .	120
Appendix A: Species property fits . . . . .		123
A.1	Collision integral fits . . . . .	123
A.2	Species property fits . . . . .	123
Appendix B: Sensitivity analysis of flame instability length scales . . . . .		126
B.1	Methodology . . . . .	126
B.2	Sensitivity analyses . . . . .	129
B.2.1	Sensitivity analysis of $Y_{\text{H}_2\text{O}}^{\text{iso}}$ and $\dot{\omega}_{\text{H}_2\text{O}}^{\text{th}}$ . . . . .	130
B.2.2	Sensitivity analysis of $T^{\text{iso}}$ and $\kappa^{\text{th}}$ . . . . .	134
B.2.3	Sensitivity analysis conclusions . . . . .	136
Bibliography . . . . .		138

## LIST OF ILLUSTRATIONS

<i>Number</i>	<i>Page</i>
1.1 Schematic of a thermo-diffusive instability, showing relative diffusion rates toward the flame. Figure from Sánchez and Williams [107]. . . . .	3
1.2 Lewis number for each species in the nine-species hydrogen model of Hong et al. [59, 60, 72] as a function of temperature. . . . .	5
1.3 Thermo-diffusive instability in a premixed lean hydrogen–air simulation. . . . .	5
2.1 One-dimensional representation of the temporal discretization, showing the half-time stepping and location of mass conservation. . . . .	22
2.2 Two-dimensional representation of the computational domain discretization. . . . .	26
2.3 (a) Interpolation of $v$ to $\bar{v}^x$ , (b) interpolation of $g_x$ to $\bar{g}_x^y$ , and (c) differentiation of $\bar{g}_x^y \bar{v}^x$ . . . . .	27
2.4 Schematic of the one-dimensional cartesian flame configuration. . . . .	33
2.5 Methodology of finding the flame position based on an equal-area approach, using a one-dimensional flat flame at $\phi = 0.4$ (red line). . . . .	35
2.6 Schematic of the one-dimensional cylindrical flame configuration. . . . .	35
2.7 Schematic of the two-dimensional tubular flame configuration. . . . .	36
2.8 Initial perturbation for the two-dimensional freely propagating hydrogen–air flame with $\phi = 0.4$ . . . . .	38
2.9 Two-dimensional schematic of the three-dimensional laminar flame configuration. . . . .	39
2.10 Two-dimensional schematic of the three-dimensional flame configuration. Adapted from [108]. . . . .	40
3.1 Laminar flame speed comparison of the MA–MA (red circles), MA–FM [45] (orange squares), MA–RM [113] (green diamonds), and MA–xx (blue crosses) models with the MA–MC model. The MA–MA and MA–RM cases overlap at many equivalence ratios. . . . .	44

3.2	Comparison of species mass fractions as functions of temperature for the different diffusion models. MA–MC (black), MA–MA (dashed red), MA–FM [45] (dot-dashed orange), MA–RM [113] (dot-dashed green), and MA–xx (dotted blue) results are shown. The cases including any thermal diffusion model overlap in these figures. . . . .	45
3.3	Normalized flame speed as a function of normalized flame curvature with $\phi = 0.4$ . . . . .	46
3.4	(a) H and (b) OH number density contours for the (clockwise from top left) MA–xx, MA–MC, MA–MA, and experimental [53] results. . . . .	47
3.5	Profiles of the (a) maximum $n_{\text{OH}}$ and (b) radial location of maximum $n_{\text{OH}}$ as functions of the azimuthal coordinate. MA–MC (black), MA–MA (dashed red), MA–xx (dotted blue), and experimental data [53] (black symbols) results are shown. Experimental uncertainty for $n_{\text{OH}}$ is $\pm 2 \times 10^{15} \text{ cm}^{-3}$ . . . . .	48
3.6	Temperature (top) and normalized $\text{H}_2\text{O}$ source term (bottom) contours for the MA–MA model. . . . .	49
3.7	(a) Flame speed history and (b) PDF of normalized flame speed for the MA–MC (black), MA–MA (red), and MA–xx (blue) models. The dashed lines represent the temporal mean of the flame speeds. . . . .	50
3.8	(a) PDF of flame surface area normalized by domain cross-sectional area and (b) normalized chemical source term as a function of normalized local flame curvature for the MA–MC (black), MA–MA (red), and MA–xx (blue) models. The dashed lines on the left figure represent the temporal mean of the flame area. The MA–MC and MA–MA means overlap. . . . .	51
3.9	Isosurface of the three-dimensional laminar flame with the MA–MA model. The isosurface corresponds to $T_{\text{peak}}$ . The colors correspond to the normalized source term $\dot{\omega}_{\text{H}_2\text{O}}/\dot{\omega}_{\text{H}_2\text{O}}^{1D} \in [0, 5]$ . . . . .	52
3.10	Flame speed history (left) and PDF of normalized flame speed (right) for the MA–MA (red) and MA–xx (blue) models. The dashed lines represent the temporal mean of the flame area. . . . .	53

3.11	PDF of laminar three-dimensional flame surface area normalized by domain cross-sectional area (left) and normalized chemical source term as a function of normalized local flame curvature (right) for the MA–MA (red) and MA–xx (blue) models. The dashed lines represent the temporal mean of the flame area (left) and the two-dimensional conditional means (right). . . . .	54
3.12	Isosurface of the three-dimensional turbulent flame with the MA–MA model. The isosurface corresponds to $T_{\text{peak}}$ . The colors correspond to the normalized source term $\dot{\omega}_{\text{H}_2\text{O}}/\dot{\omega}_{\text{H}_2\text{O}}^{1D} \in [0, 15]$ . . . . .	55
3.13	Temperature (top) and normalized H <sub>2</sub> O source term (bottom) contours for a section of the three-dimensional turbulent MA–MA case. . . . .	55
3.14	Flame speed history (left) and PDF of normalized flame speed (right) for the MA–MA (red) and MA–xx (blue) models. The dashed lines represent the temporal mean of the flame speeds. . . . .	56
3.15	PDF of turbulent three-dimensional flame surface area normalized by domain cross-sectional area (left) and normalized chemical source term as a function of normalized local flame curvature (right) for the MA–MA (red) and MA–xx (blue) models. The dashed lines represent the temporal mean of the flame area (left) and the laminar three-dimensional conditional means (right). . . . .	57
3.16	Statistics for the (a) cell length and (b) extinction zone length for the $L_y = 30 l_F$ computational domain. The MA–MC (solid black), MA–MA (dashed red), and MA–xx (dotted blue) cases are all presented. . . . .	58
3.17	$Y_{\text{H}_2\text{O}}$ contour plots showing the time history of a larger lobe breaking down into smaller cellular instabilities. . . . .	59
3.18	Statistics for the (a) cell length and (b) extinction zone length for the $L_y = 60 l_F$ computational domain using the MA–MA model. . . . .	60
3.19	Computational time per grid point for each part of the code for four flame configurations. All timings reported use the MA–MA model, except for the MA–MC diffusion coefficient timings. . . . .	62
4.1	Rational function fit of $\Omega_i^{(2,2)*}$ using coefficients from FlameMaster [100] (black line), tabulated data from Monchick and Mason [87] (red circles), and the fit from Rosner [105] (blue line). . . . .	67
4.2	$\Phi'_{ij}$ , computed using Eq. 4.17, as a function of $W_i/W_j \in [0.01, 100]$ , approximating the range of $W_i/W_j$ in CaltechMech [14]. . . . .	68

4.3	Thermal diffusion coefficients for H (filled symbols) and H <sub>2</sub> (open symbols) for all cases using the multicomponent model ( $D_{i,MC}^T$ ) and Eq. 4.25 (corrected to satisfy mass conservation). A zoom of the data near maximum $ D_i^T $ is provided on the right with linear axes. . . . .	71
4.4	Thermal diffusion fluxes for (a) H and (b) H <sub>2</sub> as a function of $T$ for Case 1 using the MC (solid black), MA (dotted blue), unfitted reduced (dot-dashed green), and RM (dashed red) models. Note the MC and RM cases nearly overlap, and Eq. 4.25 has been corrected to satisfy mass conservation. . . . .	72
4.5	Conditional mean of the thermal diffusion fluxes for (a) H and (a) H <sub>2</sub> as a function of $T$ for the turbulent flame case using the MC (solid black), MA (dotted blue), and RM (dashed red) models. The vertical dashed line indicates $T_{max}$ for Case 1. . . . .	74
4.6	Probability density functions of $D_H^T$ and $D_{H_2}^T$ , taken at temperatures of the peak thermal diffusion fluxes using the MC (solid black), MA (dotted blue), and RM (dashed red) models. . . . .	74
4.7	Computational cost for Eq. 4.25 (red crosses), applying the correction factor $S$ to all thermal diffusion coefficients (blue circles), total cost of $D_{i,RM}^T$ (black triangles), and a non-iterative multicomponent method [66] (green diamonds). . . . .	75
5.1	Magnitudes of the chemical source terms for the fuel (solid black), oxidizer (dot-dashed red), and the one-step chemistry approximation (dashed blue) as functions of $C$ for a one-dimensional solution of H <sub>2</sub> –air at $\phi = 0.4$ . . . . .	79
5.2	Magnitudes of the contributions to Eq. 5.7, including the convective (solid black), diffusive (dot-dashed red), and one-step chemistry approximation (dashed blue) as functions of $C$ for a one-dimensional solution of H <sub>2</sub> –air at $\phi = 0.4$ . . . . .	80
5.3	Diffusion coefficients of all species in the H <sub>2</sub> –air chemical mechanism, normalized by the thermal diffusivity $\alpha$ , as functions of $C$ for a one-dimensional solution of H <sub>2</sub> –air at $\phi = 0.4$ . . . . .	82
5.4	Magnitudes of the components of $\mathbf{j}_Z$ , given by Eq. 5.14, normalized by the thermal diffusivity, as functions of $C$ for a one-dimensional solution of H <sub>2</sub> –air at $\phi = 0.4$ . . . . .	83
5.5	Comparison of the finite-rate chemistry mass fraction profiles and mass fraction profiles under the OSIR assumption. . . . .	84

5.6	Magnitudes of the four terms in Eq. 5.21 for a one-dimensional solution of H <sub>2</sub> –air at $\phi = 0.4$ . . . . .	85
5.7	Comparison of the outlet boundary condition for $Z$ as a function of $C$ for a one-dimensional unstretched premixed hydrogen–air flame at $\phi = 0.4$ . . . . .	86
5.8	Comparison of $Z$ (solid black, computed using Eq. 5.23) and $\mathcal{Z}$ (dashed red, computed using Eq. 5.8 with a nine-species finite-rate chemistry model) as a function of $C$ for a one-dimensional unstretched premixed hydrogen–air flame at $\phi = 0.4$ . . . . .	87
5.9	Progression of the chemistry table creation, showing (a) a single flame solution at $\phi = 0.4$ , (b) the bounds of the chemistry table, (c) all flame solutions in the chemistry table, (d) all flame solutions colored by their corresponding progress variable source term, and (e) the complete chemistry table with specific regions described in Section 5.2.2. . . . .	90
5.10	Conditional mean of $\dot{\omega}_{\text{H}_2\text{O}}$ , conditioned on $C$ and $Z$ for the (a) two-dimensional unsteady and (b) three-dimensional turbulent flame configurations, computed using finite-rate chemistry. The vertical dashed lines represent $C_{peak}$ . Note that the range of the colorbar changes. . .	94
5.11	Conditional mean of $\dot{\omega}_C$ , conditioned on $C_{peak}$ and $Z$ for the two-dimensional unsteady (red diamonds) and three-dimensional turbulent flame configurations (blue squares). . . . .	94
6.1	Comparison of (a) progress variable source term and (b) mixture fraction as functions of progress variable for the one-dimensional unstretched flame at $\phi = 0.4$ . Detailed chemistry (solid black line) and tabulated chemistry (dotted red line) profiles agree very well. . .	96
6.2	(a) Comparison of the unstretched laminar flame speeds and (b) percent error in the computed flame speeds, computed using finite-rate chemistry (black crosses) and tabulated chemistry (red circles) for a range of equivalence ratios. . . . .	97
6.3	Flame speed of outwardly propagating flames, normalized by their corresponding one-dimensional unstretched laminar flame speed, as a function of normalized curvature. Detailed chemistry results (solid black) are shown along with tabulated chemistry results (dashed). The constant Lewis number tabulated chemistry model [102] is in red. . .	98

6.4	Scatter plot of the mixture fraction as a function of progress variable using tabulated chemistry with thermal diffusion for the one-dimensional outwardly-propagating cylindrical flame (red circles) at $\kappa l_F = 0.06$ . An a priori case (finite-rate chemistry transporting $Z$ ) is also shown (black crosses). The thermodynamic equilibrium line is also shown (black dot-dashed line). . . . .	99
6.5	Contours of the progress variable source term for the (clockwise from top right) detailed chemistry, tabulated chemistry with thermal diffusion, and tabulated chemistry assuming constant Lewis numbers.	100
6.6	Scatter plot of the mixture fraction as a function of progress variable for (a) all data and (b) data at small $C$ using tabulated chemistry with thermal diffusion for the two-dimensional tubular flame (red points). The one-dimensional flames contained in the chemistry table, and the thermodynamic equilibrium line, are also shown (black). . . . .	100
6.7	Profiles of the (a) maximum $\dot{\omega}_C$ and (b) radial location of maximum $\dot{\omega}_C$ as functions of the azimuthal coordinate. Cases with mixture-averaged diffusion and thermal diffusion (black) and constant Lewis number diffusion (red) are shown, using finite-rate chemistry (solid lines) and tabulated chemistry (dashed lines). . . . .	101
6.8	(Left) Contour plot of the progress variable source term with isosurface of $C_{peak}$ (dashed line) and (right) normalized progress variable source term on $C_{peak}$ isosurface for the detailed chemistry (black crosses) and $Z$ - $C$ tabulation (red circles). The y-axis is identical for both figures. . . . .	102
6.9	Contour plots of the local equivalence ratio (top) and mixture fraction (bottom), transported in a finite-rate chemistry simulation, for two time instances of the two-dimensional freely propagating flame. Both parameters are normalized by their respective inlet values. . . . .	103
6.10	Scatter plot of the mixture fraction as a function of progress variable using tabulated chemistry with thermal diffusion for the two-dimensional freely propagating flame (red points). The one-dimensional flames contained in the chemistry table, and the thermodynamic equilibrium line, are also shown (black). . . . .	104

6.11	Flame speed history (left) and PDF of normalized flame speed (right) for detailed chemistry (solid black), tabulated chemistry with thermal diffusion (dot-dashed red), and tabulated chemistry assuming constant Lewis numbers [102] (dotted blue). The vertical dashed lines represent the temporal mean of the corresponding flame speeds.	105
6.12	PDF of flame surface area normalized by domain cross-sectional area (left) and normalized product source term as a function of normalized local flame curvature (right) for detailed chemistry (solid black), tabulated chemistry with thermal diffusion (dot-dashed red), and tabulated chemistry assuming constant Lewis numbers [102] (dotted blue). The vertical dashed lines on the left figure represent the temporal mean of the flame area.	106
6.13	Two-dimensional slice of the vorticity magnitude (with isolines representing $C_{peak}/10$ (yellow) and $C_{peak}$ (red)) and progress variable source term.	107
6.14	Scatter plot of the mixture fraction as a function of progress variable using tabulated chemistry with thermal diffusion for the three-dimensional turbulent flame (red points). The one-dimensional flames contained in the chemistry table, and the thermodynamic equilibrium line, are also shown (black).	107
6.15	Flame speed history (left) and PDF of normalized flame speed (right) for detailed chemistry (solid black), tabulated chemistry with thermal diffusion (dot-dashed red), and tabulated chemistry assuming constant Lewis numbers [102] (dotted blue). The dashed lines represent the temporal mean of the flame speeds.	109
6.16	PDF of turbulent three-dimensional flame surface area normalized by domain cross-sectional area for detailed chemistry (solid black), tabulated chemistry with thermal diffusion (dot-dashed red), and tabulated chemistry assuming constant Lewis numbers [102] (dotted blue). The vertical dashed lines on the left figure represent the temporal mean of the flame area.	109
6.17	Conditional mean of the normalized progress variable source term for the detailed chemistry (black), proposed tabulated chemistry (red), and constant Lewis number tabulated chemistry (blue) models. A one-dimensional flame profile is shown for reference (dashed black line).	110

6.18	Conditional mean of the progress variable source term as a function of normalized local flame curvature for detailed chemistry (black), tabulated chemistry with thermal diffusion (red), and tabulated chemistry assuming constant Lewis numbers [102] (blue). . . . .	111
6.19	Computational time per grid point for each part of NGA for the three-dimensional turbulent configuration. The detailed chemistry (black) and proposed tabulated chemistry model (red) are shown. “Chemistry” includes the cost of computing diffusion coefficients (for detailed chemistry) and all chemistry table interpolation (for tabulated). . . . .	113
6.20	Errors of various parameters for (a) detailed chemistry and (b) tabulated chemistry for a range of simulation time step, normalized by $\psi_V^{\text{fine}}$ at $\Delta t = 0.1 \mu\text{s}$ , with a fixed $\Delta x = l_F/20$ . . . . .	115
6.21	Comparison of the error in the volume integral of the temperature for detailed chemistry (black diamonds) and tabulated chemistry (red circles), normalized by $\psi_V^{\text{fine}}$ at $\Delta t = 0.1 \mu\text{s}$ , as a function of time step. . . . .	116
6.22	Errors of various parameters for (a) detailed chemistry and (b) tabulated chemistry for a range of grid spacing, normalized by $\psi_V^{\text{fine}}$ at $l_F/\Delta x = 80$ , with a fixed $\Delta t = 1 \mu\text{s}$ . . . . .	116
6.23	Comparison of the error in the volume integral of the temperature for detailed chemistry (filled symbols) and tabulated chemistry (open symbols), normalized by $\psi_V^{\text{fine}}$ at $l_F/\Delta x = 80$ , as a function of grid spacing. . . . .	117
A.1	Rational function fits of (a) $\Omega_i^{(1,1)*}$ , (b) $\Omega_i^{(2,2)*}$ and (c) $C_{ij}^*$ (black lines), using coefficients from FlameMaster [100] and tabulated data (red circles) from Monchick and Mason [87]. . . . .	124
A.2	Power law fits (black lines) of (a) $\sigma_i$ using Eq. 4.13 and (b) $\epsilon_i/k_B$ using Eq. 4.15 as functions of $W_i$ . The fit coefficients are from FlameMaster [100] and the transport property data (symbols) are from multiple references [14]. H is the red triangle and $\text{H}_2$ is the blue circle. . . . .	125
B.1	Method of extracting cellular structures: (a) filled contour plot of $Y_{\text{H}_2\text{O}}$ , (b) isosurface of $Y_{\text{H}_2\text{O}}^{\text{iso,nom}}$ with detached pocket, (c) isosurface with pocket removed, and (d) isosurface with two cells indicated (blue and red segments), and the extinction regions between adjacent cells (green segments). . . . .	127

B.2	Depiction of the cellular instability length scales, showing two cellular instabilities (red and blue sections), and two extinction length scales (green lines). Note that one extinction region exists across the periodic boundary. . . . .	129
B.3	Varying (a) $Y_{\text{H}_2\text{O}}^{\text{iso}}$ and (b) $\dot{\omega}_{\text{H}_2\text{O}}^{\text{th}}$ for a single data file. Arrows indicate direction of increasing sensitivity variable. . . . .	130
B.4	PDF of the cell length for an isosurface of $Y_{\text{H}_2\text{O}}^{\text{iso,nom}}$ and source term threshold $\dot{\omega}_{\text{H}_2\text{O}}^{\text{th,nom}}$ for the MA–MA diffusion model. . . . .	131
B.5	Cellular instability length sensitivity maps, varying (a) $Y_{\text{H}_2\text{O}}^{\text{iso}}$ and (b) $\dot{\omega}_{\text{H}_2\text{O}}^{\text{th}}$ . Colors indicate values of the PDF. . . . .	131
B.6	Extinction zone length sensitivity maps, varying (a) $Y_{\text{H}_2\text{O}}^{\text{iso}}$ and (b) $\dot{\omega}_{\text{H}_2\text{O}}^{\text{th}}$ . Colors indicate values of the PDF. . . . .	132
B.7	$Y_{\text{H}_2\text{O}}$ contour plots showing the time history of a larger lobe breaking down into smaller cellular instabilities. . . . .	133
B.8	Flame isosurface (showing only burning regions) with two extinction zones visible: one at $l_e/l_F < 1$ and one at $l_e/l_F > 1$ . . . . .	133
B.9	Fixed $\dot{\omega}_{\text{H}_2\text{O}}^{\text{th,nom}}$ for a range of $Y_{\text{H}_2\text{O}}^{\text{iso}}$ , showing the variation in extinction length scales between two cellular structures. . . . .	134
B.10	Fixed $Y_{\text{H}_2\text{O}}^{\text{iso}}$ for a range of $\dot{\omega}_{\text{H}_2\text{O}}^{\text{th}}$ , showing the movement of extinction points (red crosses and green circles) near a highly-negative curvature cusp. . . . .	135
B.11	Cellular instability length sensitivity maps, varying (a) $T^{\text{iso}}$ and (b) $\kappa^{\text{th}}$ . Colors indicate values of the PDF. . . . .	135
B.12	Extinction zone length sensitivity maps, varying (a) $t^{\text{iso}}$ and (b) $\kappa^{\text{th}}$ . Colors indicate values of the PDF. . . . .	136

## LIST OF TABLES

<i>Number</i>	<i>Page</i>
2.1 Definitions of the diffusion model abbreviations. MC: multicomponent, MA: mixture-averaged, RM: reduced thermal diffusion model [113], FM: Fristrom and Monchick “back-of-the-envelope” [45], xx: none. . . . .	15
2.2 Parameters of the simulations. The domain is the physical dimensions of the configuration, while the grid specifies the number of computational points in the domain. . . . .	32
2.3 Parameters of the one-dimensional unstretched laminar flames using the MA–MA diffusion model. Both $l_F$ and $S_L^o$ are computed using FlameMaster [100]. . . . .	34
3.1 Cases considered to evaluate and apply the mixture-averaged thermal diffusion model. See Section 2.6 for a detailed description of the models. . . . .	43
4.1 One-dimensional flame cases used for the reduced thermal diffusion model evaluation. . . . .	70
A.1 Coefficients of the rational functions fitting $\Omega_i^{(2,2)*}$ and $C_{ij}^*$ . . . . .	123
B.1 Range of the sensitivity analysis variables. Note that the maximum considered $Y_{\text{H}_2\text{O}}^{\text{iso}}$ and $T^{\text{iso}}$ is dependent on isosurfaces remaining inside the computational domain. . . . .	129

*Chapter 1*

## INTRODUCTION

**1.1 Background and motivation**

Energy production and consumption in the United States are both projected to grow over the next several decades; natural gas is expected to have the largest absolute growth (in consumption and production) as an energy source [1]. This projection suggests that the amount of carbon dioxide produced by burning natural gas will increase at a rate of nearly 1% per year for the next 30 years. The energy outlook predictions also include a substantial growth in renewable energy production. However, every growing energy source has challenges which must be overcome. Among other difficulties, natural gas consumption releases pollutants such as carbon monoxide, carbon dioxide, unburnt hydrocarbons, and soot. Alternatively, renewable energy technologies (e.g., wind and solar) suffer from production intermittency. Solving these problems would significantly increase the impact of each energy technology.

Hydrogen combustion provides viable solutions to the natural gas and renewable energy challenges mentioned above. One proposed improvement for natural gas combustion is adding hydrogen to the natural gas mixture during the combustion process [85]. This addition (in hydrogen quantities up to 20% by volume) was found to be possible without changes to end-user devices [119]. Further, introduction of 15% hydrogen by volume to a natural gas mixture shows potential to reduce nitrogen oxide ( $\text{NO}_x$ ) emissions to 3 parts per million (ppm), comparable to other  $\text{NO}_x$  reduction strategies, with small changes to the combustor [118]. Additionally, a mixture of  $\text{H}_2$  with  $\text{CH}_4$  and air was shown to reduce  $\text{NO}_x$  emissions to levels below that of a  $\text{CH}_4$ -air mixture [78]. Alternatively, several studies have considered replacing hydrocarbon fuels entirely with premixed hydrogen mixtures [25, 26, 32, 78]. Burning hydrogen exclusively would eliminate CO,  $\text{CO}_2$ , unburnt hydrocarbon, and soot emissions.

In renewable energy applications, hydrogen can be used as a storage medium during periods of excess energy generation [47]. The excess energy could then be recovered by combusting the hydrogen in gas turbines. Burning hydrogen in this manner would use similar power plant technologies which already exist and have been shown capable of utilizing hydrogen-enriched natural gas and syngas (a mixture of  $\text{H}_2$ , CO,

and often  $\text{CO}_2$ ). The reuse of existing facilities and technology would drastically reduce implementation costs; modifications would only be necessary to the burner geometry and gas turbine [35].

The importance of understanding hydrogen combustion is not limited to the power sector, but extends also to uncontrolled (or undesired) combustion. There has been a significant increase in both construction and usage of hydrogen refueling stations for hydrogen fuel cell vehicles in California [71]. The further adoption of hydrogen powered vehicles will require informing the public of their safety [70]. Additionally, the Fukushima Daiichi nuclear reactor accident involved a hydrogen explosion at one of the reactor buildings. This failure led to multiple reports detailing the catastrophic events which resulted in a build-up of hydrogen gas and its ultimate detonation [56, 127].

This thesis investigates premixed hydrogen–air combustion, primarily for power plant applications. Being able to accurately and effectively characterize the safety of hydrogen as a fuel source requires a more complete understanding of its combustion. Further, the design process of novel burner geometries for power plant applications must include the effects of the combustion process. Of particular interest are the capabilities of numerical simulations to predict fundamental flow phenomena present in the hydrogen combustion process.

## 1.2 Premixed hydrogen combustion

This thesis focuses on premixed combustion, where the reactants (fuel, oxidizer, and often a diluent) are fully mixed prior to combustion. At stoichiometric conditions (where complete combustion of fuel and oxidizer occurs), with an unburnt temperature of  $T_u = 298 \text{ K}$  and pressure of  $p_o = 1 \text{ atm}$ , the combustion of hydrogen has a flame temperature of approximately  $T_{ad} = 2360 \text{ K}$ , where  $T_{ad}$  is the adiabatic flame temperature in the burnt mixture. This high flame temperature would generate large amounts of  $\text{NO}_x$  [97], on which government agencies have placed stringent emission standards [2]. One method to decrease  $\text{NO}_x$  emissions is to lower the flame temperature by reducing the mixture fuel-air equivalence ratio (i.e., having a fuel-lean mixture). The equivalence ratio,  $\phi$ , is defined as the mass ratio of fuel to oxidizer, normalized by the stoichiometric mass ratio of fuel to oxidizer. Reducing the equivalence ratio to a fuel-lean mixture implies having an excess of oxidizer while fully consuming the fuel.

One of the primary challenges facing adoption of lean hydrogen combustion is the

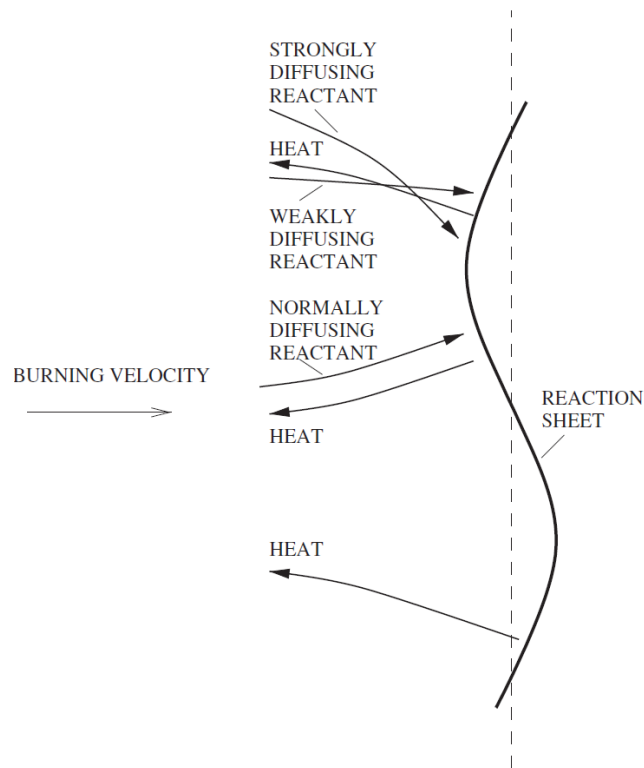


Figure 1.1: Schematic of a thermo-diffusive instability, showing relative diffusion rates toward the flame. Figure from Sánchez and Williams [107].<sup>1</sup>

presence of flame instabilities. These thermo-diffusive instabilities (which result from preferential diffusion between heat and molecular diffusion) [83, 115] cause an increase in the flame propagation speed and may lead to flame flashback, blowoff, and acoustic noise [26]. Understanding these instabilities would lead to improved combustor designs for gas turbines (e.g., the low-swirl burner [25, 26]) and the development of accident prevention measures for refueling stations and nuclear power plants (e.g., flame arresters). As part of understanding the flame instabilities, it is necessary to characterize and accurately predict the formation, structure, and effects of the flame instabilities.

### 1.3 Thermo-diffusive instabilities

The causes and effects of thermo-diffusive instabilities have been investigated theoretically [10, 27, 96], experimentally [18, 76, 86], and numerically [5, 9, 46, 51, 94, 129]. These instabilities result from unequal mass and temperature diffusivi-

<sup>1</sup>Reprinted from Progress in Energy and Combustion Science, 41, Antonio L. Sánchez and Forman A. Williams, Recent advances in understanding of flammability characteristics of hydrogen, 1–55, Copyright (2014), with permission from Elsevier.

ties, i.e., non-unity Lewis numbers where thermal diffusivity,  $\alpha$ , and species mass diffusivities,  $D_{i,m}$ , are different, and are shown schematically in Fig. 1.1. This illustration represents a flame front and the paths of various reactants. For a lean hydrogen–air flame, strongly diffusing reactants include H and H<sub>2</sub>, while weakly diffusing reactants include species such as O<sub>2</sub> and H<sub>2</sub>O<sub>2</sub>. The strongly diffusing reactants propagate toward the convex region behind the reaction sheet, resulting in an increase in heat release and temperature. This section of the reaction sheet propagates faster than the concave region, due to the increased heat release, causing the instability to grow.

The Lewis number, which helps delineate strongly diffusing species from weakly diffusing species, is defined as  $Le_i = \alpha/D_i$ , where  $\alpha$  is the thermal diffusivity and  $D_i$  is the mass diffusivity of species  $i$ . An example of the Lewis numbers for a lean hydrogen–air mixture (with an equivalence ratio of  $\phi = 0.4$ ) is shown in Fig. 1.2. For light species, such as H and H<sub>2</sub> with sub-unity Lewis numbers, the species diffuse more rapidly than temperature, causing the focusing effect of the fuel and radicals in regions of the reaction sheet convex to the unburnt mixture found in Fig. 1.1; this process has been studied extensively [5, 51, 94, 115].

In addition to differential diffusion, thermal diffusion, i.e., species flux due to temperature gradients (Soret effect) and energy flux due to species gradients (Dufour effect), may also enhance thermo-diffusive instabilities. The thermal diffusion coefficients,  $D_i^T$ , of H and H<sub>2</sub> are negative (mass diffusion in the direction of increasing temperature), leading to increased fuel diffusion toward the reaction zone [51]. This diffusion results in a strengthening of the previous fuel-focusing effect which, in turn, increases the flame speed of lean hydrogen flames in multidimensional configurations. As an example, Fig. 1.3 shows a thermo-diffusive instability along an isosurface (representing the reaction sheet) of a simulation result which will be investigated further in Chapter 3.

Diffusion and reaction rates are both critical to the formation of thermo-diffusive instabilities. Thus, extensive investigations of the models used in simulations of lean hydrogen–air combustion must be undertaken. These two effects are discussed in the following sections.

#### 1.4 Mass and thermal diffusion models

As supercomputing clusters become more powerful, the natural trend in many fields is to implement more complex physics in numerical simulations. For combustion

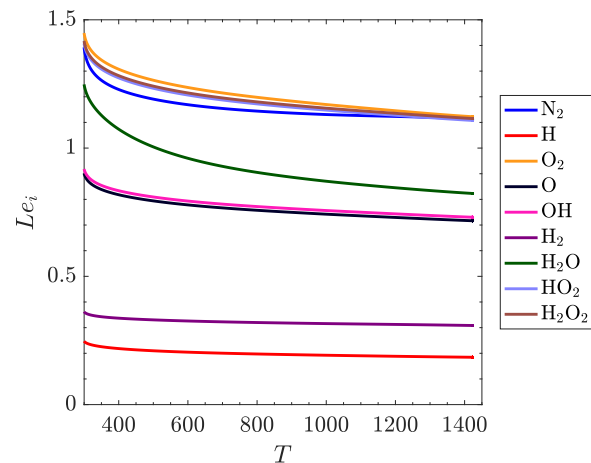


Figure 1.2: Lewis number for each species in the nine-species hydrogen model of Hong et al. [59, 60, 72] as a function of temperature.

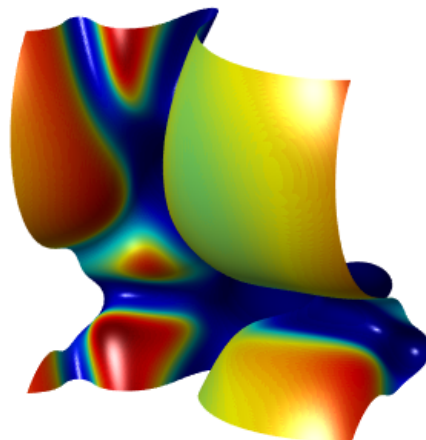


Figure 1.3: Thermo-diffusive instability in a premixed lean hydrogen–air simulation.

applications, this advancement takes many forms. First, increasingly complex domains are being considered, including three-dimensional turbulent flames [5–8, 11, 20, 33, 34]. Additional uses of the increased computing resources include detailed kinetic modeling with large chemical models (e.g., CaltechMech with 190 chemical species and 1938 reactions), refined grids which resolve turbulent features (moving toward larger direct numerical simulations), and incorporating detailed descriptions of transport properties that are frequently neglected (such as multicomponent diffusion).

A wide variety of models and computational methods have been used in the study of mass diffusion (i.e., diffusion of species due to species concentration gradients). These techniques include multicomponent, mixture-averaged, and constant Lewis number models. For the study of lean hydrogen–air flames, constant Lewis numbers

[20, 62], mixture-averaged models (with or without thermal diffusion) [3, 6–9, 11, 20, 33, 34, 46, 51], and full multicomponent diffusion with thermal diffusion [51, 53, 128] have all been used. In particular, Grcar et al. [51] showed that, for a two-dimensional flame, full multicomponent transport with thermal diffusion resulted in average flame speeds 22% higher than mixture-averaged mass diffusion neglecting thermal diffusion. Hall and Pitz [53] also showed that multicomponent and mixture-averaged mass diffusion both predicted nearly-identical flame structures. In many of these investigations, thermal diffusion is neglected.

The tendency to use mixture-averaged diffusion and neglect thermal diffusion extends from one-dimensional flames to turbulent three-dimensional flames. Further, to the author's knowledge, no thermal diffusion model has been included (multicomponent or otherwise) in a turbulent lean hydrogen flame simulation, with only limited exploration in other turbulent fuel mixtures (e.g.,  $\text{CH}_4/\text{H}_2/\text{air}$  [23], syngas [19], and high hydrogen content syngas [101]). There is a need to evaluate the importance of thermal diffusion in lean hydrogen flames, especially in three-dimensional and turbulent flame configurations.

### 1.5 Importance and inclusion of thermal diffusion

Traditional mixture-averaged diffusion models [12] and the constant Lewis number assumption both neglect thermal diffusion. A brief review of literature concerning effects of thermal diffusion on lean hydrogen–air premixed flames shows the importance of thermal diffusion in simplified configurations. In their early contributions of premixed flame theoretical analyses, García-Ybarra et al. [48] demonstrated that the Soret and Dufour effects have a non-negligible impact on hydrogen–air mixtures, especially in wrinkled configurations. Numerical results of hydrogen–air flames have demonstrated similar findings, using various levels of approximation for chemistry and diffusion, as well as different flame configurations [15, 39, 41, 51, 123, 128]. Collectively, these works indicate that thermal diffusion has a critical effect on lean hydrogen–air flames, and its influence is greater in the presence of flame curvature and stretch.

The computational cost is often the limiting factor when using the multicomponent diffusion model (where Soret and Dufour effects are typically included) in three-dimensional turbulent flame configurations. What is needed, then, are computationally-efficient models to calculate the thermal diffusion coefficients. In order to reduce the cost of applying thermal diffusion to complex three-dimensional

flames with curvature, a few reduced-order models for thermal diffusion have been proposed, in addition to iterative techniques for the multicomponent model [40]. One of the first mixture-averaged thermal diffusion models is attributed to Chapman and Cowling [24] (in particular, §18.43). This model, based on the first approximation of the thermal diffusion ratio,  $[k_{Ti}]_1$ , is derived from kinetic theory and reduces the cost of finding thermal diffusion coefficients by evaluating a simple set of algebraic equations. This is in contrast to inverting a large linear system as is done in classical multicomponent diffusion modeling [37, 66]. Recently, a semi-empirical model [66] and polynomial fits [53] for the thermal diffusion coefficients have been proposed. While a fourth-order polynomial fit seemed to predict the species profiles in a specific configuration, the polynomial was acquired a posteriori [53] and, as such, extensive work would be necessary to show that the model is valid for a range of fuel mixtures and operating conditions. Thus, there is also a need to develop and evaluate a reduced-order thermal diffusion model applicable to a wide range of fuel mixtures and flame configurations.

## 1.6 Chemistry models

Similar to mass and thermal diffusion, multiple models exist to describe all the chemical reactions occurring in hydrogen mixtures. Two common approaches, finite-rate and tabulated chemistry, are introduced in this section. Full details of the governing equations for finite-rate chemistry are provided in Section 2.3.1, while derivations involving tabulated chemistry are the focus of Chapter 5.

### 1.6.1 Brief overview of finite-rate chemistry

Finite-rate chemistry (or, equivalently, detailed chemistry) describes the complete combustion process from a fuel and oxidizer mix to the products. Whereas a global reaction might be given as  $2\text{H}_2 + \text{O}_2 \longrightarrow 2\text{H}_2\text{O}$ , finite-rate chemistry instead solves elementary reactions. Several critical reactions included in these mechanisms include the decomposition of the fuel ( $\text{H}_2 + \text{O} \longrightarrow \text{OH} + \text{H}$ ) and oxidizer ( $\text{H} + \text{O}_2 \longrightarrow \text{OH} + \text{O}$ ), as well as product formation ( $\text{H}_2 + \text{OH} \longrightarrow \text{H} + \text{H}_2\text{O}$  and  $\text{OH} + \text{H} \longrightarrow \text{H}_2\text{O}$ ). These elementary reactions not only demonstrate physical collisions between molecules, but they also help in identifying reactions which may accelerate the chemistry (chain-branching reactions) or terminate the reactions (chain-breaking reactions).

The previously mentioned elementary reactions are only a small selection of those implemented in finite-rate chemistry. For example, one common hydrogen–air

chemical model contains nine species participating in 54 chemical reactions (forward and backward reactions counted separately) [59]. Chemical models describing hydrocarbon combustion can contain hundreds of species and thousands of reactions [14]. These reactions are described using Arrhenius reaction rates fit to experimental data. In simulations using finite-rate chemistry, one transport equation is required for each species, and the computation of chemical source terms requires considering each reaction that a species participates in. A description of the finite-rate chemistry equations is given in Section 2.3.1.

### 1.6.2 Tabulated chemistry

Tabulated chemistry reduces the number of partial differential equations from one equation per chemical species in the mixture (potentially in the hundreds) to only a few (often one or two). This chemistry reduction technique has been used widely in various forms, e.g., intrinsic low-dimensional manifolds (ILDM) [80], the flamelet prolongation of ILDM (FPI) [49], flamelet generated manifolds (FGM) [90], and the flamelet/progress variable method (FPV) [68, 69, 99], among others. Chemistry tabulation finds significant use in turbulent flame configurations using both direct numerical simulations and large eddy simulations [44, 89, 122].

Tabulation on a single reaction progress variable,  $C$ , has been considered in the past (see, among others, [89–91]), leading to a transport equation of the form

$$\partial_t (\rho C) + \nabla \cdot (\rho \mathbf{u} C) = \nabla \cdot (\rho D_C \nabla C) + \rho \dot{\omega}_C. \quad (1.1)$$

In this equation,  $\mathbf{u}$  is the velocity,  $\rho$  is the gas density,  $D_C$  represents the diffusion coefficient of the progress variable, and  $\dot{\omega}_C$  is the progress variable source term. Note that a progress variable represents the completeness of the governing global reaction and often takes the form of fuel or product mass fractions.

Tabulating the chemistry on only a progress variable from one-dimensional unstretched flames does not capture stretch or curvature effects [89, 91]. These effects play a significant role in thermo-diffusive instabilities and turbulent flames (e.g., altering the flame structure, chemical source terms, and flame speed [4, 34, 109]); thus, inclusion of curvature or stretch in tabulated chemistry models is critical. Previous works have explored methods to include stretch and curvature by either changing the underlying one-dimensional flames (e.g., stretched flames) or changing the tabulation variables. Several of these methods include using constant stretch or curvature in one-dimensional flames [89], varying the unburnt mixture properties of

the one-dimensional flames [9], and using a mixture fraction-like tabulation variable ( $Z$ ) to capture local equivalence ratio fluctuations [102].

Regele et al. re-derived a mixture fraction transport equation allowing for differential diffusion (i.e., non-unity Lewis numbers) [102]. The mixture fraction,  $Z$ , is a measure of local equivalence ratio, most commonly found in diffusion flame literature. In those flames,  $Z$  typically ranges from 0 (pure fuel) to 1 (pure oxidizer). By adding a differential diffusion term to the  $Z$  transport equation, Regele et al. were able to create a mixture-fraction like variable for premixed flames; their equation for  $Z$  was [102]

$$\partial_t (\rho Z) + \nabla \cdot (\rho \mathbf{u} Z) = \nabla \cdot (\rho D_Z \nabla Z) - \nabla \cdot (\rho D_Z^* \nabla C) . \quad (1.2)$$

The mixture fraction diffusivity,  $D_Z$ , and cross-diffusivity,  $D_Z^*$ , were given by

$$D_Z = D \left[ 1 + \left( \frac{1}{Le} - 1 \right) (1 - Z) \right] \quad (1.3)$$

and

$$D_Z^* = D \left( \frac{1}{\nu + 1} \right) \left( \frac{1}{Le} - 1 \right) (1 - Z) , \quad (1.4)$$

where  $\nu$  is the mass stoichiometric ratio (defined in Section 5.1.1) and  $Le$  is the fuel Lewis number. Equation 1.2 was then solved in conjunction with Eq. 1.1 in their tabulated chemistry approach.

The fluctuations in mixture fraction (due to  $D_Z^*$ ) can be thought of as fluctuations in the local equivalence ratio by considering a one-step irreversible chemistry approximation. This phenomenon arises via the increased transport of light species and focusing/de-focusing effects (due to differential diffusion) of the fuel behind curved regions of the flame as discussed in Section 1.3. These fluctuations are critical in predicting the behavior of lean  $H_2$ -air flames as they promote the growth of thermo-diffusive instabilities [125]. The  $Z$ - $C$  model of Regele et al. [102] was shown to capture some curvature effects in lean  $H_2$ -air and rich propane-air flames [102]. However, several limiting assumptions were made in the development of the model, i.e., using unity Lewis numbers (with a constant, non-unity fuel Lewis number) and neglecting thermal diffusion, both of which play critical roles in local and global flame properties [114]. Additionally, the model verification and evaluation only considered comparisons in one- and two-dimensional flames, and few quantifiable comparisons were given.

## 1.7 Objectives and outline

The overall goal of this thesis is to quantify the effects of various modeling strategies on the global and local flame structure of lean premixed hydrogen–air flames. A particular focus is the evaluation of computationally efficient methods of calculating transport and chemistry properties. These goals will be met by completing the following objectives:

1. Determine which physical phenomena are necessary to include for accurate predictions of lean premixed hydrogen–air flame structures;
2. Evaluate Chapman and Cowling’s mixture-averaged thermal diffusion model [24];
3. Reduce computational costs of thermal diffusion by deriving a reduced-order transport model;
4. Include differential diffusion and thermal diffusion in the development of a new tabulated chemistry model;
5. Quantify the performance of the newly developed models through comparisons with multicomponent diffusion and finite-rate chemistry.

In performing these evaluations, there are several baseline test scenarios upon which all comparisons are drawn: for the one- and two-dimensional simulations evaluating the mixture-averaged thermal diffusion model, the benchmark test case is a detailed chemistry direct numerical simulation (DNS) with mixture-averaged mass diffusion and multicomponent thermal diffusion. For the three-dimensional cases investigating thermal diffusion, comparisons are made between mixture-averaged mass diffusion with and without mixture-averaged thermal diffusion (multicomponent thermal diffusion is not considered in the three-dimensional configurations due to the large computational expense). The baseline case for all tabulated chemistry work is a detailed chemistry DNS with mixture-averaged mass and thermal diffusion.

The thesis is structured as follows. The governing equations and numerical solver are detailed in Chapter 2. Chapter 3 presents the evaluation of Chapman and Cowling’s thermal diffusion model [24], fulfilling Objectives 1 and 2. Objective 3 and portions of Objective 5 are satisfied by providing a derivation for a reduced-order thermal diffusion model and comparisons with multicomponent thermal diffusion in Chapter 4. Development of a tabulated chemistry model, including differential

and thermal diffusion, is presented in Chapter 5; this chemistry model is then investigated in Chapter 6, completing Objectives 4 and 5. Conclusions and possible future directions for this work are given in Chapter 7.

## Chapter 2

### GOVERNING EQUATIONS AND SIMULATION METHODOLOGY

In this chapter, the governing equations for variable density, low Mach number, reacting flows are first presented. After the governing equations are given, descriptions of the transport property models and chemistry techniques considered in this thesis are provided. Then, details of the numerical methods used to solve the reacting flows are given. A special case of the transport equations for a tubular flame configuration is given. Finally, all flame configurations used in this work are detailed.

#### 2.1 Governing equations

The variable density, low Mach number, reacting flow equations are solved using the finite difference code NGA [36]; the numerical methods used to solve these equations are described in Section 2.4.

The low Mach number approximation arises from the desire to decouple the energy and momentum equations such that acoustic waves need not be resolved. This formulation of the governing equations has been reviewed in many works, e.g., Majda and Sethian [81] and Day and Bell [31]; a brief description of the approximation is given here. By expressing all desired flow quantities using a regular perturbation of the small parameter  $M^2$ , where  $M$  is the Mach number, it can be approximated that the leading order term for pressure must be spatially uniform, and thus does not appear in the momentum equation. This leading order term, denoted  $p_o$ , is referred to as the *thermodynamic* pressure. The next contribution to pressure, denoted  $p$ , is small (of order  $M^2$ ) and is thus neglected in the equation of state. However, this pressure does appear in the momentum equation and is referred to as the *hydrodynamic* pressure. Under this approximation, the conservation equations are given as

$$\frac{\partial \rho}{\partial t} + \nabla \cdot \rho \mathbf{u} = 0 \quad (2.1)$$

$$\frac{\partial \rho \mathbf{u}}{\partial t} + \nabla \cdot (\rho \mathbf{u} \otimes \mathbf{u}) = -\nabla p + \nabla \cdot \boldsymbol{\tau} \quad (2.2)$$

$$\frac{\partial \rho T}{\partial t} + \nabla \cdot (\rho \mathbf{u} T) = \nabla \cdot (\rho \alpha \nabla T) + \dot{\omega}_T - \frac{1}{c_p} \sum_i c_{p,i} \mathbf{j}_i \cdot \nabla T + \frac{\rho \alpha}{c_p} \nabla c_p \cdot \nabla T \quad (2.3)$$

$$\frac{\partial \rho Y_i}{\partial t} + \nabla \cdot (\rho \mathbf{u} Y_i) = -\nabla \cdot \mathbf{j}_i + \rho \dot{\omega}_i, \quad (2.4)$$

where  $\rho$  is the mixture density,  $\mathbf{u}$  is the velocity,  $p$  is the hydrodynamic pressure,  $\boldsymbol{\tau}$  is the viscous stress tensor,  $T$  is the temperature,  $\alpha$  is the mixture thermal diffusivity,  $\dot{\omega}_T$  is the temperature source term,  $c_p$  is the mixture specific heat capacity,  $c_{p,i}$  is the species specific heat capacity,  $\mathbf{j}_i$  is the species diffusion flux,  $Y_i$  is the mass fraction of species  $i$ , and  $\dot{\omega}_i$  is the production rate of species  $i$ . The viscous stress tensor is given by

$$\boldsymbol{\tau} = \mu \left( \nabla \mathbf{u} + (\nabla \mathbf{u})^T \right) - \frac{2}{3} \mu (\nabla \cdot \mathbf{u}) \mathbf{I}, \quad (2.5)$$

where  $\mu$  is the dynamic viscosity of the mixture and  $\mathbf{I}$  is the identity tensor. Bulk viscosity is not considered as its influence is often small in low Mach number flows [50]. The temperature source term is given by  $\dot{\omega}_T = - (c_p)^{-1} \sum_i h_i(T) \dot{\omega}_i$  with species specific enthalpies as a function of temperature,  $h_i(T)$ . The equation of state is given by the perfect gas law

$$\rho = \frac{p_o W}{RT}, \quad (2.6)$$

where  $p_o$  is the thermodynamic pressure (a constant value is used for this thesis),  $R$  is the universal gas constant, and  $W = [\sum_i Y_i / W_i]^{-1}$  is the mixture molecular weight. The above  $(7 + N)$  equations (conservation of mass, momentum, energy, and chemical species, the equation of state, and  $W$ ), where  $N$  is the number of chemical species considered, form a closed set of equations. These equations may be solved for the  $(7 + N)$  unknown variables ( $p$ ,  $\mathbf{u}$ ,  $T$ ,  $Y_i$ ,  $\rho$ ,  $W$ ), respectively, assuming the thermodynamic pressure is defined at every time instant. It should be noted that the hydrodynamic pressure field is found through a Poisson equation to satisfy mass conservation, while the thermodynamic pressure is specified as an input parameter.

The species diffusion flux, for a mixture-averaged diffusion model (considered for nearly all of this work), is defined as

$$\mathbf{j}_i = -\rho Y_i D_{i,m} \frac{\nabla X_i}{X_i} - D_i^T \frac{\nabla T}{T} + \rho Y_i \mathbf{u}_c, \quad (2.7)$$

where  $D_{i,m}$  is the mixture-averaged mass diffusion coefficient of species  $i$ ,  $X_i$  are the species mole fractions,  $D_i^T$  are the species thermal diffusion coefficients, and  $\mathbf{u}_c$  is a correction velocity used to ensure zero net diffusion mass flux [28, 65]. The mass and thermal diffusion coefficients are defined in Section 2.2.

It is convenient to define the correction velocity such that it contains separate corrections for mass diffusion and thermal diffusion by using

$$\mathbf{u}_c = \mathbf{u}_c^D + \mathbf{u}_c^T. \quad (2.8)$$

These correction velocities are evaluated by requiring zero net diffusion flux, i.e.,  $\sum_i \mathbf{j}_i = 0$ , and matching each correction velocity with its corresponding diffusion terms, yielding

$$\mathbf{u}_c^D = \frac{\nabla W}{W} \sum_i D_{i,m} Y_i + \sum_i D_{i,m} \nabla Y_i \quad (2.9)$$

and

$$\mathbf{u}_c^T = \frac{1}{\rho} \frac{\nabla T}{T} \sum_i D_i^T. \quad (2.10)$$

## 2.2 Transport property definitions

The transport property and diffusion models considered for this work are detailed in the following section. As a variety of diffusion models are implemented, Table 2.1 lists all of the diffusion models, and their abbreviated names, used.

### 2.2.1 Conductivity and viscosity models

The mixture thermal conductivity is defined as [84]

$$\lambda = \frac{1}{2} \left( \sum_{i=1} X_i \lambda_i + \left[ \sum_{i=1} \frac{X_i}{\lambda_i} \right]^{-1} \right) \quad (2.11)$$

and the mixture viscosity is modeled using an identical form [74]

$$\mu = \frac{1}{2} \left( \sum_{i=1} X_i \mu_i + \left[ \sum_{i=1} \frac{X_i}{\mu_i} \right]^{-1} \right). \quad (2.12)$$

The species thermal conductivity,  $\lambda_i$ , is given by a modified Eucken formulation [42], and the species viscosity,  $\mu_i$ , is given using its traditional kinetic theory definition [58]. The mixture thermal diffusivity is then computed using the mixture thermal conductivity and specific heat capacity

$$\alpha = \frac{\lambda}{\rho c_p}. \quad (2.13)$$

These chosen viscosity and conductivity models have been widely implemented in previous works for a range of configurations [23, 67, 74, 103, 124, 130], and can be found in standalone transport property packages (e.g., CHEMKIN [66]). While more precise transport properties based on Chapman-Enskog theory are available, the chosen viscosity and conductivity definitions are not particularly important for the analyses in this thesis. This work focuses on diffusion and chemistry model development and validation; the use of any reasonable conductivity and viscosity model is sufficient, provided the same transport models are used for all comparisons [53].

Table 2.1: Definitions of the diffusion model abbreviations. MC: multicomponent, MA: mixture-averaged, RM: reduced thermal diffusion model [113], FM: Fristrom and Monchick “back-of-the-envelope” [45], xx: none.

Mass diffusion	Thermal diffusion
MA	MC
	MA
	RM
	FM
	xx

### 2.2.2 Mixture-averaged mass diffusion model

The mixture-averaged (MA) mass diffusion model is used throughout the entirety of this work. This diffusion model defines mass diffusion coefficients as [12]

$$D_{i,m} = \frac{1 - Y_i}{\sum_{j \neq i} X_j / \mathcal{D}_{ij}}, \quad (2.14)$$

where  $\mathcal{D}_{ij}$  is the binary diffusion coefficient between species  $i$  and  $j$ , defined as

$$\mathcal{D}_{ij} = \frac{3}{16} \frac{\sqrt{2\pi k_B^3 T^3 / m_{ij}}}{p\pi\sigma_{ij}^2 \Omega_{ij}^{(1,1)*}}. \quad (2.15)$$

In this expression,  $m_{ij} = m_i m_j / (m_i + m_j)$  is the reduced molecular mass of the  $i$ - $j$  species pair for species with molecular mass  $m_i$ . Similarly,  $\sigma_{ij} = (\sigma_i + \sigma_j) / 2$  is the collision diameter of the  $i$ - $j$  species pair for species with collision diameter  $\sigma_i$ . The values of  $\sigma_i$  are found from Davis et al. [30]. Further,  $\Omega_{ij}^{(1,1)*}$  is a collision integral which is fit to experimental data [87]. A fit of  $\Omega^{(1,1)*}$  is provided in Appendix A.1.

The mixture-averaged mass diffusion model is an approximation of multicomponent mass diffusion. The MA model computes diffusion coefficients from only the first term of a convergent series expansion of the diffusion matrix (see, for example, Giovangigli [50]). The importance of multicomponent mass diffusion has been considered in other works for a variety of flame configurations and mixtures [19, 39, 50]. In these studies, planar hydrogen–air and turbulent syngas configurations were investigated; these are also just a few examples of investigations comparing multicomponent and mixture-averaged diffusion. It was found that the necessity of multicomponent mass diffusion over mixture-averaged mass diffusion was not important compared to the neglect of thermal diffusion effects (discussed in Section 2.2.3). For example, at their lowest equivalence ratio for a hydrogen–air mixture,

Ern and Giovangigli [39, 50] found the flame speeds computed using multicomponent mass diffusion and mixture-averaged mass diffusion (both neglecting thermal diffusion) were identical, while a 10% difference was found by including thermal diffusion. Thus, multicomponent mass diffusion is not considered in this work. However, ongoing analysis of the impact and accuracy of mixture-averaged mass diffusion compared to the multicomponent model in turbulent flames is under investigation through a collaboration with another university [43].<sup>1</sup> A detailed analysis of the necessity, accuracy, and efficient implementations of the multicomponent mass diffusion model is ongoing, but beyond the scope of this thesis.

### 2.2.3 Thermal diffusion models

Several thermal diffusion models are considered throughout this work. The primary model is the mixture-averaged thermal diffusion (MA) model proposed by Chapman and Cowling [24]. In Chapter 3, this technique is compared to the multicomponent thermal diffusion (MC) model, a simplified “back-of-the-envelope” model proposed by Fristrom and Monchick (FM) [45], and a newly developed reduced model (RM) which will be described in full in Chapter 4. Computational costs of the MC and MA models will be discussed in Section 3.7.3.

#### Multicomponent thermal diffusion model (MC)

The most complete thermal diffusion model is the multicomponent (MC) thermal diffusion formulation. The MC thermal diffusion model will be used in many of the configurations as a validation tool for the simpler thermal diffusion techniques. Multicomponent thermal diffusion is based on Chapman-Enskog theory; this traditional kinetic theory has been explored and described in classic texts for decades [12, 24, 37, 58]. Thermal diffusion coefficients for the multicomponent model are computed using CHEMKIN II routines [66]. Computing thermal diffusion coefficients involves simply calling the MCMCDT subroutine of CHEMKIN II and passing the local pressure, temperature, and species mole fractions. This subroutine then inverts the linear system given by

$$\overbrace{\begin{bmatrix} L^{00,00} & L^{00,10} & 0 \\ L^{10,00} & L^{10,10} & L^{10,01} \\ 0 & L^{01,10} & L^{01,01} \end{bmatrix}}^{\mathbf{L}} \overbrace{\begin{bmatrix} a_{00}^1 \\ a_{10}^1 \\ a_{01}^1 \end{bmatrix}}^{\mathbf{a}} = \overbrace{\begin{bmatrix} 0 \\ \mathbf{X} \\ \mathbf{X} \end{bmatrix}}^{\mathbf{X}}. \quad (2.16)$$

<sup>1</sup>The author of this thesis is a co-author on the paper and presentation of Fillo, Schlup, Blanquart, and Niemeyer, 10th Meeting of the WSSCI, Laramie, WY, 2017.

Each element in the  $\mathbb{L}$  matrix is an  $N \times N$  block sub-matrix (where  $N$  is the number of species in the chemical model). The vector  $\mathbf{X} = [X_1, X_2, \dots, X_N]$  (contained in  $\mathbb{X}$ ) consists of the mole fractions of each species [66]. Each component of the seven  $L$  block sub-matrices can be found in Dixon-Lewis [37]. This linear system must be solved at each grid point and at each computational time step. Then, the thermal diffusion coefficients are found via

$$D_i^T = \frac{8m_i X_i}{5R} a_{i00}^1. \quad (2.17)$$

### Mixture-averaged thermal diffusion model (MA)

The mixture-averaged thermal diffusion model of Chapman and Cowling is thoroughly investigated and validated in Chapter 3, as it is computationally efficient due to its formulation. Following Paul and Warnatz [95], the thermal diffusion ratio,  $k_{Ti}$ , can be used to relate thermal diffusion coefficients to mixture-averaged mass diffusion; this can be seen by rewriting  $\mathbf{j}_i$  as

$$\mathbf{j}_i = -\rho \frac{W_i}{W} D_{i,m} \left( \nabla X_i + k_{Ti} \frac{\nabla T}{T} \right) + \rho Y_i \mathbf{u}_c, \quad (2.18)$$

or, for the thermal diffusion coefficients themselves,

$$D_i^T = \rho \frac{W_i}{W} D_{i,m} k_{Ti}. \quad (2.19)$$

Here,  $W_i$  is the species molecular weight. Chapman and Cowling proposed a first order approximation of the thermal diffusion ratio [24]

$$[k_{Ti}]_1 = \frac{W^2}{R\rho} \sum_j \frac{1.2C_{ij}^* - 1}{\mathcal{D}_{ij}} \frac{Y_i a_j - Y_j a_i}{W_i + W_j}, \quad (2.20)$$

where  $C_{ij}^*$  is a ratio of collision integrals given by [37]

$$C_{ij}^* = \frac{1}{3} \frac{\Omega_{ij}^{(1,2)}}{\Omega_{ij}^{(1,1)}} \quad (2.21)$$

and  $a_i$  is given by [93]

$$a_i = \lambda_{i,mon} \left[ 1 + \frac{1.065}{2\sqrt{2}X_i} \sum_{j \neq i} X_j \Phi_{ij} \right]^{-1}. \quad (2.22)$$

In Eq. 2.22, the species conductivities,  $\lambda_{i,mon}$ , are approximated using their monatomic values [24]

$$\lambda_{i,mon} = \frac{15 R \mu_i}{4 W_i} \quad (2.23)$$

and  $\Phi_{ij}$  is given by [93]

$$\Phi_{ij} = \frac{\left[1 + \left(\frac{\mu_i}{\mu_j}\right)^{1/2} \left(\frac{w_j}{w_i}\right)^{1/4}\right]^2}{\left[1 + \left(\frac{w_i}{w_j}\right)\right]^{1/2}}. \quad (2.24)$$

All collision integrals and  $C_{ij}^*$  are computed using rational polynomial fits of tabulated data from Monchick and Mason [87]. These fits, shown in Appendix A.1, are a function of the Lennard-Jones reduced temperature,  $T_{ij}^* = Tk_B/\epsilon_{ij}$ , where  $\epsilon_{ij} = (\epsilon_i\epsilon_j)^{1/2}$  is the interaction well depth between species  $i$  and  $j$ , and  $k_B$  is the Boltzmann constant. Once the thermal diffusion coefficients have been calculated, the diffusion flux given in Eq. 2.7 is used in the species and energy conservation equations.

### Fristrom and Monchick's thermal diffusion model (FM)

The so-called ‘‘back-of-the-envelope’’ thermal diffusion model, given by Fristrom and Monchick (FM) [45], computes the thermal diffusion coefficients using Eq. 2.19, where now  $k_{Ti}$  is defined to be

$$k_{Ti} = X_i \sum_{j \neq i} X_j \alpha_{ij}. \quad (2.25)$$

Here,  $\alpha_{ij}$  is defined as

$$\alpha_{ij} \approx 0.39 \sigma_{ij}^2 m_{ij}^{3/2} (\epsilon_{ij}/k_B)^{0.17} \times \left( \frac{1}{\sigma_j^2 (\epsilon_j/k_B)^{0.17} m_j^{3/2} B_j} - \frac{1}{\sigma_i^2 (\epsilon_i/k_B)^{0.17} m_i^{3/2} B_i} \right), \quad (2.26)$$

and  $B_j$  is defined as

$$B_j = X_j + \sum_{i \neq j} \left( 1 + \frac{\sigma_i}{\sigma_j} \left( \frac{\epsilon_j/k_B}{\epsilon_i/k_B} \right)^{0.085} \right)^2 \left[ 8 \left( 1 + \frac{m_j}{m_i} \right) \right]^{-1/2}. \quad (2.27)$$

### Reduced thermal diffusion model (RM)

Finally, the reduced model (RM) for H and H<sub>2</sub> thermal diffusion [113] is derived from the thermal diffusion model of Chapman and Cowling [24]. The primary advantage of this model is that the computation of  $D_i^T$  for species  $i$  no longer requires information about all other species; instead, each thermal diffusion coefficient for H

and  $\text{H}_2$  may be computed independent of the remaining species, drastically reducing computational costs (see Section 4.3.3). While a full description of the model development is one focus of Chapter 4, a brief description is given here.

The reduced model considers mixture-averaged mass diffusion for all chemical species and thermal diffusion acting on H and  $\text{H}_2$  only, while maintaining  $\sum \mathbf{j}_i = 0$  for the remaining terms. The model development in Chapter 4 indicates that the thermal diffusion coefficients for H and  $\text{H}_2$  can be expressed as

$$D_{i,RM}^T \equiv -\alpha_i \frac{15 X_i \mu_i}{4 \Phi_{i,m}} \left( 1.2 C_{i,m}^* - 1 \right) (1 - Y_i) - Y_i S, \quad (2.28)$$

where  $\alpha_i$  are scaling parameters which correct for systematic errors made in the model development, and  $S$  is a scalar which enforces mass conservation via the thermal diffusion fluxes, i.e.,  $\sum_i D_{i,RM}^T = 0$ . It is found that  $\alpha_{\text{H}} = 0.895$  and  $\alpha_{\text{H}_2} = 0.910$ .  $\Phi_{i,m}$  and  $C_{i,m}$  are fully expressed in Chapter 4, and depend only on properties of H and  $\text{H}_2$ .

## 2.3 Chemistry models

Two chemistry models are investigated; the first is the finite-rate chemistry description which makes no assumptions, and considers the detailed chemical reactions of a hydrogen–air mixture. The second chemistry model simplifies the description of the chemical processes by constructing a low-dimensional manifold, through which thermo-chemical properties can be extracted.

### 2.3.1 Finite-rate chemistry

The hydrogen chemistry model used throughout this work is the hydrogen model from Hong et al. [59]. A few of the rate constants for this chemical model have been updated recently using experimental data from the same group [60, 72]. The chemical model contains nine species with  $\text{N}_2$  serving as a non-reacting species (i.e., diluent). The model also contains 54 chemical reactions, considering both forward and backward reactions. When other chemistry models are used (primarily in Chapter 4), they will be detailed specifically.

For a chemical model containing  $N$  species and  $K$  reactions (forward and backward reactions counted separately), the chemical source terms for species  $i$  can be decomposed into

$$\dot{\omega}_i = \dot{\omega}_i^+ - \dot{\omega}_i^-, \quad (2.29)$$

where  $\dot{\omega}_i^+$  and  $\dot{\omega}_i^-$  are the production and consumption rates of species  $i$ , respectively. The production rate term considers all chemical reactions where species  $i$  is

produced, yielding the expression

$$\dot{\omega}_i^+ = \frac{W_i}{\rho} \sum_{\substack{j=1 \\ \nu_{ji} > 0}}^r \left[ \nu_{ji} k_j \prod_{\substack{s=1 \\ \nu_{js} < 0}}^N \left( \frac{\rho Y_s}{W_s} \right)^{-\nu_{js}} \right]. \quad (2.30)$$

Similarly, the consumption rate term considers all chemical reactions where species  $i$  appears as a reactant, with the form

$$\dot{\omega}_i^- = -\frac{W_i}{\rho} \sum_{\substack{j=1 \\ \nu_{ji} < 0}}^r \left[ \nu_{ji} k_j \prod_{\substack{s=1 \\ \nu_{js} < 0}}^N \left( \frac{\rho Y_s}{W_s} \right)^{-\nu_{js}} \right]. \quad (2.31)$$

In these expressions,  $r$  is the number of chemical reactions containing species  $i$  and  $\nu_{ji}$  is the stoichiometric coefficient of species  $i$  in reaction  $j$ . The stoichiometric coefficients are positive when species  $i$  is a product, and negative when species  $i$  is a reactant, in the given chemical reaction. Finally, the reaction rate constant for reaction  $j$ ,  $k_j$ , is given in an Arrhenius form,

$$k_j(T) = A_j T^{b_j} \exp^{-E_{a,j}/RT}, \quad (2.32)$$

where  $E_{a,j}$  is the activation energy for this reaction and  $b_j$  is an empirical parameter found in the chemistry models.

### 2.3.2 Tabulated chemistry

In general, tabulated chemistry operates under the principle of using a low-dimensional manifold (i.e., chemistry table) to describe the chemical processes in a reacting mixture. This class of chemistry reduction techniques has been used widely in various forms, e.g., intrinsic low-dimensional manifolds (ILDM) [80], flamelet prolongation of ILDM (FPI) [49], flamelet generated manifolds (FGM) [90], and flamelet/progress variable method (FPV) [68, 69, 99] (among others), and finds significant use in turbulent flame configurations using both direct numerical simulations and large eddy simulations (e.g., [44, 89, 122]).

In their review of state-of-the-art tabulation methods, van Oijen et al. [92] detail many uses of flamelet-generated manifolds; the reader is referred to this work for a complete review of existing literature. In particular, these manifold methods were shown to perform well in premixed, partially premixed, and non-premixed laminar flames. Further, flame-turbulence interactions of a unity Lewis number fuel

mixture (from van Oijen et al. [91]) and the effects of differential diffusion in a methane/hydrogen fuel mixture using a two-parameter manifold (constructed with stretched flamelets) were reviewed. However, no discussion on pure hydrogen–air mixtures was given, and direct comparisons with finite-rate chemistry solutions were sparse.

While many methodologies of tabulated chemistry exist, the method used here closely resembles the flamelet/progress variable (FPV) approach [68, 69, 99]. The chemistry table approach considered in this work transports two controlling parameters: a progress variable,  $C$ , and a mixture fraction-like variable,  $Z$ . Each of these variables is transported using a scalar transport equation, and thus is quite simple to implement in the pre-existing NGA framework. After  $C$  and  $Z$  have been transported, all necessary fluid and thermo-chemical properties can then be retrieved, e.g.,  $\rho = \rho(C, Z)$ ,  $D_C = D_C(C, Z)$ , or  $\dot{\omega}_C = \dot{\omega}_C(C, Z)$ , where  $D_C$  is the diffusion coefficient of the progress variable. The reduction in the number of transported scalars is one contributing factor to the cost reduction using tabulated chemistry. Additionally, the removal of stiff chemistry source terms (i.e., elementary reactions which have very small time scales and often involve short-lived intermediate species) permits reduced computational costs through increased time step size and a larger grid spacing. The proposed tabulated chemistry model will be detailed in Chapter 5 and investigated in Chapter 6.

## 2.4 Numerics of the NGA flow solver

NGA solves the low Mach number reacting flow equations (Eqs. 2.1 – 2.6) and discretely conserves mass, momentum, and kinetic energy [36]. This software can simulate three-dimensional reacting flows in complex geometries with either uniform or non-uniform structured grids. For this thesis work, one-, two-, and three-dimensional configurations are considered using uniform grids. In the following sections, a high-level overview of the time integration, discretization procedure, pressure solvers, velocity scheme, and scalar transport scheme are given. Novel contributions of this thesis to the NGA framework will be explicitly stated.

### 2.4.1 Semi-implicit time integration<sup>2</sup>

NGA uses a second-order in time semi-implicit Crank-Nicolson scheme [98] to advance the simulation variables. In the description of one time step given below, a

---

<sup>2</sup>The semi-implicit time integration discussion in this section follows closely that of Savard et al., *J. Comput. Phys.* 295 (2015) 740 – 769.



in order to discretely conserve mass prior to beginning the iterative procedure [98]. Finally, the vector of chemical source terms,  $\mathbf{\Omega} = [\dot{\omega}_1, \dots, \dot{\omega}_N]$ , has a corresponding (non-preconditioned) initial guess computed using thermo-chemical properties from the converged previous time step,  $\mathbf{\Omega}_0^{n+3/2}$ . The treatment of the chemical source terms is addressed in Section 2.4.2 [112].

For each subiteration  $k = [0, \dots, Q]$ , the following five steps are performed in order: advance the scalar field, calculate the density field, predict the velocity field (without satisfying continuity), solve a pressure Poisson equation and apply to the velocity field (thus satisfying mass conservation), and update the solution. The details of this methodology are presented in Savard et al. [112], and a brief overview is included here.

1. The scalar fields are advanced in time using the semi-implicit Crank-Nicolson method. First, one defines  $\mathbf{Y}_k^*$ ,

$$\mathbf{Y}_k^* = \frac{\mathbf{Y}^{n+1/2} + \mathbf{Y}_k^{n+3/2}}{2}, \quad (2.35)$$

such that the scalar transport equation can be discretized, and one iteration of the semi-implicit scheme thus requires solving

$$\begin{aligned} \rho_k^{n+3/2} \mathbf{Y}_{k+1}^{n+3/2} &= \rho^{n+1/2} \mathbf{Y}^{n+1/2} + \Delta t [(\mathbf{C} + \mathbf{D})_k^{n+1} \cdot \mathbf{Y}_k^* + \mathbf{\Omega}_k^*] \\ &+ \frac{\Delta t}{2} \left( \frac{\partial \mathbf{C}}{\partial \mathbf{Y}} + \frac{\partial \mathbf{D}}{\partial \mathbf{Y}} \right)_k^{n+1} \cdot (\mathbf{Y}_{k+1}^{n+3/2} - \mathbf{Y}_k^{n+3/2}). \end{aligned} \quad (2.36)$$

Here,  $\mathbf{C}$  and  $\mathbf{D}$  are abbreviated notations for the convective and diffusive terms in the scalar transport equation, respectively. Similarly,  $\partial \mathbf{C} / \partial \mathbf{Y}$  and  $\partial \mathbf{D} / \partial \mathbf{Y}$  are the Jacobian matrices of the convective and diffusive terms, respectively.  $\mathbf{\Omega}_k^*$  is a vector of chemical source terms and is not treated using the semi-implicit Crank-Nicolson method due to computational cost considerations of using its full Jacobian,  $(\partial \mathbf{\Omega} / \partial \mathbf{Y})_k^{n+1}$  [112].

2. Next, the ideal gas law is used to predict the updated density field,

$$\rho_{k+1}^{n+3/2} = \frac{p_0 \left( \sum_{i=1}^N Y_{i,k+1}^{n+3/2} / W_i \right)^{-1}}{RT_{k+1}^{n+3/2}}. \quad (2.37)$$

Upon convergence of the iterative method (steps 1 to 5),  $\rho Y_i$  will satisfy the conservation of species densities [112].

3. The momentum equation is now advanced using a semi-implicit Crank-Nicolson formulation. First, one can define

$$\mathbf{u}_k^* = \frac{\mathbf{u}^n + \mathbf{u}_k^{n+1}}{2}, \quad (2.38)$$

which allows the Crank-Nicolson method to be applied as

$$\begin{aligned} \frac{\rho^{n+1/2} + \rho_{k+1}^{n+3/2}}{2} \widehat{\mathbf{u}}_{k+1}^{n+1} &= \frac{\rho^{n-1/2} + \rho^{n+1/2}}{2} \mathbf{u}^n \\ &+ \Delta t \left[ (\mathbf{C}_u + \mathbf{D}_u)_k^{n+1/2} \cdot \mathbf{u}_k^* + \nabla p_k^{n+3/2} \right] \\ &+ \frac{\Delta t}{2} \left( \frac{\partial \mathbf{C}_u}{\partial \mathbf{u}} + \frac{\partial \mathbf{D}_u}{\partial \mathbf{u}} \right)_k^{n+1/2} \cdot \left( \widehat{\mathbf{u}}_{k+1}^{n+1} - \mathbf{u}_k^{n+1} \right). \end{aligned} \quad (2.39)$$

Similar to the scalar transport equation,  $\mathbf{C}_u$  and  $\mathbf{D}_u$  are the convective and viscous terms of the momentum equation. Further,  $\widehat{\mathbf{u}}$  is a predicted velocity field that does not necessarily satisfy mass conservation; thus, the pressure field is next found such that mass conservation will be satisfied.

4. As mentioned above, solving a pressure Poisson equation for the temporally- and spatially-varying hydrodynamic pressure allows one to ensure mass conservation. The time discretization of the Poisson equation takes the form of

$$\nabla^2 (\delta p)_{k+1}^{n+3/2} = \frac{1}{\Delta t} \left[ \nabla \cdot \left( \frac{\rho^{n+1/2} + \rho_{k+1}^{n+3/2}}{2} \widehat{\mathbf{u}}_{k+1}^{n+1} \right) + \frac{\rho_{k+1}^{n+3/2} - \rho^{n+1/2}}{\Delta t} \right]. \quad (2.40)$$

The Poisson equation is solved using either the BiCGSTAB [121] method or the AMG [106] method implemented in the HYPRE package [61]. Once the hydrodynamic pressure field is determined, the predicted velocity field is updated using

$$\mathbf{u}_{k+1}^{n+1} = \widehat{\mathbf{u}}_{k+1}^{n+1} - \frac{2\Delta t}{\rho^{n+1/2} + \rho_{k+1}^{n+3/2}} \left( \nabla (\delta p)_k^{n+3/2} \right), \quad (2.41)$$

while the pressure field is updated using

$$p_{k+1}^{n+3/2} = p_{k+1}^{n+3/2} + \delta p_{k+1}^{n+3/2}. \quad (2.42)$$

5. The above process is repeated until the sub-iterations converge, whereupon the solution fields are updated for the next time step,

$$\begin{aligned} \rho^{n+3/2} &= \rho_Q^{n+3/2}, \quad p^{n+3/2} = p_Q^{n+3/2}, \\ \mathbf{u}^{n+1} &= \mathbf{u}_Q^{n+1}, \quad \text{and } \mathbf{Y}^{n+3/2} = \mathbf{Y}_Q^{n+3/2}. \end{aligned} \quad (2.43)$$

### 2.4.2 Preconditioner for the chemical source terms

The above description does not consider semi-implicit treatment of the chemical source terms,  $\mathbf{\Omega}$ . To improve the performance of the semi-implicit time integration, Savard et al. [112] proposed a simple preconditioner which is applied to the scalar transport equation, Eq. 2.36, leaving the remainder of the semi-implicit method identical to the above description. The chosen preconditioner takes the form

$$\mathbf{J} = \rho_k^{n+3/2} \mathbf{I} - \frac{\Delta t}{2} \left( \frac{\partial \mathbf{C}}{\partial \mathbf{Y}} + \frac{\partial \mathbf{D}}{\partial \mathbf{Y}} - \mathbf{\Lambda} \right)_k^{n+1}, \quad (2.44)$$

where  $\mathbf{\Lambda}$  is a diagonal matrix defined as

$$\Lambda_{i,i} = \frac{\dot{\omega}_i^-}{Y_i}, \quad (2.45)$$

which is a close approximation of the diagonal of the chemical Jacobian matrix [112]. When applied to Eq. 2.36, the semi-implicit time integration, including treatment of the chemical source terms, reads (in residual form)

$$\mathbf{Y}_{k+1}^{n+3/2} = \mathbf{Y}_k^{n+3/2} - \Delta t \mathbf{J}^{-1} \cdot \mathbf{\Theta}_k, \quad (2.46)$$

where  $\mathbf{\Theta}_k$  is the error in the species transport equation from previous sub-iterations

$$\mathbf{\Theta}_k = \frac{\rho_k^{n+3/2} \mathbf{Y}_k^{n+3/2} - \rho_k^{n+1/2} \mathbf{Y}_k^{n+1/2}}{\Delta t} - \left[ \left( \mathbf{C}_k^{n+1} + \mathbf{D}_k^{n+1} \right) \cdot \mathbf{Y}_k^* + \mathbf{\Omega}_k^* \right]. \quad (2.47)$$

### 2.4.3 Finite difference scheme for velocity discretization <sup>3</sup>

Figure 2.2 shows a two-dimensional example of the computational domain discretization. Cell-centered locations are indicated with a subscript  $i$  and  $j$ , and faces of the computational cells are denoted using  $i + 1/2$  and  $j + 1/2$ . For clarity, the definitions below will be explicitly provided in two-dimensions and assume a uniform grid spacing with  $\Delta x = \Delta y$ . Descriptions of the discretization using higher-order schemes and three-dimensions can be found elsewhere [36].

Second-order finite difference schemes are used throughout this work. Two operators are needed for the discretization of the governing equations: interpolation and differentiation. Interpolation of a quantity  $\psi$  in the  $x$ -direction is given as

$$\overline{\psi}^x \Big|_{(i+1/2,j)} = \frac{\psi_{(i+1,j)} + \psi_{(i,j)}}{2}, \quad (2.48)$$

<sup>3</sup>The description of the finite differencing scheme found in this section follows closely that of Desjardins et al., J. Comput. Phys. 227 (2008) 7125–7159.

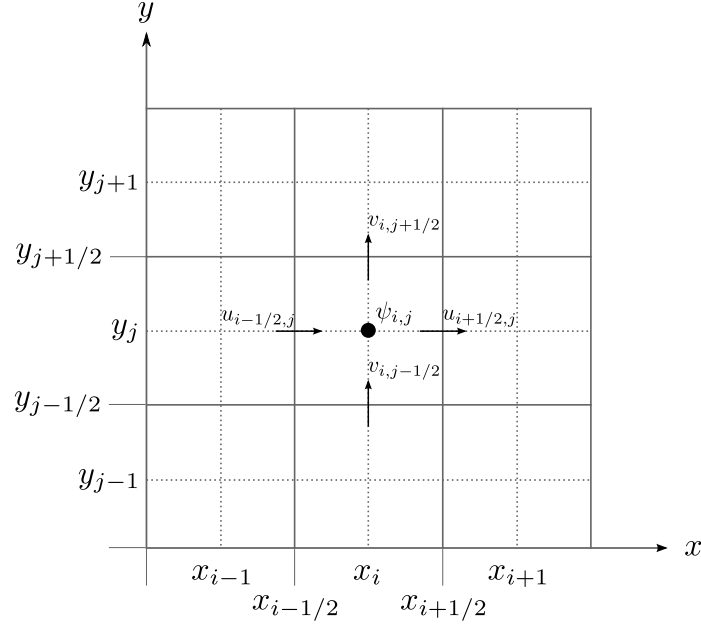


Figure 2.2: Two-dimensional representation of the computational domain discretization.

while differentiation of  $\psi$  in the  $x$  direction is given as

$$\left. \frac{\delta \psi}{\delta x} \right|_{(i+1/2,j)} = \frac{\psi_{(i+1,j)} - \psi_{(i,j)}}{\Delta x}. \quad (2.49)$$

Similar definitions can be written for operators in the  $y$ -direction, and these operators may be used on face-centered or cell-centered values.

Two examples of the spatial discretization are provided; first, the continuity equation is fully discretized, followed by a single term from the momentum equations. Prior to discretizing the continuity equation, the densities and velocities must be collocated. This is done by interpolating the density from cell centers to cell faces at the same location of the velocity. Thus, values of  $\bar{\rho}^x$  and  $\bar{\rho}^y$  are expressed at each corresponding cell face. The momentum vector component in the  $x$ -direction is defined as  $g_x = \bar{\rho}^x u$ , with a similar definition for  $g_y$ ;  $\mathbf{g}$  is thus collocated with the velocity vector. The continuity equation can then be spatially discretized as

$$\left. \frac{\partial \rho}{\partial t} \right|_{(i,j)} + \left. \frac{\delta g_x}{\delta x} \right|_{(i,j)} + \left. \frac{\delta g_y}{\delta y} \right|_{(i,j)} = 0, \quad (2.50)$$

or, in full,

$$\begin{aligned} \left. \frac{\partial \rho}{\partial t} \right|_{(i,j)} + \frac{1}{2\Delta x} [(\rho_{(i+1,j)} + \rho_{(i,j)}) u_{(i+1/2,j)} - (\rho_{(i,j)} + \rho_{(i-1,j)}) u_{(i-1/2,j)}] \\ + \frac{1}{2\Delta y} [(\rho_{(i,j+1)} + \rho_{(i,j)}) v_{(i,j+1/2)} - (\rho_{(i,j)} + \rho_{(i,j-1)}) v_{(i,j-1/2)}] = 0. \end{aligned} \quad (2.51)$$

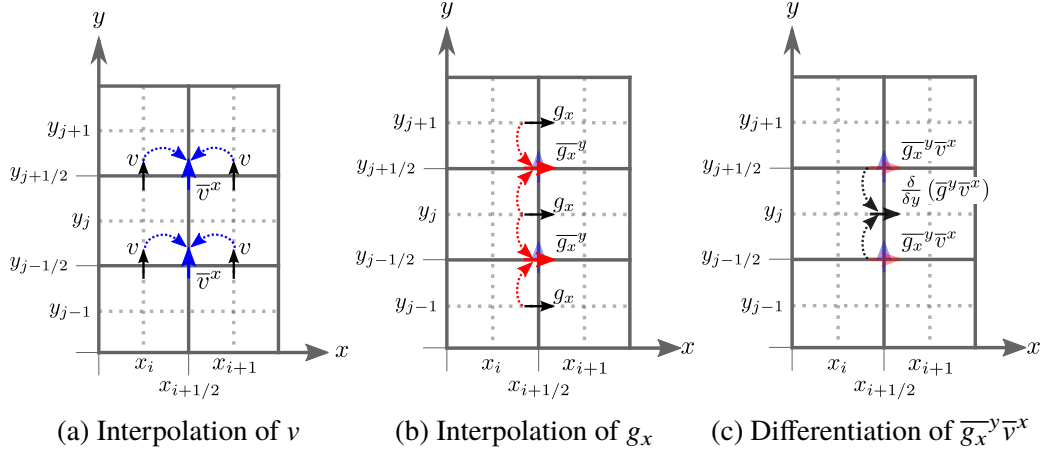


Figure 2.3: (a) Interpolation of  $v$  to  $\bar{v}^x$ , (b) interpolation of  $g_x$  to  $\bar{g}_x^y$ , and (c) differentiation of  $\bar{g}_x^y \bar{v}^x$ .

As a second example, the convective term  $\frac{\partial}{\partial y} (\rho uv)$  in the  $x$ -momentum equation is discretized. Figure 2.3 provides a schematic of this procedure. First,  $g_x$  is computed as described previously. Then, the  $v$  velocity is interpolated in the  $x$ -direction such that  $\bar{v}^x$  exists at the corners of a cell (Fig. 2.3a), i.e.,

$$\bar{v}^x \Big|_{(i+1/2, j+1/2)} = \frac{v_{i+1, j+1/2} + v_{i, j+1/2}}{2}. \quad (2.52)$$

Next,  $g_x$  is interpolated in the  $y$ -direction (Fig. 2.3b),

$$\begin{aligned} \bar{g}_x^y \Big|_{(i+1/2, j+1/2)} &= \bar{\rho}^x u \Big|_{(i+1/2, j+1/2)} \\ &= \frac{g_{x(i+1/2, j)} + g_{x(i+1/2, j+1)}}{2}. \end{aligned} \quad (2.53)$$

$\bar{g}_x^y$  and  $\bar{v}^x$  are now collocated, such that the derivative of  $\bar{g}_x^y \bar{v}^x$  may be taken as (Fig. 2.3c)

$$\begin{aligned} \frac{\partial (\rho uv)}{\partial y} \Big|_{(i+1/2, j)} &= \frac{\delta (\bar{g}_x^y \bar{v}^x)}{\delta y} \Big|_{(i+1/2, j)} \\ &= \frac{1}{\Delta y} \left( \bar{g}_x^y \bar{v}^x \Big|_{(i+1/2, j+1/2)} - \bar{g}_x^y \bar{v}^x \Big|_{(i+1/2, j-1/2)} \right). \end{aligned} \quad (2.54)$$

After spatial discretization of the governing equations in this manner, conservation properties (including mass, momentum, and kinetic energy) are all ensured [36].

#### 2.4.4 Finite volume scheme for scalar transport <sup>4</sup>

For all cases considered in this work, the bounded quadratic upwind biased interpolative convective scheme (BQUICK) [57] is used. This method is an extension of

<sup>4</sup>The scalar transport scheme discussion in this section follows closely that of Herrmann et al., AIAA J. 44.12 (2006).

the QUICK scheme [77], where a flux correction ensures that scalar physical bounds are observed. In NGA, the finite volume approach to solving the scalar transport equations is implemented at a cell-centered location,  $(i, j, k)$ . While fully implemented in three-dimensions, the discussion here will consider only the uniformly spaced one-dimensional case for brevity. Cell  $i$  thus has neighboring cell centers  $i + 1$  (to the right) and  $i - 1$  (to the left). The faces of cell  $i$  are located at  $i + 1/2$  and  $i - 1/2$ . Figure 2.2 shows a two-dimensional representation of the grid with the location of each variable. Velocity vectors and momentum vectors,  $\rho\mathbf{u}$ , are located at cell faces, while all scalar quantities are at cell centers. Then, the finite-volume transport equation for the scalar  $\phi$  (e.g., Eq. 2.4) is discretized as

$$\frac{\partial (\rho\phi)_{i,j,k}}{\partial t} + \frac{(\rho u\phi)_{i+1/2,j,k} - (\rho u\phi)_{i-1/2,j,k}}{\Delta x} = \frac{\left(\rho\mathcal{D}\frac{\partial\phi}{\partial x}\right)_{i+1/2,j,k} - \left(\rho\mathcal{D}\frac{\partial\phi}{\partial x}\right)_{i-1/2,j,k}}{\Delta x} + (\dot{\omega}\phi)_{i,j,k}, \quad (2.55)$$

where  $\mathcal{D}$  is some diffusive term (e.g., only mass diffusion). While the values of  $\rho u$  at  $i + 1/2$  and  $i - 1/2$  are known, the scalar field  $\phi$  is only defined at cell centers. The flux of  $\phi$  is computed at the cell faces, as the scalar field is multiplied by the momentum vector, resulting in

$$(\rho u\phi)_{i-1/2,j,k} = (\rho u)_{i-1/2,j,k} \bar{\phi}_{i-1/2,j,k}, \quad (2.56)$$

and thus  $\phi$  itself must be interpolated to the cell faces, denoted as  $\bar{\phi}_{i-1/2,j,k}$ . The value  $\bar{\phi}_{i-1/2,j,k}$  represents a polynomial fitting of  $\phi$  to the  $i - 1/2$  cell face. For the QUICK scheme, this polynomial interpolation takes the form

$$\bar{\phi}_{i-1/2,j,k} = -\frac{1}{6}\phi_{i-2,j,k} + \frac{5}{6}\phi_{i-1,j,k} + \frac{1}{3}\phi_{i,j,k}. \quad (2.57)$$

BQUICK operates as a predictor-corrector scheme by splitting the time step. First, the solution is advanced from the previous time step  $t^n$  to an intermediate time-step  $t^*$  using the QUICK scheme [77]. Then, in cells where a scalar exceeds its a priori defined physical bounds (e.g.,  $0 \leq Y_i \leq 1$  for species mass fractions), the interpolative scheme is switched to a first-order upwind scheme such that the scalar values remain bounded,

$$\bar{\phi}_{i-1/2,j,k} = \phi_{i-1,j,k}, \quad (2.58)$$

while the remainder of the computational domain retains the QUICK scheme. Based on the new interpolation stencils, the corrector step advances the solution to the next time step,  $t^{n+1}$ . Further analysis of this scalar scheme, including its stability properties, can be found in Herrmann et al. [57].

## 2.5 Special case: Governing equations for tubular flames<sup>5</sup>

A specialized flame configuration, the tubular flame, will be introduced in Section 2.6.3. This configuration (shown schematically in Fig. 2.7) still uses the low Mach number Navier-Stokes equations; however, modifications to the general Navier-Stokes equations are necessary in the form of simplifying assumptions. The assumptions used here are the same as in Hall and Pitz [53]:

1. Each variable (except for the axial velocity,  $u_z$ , and hydrodynamic pressure,  $p$ ) is assumed to be independent of the axial direction, i.e.,  $\psi = \psi(r, \theta)$ .
2.  $u_z$  is defined using a linear velocity gradient, i.e.,  $u_z(r, \theta, z) = zW(r, \theta)$ .
3. The hydrodynamic pressure is expressed as  $p = \frac{z^2}{2}H + I(r, \theta)$ , where  $H = \frac{1}{z} \frac{\partial p}{\partial z}$  is the pressure eigenvalue and  $I$  is the radial and azimuthal dependence of the hydrodynamic pressure [53].

The continuity equation in cylindrical coordinates, assuming no dependence in the axial ( $z$ ) direction and no azimuthal symmetry, is given by

$$\frac{\partial \rho}{\partial t} + \frac{1}{r} \frac{\partial}{\partial r} (r \rho u_r) + \frac{1}{r} \frac{\partial}{\partial \theta} (\rho u_\theta) + \frac{\partial}{\partial z} (\rho u_z) = 0 \quad (2.59)$$

where  $\rho$ ,  $u_r$ , and  $u_\theta$  are functions of  $r$  and  $\theta$  only. The axial velocity is then expressed using a linear velocity gradient  $W(r, \theta)$  [63, 117] so the continuity equation can be re-expressed as

$$\frac{\partial \rho}{\partial t} + \frac{1}{r} \frac{\partial}{\partial r} (\rho r u_r) + \frac{1}{r} \frac{\partial}{\partial \theta} (\rho u_\theta) = -\rho W. \quad (2.60)$$

In this sense, the left hand side of Eq. 2.60 can be thought of as the time rate of change of density and the two-dimensional divergence of  $\rho \mathbf{u}$ , henceforth notated  $\nabla_{2D} \cdot (\rho \mathbf{u})$ . The right hand side of Eq. 2.60 is a source term for the continuity equation; when the axial velocity gradient,  $W$ , is positive, mass is leaving the domain in the axial direction. Using the notation of  $\nabla_{2D}$  (denoting no derivatives in the  $z$ -direction), the continuity equation can be written as

$$\frac{\partial \rho}{\partial t} + \nabla_{2D} \cdot (\rho \mathbf{u}) = -\rho W. \quad (2.61)$$

The conservation of momentum equations in the  $r$  and  $\theta$  directions can be expressed similarly as

$$\frac{\partial (\rho \mathbf{u})}{\partial t} \cdot \hat{\mathbf{e}}_r + (\nabla_{2D} \cdot (\rho \mathbf{u} \otimes \mathbf{u})) \cdot \hat{\mathbf{e}}_r = -(\nabla_{2D} p) \cdot \hat{\mathbf{e}}_r + (\nabla_{2D} \cdot \boldsymbol{\tau}) \cdot \hat{\mathbf{e}}_r - \rho u_r W + \mu \frac{\partial W}{\partial r} \quad (2.62)$$

<sup>5</sup>The governing equations, as presented in this section, are adapted from Hall et al. [53].

and

$$\frac{\partial(\rho\mathbf{u})}{\partial t} \cdot \hat{\mathbf{e}}_\theta + (\nabla_{2D} \cdot (\rho\mathbf{u} \otimes \mathbf{u})) \cdot \hat{\mathbf{e}}_\theta = -(\nabla_{2D} p) \cdot \hat{\mathbf{e}}_\theta + (\nabla_{2D} \cdot \boldsymbol{\tau}) \cdot \hat{\mathbf{e}}_\theta - \rho u_\theta W + \frac{\mu}{r} \frac{\partial W}{\partial \theta}. \quad (2.63)$$

The hydrodynamic pressure component is again given by

$$p = \frac{z^2}{2} H + I(r, \theta), \quad (2.64)$$

where  $H = \frac{1}{z} \frac{\partial p}{\partial z}$  is the constant and uniform pressure eigenvalue and  $I$  is the radial and azimuthal dependence of the hydrodynamic pressure [53]. Then, the axial momentum equation can be written as a scalar transport equation for the axial velocity gradient,

$$\frac{\partial(\rho W)}{\partial t} + \nabla_{2D} \cdot (\rho\mathbf{u}W) = \nabla_{2D} \cdot (\mu\nabla_{2D}W) - H - 2\rho W^2. \quad (2.65)$$

Finally, the energy equation is expressed as

$$\begin{aligned} \frac{\partial(\rho T)}{\partial t} + \nabla_{2D} \cdot (\rho\mathbf{u}T) &= \nabla_{2D} \cdot (\rho\alpha\nabla_{2D}T) + \dot{\omega}_T - \frac{1}{c_p} \sum_i c_{p,i} \mathbf{j}_i \cdot \nabla_{2D}T \\ &+ \frac{\rho\alpha}{c_p} \nabla_{2D}c_p \cdot \nabla_{2D}T - \rho WT \end{aligned} \quad (2.66)$$

and the species conservation equations are

$$\frac{\partial(\rho Y_i)}{\partial t} + \nabla_{2D} \cdot (\rho\mathbf{u}Y_i) = -\nabla_{2D} \cdot \mathbf{j}_i + \dot{\omega}_i - \rho W Y_i. \quad (2.67)$$

### Implementation of the tubular equations in NGA<sup>6</sup>

The above numerical description (Eqs. 2.61 - 2.63 and Eqs. 2.65 - 2.67), along with the equation of state (Eq. 2.6), represents a nearly closed set of  $N + 6$  equations governing this configuration and has been previously investigated [53, 63]. However, the implementation in NGA requires treatment of several aspects which have not been considered elsewhere and are presented here.

First, the pressure eigenvalue  $H$  must be determined. Hall and Pitz solved an additional equation,  $0 = (\partial H / \partial r)$  with boundary condition  $0 = (\partial H / \partial \theta)$  in order to enforce a uniform  $H$  in the domain. In this work, the value for  $H$  is found by considering the scalar transport equation for  $W$  (Eq. 2.65). At steady-state (which the tubular flame reaches), this equation simplifies to

$$\nabla_{2D} \cdot (\rho\mathbf{u}W) = \nabla_{2D} \cdot (\mu\nabla_{2D}W) - H - 2\rho W^2. \quad (2.68)$$

<sup>6</sup>The implementation of the tubular equations into NGA, as detailed in this section, is novel to this thesis.

Integration of Eq. 2.68 over the entire domain yields, for  $H$ ,

$$H = \frac{1}{V} \left( \rho_u |\mathbf{u}_{in}| W_{in} A_{BC} - \int_V \rho W^2 dV \right), \quad (2.69)$$

where  $A_{BC}$  is the area of the computational domain inlet at  $r = R$ . Equation 2.69 is evaluated at each time step; once the flame reaches a steady-state configuration, the value of  $H$  has converged to a constant value.

Next, it is clear that additional ‘‘source’’ terms appear which would not be included in a traditional axisymmetric two-dimensional configuration. These terms are:

$$-\rho W \quad (\text{Eq. 2.60})$$

$$-\rho u_r W + \mu \frac{\partial W}{\partial r} \quad (\text{Eq. 2.62})$$

$$-\rho u_\theta W + \frac{\mu}{r} \frac{\partial W}{\partial \theta} \quad (\text{Eq. 2.63})$$

$$-H - 2\rho W^2 \quad (\text{Eq. 2.65})$$

$$-\rho W T \quad (\text{Eq. 2.66})$$

$$-\rho W Y_i \quad (\text{Eq. 2.67}).$$

These source terms can be split into two categories. The first category of terms appears from derivatives of the axial velocity in the axial direction (e.g., in the  $r$ -momentum equation, Eq. 2.62),

$$\frac{\partial}{\partial r} \left( \frac{\partial u_z}{\partial z} \right) = \frac{\partial}{\partial r} \left( \frac{\partial (zW)}{\partial z} \right) = \frac{\partial W}{\partial r}, \quad (2.70)$$

which would otherwise be set to zero in axisymmetric configurations. This category of source terms includes  $\mu (\partial W / \partial r)$  in Eq. 2.62,  $(\mu/r) (\partial W / \partial \theta)$  in Eq. 2.63, and  $-H - \rho W^2$  in Eq. 2.65.

The second category of terms derives from the use of conservative (rather than non-conservative) forms of the governing equations. If the non-conservative forms were used, then the left-hand side of Eq. 2.4, for example, would become

$$\begin{aligned} \frac{\partial (\rho Y_i)}{\partial t} + \nabla \cdot (\rho \mathbf{u} Y_i) &= Y_i \left[ \frac{\partial \rho}{\partial t} + (\nabla \cdot \rho \mathbf{u}) \right] + \rho \left( \frac{\partial Y_i}{\partial t} + \mathbf{u} \cdot \nabla Y_i \right) \\ &= \rho \left( \frac{\partial Y_i}{\partial t} + \mathbf{u} \cdot \nabla Y_i \right) \\ &= \rho \left( \frac{\partial Y_i}{\partial t} + u_r \frac{\partial Y_i}{\partial r} + \frac{u_\theta}{r} \frac{\partial Y_i}{\partial \theta} \right), \end{aligned} \quad (2.71)$$

Table 2.2: Parameters of the simulations. The domain is the physical dimensions of the configuration, while the grid specifies the number of computational points in the domain.

Configuration	$l_F/\Delta x$	Grid	$\phi$	$u_{in}$ [m/s]
1D Cartesian	20	Varies	$0.35 < \phi < 1.0$	$S_L^o$
1D Cylindrical	20	$2000 \times 1 \times 1$	0.40	0
2D Tubular	43	$800 \times 256 \times 1$	0.25	0.7647
2D Freely prop.	16	$1888 \times 472 \times 1$	0.40	$S_{eff}^{2D}$
3D Laminar	16	$1520 \times 190 \times 190$	0.40	$S_{eff}^{3D}$
3D Turbulent	16	$1520 \times 190 \times 190$	0.40	$S_T$

by removing the continuity equation. This procedure leads to the forms of the tubular transport equations given in Hall and Pitz [53]. However, as NGA solves the equations in conservative form, the left-hand side of Eq. 2.4 is instead rearranged as

$$\begin{aligned}
 \frac{\partial (\rho Y_i)}{\partial t} + \nabla \cdot (\rho \mathbf{u} Y_i) &= \frac{\partial (\rho Y_i)}{\partial t} + \frac{1}{r} \frac{\partial}{\partial r} (r \rho u_r Y_i) + \frac{1}{r} \frac{\partial}{\partial \theta} (\rho u_\theta Y_i) + \frac{\partial}{\partial z} (\rho Y_i u_z) \\
 &= \frac{\partial (\rho Y_i)}{\partial t} + \frac{1}{r} \frac{\partial}{\partial r} (r \rho u_r Y_i) + \frac{1}{r} \frac{\partial}{\partial \theta} (\rho u_\theta Y_i) + \frac{\partial}{\partial z} (\rho Y_i z W) \\
 &= \frac{\partial (\rho Y_i)}{\partial t} + \nabla^{2D} \cdot (\rho \mathbf{u} Y_i) + \rho Y_i W.
 \end{aligned} \tag{2.72}$$

As a result of NGA using the conservative forms of the governing equations, a source term is first added to the continuity equation ( $-\rho W$  on the right-hand side of Eq. 2.60). This term directly impacts global mass conservation, and is thus treated as a source term in the pressure Poisson equation. The remaining source terms ( $\rho W u_r$ ,  $\rho W u_\theta$ ,  $\rho W^2$ ,  $\rho W T$ , and  $\rho W Y_i$ ) thus also arise due to the source term in the continuity equation.

## 2.6 Computational configurations

In this section, six flame configurations are detailed in Sections 2.6.1 – 2.6.6. These six configurations are utilized throughout this thesis work to validate the proposed diffusion and chemistry models. Each configuration was chosen to systematically increase the flame complexity such that curvature, dimensionality, and turbulence effects could be isolated. Only premixed mixtures are considered; primarily, hydrogen–air mixtures are used (when this is not the case, the mixture will be explicitly stated). The equivalence ratio is altered for specific configurations as detailed in their respective sections. Additionally, the maximum allowable time step

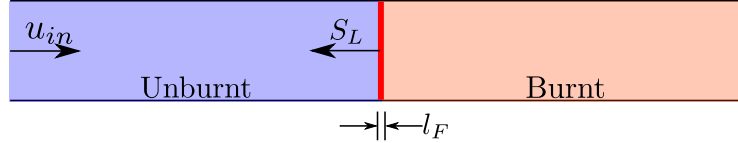


Figure 2.4: Schematic of the one-dimensional cartesian flame configuration.

is constrained to  $\Delta t_{max} = 2 \times 10^{-6}$  s, which was found to result in negligible numerical errors as discussed in Section 6.7.2. This time step is similar to those identified in Savard et al. [112]. An additional constraint of a maximum convective CFL of 0.8 is also imposed. Table 2.2 lists the grid spacing, number of computational points, mixture equivalence ratio, and inlet velocities for each flame configuration described in the following sections.

### 2.6.1 One-dimensional flat unstretched flames

The most basic flame configuration considered is that of a one-dimensional, flat, unstretched flame propagating freely into the premixed reactants. The inlet mixture has an unburnt temperature of  $T_u = 298$  K and pressure of  $p_o = 1$  atm. In Chapter 3, premixed hydrogen–air mixtures with a range of equivalence ratios from  $\phi = 0.35$  to  $\phi = 1.0$  are considered. In Chapter 4, an extensive set of fuels, diluents, equivalence ratios, unburnt temperatures, and pressures are considered; these mixtures will be detailed later. The inlet velocity boundary condition,  $u_{in}$ , is set to closely match the corresponding laminar flame speed. Figure 2.4 shows a schematic of this configuration. Flame speeds throughout this work will be defined as

$$S_L = \frac{\int_V \rho \dot{\omega}_{H_2O} dV}{\rho_u Y_{H_2O,b} A}, \quad (2.73)$$

where the subscripts  $u$  and  $b$  represent an unburnt or burnt mixture property, respectively, the subscript  $L$  represents a laminar burning velocity, and  $A$  is the cross-sectional area of the domain ( $A = L_y \cdot L_z$ , where  $L_y$  and  $L_z$  are the physical lengths of the domain in the  $y$ - and  $z$ -directions, respectively). Additional superscripts/subscripts will be used to differentiate various flame speeds. A superscript  $o$  is used ( $S_L^o$ ) when unstretched laminar flame speeds are computed, a subscript  $eff$  (e.g.,  $S_{eff}^{2D}$ ) indicates effective burning velocities of unstable laminar flames, and a subscript  $T$  denotes turbulent flame speeds.

Each simulation, for the range equivalence ratios, uses a uniformly-spaced grid with at least 15 points through the corresponding laminar flame thickness defined using

Table 2.3: Parameters of the one-dimensional unstretched laminar flames using the MA–MA diffusion model. Both  $l_F$  and  $S_L^o$  are computed using FlameMaster [100].

	$l_F$ [ $\mu\text{m}$ ]	$S_L$ [cm/s]	$\Delta x$ [ $\mu\text{m}$ ]	$\dot{\omega}_{\text{H}_2\text{O}}^{\text{ID}}$ [1/s]	$T_{peak}$ [K]	$Y_{\text{H}_2\text{O}}^{\text{peak}}$
0.35	992	11.2	49.6	66	1138	0.0769
0.40	650	21.8	32.5	192	1180	0.0836
0.50	437	50.7	21.9	746	1244	0.0964
0.60	375	85.7	18.8	1768	1287	0.1076
$\phi$ 0.70	356	121.1	17.8	3179	1317	0.1177
0.80	352	153.9	17.6	4827	1338	0.1267
0.90	355	183.0	17.8	6561	1351	0.1344
1.00	356	207.8	17.8	8233	1380	0.1460

the maximum temperature gradient

$$l_F = \frac{(T_{max} - T_{min})}{|\nabla T|_{max}}. \quad (2.74)$$

A similar criterion on the grid resolution has been utilized elsewhere [4, 20, 55]. Resolution error for the  $\phi = 0.4$  flame is discussed in Section 6.7.2. An identical grid is used at a given equivalence ratio, regardless of the chosen diffusion or chemistry model; the laminar flame thickness is found to be similar between the various models (e.g.,  $l_F^{MA-MA} = 650 \mu\text{m}$  and  $l_F^{MA-xx} = 647 \mu\text{m}$ ). Table 2.3 provides details on the values of  $l_F$ ,  $S_L^o$ , and  $\Delta x$  for each equivalence ratio. Values of the peak H<sub>2</sub>O source term,  $\dot{\omega}_{\text{H}_2\text{O}}^{\text{ID}}$ , temperature at peak H<sub>2</sub>O source term,  $T_{peak}$ , and mass fraction of H<sub>2</sub>O at peak H<sub>2</sub>O source term,  $Y_{\text{H}_2\text{O},peak}$  for the one-dimensional flames are also given in Table 2.3. These values, computed here using the MA–MA model, are used extensively in the analyses presented in Chapters 3 - 6.

The flat one-dimensional flames are initialized using fully-converged one-dimensional solutions obtained from FlameMaster [100]. The FlameMaster solution is then interpolated onto the NGA computational domain so that the NGA solution reaches steady-state rapidly. The flame position can be used to help identify when a steady-state solution has been reached; the flame position is defined using an equal-area concept, i.e.,

$$x_F = L_x - \frac{\int_V \rho Y_{\text{H}_2\text{O}} dV}{\rho_b Y_{\text{H}_2\text{O},b} A}. \quad (2.75)$$

This concept is shown schematically in Fig. 2.5. Tracking the flame position during run-time is also useful to ensure the flames remain in the computational domain (especially for the unstable and turbulent flame configurations).

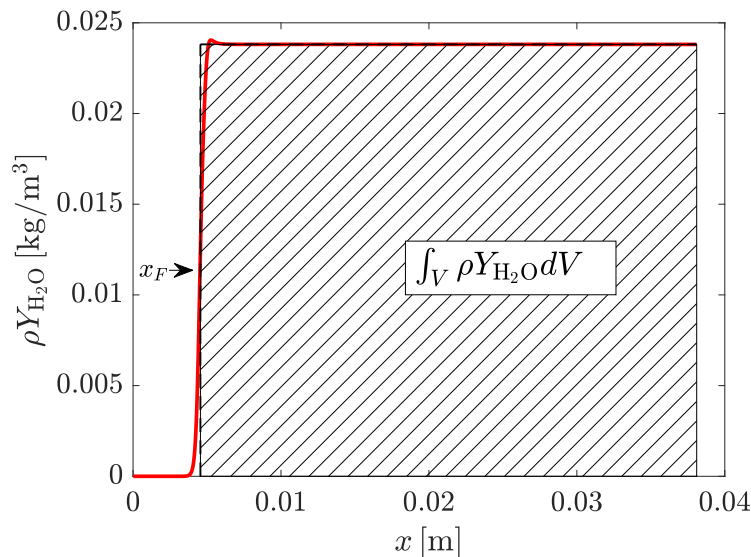


Figure 2.5: Methodology of finding the flame position based on an equal-area approach, using a one-dimensional flat flame at  $\phi = 0.4$  (red line).

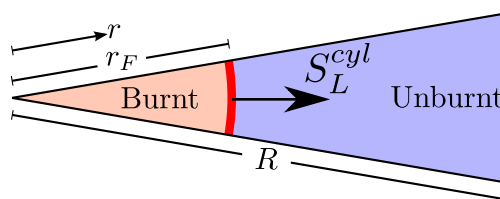


Figure 2.6: Schematic of the one-dimensional cylindrical flame configuration.

### 2.6.2 One-dimensional cylindrical flames

As the next logical step in flame complexity, curvature is introduced to the flame configuration by considering an outwardly-propagating, one-dimensional, cylindrical stretched flame. Figure 2.6 shows a schematic of the one-dimensional cylindrical flame. This flame is always convex to the unburnt mixture, indicating positive curvature, where the curvature is defined as the reciprocal of the flame radius, i.e.,  $\kappa = 1/r_F$ . The location of the cylindrical flame must be calculated using a modified form of Eq. 2.75. An equal-area method is still applied to  $\rho Y_{H_2O}$ , and the flame position takes the form

$$r_F = \sqrt{R^2 - \frac{2 \int_V \rho Y_{H_2O} dV}{\rho_b Y_{H_2O,b} L_x L_\theta}}. \quad (2.76)$$

Only one premixed hydrogen–air mixture is considered, with an equivalence ratio of  $\phi = 0.4$ ,  $T_u = 298$  K, and  $p_o = 1$  atm. The computational domain has a maximum radius  $R = 0.2$  m with the boundary at  $r = R$  set as a convective outflow boundary condition; there is no inlet boundary in this configuration. Due to the changing

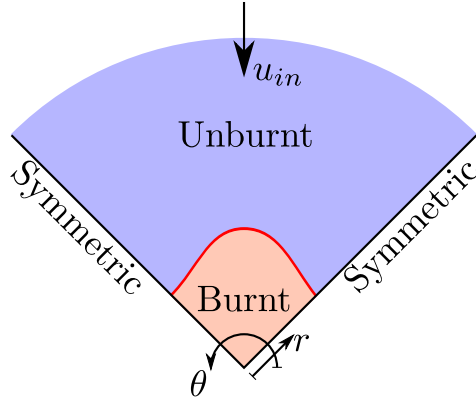


Figure 2.7: Schematic of the two-dimensional tubular flame configuration.

flame curvature (and thus a potentially varying flame thickness), a more refined computational grid is implemented. Here, a uniform grid spacing of  $\Delta r = l_F/40$  is utilized.

The flame is initialized using a one-dimensional steady-state tubular flame solution (the tubular flame configuration is described below). The flame is positioned such that the initial flame radius is as close to the origin as possible while still allowing the flame to propagate outwardly in the one-dimensional cylindrical configuration. As an example, the initial flame radius (denoted by a subscript 0) for the detailed chemistry simulation with mixture-averaged mass and thermal diffusion is  $r_{F,0} = 0.0013$  m, corresponding approximately to an initial normalized flame curvature of  $(\kappa l_F)_0 = 0.5$ . Once initialized, the flame propagates outwardly into the (initially) quiescent mixture until it exits the computational domain.

For the one-dimensional cylindrical flame,  $r_F$  provides a radius by which one can compute a cross-sectional area ( $A^{cyl} = r_F L_z L_\theta$ ) to determine the flame speed,

$$S_L^{cyl} = \frac{\int_V \rho \dot{\omega}_{H_2O} dV}{\rho_u Y_{H_2O,b} A^{cyl}}. \quad (2.77)$$

### 2.6.3 Two-dimensional tubular flames

The next configuration removes the axisymmetric constraint of the one-dimensional cylindrical flame by investigating a tubular flame configuration exhibiting thermo-diffusive instabilities. This configuration presents the first opportunity to investigate the effects of extinction and local fuel enrichment on the flame structure. Despite the instabilities, these cellular tubular flames are stable, allowing for experimental measurements to be made and subsequently used for model validation. The governing equations for this configuration were provided previously in Section 2.5.

This configuration is an outwardly burning cylindrical flame similar to that described in Section 2.6.2. However, as axisymmetry is no longer enforced on this configuration, differential diffusion effects cause cellular flame instabilities to form. The flame is kept at a fixed radius by injecting the unburnt mixture radially inward, and the flame stabilizes at the radius whose unburnt mixture velocity matches the flame speed. A schematic of the tubular flame configuration is given in Fig. 2.7.

The physical dimensions of the computational domain are selected to match previous experiments [52, 54] and simulations [53]. The radial coordinate spans the range  $0 \leq r \leq R = 0.012$  m, and the azimuthal range is  $-\pi/4 \leq \theta \leq \pi/4$  (to enforce four-fold symmetry of the flame front [53]). The unburnt premixed hydrogen–air mixture corresponds to the low-stretch case of Hall and Pitz [52, 54], with premixed mixture properties of  $\phi = 0.25$ ,  $T_u = 295$  K,  $p_o = 1$  atm, and a radial velocity boundary condition of  $u_{r,in} = 0.7647$  m/s at  $r = R$ . The axial velocity gradient at the inlet (denoted as  $W_{in}$ ) is unknown from experiments and is chosen to match the computed flame radius with the experimental flame radius. By increasing  $W$ , more mass will leave the domain in the axial direction, altering the velocity field and flame position. This procedure was used by Hall and Pitz [53], where they found  $W_{in} = 50$  s<sup>-1</sup>. A different chemical model and numerical implementation of the governing equations than those used by Hall and Pitz are implemented in this study, and thus  $W_{in} = 35$  s<sup>-1</sup> was found to match the flame radius based on the experimental OH profiles.

The computational domain for this case consists of 800 points in the radial direction and 128 points in the azimuthal direction. This grid results in  $\Delta r \approx l_F/40$  and closely matches the highest resolution level of the adaptive mesh refinement used in Hall and Pitz [53]. The inflow boundary is located at  $r = R$  and the origin at  $r = 0$  is a centerline boundary condition. It should be noted that in the experiments, the flames may arbitrarily rotate and an experimental stabilization method was used to prevent this rotation [52, 54]. In the computational investigation, symmetry boundary conditions are applied at the azimuthal boundaries to prevent the flame from rotating.

The flame is initialized using a one-dimensional flat unstretched flame, interpolated on the cylindrical grid. While this initial flame solution assumes no stretch or curvature of the flame front, these effects rapidly develop once the simulation is started. To prevent the flame from remaining perfectly cylindrical, a slight perturbation in the flame front is used to initialize the cellular flame instabilities.

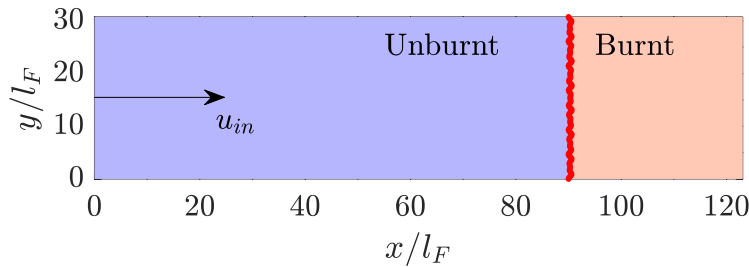


Figure 2.8: Initial perturbation for the two-dimensional freely propagating hydrogen–air flame with  $\phi = 0.4$ .

This perturbation of the initial flame front,  $r_F(\theta)$ , takes the form

$$r_F(\theta) = r_F^{\text{exp}} + A \cos\left(\frac{\pi\theta}{L_\theta}\right), \quad (2.78)$$

where  $r_F^{\text{exp}}$  is the approximate flame radius from the experimental results and  $A = 1 \times 10^{-5}$  m. Once the simulation is initialized, an iterative procedure of changing  $W_{in}$  and arriving at a steady-state solution is repeated until the numerical flame radius matched the experimental flame radius.

#### 2.6.4 Two-dimensional freely-propagating flames

The two-dimensional flame configuration allows the cellular flame instabilities to propagate freely into the unburnt premixed hydrogen–air mixture. These cellular instabilities will then split and merge, creating various length scales over which extinction and local fuel enrichment effects are seen. Simulations using a similar configuration have been used in previous numerical works [9, 20, 51, 102]. Figure 2.8 shows a schematic of the configuration, with the initial flame perturbation (described below).

One inlet premixed mixture is considered with inlet properties set to  $\phi = 0.4$ ,  $T_u = 298$  K, and  $p_o = 1$  atm. The initial velocity boundary condition is set as  $u_{in} = S_L^o$  as the instabilities develop in the domain. Once the instabilities have formed,  $u_{in}$  is set to match the mean effective burning velocity,  $S_{\text{eff}}^{2D}$ , computed using Eq. 2.73. This matched velocity condition allows the simulation to run for an arbitrary length of time such that the cellular instabilities are allowed to propagate freely and flame statistics can be time-averaged. The physical dimensions of the computational domain are approximately  $L_x = 120 l_F$  in the streamwise direction and  $L_y = 30 l_F$  in the spanwise direction.

The grid consists of 1888 points in the streamwise direction and 472 points in the spanwise direction. This corresponds to a grid size of  $\Delta x = \Delta y = l_F/16$ . The

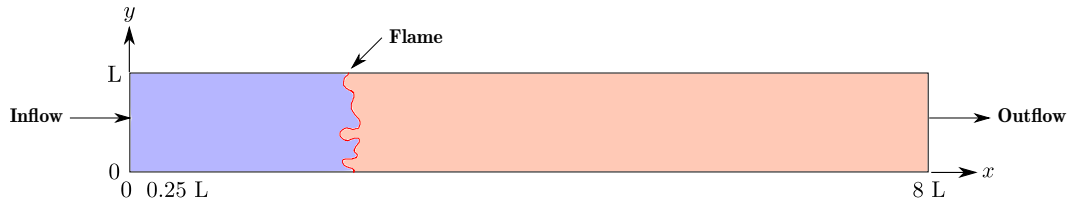


Figure 2.9: Two-dimensional schematic of the three-dimensional laminar flame configuration.

top and bottom boundaries are periodic boundary conditions, with the inflow at the left boundary and outflow at the right boundary. The scalar and velocity fields are initialized with a one-dimensional flat flame solution at  $\phi = 0.4$ . The initial location of the one-dimensional flame is perturbed in the streamwise direction using a combination of two sinusoidal modes defined as

$$x_{F,0} = E + A \sum_{i=1,2} \cos\left(\frac{2\pi k_i y}{L_y}\right), \quad (2.79)$$

where  $E$  is the nominal flame position,  $A = 1 \times 10^{-4}$  is the amplitude of the perturbations, and  $k_i = (13, 20)$  control the spatial frequencies of the perturbation. The initial flame profile and simulation configuration are shown in Fig. 2.8. Note that the asymmetric perturbation promotes rapid growth of the cellular instabilities. An identical set of disturbance parameters were used in Burali et al. [20]

### 2.6.5 Three-dimensional laminar flames

Similar to the two-dimensional freely-propagating configuration, a single premixed hydrogen–air mixture is considered. The incoming mixture has inlet properties of  $\phi = 0.4$ ,  $T_u = 298$  K, and  $p_o = 1$  atm. A uniform velocity,  $u_{in}$ , which matches the effective flame speed of the three-dimensional flame,  $S_{\text{eff}}^{3D}$  (calculated using Eq. 2.73) is used. Again, this matched velocity boundary condition allows the simulation to run for an arbitrary duration, permitting the collection of flame statistics. The physical dimensions of the domain are approximately  $L_x = 100 l_F$  the streamwise direction and  $L_y = L_z = 12 l_F$  in the spanwise directions; thus, the spanwise dimensions of this case are approximately 40% of the two-dimensional freely-propagating configuration. Figure 2.9 provides a to-scale schematic of the three-dimensional configuration. The domain height  $L_y = L_z$  was selected to emphasize the cellular instabilities during the subsequent analyses. Briefly, it was found that the small thermo-diffusive instabilities are independent of the domain height if the domain is sufficiently large; a discussion of the domain size influence is presented in Section 3.7.1.

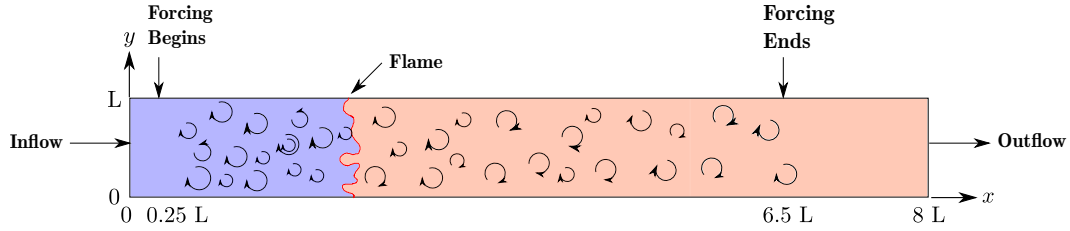


Figure 2.10: Two-dimensional schematic of the three-dimensional flame configuration. Adapted from [108].

The computational grid has 1520 points in the streamwise direction and 190 points in both spanwise directions, with a uniform grid size of  $\Delta x = l_F/16$ . The inflow and outflow boundary conditions are in the  $x$ -direction while the two spanwise directions have periodic boundaries. The flame is kept near the center of the domain to prevent effects from the inlet and outlet. The three-dimensional laminar flame is initialized by performing a similar sinusoidal perturbation of a two-dimensional freely-propagating flame in the  $z$ -direction. The properties of the initial perturbation match those given in the two-dimensional freely propagating configuration description. The perturbations in the  $z$ -direction is handled in an identical manner. This initial condition has instabilities present which rapidly propagate in an unsteady manner, creating fully three-dimensional flame instabilities after the initial transient.

### 2.6.6 Three-dimensional turbulent flames

The final configuration is implemented to consider turbulent flames. The computational configuration is identical to that of the three-dimensional laminar flame configuration detailed above. Additionally, the unburnt premixed mixture has the same inlet properties. A single unburnt Karlovitz number,  $Ka_u = \tau_F/\tau_\eta = 149$ , is selected for analysis in this thesis work. Here,  $\tau_F = l_F/S_L^o$  is the flame time scale and  $\tau_\eta = (\nu/\epsilon)^{1/2}$  is the Kolmogorov time scale of the incoming turbulence with unburnt kinematic viscosity,  $\nu$ , and turbulent energy dissipation,  $\epsilon$ . The Karlovitz number is a measure of how turbulence and the flame chemistry interact. For a value of  $Ka_u = 149$ , the turbulence time and length scales are sufficient to disrupt the flame structure [7]. The unburnt turbulent Reynolds number is  $Re_t = u'l/\nu = 289$ , where  $u'$  is the velocity fluctuation around the mean velocity and  $l$  is the integral length scale. A single set of turbulence parameters is investigated in this thesis; this allows one to determine the applicability of the proposed diffusion and chemistry models under moderate turbulence conditions. The chosen Karlovitz number was selected such that the turbulence interacts with and changes the flame structure (e.g., source

term profiles). However, the turbulence is not strong enough to disrupt the cellular instabilities of interest [7, 20]. Investigations of the importance of thermal diffusion (at various  $Ka_u$  and  $Re_t$ ) should be the focus of future work. Given the prescribed turbulence intensity, this mesh has a grid spacing equivalent to  $\Delta x \approx 2\eta$ , where  $\eta$  is the Kolmogorov length scale. Periodic boundary conditions are used in the two spanwise directions, with the inflow at the left boundary and outflow at the right boundary.

The inlet boundary condition has a mean inflow velocity approximately matching the turbulent flame speed,  $S_T$  (calculated from Eq. 2.73), allowing arbitrarily long simulations to be performed. The turbulent inflow velocity profiles are obtained from a separate triply-periodic DNS of homogeneous isotropic turbulence (HIT) with zero mean velocity. This HIT simulation was performed using a cubic domain with  $190^3$  grid points, exactly matching the grid spacing of the turbulent flame configuration. During the HIT simulation, velocity values at the  $yz$ -midplane are extracted and stored in a separate data file, along with the corresponding time step. Data is extracted at an interval of  $1 \times 10^{-6}$  s for a total of  $1 \times 10^{-3}$  s. Each extracted plane is then used as an inlet velocity for the turbulent flame configuration by applying a mean streamwise velocity set approximately equal to  $S_T$ .

In order to initialize the turbulent flame profile, a non-reacting flow simulation was first performed on the  $1520 \times 190^2$  domain, in order to advect the turbulent velocity profile throughout the computational space. A forcing technique is employed to maintain the production of turbulent kinetic energy throughout the domain, as no mean shear exists to sustain the turbulence. The linear forcing method of Carroll and Blanquart [22] (which is a modification of the linear forcing technique proposed by Lundgren [79] and investigated by Rosales and Meneveau [104]) is used. This forcing technique has been used extensively in DNS of turbulent reacting flows. The turbulence forcing is applied gradually near the inlet to prevent large negative velocities at the inlet plane. Similarly, after the flame, the turbulence forcing is reduced and the production of turbulent kinetic energy decreases toward the outlet to prevent negative velocities at the outlet. A schematic of the computational domain, with a cartoon of the flame position and the turbulence forcing locations, is shown in Fig. 2.10.

After the turbulent velocity field is fully developed, a flat one-dimensional flame is superimposed near the center of the computational domain. The turbulent velocity field rapidly disrupts the flat flame structure. This initialization procedure is allowed

to continue for 5 eddy turnover times,  $\tau = k/\epsilon \approx 500 \mu s$ , to ensure the flame has adjusted fully to the turbulent velocity field. After this setup procedure, the flames are allowed to propagate until the desired statistics are collected.

*Chapter 3*

VALIDATION OF A MIXTURE-AVERAGED THERMAL  
DIFFUSION MODEL

- [1] J. Schlup and G. Blanquart. “Validation of a mixture-averaged thermal diffusion model for premixed lean hydrogen flames”. In: *Combust. Theor. Model.* 22.2 (2018), pp. 264–290. doi: [10.1080/13647830.2017.1398350](https://doi.org/10.1080/13647830.2017.1398350).

Using the numerical framework outlined in Chapter 2, an evaluation of the mixture-averaged (MA) thermal diffusion model is now presented. This evaluation underscores the importance of Soret and Dufour effects in lean premixed hydrogen–air flames. The six flame configurations described in Chapter 2 are considered to evaluate the mixture-averaged thermal diffusion model; these cases are listed in Table 3.1, along with the diffusion models considered for each case. The results using MA thermal diffusion are then compared to the exact multicomponent (MC) model for the one- and two-dimensional cases. MC thermal diffusion is not considered in the three-dimensional configurations (due to high computational costs) and thus the primary comparison in these configurations is the importance of thermal diffusion, not the performance of the MA model.

### 3.1 One-dimensional unstretched (flat) laminar flames

Using the one-dimensional flame configuration detailed in Section 2.6.1, a range of equivalence ratios are considered,  $\phi \in [0.35, 1.0]$ , to determine the effect of thermal diffusion on laminar unstretched flame speeds. Figure 3.1 shows the percent deviation (from the MA–MC laminar flame speed) of the flame speeds calculated

Table 3.1: Cases considered to evaluate and apply the mixture-averaged thermal diffusion model. See Section 2.6 for a detailed description of the models.

	1D Flat Sec. 3.1	1D Stretched Sec. 3.2	2D Steady Sec. 3.3	2D Unsteady Sec. 3.4	3D Lam. Sec. 3.5	3D Turb. Sec. 3.6
MA–MC	X	X	X	X	—	—
MA–MA	X	X	X	X	X	X
MA–FM	X	X	—	—	—	—
MA–RM	X	X	—	—	—	—
MA–xx	X	X	X	X	X	X

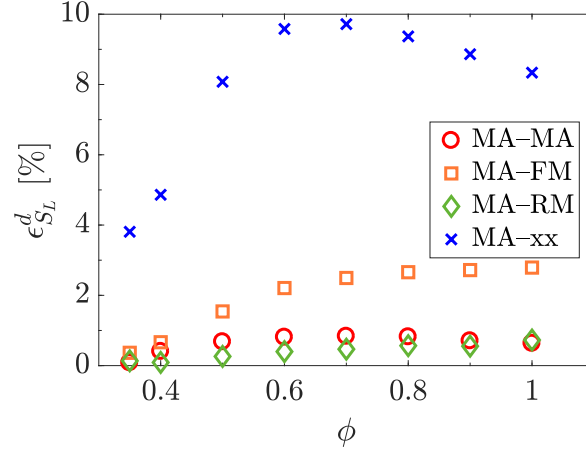


Figure 3.1: Laminar flame speed comparison of the MA–MA (red circles), MA–FM [45] (orange squares), MA–RM [113] (green diamonds), and MA–xx (blue crosses) models with the MA–MC model. The MA–MA and MA–RM cases overlap at many equivalence ratios.

using the various thermal diffusion models. This percent deviation is defined as

$$\epsilon_{S_L}^d = \left| \frac{S_L^{o,MA-MC} - S_L^{o,d}}{S_L^{o,MA-MC}} \right| \quad (3.1)$$

with the superscript  $d$  specifying the diffusion model. The flame speeds are computed using Eq. 2.73.

As can be seen,  $S_L^{o,MA-MA}$  and  $S_L^{o,MA-RM}$  most closely agrees with  $S_L^{o,MA-MC}$  for all equivalence ratios. Additionally, the errors incurred by the thermal diffusion models are an order of magnitude lower than the error incurred by neglecting thermal diffusion. Further, at  $\phi = 0.4$  (the equivalence ratio chosen for most of the subsequent cases), all models indicate that  $S_L^o$  decreases by approximately 5% if thermal diffusion is included. This reduction in flame speed is consistent with previous studies of thermal diffusion in one-dimensional flat flames [15]. Finally, while there is a clear difference between flame speeds with and without thermal diffusion, the chosen thermal diffusion model (at  $\phi = 0.4$ ) has little impact on the results. Due to the similar trends in laminar flame speeds seen across the wide range of equivalence ratios, and the increased effect of thermo-diffusive instabilities at lean conditions, a single lean value of  $\phi$  is considered for each of the following flame configurations. A value of  $\phi = 0.25$  is used for the steady, two-dimensional tubular configuration (to match experiments), and a value of  $\phi = 0.4$  is used for all other configurations.

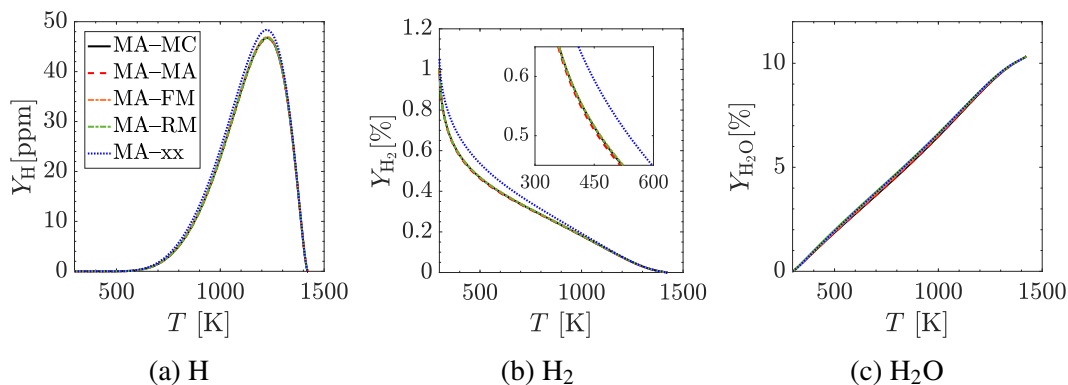


Figure 3.2: Comparison of species mass fractions as functions of temperature for the different diffusion models. MA–MC (black), MA–MA (dashed red), MA–FM [45] (dot-dashed orange), MA–RM [113] (dot-dashed green), and MA–xx (dotted blue) results are shown. The cases including any thermal diffusion model overlap in these figures.

While the laminar flame speeds provide insight into the global effect of thermal diffusion, local comparisons between the multicomponent and mixture-averaged models can be made by examining species mass fraction profiles. Figure 3.2 shows a comparison of the mass fractions of two major chemical species ( $H_2$  and  $H_2O$ ) and the H radical for all cases. For the light species ( $H$  and  $H_2$ ), including thermal diffusion causes a deviation of the mass fraction profiles from those found by neglecting thermal diffusion. However, the inclusion of thermal diffusion has little impact on the profiles of heavier chemical species. These local and global results show that, for a one-dimensional flame, using the MA–MA model (among other models) accurately predicts the laminar flame speeds and species profiles of the MA–MC case.

### 3.2 One-dimensional stretched laminar flames

As the next logical step in flame complexity, this section examines a one-dimensional stretched flame. The flame considered is a one-dimensional, outwardly propagating, cylindrical flame such that the flame is always convex to the unburnt mixture (positive curvature). The unburnt mixture properties, computational configuration, and simulation initialization procedure were described in Section 2.6.2.

An initial transient exists due to the initial flame profile being an approximate stretched solution; thus, Fig. 3.3 shows only the portion after the transient has been removed. This figure shows the flame speed computed using Eq. 2.77, normalized by the laminar flame speed. It is found that, regardless of the inclusion of thermal

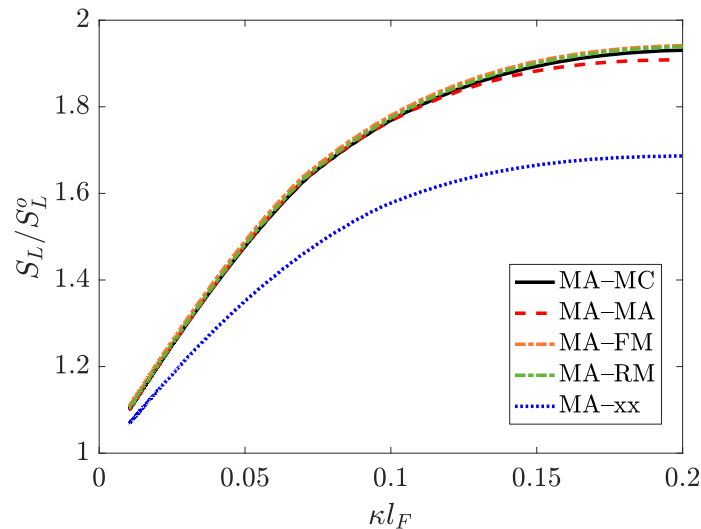


Figure 3.3: Normalized flame speed as a function of normalized flame curvature with  $\phi = 0.4$ .

diffusion, the flame speed approaches the unstretched laminar flame speed as the curvature decreases. This behavior is expected, and in the limit of an infinitely large flame radius,  $S_L/S_L^o \rightarrow 1$ . Additionally, Fig. 3.3 shows that the inclusion of thermal diffusion, using any of the thermal diffusion models, increases the flame speed at a given positive curvature. For the entire range of flame curvature presented, the increase of  $S_L$  over  $S_L^o$ , i.e.,  $S_L/S_L^o - 1$ , is consistently 33% larger for the thermal diffusion cases than the MA-xx case. This result is also expected as thermal diffusion acts to increase the local equivalence ratio in regions of positive curvature [51], leading to a strengthening of the flame speed. Central to the MA thermal diffusion investigation, the MA-MA model reproduces accurately (to within 1.5% of  $S_L/S_L^o$ ) the effects of curvature on the flame speed computed using multicomponent thermal diffusion.

In summary, all thermal diffusion models accurately predict the multicomponent diffusion results. The FM model produces results which are, at best, as good as the MA model. However, since the FM model is neither more accurate nor more computationally efficient than the MA model, is not considered further in this work.

### 3.3 Two-dimensional tubular flame

This section removes the axisymmetric constraint used in the previous section by investigating the tubular flame configuration exhibiting thermo-diffusive instabilities. Despite the instabilities, these cellular tubular flames are stable, allowing for

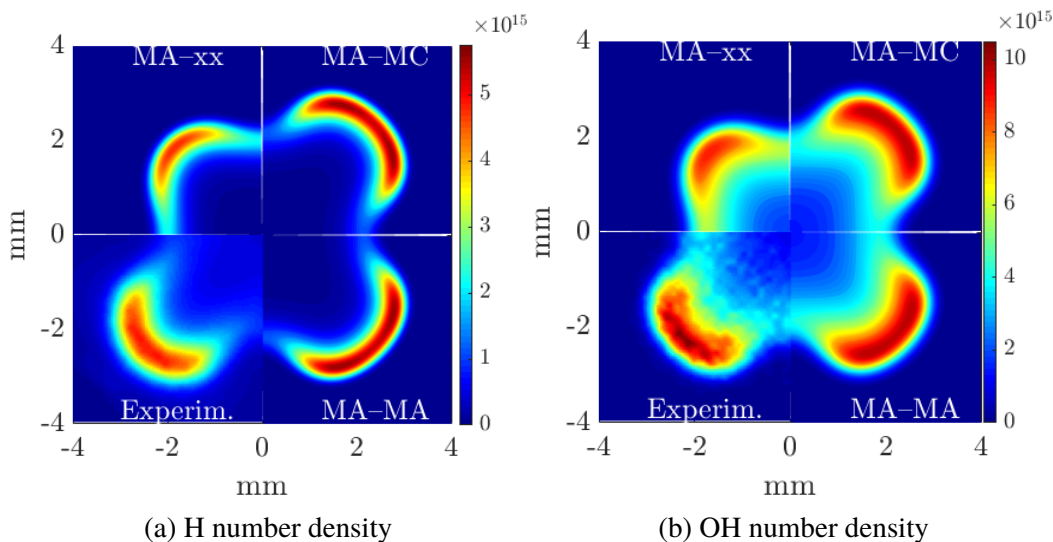


Figure 3.4: (a) H and (b) OH number density contours for the (clockwise from top left) MA-xx, MA-MC, MA-MA, and experimental [53] results.

experimental measurements to be made and subsequently used for model validation.

The computational domain dimensions are selected to match previous experiments [52, 54] and simulations [53]. In their experiments, a variety of measurement techniques were used, including Raman scattering, chemiluminescence, and laser-induced fluorescence, each with their own experimental uncertainties. Due to differential diffusion effects, cellular structures are visible in the flame. The flame is kept at a fixed radius by injecting the unburnt mixture radially inward, and the flame stabilizes at the radius whose unburnt mixture velocity matches the flame speed. The inlet mixture properties and computational configuration were described in Section 2.6.3.

Figure 3.4 shows a qualitative comparison of the H and OH number densities between the numerical results and experimental measurements. In general, the agreement between the results using mixture-averaged thermal diffusion and the experimental measurements are reasonable. Primarily, the MA-MA model predicts the same number of cells along the flame front for the given experimental conditions. Further, the MA-MC results agree very closely with the MA-MA results.

A more quantitative evaluation of the MA-MA results using the MA-MC and experimental results is done by plotting species number densities as functions of the azimuthal angle. Figure 3.5a shows the peak OH number density at each azimuthal location plotted against the azimuthal angle. This figure shows that the

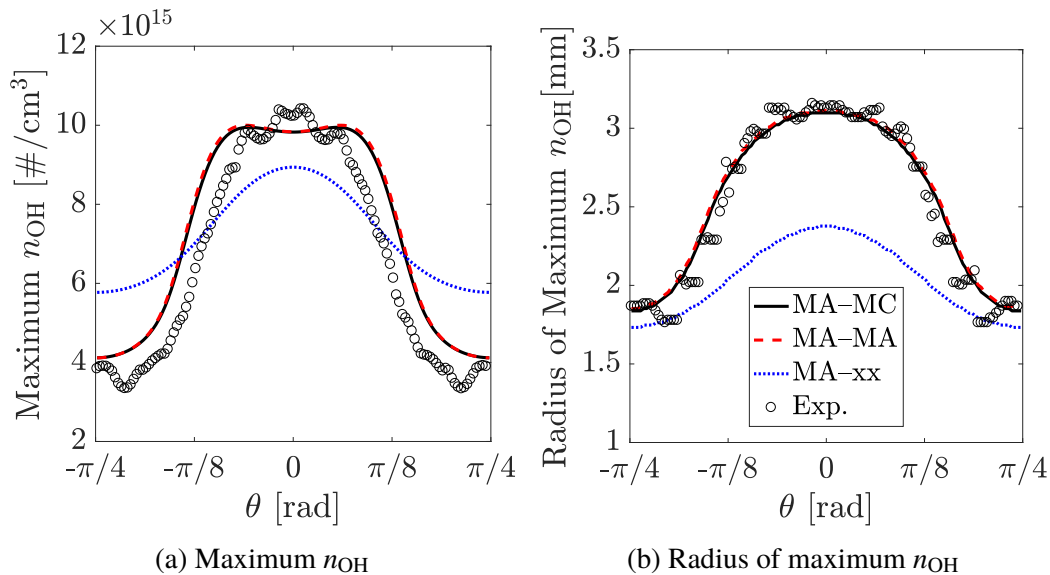


Figure 3.5: Profiles of the (a) maximum  $n_{\text{OH}}$  and (b) radial location of maximum  $n_{\text{OH}}$  as functions of the azimuthal coordinate. MA-MC (black), MA-MA (dashed red), MA-xx (dotted blue), and experimental data [53] (black symbols) results are shown. Experimental uncertainty for  $n_{\text{OH}}$  is  $\pm 2 \times 10^{15} \text{ cm}^{-3}$ .

inclusion of thermal diffusion leads to stronger thermo-diffusive instabilities, i.e., regions of negative curvature have reduced radical concentrations and regions of positive curvature have higher radical concentrations than the MA-xx case. There exists a slight disagreement in the number density profile of OH for both the MA-MA and MA-MC models compared to the experimental results, especially near extinction regions. This discrepancy, however, is within the range of experimental uncertainties,  $\pm 2 \times 10^{15} \text{ cm}^{-3}$  [54]; the agreement between the two diffusion models remains excellent.

Figure 3.5b shows an analysis of the flame front geometry by plotting the radial location of peak OH number density as a function of azimuthal angle. The flame radius is accurately predicted for both the MA-MC and MA-MA cases (both in the instability and in the region between cells), while it is underpredicted for the MA-xx case throughout the flame. The predicted radius for the MA-MC and MA-MA results also very closely match experimental measurements.

### 3.4 Two-dimensional freely propagating flame

The previous configurations have considered only steady flames. The remaining three configurations examine flames that are freely propagating, and thus have highly oscillatory flame structures. First, an investigation of a two-dimensional

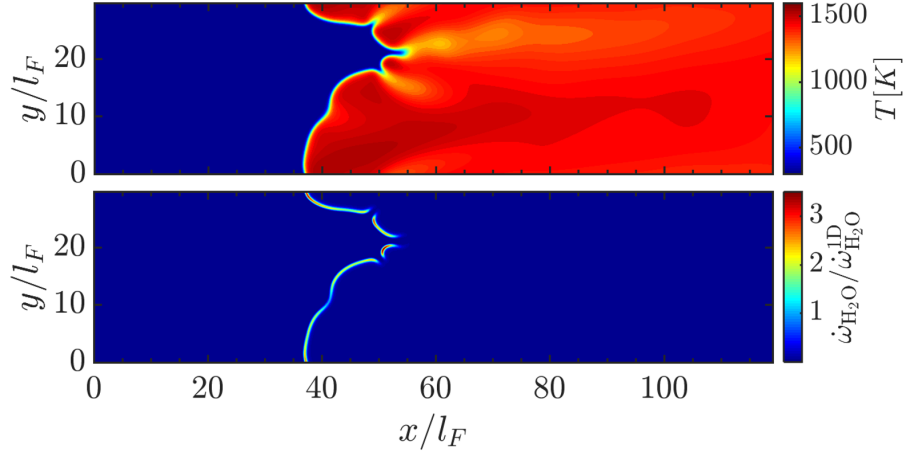


Figure 3.6: Temperature (top) and normalized H<sub>2</sub>O source term (bottom) contours for the MA–MA model.

freely propagating flame is considered. The inlet mixture properties, computational configuration, and initialization procedure were again described in Section 2.6.4.

The MA–MC, MA–MA, and MA–xx diffusion models are used in this configuration, and the simulations are run for approximately  $t = 200 \tau_F$  after the initial transient has been removed. The flame time scale,  $\tau_F$ , is defined as  $\tau_F = l_F/S_L^o$ .

Figure 3.6 shows contours of the temperature and H<sub>2</sub>O source term,  $\dot{\omega}_{\text{H}_2\text{O}}$ . The contours show locally increased temperatures and source terms (compared to one-dimensional unstretched flames at the same equivalence ratio) as well as extinction regions.

The effects of thermal diffusion can be analyzed quantitatively by comparing global and local properties of the three diffusion models. First, the effects of thermal diffusion on the effective flame speed,  $S_{eff}^{2D}$  (as computed using Eq. 2.73), are investigated, and a time history is shown in Fig. 3.7a. Each flame speed in Fig. 3.7a is normalized with the  $S_L^o$  obtained using the same thermal diffusion model as for the two-dimensional simulations. Several observations can be made. First, regardless of the diffusion model, the flame speed increases over the laminar value due to the unstable flame front (i.e.,  $S_{eff}^{2D}/S_L^o > 1$ ). Second, the flame speeds are highly oscillatory (as expected for unstable flames), thus statistical quantities are considered so that direct comparisons between the diffusion models can be made. The PDFs of the normalized effective flame speeds are given in Fig. 3.7b along with the mean values shown as the dashed vertical lines. Both thermal diffusion models predict similar mean normalized flame speeds (around  $S_{eff}^{2D}/S_L^o = 2.6$ ), while the

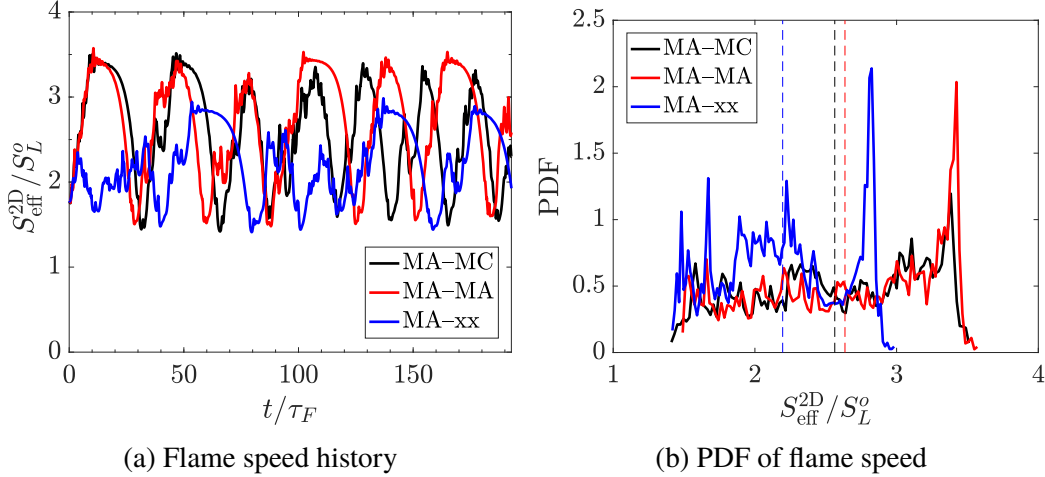


Figure 3.7: (a) Flame speed history and (b) PDF of normalized flame speed for the MA-MC (black), MA-MA (red), and MA-xx (blue) models. The dashed lines represent the temporal mean of the flame speeds.

case neglecting thermal diffusion predicts a 16% decrease in the mean normalized flame speed to  $S_{\text{eff}}^{2D}/S_L^0 = 2.2$ . Further, Fig. 3.7b indicates that the MA-MC and MA-MA cases predict larger values of the flame speed, as well as a wider distribution of values. This supports the earlier observations that thermal diffusion promotes more intense instabilities. It should be noted that the statistical noise in the PDFs of global quantities (e.g., flame speed and surface area) throughout this work is primarily due to the relatively limited sample size as only one value is obtained at each time step.

Next, the effect of thermal diffusion on the flame geometry is analyzed. Figure 3.8a shows the PDF of the flame surface area, where the flame surface is defined as the isosurface of  $T_{\text{peak}}$ . It should be noted that, for the remainder of this thesis, the subscript or superscript “peak” dictates the variable (e.g.,  $T$ ) takes its value at the peak source term of  $\text{H}_2\text{O}$  in a one-dimensional unstretched flame,  $\dot{\omega}_{\text{H}_2\text{O}}^{1D}$ , at the corresponding unburnt equivalence ratio. For example, the temperature at  $\dot{\omega}_{\text{H}_2\text{O}}^{1D}$  for the  $\phi = 0.4$  flame is  $T_{\text{peak}} = 1180$  K. For this two-dimensional case, the flame “area” is the arc length defined by the temperature isosurface. The mean surface areas are included for each case as vertical dashed lines. As can be seen, the MA-MA and MA-MC mean surface areas exceed that of the MA-xx case, providing further support that thermal diffusion acts to increase the flame speed, and the effects of thermal diffusion are accurately captured by the MA-MA model. The PDF also reveals that the inclusion of thermal diffusion acts to make the flame more unstable, i.e., the range of possible flame surface areas has greatly increased.

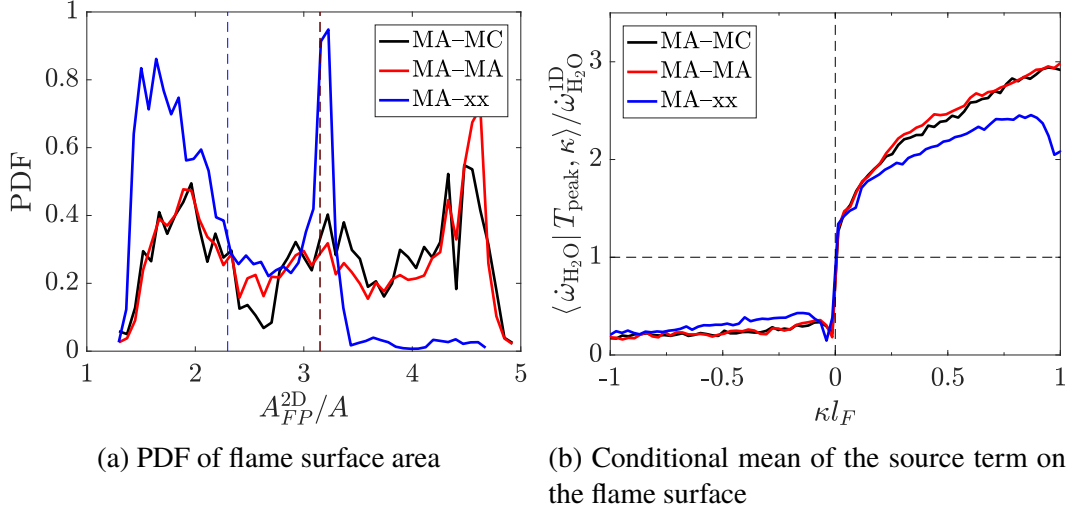


Figure 3.8: (a) PDF of flame surface area normalized by domain cross-sectional area and (b) normalized chemical source term as a function of normalized local flame curvature for the MA-MC (black), MA-MA (red), and MA-xx (blue) models. The dashed lines on the left figure represent the temporal mean of the flame area. The MA-MC and MA-MA means overlap.

Finally, one can identify the local effects of thermal diffusion on the flame by investigating the production rate of  $H_2O$ . Figure 3.8b shows the mean of  $\dot{\omega}_{H_2O}$  conditioned on the flame curvature along the  $T_{peak}$  isosurface. The conditional mean is normalized by the peak one-dimensional source term, and is plotted against the flame curvature normalized by the laminar flame thickness. Here, the flame curvature is defined as

$$\kappa = -\nabla \cdot \mathbf{n} \quad (3.2)$$

and  $\mathbf{n} = \nabla T / |\nabla T|$  is the surface normal. From this figure, it is clear that the inclusion of thermal diffusion increases the local production rate in regions of high positive curvature. This can be attributed to the enhanced focusing effect of thermal diffusion and differential diffusion on the fuel and light radicals in regions of positive curvature. Concurrently, in regions of negative curvature, there is a decrease of  $H_2O$  production from the one-dimensional flat flame, indicating a localized lean mixture and possible extinction. The extinction effects are more prevalent in the MA-MC and MA-MA cases, with the source term being nearly half that of the MA-xx case at equivalent  $\kappa l_F$ . This is consistent with the fuel enrichment hypothesis above.

Given the qualitative and quantitative agreement found between the MA-MC and MA-MA models in the above one- and two-dimensional configurations, the MA-MA model is now applied to flame configurations where experimental data and

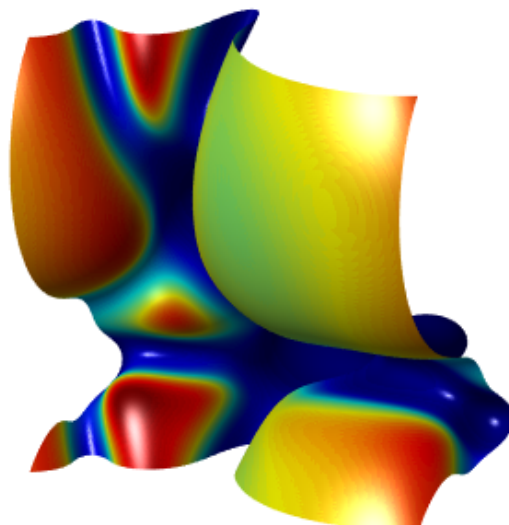


Figure 3.9: Isosurface of the three-dimensional laminar flame with the MA–MA model. The isosurface corresponds to  $T_{\text{peak}}$ . The colors correspond to the normalized source term  $\dot{\omega}_{\text{H}_2\text{O}}/\dot{\omega}_{\text{H}_2\text{O}}^{1D} \in [0, 5]$ .

MA–MC simulations are not readily available. More specifically, the MA–MA model is applied to both laminar and turbulent three-dimensional freely propagating flames.

### 3.5 Three-dimensional, laminar, freely propagating flame

A three-dimensional case without turbulence is now considered to isolate the effects of turbulence and multi-dimensionality on the transport processes. Additionally, while not the primary focus of this work, a future study regarding the importance of thermal diffusion for varying turbulence intensities would require a baseline case for comparison. This three-dimensional, laminar flame provides such a baseline. A temperature isosurface, colored by normalized  $\dot{\omega}_{\text{H}_2\text{O}}$ , is provided in Figure 3.9 to show an example of the freely propagating flame front. These simulations are run for approximately  $t = 80 \tau_F$ , and statistics are collected after removing the initial transient from each case. Details of the computational configuration, mixture parameters, and initialization procedure were presented in Section 2.6.5.

The effective flame propagation speeds for the two cases are shown in Fig. 3.10a. In a similar manner to the two-dimensional freely propagating flames, these flame speeds are calculated using Eq. 2.73. The flame speeds in Fig. 3.10a are normalized by their respective one-dimensional laminar flame speeds, and plotted against a normalized flame time,  $t/\tau_F$ . The inclusion of thermal diffusion acts to increase the flame propagation speed, providing a 25% increase (from 2.50 to 3.14) as shown in

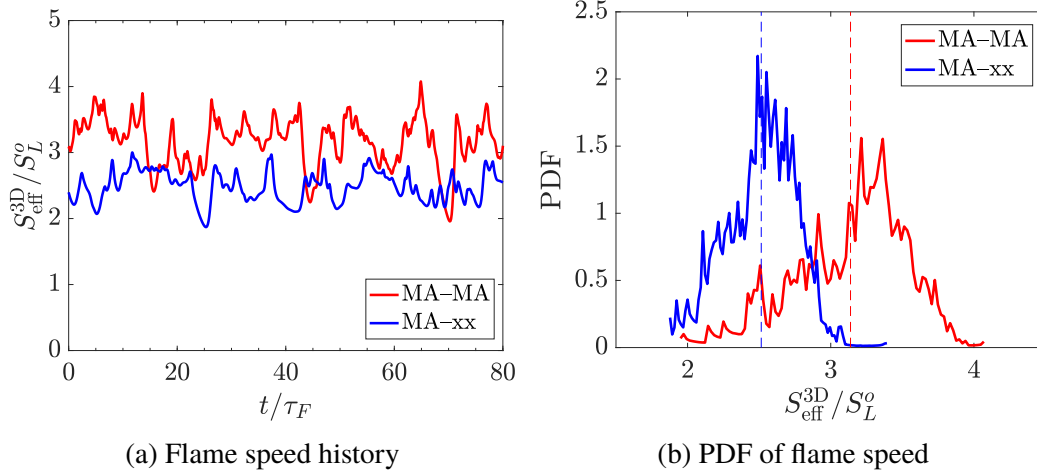


Figure 3.10: Flame speed history (left) and PDF of normalized flame speed (right) for the MA-MA (red) and MA-xx (blue) models. The dashed lines represent the temporal mean of the flame area.

the PDFs and mean flame speeds in Fig. 3.10b. This increase in flame speed is more than that found in the two-dimensional case for two reasons. First, the flame has an additional degree of freedom to increase its surface area (global effect). Second, larger flame curvatures are possible due to the flame being curved in an additional direction, allowing for more fuel enrichment (local effect). Both of these effects contribute to increasing the flame speed.

The PDFs and means of the flame surface area for the MA-MA and MA-xx cases are shown in Fig. 3.11a. As mentioned previously, the flame surface area increases with the inclusion of thermal diffusion, as the mean normalized surface area for the MA-MA model is  $A_{FP}^{3D}/A = 2.6$ , compared to  $A_{FP}^{3D}/A = 2.1$  for the MA-xx model. Additionally, the standard deviation of the flame area increases ( $\sigma_{\text{MA-MA}} = 0.32$  for the MA-MA case,  $\sigma_{\text{MA-xx}} = 0.20$  for the MA-xx case), indicating thermal diffusion affects global flame properties and promotes a more unstable flame front with greater variability in the flame surface area. Note that, due to the size reduction of the domain, the flame may be more constrained in the three-dimensional case than it was in the two-dimensional case. The effects of domain height are discussed in Section 3.7.1.

Finally, the local effects of thermal diffusion can be investigated by looking at the conditional mean of  $\dot{\omega}_{\text{H}_2\text{O}}$  on an isosurface of  $T_{\text{peak}}$  as a function of flame curvature (Fig. 3.11b). Again, as in the two-dimensional freely propagating case, regions with large negative curvature have source terms significantly below the peak one-

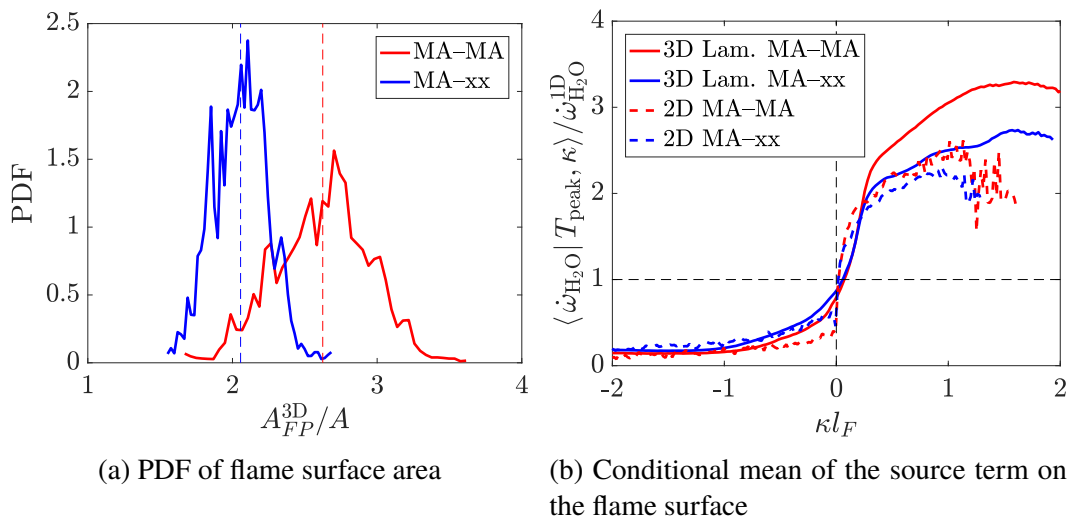


Figure 3.11: PDF of laminar three-dimensional flame surface area normalized by domain cross-sectional area (left) and normalized chemical source term as a function of normalized local flame curvature (right) for the MA-MA (red) and MA-xx (blue) models. The dashed lines represent the temporal mean of the flame area (left) and the two-dimensional conditional means (right).

dimensional source term. Also, the MA-xx case experiences less pronounced extinction, as demonstrated by the slightly higher source term where  $\kappa < 0$ . In regions of  $\kappa > 0$ , the conditional mean is greater than the one-dimensional source term. Similar to the two-dimensional case, the MA-MA model predicts greater source terms than the MA-xx model. Overall, the three-dimensional case predicts a greater increase in the source term over the two-dimensional flames and a wider range of positive curvatures.

### 3.6 Three-dimensional, turbulent, freely propagating flame

As a final demonstration of the thermal diffusion model, a three-dimensional, turbulent, freely propagating flame is simulated. The simulations are each run for 25 eddy turnover times,  $\tau$ , after allowing for initial transients to dissipate. Again, the incoming mixture and turbulence properties, flame configuration, and initialization procedure were detailed in Section 2.6.6.

Figure 3.12 shows a three-dimensional view of the isosurface of  $T_{\text{peak}}$  defining the flame front. The flame surface shows the complex behavior of the flame in the turbulent field, with large-scale cellular structures not as clearly defined as they appeared in the laminar two- and three-dimensional freely propagating cases. Figure 3.13 shows two-dimensional slices of the simulation, with contours of both

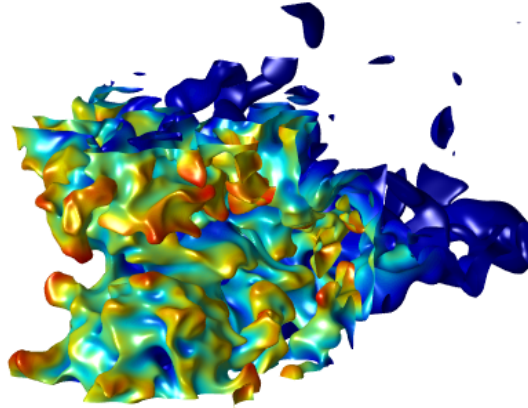


Figure 3.12: Isosurface of the three-dimensional turbulent flame with the MA–MA model. The isosurface corresponds to  $T_{\text{peak}}$ . The colors correspond to the normalized source term  $\dot{\omega}_{\text{H}_2\text{O}}/\dot{\omega}_{\text{H}_2\text{O}}^{1D} \in [0, 15]$ .

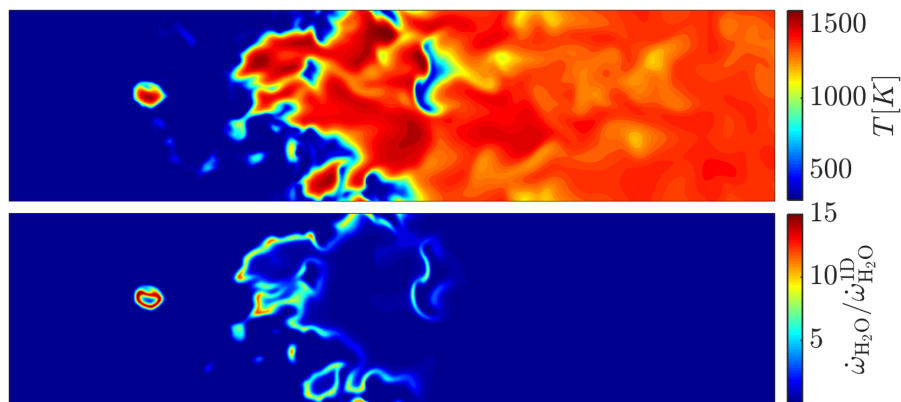


Figure 3.13: Temperature (top) and normalized H<sub>2</sub>O source term (bottom) contours for a section of the three-dimensional turbulent MA–MA case.

temperature and normalized source term. In regions of very high positive curvature, the normalized source term is over 10 times that of the one-dimensional flame. In areas with large negative curvature, the source term is nearly zero.

Figure 3.14a shows a time-history of the turbulent flame speed, calculated using Eq. 2.73, normalized by the respective laminar flame speeds and plotted as a function of time normalized by  $\tau$ . The mean normalized turbulent flame speed for the thermal diffusion case is  $S_T^{\text{MA-MA}}/S_L^o = 37.6$ , compared to  $S_T^{\text{MA-xx}}/S_L^o = 29.3$  for the case without thermal diffusion, an increase of 28%. The turbulent flame speed PDFs are shown in Fig. 3.14b, along with the mean turbulent flame speeds as vertical dashed lines. Once again, the inclusion of thermal diffusion increases the maximum flame speed observed and shifts the entire PDF towards higher flame speed values.

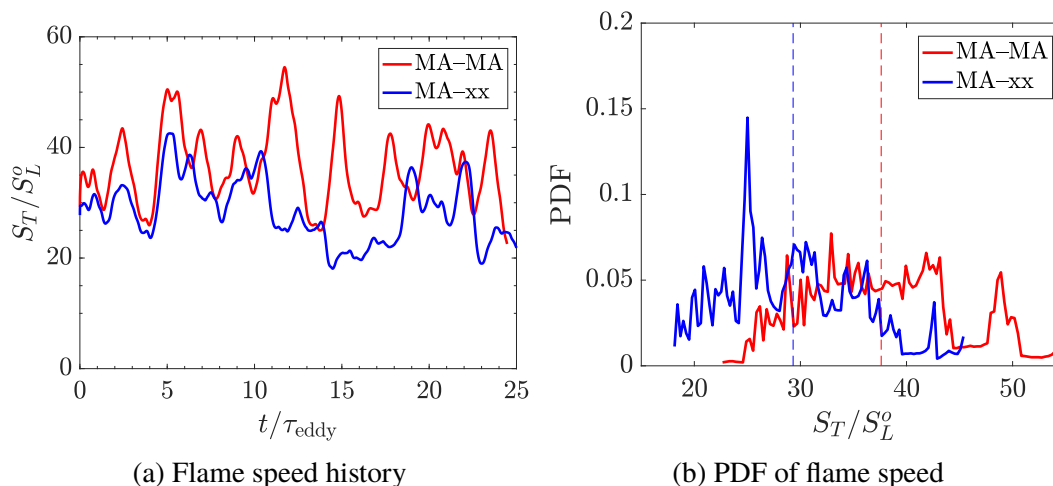


Figure 3.14: Flame speed history (left) and PDF of normalized flame speed (right) for the MA-MA (red) and MA-xx (blue) models. The dashed lines represent the temporal mean of the flame speeds.

To further quantify what effects (global and local) thermal diffusion has on turbulent flames, Fig. 3.15a shows the normalized flame surface area. The inclusion of thermal diffusion, once again, increases the mean surface area. For this flame configuration, the mean normalized surface area for the MA-MA case is  $A_T/A = 17.2$ , while the MA-xx model has a mean normalized flame surface area of  $A_T/A = 13.8$ . In addition to the increased mean surface area, there is an increase in the variance of the flame surface area; the standard deviation of the MA-MA case is  $\sigma_{\text{MA-MA}} = 3.07$  compared to the standard deviation of the MA-xx case,  $\sigma_{\text{MA-xx}} = 2.72$ . The percent increase in  $\sigma_{\text{MA-MA}}$  for the turbulence cases (12%), however, is smaller than that of the three-dimensional laminar cases (63%), indicating that turbulence acts to reduce the overall variability in the surface area due to thermal diffusion.

Finally, Fig. 3.15b shows the normalized product source term as a function of normalized flame surface curvature for the two diffusion cases. The conditional mean is plotted for values of  $\kappa$  which span 95% of the collected data. First, the maximum positive and negative curvatures observed in the turbulent cases are significantly larger than the laminar cases. The increased maximum curvature is due to the turbulent flow and the flame is curved at the scales of the smallest turbulent structures (at this Karlovitz number,  $\eta < l_F$ ). Further, the source term values for the turbulent cases are always higher than the values for the laminar cases. This result is similar to that of Aspden et al. [7], who found through their simulations (albeit

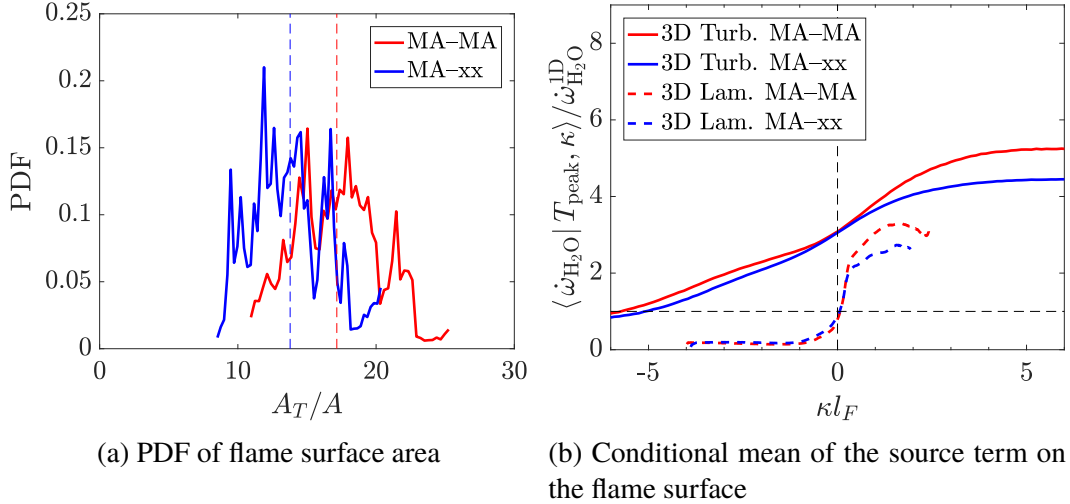


Figure 3.15: PDF of turbulent three-dimensional flame surface area normalized by domain cross-sectional area (left) and normalized chemical source term as a function of normalized local flame curvature (right) for the MA-MA (red) and MA-xx (blue) models. The dashed lines represent the temporal mean of the flame area (left) and the laminar three-dimensional conditional means (right).

neglecting Soret and Dufour effects) that increasing the Karlovitz number increased the burning intensity. The increased source term results from turbulent mixing enhancing species transport over pure molecular diffusion. Finally, the source term with thermal diffusion is once again higher than that of the case neglecting thermal diffusion, as was seen in the two-dimensional and three-dimensional laminar cases.

### 3.7 Discussion

#### 3.7.1 Size of the Cartesian computational domains

The current objectives of this thesis are to investigate the impact of various transport and chemistry models, which are particularly sensitive to flame curvature found in small cellular instability structures. It is important to note that the size of the computational domain containing these instabilities may also impact the simulation results. It is thus important to quantify the characteristic lengths of the cellular instabilities and extinction zones. A methodology to systematically identify the cellular instabilities, extinction zones, and length scales associated with each is carefully detailed in Appendix B. A short description of the method, as well as results for the two-dimensional freely propagating configuration, are given in this section.

The flame surface is first defined using an isosurface of  $Y_{\text{H}_2\text{O}}^{\text{iso}} = Y_{\text{H}_2\text{O}}^{\text{peak}}$ . The product

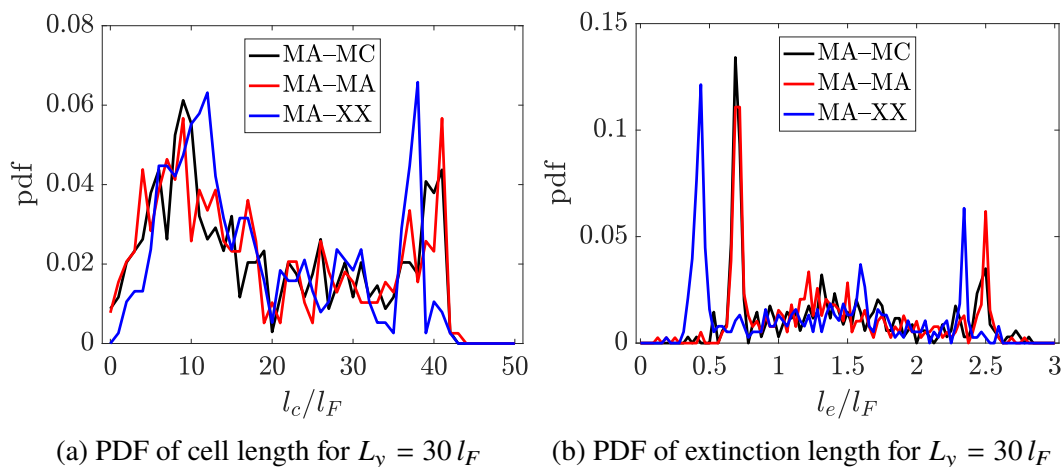


Figure 3.16: Statistics for the (a) cell length and (b) extinction zone length for the  $L_y = 30 l_F$  computational domain. The MA–MC (solid black), MA–MA (dashed red), and MA–xx (dotted blue) cases are all presented.

mass fraction is used so that this analysis could also be performed on data acquired from the tabulated chemistry detailed in Chapter 6. Then, the flame surface is segmented into “cellular structures” and “extinction zones” based on a threshold value of the  $\text{H}_2\text{O}$  source term,  $\dot{\omega}_{\text{H}_2\text{O}}^{\text{th}} = 0.2\dot{\omega}_{\text{H}_2\text{O}}^{\text{1D}}$ . These values of  $Y_{\text{H}_2\text{O}}^{\text{iso}}$  and  $\dot{\omega}_{\text{H}_2\text{O}}^{\text{th}}$  were selected after performing a sensitivity analysis; details of the sensitivity analysis, and the conclusions leading to these selections, are presented in Appendix B. Once cellular structures and extinction zones are identified, their length scales are calculated: for cellular structures, the arc length along the flame isosurface is used to define the cell length,  $l_c$ . The extinction length,  $l_e$ , is defined by connecting two neighboring cellular structures with a straight line.

Two domain heights ( $L_y = 30 l_F$  and  $L_y = 60 l_F$ ) are used to investigate the instability length scales. A minimum of 120 data files, spanning over  $200 \tau_F$ , for each diffusion model are analyzed. Figure 3.16 shows the PDFs of the cell length and extinction zone length computed using all available numerical data. The two length scales are normalized by the one-dimensional laminar flame thickness using the corresponding diffusion models.

A number of results are first evident in the length scale PDFs. First, the MA and MC thermal diffusion models both predict similar statistics of the flame front length scales. This result again confirms that the MA–MA model is sufficient to capture thermal diffusion effects present in the MA–MC model. Further, the cell length PDFs show a shift toward less extreme cell sizes by neglecting thermal diffusion. The cellular structures also have two distinct peak length scales; one peak, around

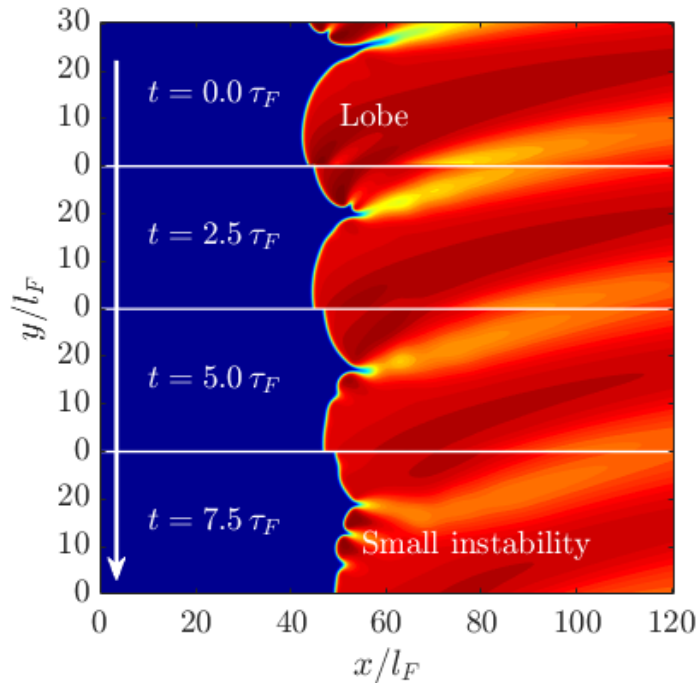


Figure 3.17:  $Y_{\text{H}_2\text{O}}$  contour plots showing the time history of a larger lobe breaking down into smaller cellular instabilities.

$l_c/l_F = 10$ , corresponds to the small cellular structures which form along the large single-cusp instabilities (lobes). The larger length scale,  $l_c/l_F = 40$ , corresponds to these larger single-cusp structures. An example of the transition between these two cellular instability sizes is given in Fig. 3.17. The extinction zone length PDFs indicate that neglecting thermal diffusion predicts a smaller extinction zone (by approximately 35%).

The reported length scales indicate that extinction zones are of the same order as the laminar flame thickness, with a large proportion of extinction zones smaller than  $l_F$ , while cellular structures are typically an order of magnitude larger than  $l_F$ . These extinction zones act to enhance the cellular instabilities through differential diffusion effects, and must be resolved or adequately modeled in numerical simulations. For simple two-dimensional cases such as those presented in this work, resolving the extinction zones is satisfied by having  $\Delta x = l_F/16$ . However, for large-scale, three-dimensional, turbulent flows which are not amenable to DNS (and must therefore be treated using a large-eddy simulation (LES) framework), the extinction regions might be sub-grid. An accurate simulation of lean hydrogen flames using LES may therefore need to consider extinction zone effects in the sub-grid scale models.

An identical analysis of the instability length scales is performed on the computa-

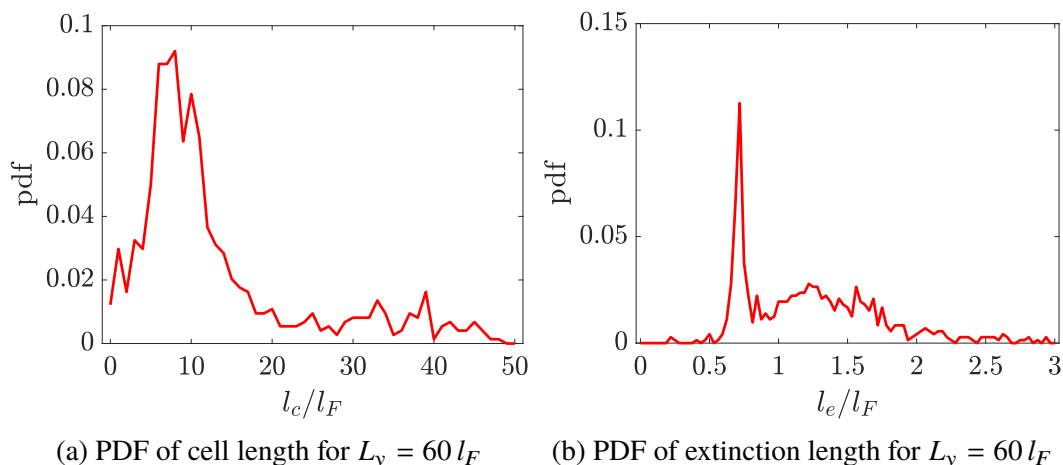


Figure 3.18: Statistics for the (a) cell length and (b) extinction zone length for the  $L_y = 60 l_F$  computational domain using the MA-MA model.

tional domain with  $L_y = 60 l_F$ . The results of  $l_c$  and  $l_e$  are shown in Fig. 3.18. The extended domain results show two key features. First, the length scales associated with the smaller cellular instabilities ( $l_c \approx 10 l_F$ ) are similar to the  $L_y = 30 l_F$  configuration. This indicates the smaller structures are not greatly influenced by reducing the domain height. Second, there are fewer instances of large, single-cusp flame structures, relative to the small instabilities. This is expected as the single-cusp structures will have a longer characteristic length, allowing more small structures to form along the flame surface.

In summary, the effect of reducing the computational domain height in half (from  $60 l_F$  to  $30 l_F$ ) appears to be an increased presence of the large single-cusp structures. By further reducing the computational domain height from  $L_y = 30 l_F$  for the two-dimensional case to  $L_y = 12 l_F$  for the three-dimensional configurations, the single-cusp structures are significantly suppressed, and only small cellular instabilities will be present. This conclusion is in agreement with previous studies on instability growth in similar computational configurations [4, 46, 129] and the three-dimensional laminar flame isosurface in Fig. 3.9 qualitatively supports this finding. Additionally, the chosen domain size for the three-dimensional configurations is similar to that of Aspden [4] who used a comparable Karlovitz number as the current turbulent configuration. By selecting a domain size which permits only small instability structures and extinction zones, the influence of these high curvature regions on the transport and chemistry processes can be efficiently investigated in three-dimensional configurations.

### 3.7.2 Thermal diffusion effects

Much of the previous work discussing thermal diffusion in the literature utilized simplified flame configurations (e.g., one-dimensional, flat flames) as the basis for determining the relative importance of thermal diffusion effects. If only the one-dimensional flat flame were considered, thermal diffusion would appear to have little significance on the laminar burning velocity, decreasing the flame speed by only 5% at  $\phi = 0.4$ . When laminar flame speeds can vary by 40% using different chemical models [51], such a small change in flame speed seems insignificant for the potential increased computational costs.

With more complex, yet steady, configurations including flame curvature (i.e., cellular tubular flames), the effects of thermal diffusion are quickly apparent. Not only does the inclusion of thermal diffusion change the flame radius, flame shape, and species profiles, but it also causes the flame instabilities to become more severe, with regions of increased burning and extinction in the MA–MA case relative to the MA–xx case.

Thermal diffusion remains important in all unsteady cases, whether laminar (two- and three-dimensional) or turbulent. In each of the multi-dimensional cases presented in this work, thermal diffusion altered both global and local flame quantities. The increase in effective flame speed can be attributed to thermal diffusion increasing both the flame surface area (global effect) and  $\dot{\omega}_{\text{H}_2\text{O}}$  (local effect). Further, the unsteadiness of these configurations, measured by the variance of the flame speed and surface area, is increased by including thermal diffusion effects.

The mixture-averaged thermal diffusion model proposed by Chapman and Cowling [24] accurately predicted the effects of thermal diffusion in each case considered here. The agreement was found by comparing the MA–MA model with both MA–MC calculations and experimental measurements.

### 3.7.3 Computational cost

The implemented mixture-averaged thermal diffusion model is an accurate method for capturing the Soret and Dufour effects. While this work is not meant to present a detailed analysis of the computational cost or scaling of the MA–MA and non-iterative MA–MC algorithms (using CHEMKIN), a brief discussion of the increased cost to include thermal diffusion is necessary.

A comparison of the time to compute the diffusion coefficients to the total computational time is thus given. Timings were acquired for the various flame configurations

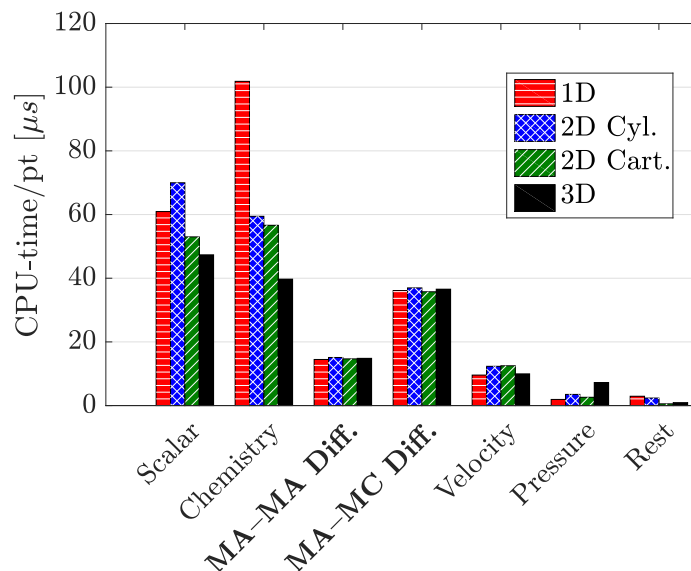


Figure 3.19: Computational time per grid point for each part of the code for four flame configurations. All timings reported use the MA–MA model, except for the MA–MC diffusion coefficient timings.

covering the cases presented in this work, including an additional timing test for the three-dimensional MA–MC case run for only 20 time steps. The computational time for each part of the code is presented in Fig. 3.19. In Fig. 3.19, the time to compute both  $D_{i,m}$  and  $D_i^T$  are combined into the “MA–MA Diff.” and “MA–MC Diff.” categories. These timings were acquired on TACC’s Stampede cluster using the Extreme Science and Engineering Discovery Environment (XSEDE) [120].

The cost of the MA–MA model is clearly less than that of the MA–MC method. The cost of CHEMKIN’s MA–MC diffusivity represents over 25% of the total simulation time. We note, however, that even this expensive, non-iterative multicomponent diffusion model is only twice as costly as the mixture-averaged diffusion model described in this work. An iterative multicomponent thermal diffusion model, such as that proposed by Ern and Giovangigli [40], would yield nearly the same thermal diffusion coefficients as the MA–MC model at a reduced cost.

While much of the code exhibits the same cost per grid point regardless of the dimensionality of the problem, the chemistry—and to a lesser extent the scalar transport—is more expensive for one- and two-dimensional cases. This cost increase is due to the code structure. The code has been written and optimized for three-dimensional configurations, thus the one- and two-dimensional cases are artificially more expensive, especially in the chemistry calculations.

These results indicate that, for hydrogen–air combustion, the MA–MA model is less expensive than the non-iterative MA–MC model; however, the total cost of computing thermal diffusion coefficients remains tractable, even for MA–MC cases. Coupled with the discussion of flame shape, structure, and global and local quantities in each of the computational configurations, the MA–MA model presents an accurate method to capture thermal diffusion effects that is computationally comparable to iterative multicomponent techniques.

## Chapter 4

### A REDUCED THERMAL DIFFUSION MODEL

- [1] J. Schlup and G. Blanquart. “A reduced thermal diffusion model for H and H<sub>2</sub>”. In: *Combust. Flame* 191 (2018), pp. 1–8. DOI: [10.1016/j.combustflame.2017.12.022](https://doi.org/10.1016/j.combustflame.2017.12.022).

Chapter 3 provided an evaluation of Chapman and Cowling’s mixture-averaged thermal diffusion model [24] across a range of flame configurations. It was found that thermal diffusion has an effect on global and local flame characteristics, and should be included in future investigations of lean premixed hydrogen–air mixtures. While the mixture-averaged thermal diffusion model was shown to be computationally efficient, especially compared to a non-iterative multicomponent method, this chapter aims to develop a reduced-order model with near-constant cost, regardless of chemical model size.

#### 4.1 Review of mixture-averaged thermal diffusion

The reduced thermal diffusion model proposed in this chapter is based on work by Chapman and Cowling [24]. While their thermal diffusion model was given in Chapter 2, the most pertinent equations are repeated in this section for reference. The thermal diffusion coefficients,  $D_{i,MA}^T$ , are given by Paul and Warnatz [95] as

$$D_{i,MA}^T = \rho \frac{W_i}{W} D_{i,m} k_{Ti}, \quad (4.1)$$

where the mixture-averaged diffusion coefficient of species  $i$  given by

$$D_{i,m} = \frac{1 - Y_i}{\sum_{j \neq i}^n X_j / \mathcal{D}_{ij}}, \quad (4.2)$$

and  $k_{Ti}$  is the thermal diffusion ratio of species  $i$ , given by Chapman and Cowling [24] as

$$k_{Ti} = \frac{W^2}{R\rho} \sum_{j=1}^n \frac{1.2C_{ij}^* - 1}{\mathcal{D}_{ij}} \frac{Y_i a_j - Y_j a_i}{W_i + W_j}. \quad (4.3)$$

In their work, it was assumed that the internal degrees of freedom associated with thermal conductivity,  $\lambda$ , do not significantly affect values of  $k_{Ti}$  [24]. In Eqs. 4.2

and 4.3,  $\mathcal{D}_{ij}$  is the binary diffusion coefficient of species  $i$  diffusing into species  $j$ , given by

$$\mathcal{D}_{ij} = \frac{3}{16} \frac{\sqrt{2\pi k_B^3 T^3 / m_{ij}}}{p\pi\sigma_{ij}^2 \Omega_{ij}^{(1,1)*}}. \quad (4.4)$$

In Eq. 4.3,  $C_{ij}^*$  is a ratio of collision integrals [37],

$$C_{ij}^* = \frac{1}{3} \frac{\Omega_{ij}^{(1,2)}}{\Omega_{ij}^{(1,1)}}, \quad (4.5)$$

and  $a_i$  is based on the forms from Mason and Saxena [82] and Oran and Boris [93], given as

$$a_i = \frac{\lambda_{i,mon} X_i}{\Delta_i}. \quad (4.6)$$

$\Delta_i$  is given by

$$\Delta_i = X_i + \sum_{j \neq i}^n X_j \Phi_{ij}, \quad (4.7)$$

where  $\Phi_{ij}$  is a term appearing in mixture-averaged viscosity formulations (examined later) and  $\lambda_{i,mon}$  is the monatomic species conductivity (i.e., neglecting internal degrees of freedom)

$$\lambda_{i,mon} = \frac{15}{4} \frac{R\mu_i}{W_i}. \quad (4.8)$$

Finally,  $C_{ij}^*$  is computed using a rational function fit detailed in Appendix A.1.

$\Phi_{ij}$  in Eq. 4.7 is a function of species molecular weights and species viscosities,  $\mu_i$ , and takes the form [82, 93]

$$\Phi_{ij} = \frac{1.065}{2\sqrt{2}} \frac{\left[1 + \left(\frac{\mu_i}{\mu_j}\right)^{1/2} \left(\frac{W_j}{W_i}\right)^{1/4}\right]^2}{\left[1 + \left(\frac{W_i}{W_j}\right)\right]^{1/2}}, \quad (4.9)$$

where  $\mu_i$  is defined using kinetic theory [58]

$$\mu_i = \frac{5}{16} \frac{(\pi m_i k_B T)^{1/2}}{\pi \sigma_i^2 \Omega_i^{(2,2)*}}. \quad (4.10)$$

In Eq. 4.10,  $m_i$  is the mass of species  $i$ ,  $k_B$  is the Boltzmann constant,  $T$  is the temperature,  $\Omega_i^{(2,2)*}$  is a collision integral normalized by its rigid sphere value (see Appendix A.1), and  $\sigma_i$  is the collision diameter of species  $i$ .

## 4.2 Model development

The reduced model development considers three approximations for various terms comprising the mixture-averaged thermal diffusion model. Briefly, the model, as developed, is aimed toward describing combustion systems where the transport of light species ( $W_i \ll W$ ) due to thermal diffusion is important. The model may also be applicable to other mixtures, yet the validity of the model assumptions should be verified.

In order to reduce the computational cost of Eq. 4.1, it is desirable to remove the summations over species. The first approximation is to write  $\Phi_{ij}$  in terms of species  $i$  only. First,  $\Delta_i$  (Eq. 4.7) is approximated to have the form

$$\Delta_i \approx \Delta'_i = \sum_{j=1}^n X_j \Phi_{ij}, \quad (4.11)$$

or, equivalently,  $\Phi_{ii} = 1.065$  instead of  $\Phi_{ii} = 1$  in Eq. 4.7.

$\Phi_{ij}$  is then simplified: upon substitution of Eq. 4.10 into Eq. 4.9,  $\Phi_{ij}$  becomes

$$\Phi_{ij} = \frac{1.065}{2\sqrt{2}} \frac{\left[ 1 + \left( \frac{\sigma_j}{\sigma_i} \right) \left( \frac{\Omega_j^{(2,2)*}}{\Omega_i^{(2,2)*}} \right)^{1/2} \right]^2}{\left[ 1 + \left( \frac{W_i}{W_j} \right) \right]^{1/2}}. \quad (4.12)$$

A simple fit of  $\sigma_i$  as a function of  $W_i$  is used, taking the form

$$\sigma_i = 1.234W_i^{0.33}. \quad (4.13)$$

A plot of  $\sigma_i(W_i)$  is provided in Appendix A.1. Additionally, Rosner [105] demonstrated that  $\Omega_i^{(2,2)*}$  can be approximated by a power law fit as a function of Lennard-Jones reduced temperature,  $T_i^* = Tk_B/\epsilon_i$ , of the form

$$\Omega_i^{(2,2)*} \approx 1.22(T_i^*)^{-0.16} \quad (4.14)$$

over a range of  $T_i^* \in [3, 300]$ , where  $\epsilon_i$  is the potential well depth of species  $i$ . A plot of this fit is given in Fig. 4.1. The fit  $\Omega_i^{(2,2)*}$  in Eq. 4.14 and the rational polynomial fit implemented in FlameMaster [100] overlap. An additional fit of  $k_B/\epsilon_i$ , given by the expression

$$\frac{\epsilon_i}{k_B} = 37.15W_i^{0.58}, \quad (4.15)$$

can be substituted into Eq. 4.14 as part of  $T^*$ , yielding

$$\Omega_i^{(2,2)*} \approx T^{-0.16}W_i^{0.0928}. \quad (4.16)$$

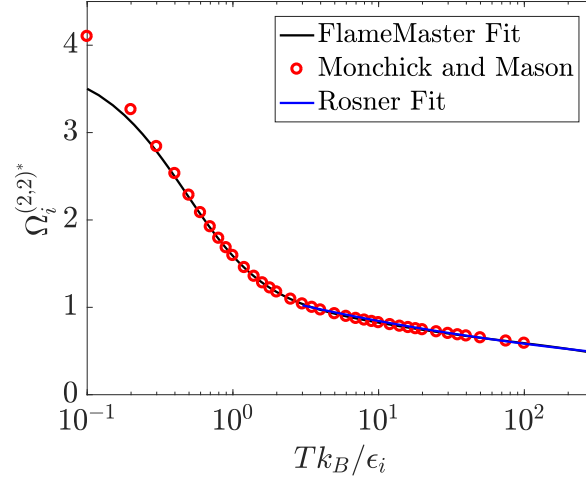


Figure 4.1: Rational function fit of  $\Omega_i^{(2,2)*}$  using coefficients from FlameMaster [100] (black line), tabulated data from Monchick and Mason [87] (red circles), and the fit from Rosner [105] (blue line).

With these fits for  $\sigma_i(W_i)$  and  $\Omega_i^{(2,2)*}(W_i)$ ,  $\Phi_{ij}$  can be approximately written as a function of molecular weights only,

$$\Phi_{ij} \approx \Phi'_{ij} = \frac{1.065 \left[ 1 + \left( \frac{W_j}{W_i} \right)^{0.376} \right]^2}{2\sqrt{2} \left[ 1 + \left( \frac{W_j}{W_i} \right) \right]^{1/2}}. \quad (4.17)$$

Figure 4.2 shows  $\Phi'_{ij}$  evaluated for  $W_i/W_j \in [0.01, 100]$  and a power law fit as a function of  $W_i/W_j$ , resulting in a relationship of the form

$$\Phi'_{ij} \approx 1.022 \left( \frac{W_j}{W_i} \right)^{0.602}. \quad (4.18)$$

Since the power law dependence on  $W_j$  is of order one, it is possible to write the mixture-averaged  $\Phi'_{ij}$  (i.e.,  $\Delta'_i$ ) by replacing  $\sum_j X_j W_j$  with  $W$ , namely

$$\Delta'_i \approx \sum_{j=1}^n X_j \Phi'_{ij} \approx 1.022 \left( \frac{W}{W_i} \right)^{0.602}. \quad (4.19)$$

Alternatively, one can utilize the final observation on the exponent of  $W_j$  in Eq. 4.18 and approximate species  $j$  properties as having properties close to the mixture. Thus,  $\Phi_{ij}$  could also be approximated using mixture properties, leading to

$$\Delta'_i \approx \Phi_{i,m} = \frac{1.065 \left[ 1 + \left( \frac{\mu_i}{\mu} \right)^{1/2} \left( \frac{W}{W_i} \right)^{1/4} \right]^2}{2\sqrt{2} \left[ 1 + \left( \frac{W_i}{W} \right) \right]^{1/2}}, \quad (4.20)$$

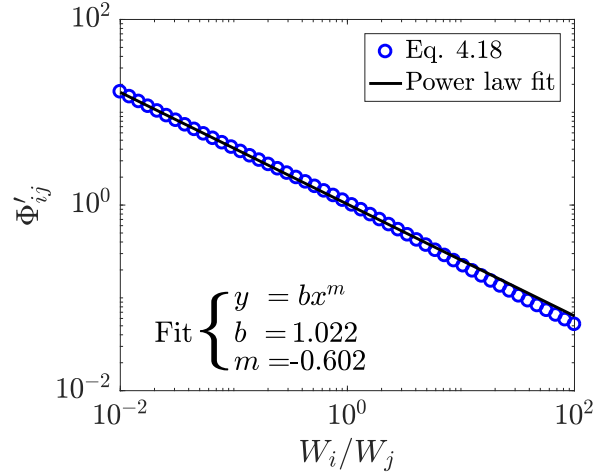


Figure 4.2:  $\Phi'_{ij}$ , computed using Eq. 4.17, as a function of  $W_i/W_j \in [0.01, 100]$ , approximating the range of  $W_i/W_j$  in CaltechMech [14].

which is now only a function of species  $i$  and mixture properties.

The factor  $a_i$  (Eq. 4.6) can then be approximated using  $\Delta_i \approx \Phi_{i,m}$ . This form of  $a_i$  is then substituted into Eq. 4.1. The first approximation (of  $\Delta_i$  being written as only a function of species  $i$ ) thus yields approximate mixture-averaged thermal diffusion coefficients,  $D_{i,MA}^T$ , defined as

$$D_{i,MA}^T \approx \frac{15}{4} W_i^2 X_i D_{i,m} \sum_{j \neq i}^n \frac{1.2 C_{ij}^* - 1}{\mathcal{D}_{ij}} X_j \frac{W_j}{W_i + W_j} \times \left( \frac{\mu_j}{W_j^2 \Phi_{j,m}} - \frac{\mu_i}{W_i^2 \Phi_{i,m}} \right). \quad (4.21)$$

The coefficients have now been reduced from a double summation over all species in Eq. 4.1 ( $\mathcal{O}(n^2)$ ) to a single summation over all species ( $\mathcal{O}(n)$ ).

The second approximation is that  $W_i \ll W_j$ , with  $i = \text{H}$  or  $\text{H}_2$ . This approximation yields two results:  $\mu_j/W_j^2 \Phi_{j,m} \ll \mu_i/W_i^2 \Phi_{i,m}$  and  $W_i + W_j \approx W_j$ . The first relation is a direct consequence of the molecular weight scalings for  $\mu_i$  (Eq. 4.10) at a given temperature, i.e.,

$$\mu_i = \frac{5 (\pi m_i k_B T)^{1/2}}{16 \pi \sigma_i^2 \Omega_i^{(2,2)*}} \propto \frac{W_i^{1/2}}{(W_i^{0.33})^2 (W_i)^{0.0928}} = W_i^{-0.253}. \quad (4.22)$$

Using  $\Phi'_{ij}$  from Eq. 4.18, it is found that  $\mu_i/W_i^2 \Phi_{i,m} \propto W_i^{-1.65} W^{-0.602}$  and thus  $\mu_j/W_j^2 \Phi_{j,m} \ll \mu_i/W_i^2 \Phi_{i,m}$ . Using the two relations of this second approximation,

Eq. 4.21 becomes

$$D_{i,MA}^T \approx -\frac{15}{4} \frac{\mu_i X_i}{\Phi_{i,m}} D_{i,m} \sum_{j \neq i}^n \left( \frac{1.2C_{ij}^* - 1}{\mathcal{D}_{ij}} X_j \right). \quad (4.23)$$

The third approximation is to replace  $C_{ij}^*$  using properties of species  $i$  and the mixture. Appendix A.1 shows that  $C_{ij}^*$  is largely independent of  $T_{ij}^*$  for a range of  $T_{ij}^* \in [1, 100]$ , representative of a reacting flow. A figure of the rational polynomial fit for  $C_{ij}^*$  is given in Appendix A.1 (Fig. A.1c). Here,  $T_{ij}^* = Tk_B/\epsilon_{ij}$  is computed using the interaction well depth  $\epsilon_{ij} = \sqrt{\epsilon_i \epsilon_j}$ . A deviation of only 5% is found around a nominal value  $C_{ij}^* \approx 0.93$  for  $T_{ij}^* > 2$ . Because  $C_{ij}^*$  is insensitive to  $T_{ij}^*$ , it is possible to find a mixture-averaged  $C_{i,m}^*$ , which would be a function of  $k_B/\epsilon_i$  and some mixture  $k_B/\epsilon_m$ . This is accomplished by utilizing the power law fit for  $k_B/\epsilon_i$  and a similar fit for the mixture,  $k_B/\epsilon_m \approx [37.15W^{0.58}]^{-1}$ . Then, one can approximate  $T_{ij}^*$  as

$$T_{i,m}^* = \frac{1}{37.15} T (W_i W)^{-0.29}. \quad (4.24)$$

Now,  $C_{i,m}^* = f(T_{i,m}^*)$  is independent of species  $j$ .

Combining the three assumptions made above, Eq. 4.21 then reduces to an expression with no summations,

$$D_{i,MA}^T \approx -\frac{15}{4} \frac{X_i \mu_i}{\Phi_{i,m}} \left( 1.2C_{i,m}^* - 1 \right) (1 - Y_i), \quad (4.25)$$

where Eq. 4.2 is used to remove  $D_{i,m}$  and  $\Phi_{i,m}$  simplifies from Eq. 4.20 to

$$\Phi_{i,m} = \frac{1.065}{2\sqrt{2}} \left[ 1 + \left( \frac{\mu_i}{\mu} \right)^{1/2} \left( \frac{W}{W_i} \right)^{1/4} \right]^2 \quad (4.26)$$

under the assumption that  $W_i \ll W$ , where  $i$  is H or H<sub>2</sub>.

In the process of making the above approximations, it is likely systematic errors have been introduced. To account for these systematic errors in arriving at Eq. 4.25, a proposed scaling parameter  $\alpha_i$  is added and thus the final reduced model (RM) thermal diffusion coefficients are given as

$$D_{i,RM}^T \equiv -\alpha_i \frac{15}{4} \frac{X_i \mu_i}{\Phi_{i,m}} \left( 1.2C_{i,m}^* - 1 \right) (1 - Y_i) - Y_i S. \quad (4.27)$$

$S$  is a scalar which enforces mass conservation via the thermal diffusion fluxes, i.e.,  $\sum_i D_{i,RM}^T = 0$ . The values of  $\mu_i$  used in Eq. 4.27 are computed using Eq. 4.10;

Table 4.1: One-dimensional flame cases used for the reduced thermal diffusion model evaluation.

Case	Fuel	Chem.	Diluent	$\phi$	$T_u$ [K]	$p$ [atm]	$L_H^2$ [%]	$L_{H_2}^2$ [%]	$\epsilon_{S_L}^{RM}$ [%]
1	H <sub>2</sub>	[59]	N <sub>2</sub>	0.4	298	1	2.89	2.69	0.26
2	H <sub>2</sub>	[59]	N <sub>2</sub>	0.4	298	5	2.06	2.79	0.38
3	H <sub>2</sub>	[59]	N <sub>2</sub>	1.0	298	1	6.43	12.00	0.70
4	H <sub>2</sub>	[59]	N <sub>2</sub>	0.4	500	1	1.16	3.65	0.27
5	H <sub>2</sub>	[59]	—	0.4	298	1	12.31	21.82	1.40
6	H <sub>2</sub>	[116]	Ar	0.4	298	1	2.29	3.91	0.90
7	CH <sub>4</sub>	[116]	N <sub>2</sub>	1.0	298	1	0.89	1.19	0.15
8	NC <sub>7</sub>	[13]	N <sub>2</sub>	1.0	298	1	0.94	1.46	0.18
9	C <sub>7</sub> H <sub>8</sub>	[14]	N <sub>2</sub>	1.0	298	1	0.79	2.13	0.38

further, the values of  $\sigma_i$  and  $\epsilon_i/k_B$  needed to compute  $\mu_i$  come from transport property databases. It should be noted that the empirical fits as functions of  $W_i$  found throughout this section and in Appendix A.2 are used only for scaling arguments and model reduction. Once this model is implemented in NGA, values of these parameters (e.g.,  $\mu_i$  and  $\Omega_i^{(2,2)*}$ ) are computed using their full definitions. Determining the values of  $\alpha_i$  is the described in Section 4.3.1.

### 4.3 Model evaluation

The reduced model presented above is evaluated using multicomponent thermal diffusion for a range of one-dimensional unstretched flame conditions and a three-dimensional turbulent flame configuration. The multicomponent model is implemented using CHEMKIN II [66], which is based on the methods of Dixon-Lewis [37]. In the evaluation of one-dimensional laminar flames, the scaling parameter inherent to the reduced model is first found, such that the reduced model accurately reproduces thermal diffusion fluxes calculated from the multicomponent model. The scaling parameters are then utilized in the three-dimensional turbulent flame configuration.

#### 4.3.1 One-dimensional unstretched laminar flame evaluation

Table 4.1 summarizes the one-dimensional unstretched laminar flame conditions tested. For this evaluation, a variety of fuels, oxidizers, diluents, equivalence ratios ( $\phi$ ), unburnt temperatures ( $T_u$ ), and pressures ( $p$ ) are used. Each case uses multicomponent thermal diffusion and mixture-averaged mass diffusion for species transport. The cases are run to steady state using NGA [36]. At steady state, the coefficients from Eq. 4.25 are computed. Four chemical models are used in this

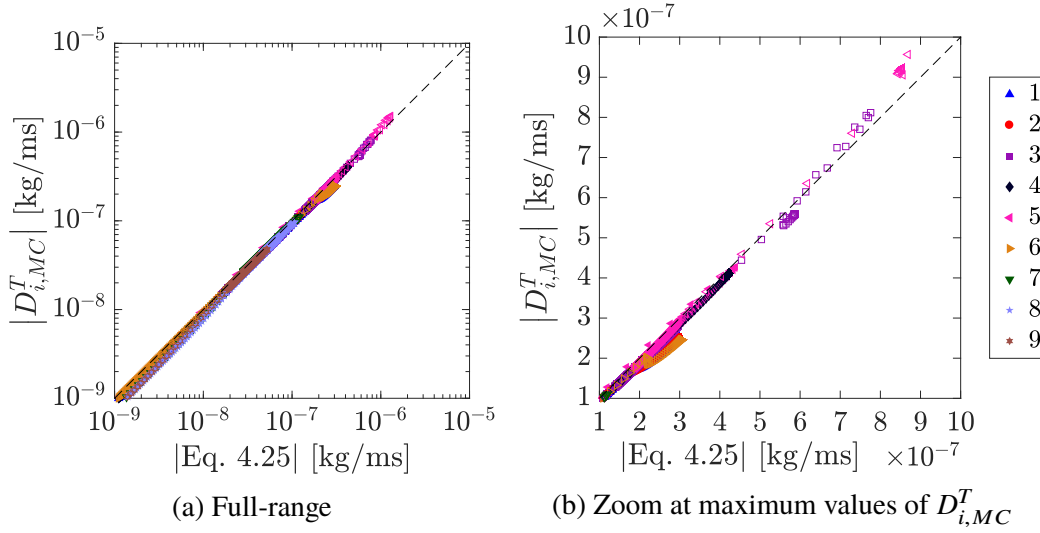


Figure 4.3: Thermal diffusion coefficients for H (filled symbols) and H<sub>2</sub> (open symbols) for all cases using the multicomponent model ( $D_{i,MC}^T$ ) and Eq. 4.25 (corrected to satisfy mass conservation). A zoom of the data near maximum  $|D_i^T|$  is provided on the right with linear axes.

evaluation: a hydrogen–air chemistry model by Hong et al. with updated reaction rates from the same group [59, 60, 72] is used for the H<sub>2</sub>/air and H<sub>2</sub>/O<sub>2</sub> cases. GRI-Mech 3.0 [116] is used for the H<sub>2</sub>/O<sub>2</sub>/Ar and CH<sub>4</sub> cases. A reduced *n*-heptane (C<sub>7</sub>H<sub>16</sub>, abbreviated NC7) model (without aromatic species) from Bisetti et al. [13] is used for the NC7/air case, and CaltechMech 2.4 [14] is used for the toluene (C<sub>7</sub>H<sub>8</sub>)/air case.

First, the thermal diffusion coefficients using the multicomponent model ( $D_{i,MC}^T$ ) and Eq. 4.25 (corrected to satisfy mass conservation) are shown in Fig. 4.3. The excellent collapse of all data on a single line with unity slope indicates agreement between the MC model and Eq. 4.25 is strong over a wide range of flame operating conditions. Small deviations from the unity line are present, especially at low values of  $D_i^T$ ; however, the important parameter for the solution of the species transport equations is the thermal diffusion flux,  $\mathbf{j}_i^T = D_i^T \nabla T / T$ .

A least squares regression (LSR) of the thermal diffusion fluxes is performed to identify a possible scaling parameter  $\alpha_i$  such that the relative  $L_i^2$  errors between  $\mathbf{j}_{i,MC}^T$  and  $\mathbf{j}_{i,RM}^T$ , defined as

$$L_i^2 = \left[ \frac{\sum (\mathbf{j}_{i,MC}^T - \mathbf{j}_{i,RM}^T)^2}{\sum (\mathbf{j}_{i,MC}^T)^2} \right]^{1/2}, \quad (4.28)$$

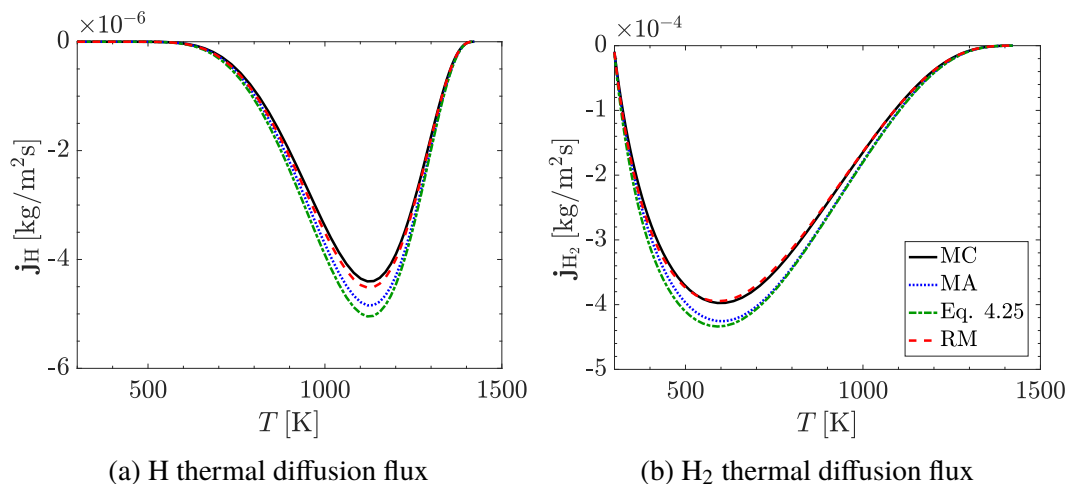


Figure 4.4: Thermal diffusion fluxes for (a) H and (b) H<sub>2</sub> as a function of  $T$  for Case 1 using the MC (solid black), MA (dotted blue), unfitted reduced (dot-dashed green), and RM (dashed red) models. Note the MC and RM cases nearly overlap, and Eq. 4.25 has been corrected to satisfy mass conservation.

are minimized across all test cases. While a LSR using data across all cases is preferable, including Cases 3 (stoichiometric H<sub>2</sub>/air) and 5 (lean hydrogen oxy-combustion) was found to result in large  $L_i^2$  across all cases; thus, the LSR is performed without Cases 3 and 5. The optimal scaling factors are found to be  $\alpha_H = 0.895$  and  $\alpha_{H_2} = 0.910$ . These scaling parameters serve two purposes: they correct systematic errors found in the original mixture-averaged model (visible in Fig. 4.4), and account for new systematic errors introduced through the reduced model development. The two values of  $\alpha_i$  are used during run-time to calculate  $D_{i,RM}^T$  from Eq. 4.27. The relative  $L_i^2$  error norms are shown in Table 4.1. For a majority of the cases, the relative errors are below 4%. The maximum  $L_i^2$  errors occur for Cases 3 and 5; this is unsurprising as  $\alpha_i$  was computed neglecting these cases.

Next, a plot of the thermal diffusion fluxes through the flame for Case 1 is given in Fig. 4.4. All four thermal diffusion models (i.e.,  $D_{i,MC}^T$ ,  $D_{i,MA}^T$ , Eq. 4.25 (corrected for mass conservation), and  $D_{i,RM}^T$ ) are included for H and H<sub>2</sub>. There is a slight discrepancy between the MC and MA models, where the MA model overpredicts the H and H<sub>2</sub> thermal diffusion coefficients. This overprediction is made larger through the approximations leading to Eq. 4.25. After performing the LSR, the RM coefficients agree extremely well with the MC model, as expected based on the value of  $L_i^2$ . The error norms indicate that the thermal diffusion fluxes can be

captured accurately for many cases using the RM model.

Each of the cases in Table 4.1 is run as a one-dimensional unstretched flame using the RM model until a steady-state solution is reached. The unstretched laminar flame speeds,  $S_L^o$ , are then calculated for the RM and MC transport cases, using the form given in Eq. 2.73. The relative error in  $S_L^o$  is calculated using

$$\epsilon_{S_L}^{RM} = \left| \frac{S_L^{o,MC} - S_L^{o,RM}}{S_L^{o,MC}} \right|. \quad (4.29)$$

The relative errors of  $S_L^o$  for each case are listed in Table 4.1. The unstretched laminar flame speeds agree extremely well across all cases. This even includes cases with higher relative  $L^2$  norms for H and H<sub>2</sub> thermal diffusion fluxes (i.e., Cases 3 and 5), indicating that the inclusion (or accuracy) of thermal diffusion fluxes have little impact on these fuel mixtures. For the remainder this work, all simulation results using the reduced model will include the factors  $\alpha_H$  and  $\alpha_{H_2}$ .

### 4.3.2 Three-dimensional turbulent flame evaluation

This section utilizes the three-dimensional turbulent configuration and flow properties detailed in Section 2.6.6. An a priori analysis is performed using data files from the turbulent case presented in Section 3.6. No new simulations are performed. The unburnt premixed mixture consists of H<sub>2</sub>/air at identical inlet properties of Case 1 from Table 4.1.

Both MC and RM thermal diffusion fluxes are computed using an instantaneous set of scalar fields. Figure 4.5 shows the conditional mean of  $\mathbf{j}_{i,MC}^T$  and  $\mathbf{j}_{i,RM}^T$  as a function of  $T$  for H and H<sub>2</sub> during one time step. The agreement of the conditional means is excellent across the entire range of temperatures, including regions which exceed the maximum temperature in a one-dimensional unstretched flame (temperatures on the right of the vertical dotted black line in Fig. 4.5).

As an additional verification, probability density functions (PDFs) of the thermal diffusion coefficients are computed at the temperatures of peak thermal diffusion flux, namely  $T_{peak,H} = 1090$  K and  $T_{peak,H_2} = 500$  K. These PDFs are shown in Fig. 4.6 and represent the scatter in thermal diffusion coefficients due to turbulent transport of species and temperature. For H, the MC and RM models predict nearly identical thermal diffusion coefficients. The agreement is still quite good for H<sub>2</sub>, where the RM case tends to slightly underpredict the thermal diffusion coefficient (as seen in Fig. 4.5). It performs, however, better than the original MA model.

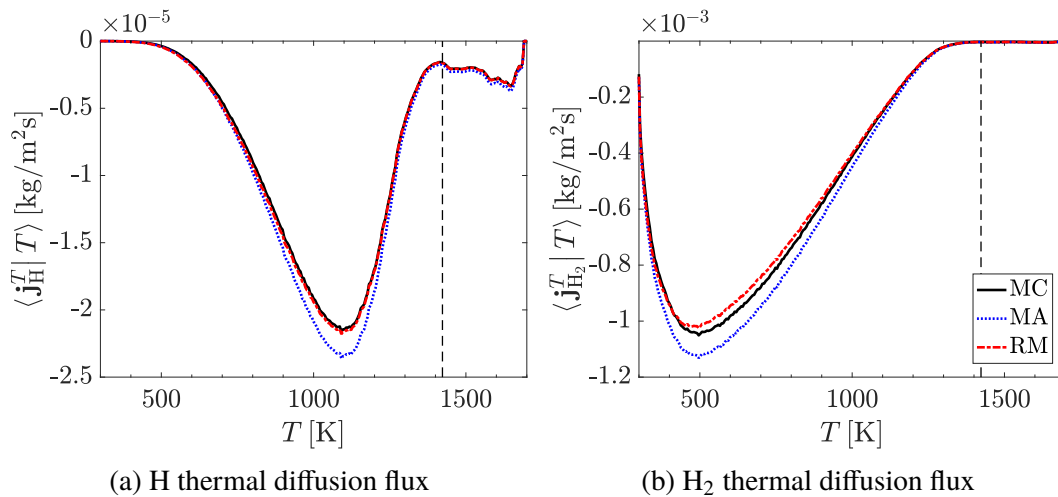


Figure 4.5: Conditional mean of the thermal diffusion fluxes for (a) H and (a) H<sub>2</sub> as a function of  $T$  for the turbulent flame case using the MC (solid black), MA (dotted blue), and RM (dashed red) models. The vertical dashed line indicates  $T_{max}$  for Case 1.

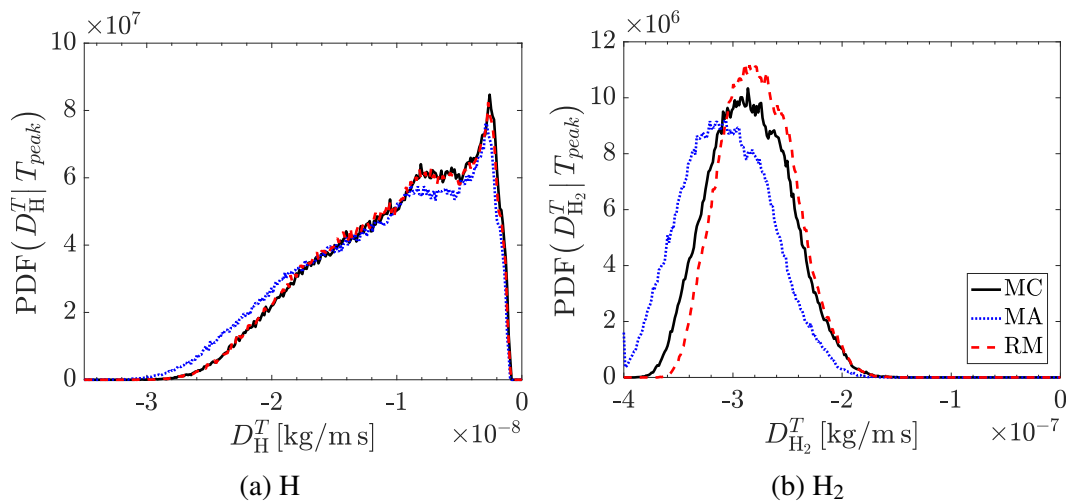


Figure 4.6: Probability density functions of  $D_H^T$  and  $D_{H_2}^T$ , taken at temperatures of the peak thermal diffusion fluxes using the MC (solid black), MA (dotted blue), and RM (dashed red) models.

### 4.3.3 Computational cost

The computational cost to include thermal diffusion using the RM method can be split into two contributions: the first cost is computing Eq. 4.25, while the second cost is computing and applying  $S$  to all species. From Section 4.2, it is evident that the cost of computing Eq. 4.25 for H and H<sub>2</sub> should be a constant value, independent

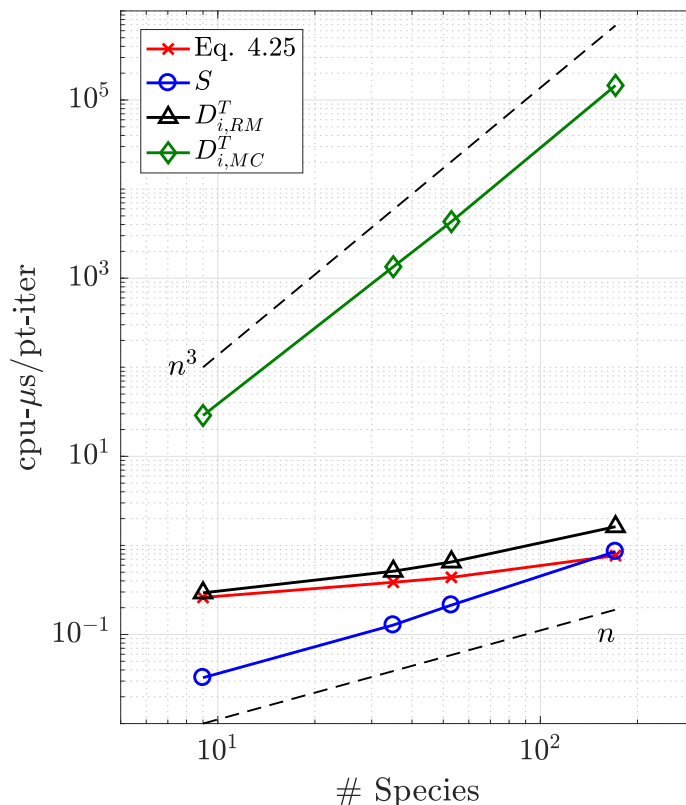


Figure 4.7: Computational cost for Eq. 4.25 (red crosses), applying the correction factor  $S$  to all thermal diffusion coefficients (blue circles), total cost of  $D_{i,RM}^T$  (black triangles), and a non-iterative multicomponent method [66] (green diamonds).

of the number of species contained in the chemical model, provided the mixture properties (e.g.,  $\mu$  and  $W$ ) are known. The cost to compute and apply  $S$ , however, scales linearly with the number of species.

In order to investigate the cost of these calculations more precisely, detailed timings of Cases 1, 7, 8, and 9 were considered, spanning chemistry model sizes from nine to 171 species. Figure 4.7 shows the time to compute both Eq. 4.25 and  $S$ , multiplied by the number of processors (one, in this case), and divided by the number of points in the computational domain. The timings presented in Fig. 4.7 do not include the time to compute  $\mu$  or  $W$ , and are found to be independent of the computational domain size.

As can be seen, the cost of Eq. 4.25 is independent of  $n$ , and the cost of  $S$  increases linearly with  $n$ . Any deviations away from either a constant- or linear-with- $n$  scaling is likely due to memory allocation and access. For chemical models up to 100 species, the total cost of the  $D_{i,RM}^T$  coefficients (Eq. 4.27) is dominated by computing Eq. 4.25 and is constant.

Timings for the multicomponent thermal diffusion coefficients are included in Fig. 4.7 using the non-iterative technique of CHEMKIN II [66]. It is well known that a non-iterative method (i.e., direct inversion of the governing transport linear systems) will require more computations than an iterative procedure. While iterative methods, such as that proposed by Ern and Giovangigli [38], can reduce the computational cost of finding  $D_{i,MC}^T$ , those methods still require more operations during each iteration than the simple, algebraic expressions listed in Section 4.2. Finally, the cost of computing  $D_i^T$  is only a portion of the diffusion flux cost. While a complete timing analysis of each term contributing to transport (using a wide range of transport models and implementations) would be a valuable contribution to the literature, it is outside the scope of this work and should be considered for future research.

One final appealing aspect of the RM formulation is its potential for use in simulations with any mass diffusion model. For example, it has been shown that (with an appropriate choice of Lewis number) the structure of a turbulent lean hydrogen–air flame can be found accurately using a constant, non-unity Lewis number approximation which scales linearly with the number of species [20]. The RM thermal diffusion model could be used in this example, as well as many others, for a negligible cost increase. The RM timings presented in Fig. 4.7 indicate this model is an extremely computationally efficient technique to find accurate thermal diffusion coefficients for H and H<sub>2</sub> for a wide range of transport models.

## Chapter 5

### TABULATED CHEMISTRY MODEL DEVELOPMENT INCLUDING CURVATURE EFFECTS

- [1] J. Schlup and G. Blanquart. “Reproducing curvature effects due to differential diffusion in tabulated chemistry”. In: *Proc. Combust. Inst.* (Under review).

The discussion of tabulated chemistry is split between Chapter 5 and Chapter 6. In this chapter, the tabulated chemistry model is derived. Assumptions are justified during the model development, verification tests are performed using the final model, and several a priori analyses show the applicability of the chosen chemistry tabulation variables.

#### 5.1 Proposed chemistry tabulation method

As described in Chapter 2, performing detailed chemistry simulations requires solving a transport equation for each species. These equations take the form (Eq. 2.4)

$$\frac{\partial (\rho Y_i)}{\partial t} + \nabla \cdot (\rho \mathbf{u} Y_i) = -\nabla \cdot \mathbf{j}_i + \rho \dot{\omega}_i, \quad (5.1)$$

Recall also that the diffusion flux,  $\mathbf{j}_i$ , is expressed (using a mixture-averaged formulation for mass diffusion) as

$$\mathbf{j}_i = -\rho Y_i D_{i,m} \frac{\nabla X_i}{X_i} - D_i^T \frac{\nabla T}{T} + \rho Y_i \mathbf{u}_c. \quad (5.2)$$

In this chapter, a chemistry tabulation methodology, which includes mixture-averaged diffusion coefficients and thermal diffusion, is developed. This tabulation will transport two scalars; the first is a progress variable, which measures the extent of the chemical reactions and the second is termed the mixture fraction  $Z$  (derived in Section 5.1.1). The progress variable,  $C$ , is defined to be the combustion product mass fraction of the hydrogen–air mixture,  $C = Y_{\text{H}_2\text{O}}$ . The progress variable can thus be transported in the NGA framework in an identical manner as Eq. 5.1, taking the form

$$\frac{\partial (\rho C)}{\partial t} + \nabla \cdot (\rho \mathbf{u} C) = \nabla \cdot (\rho D_C \nabla C) + \nabla \cdot \left( D_C^T \frac{\nabla T}{T} \right) + \rho \dot{\omega}_C, \quad (5.3)$$

where  $D_C$  and  $D_C^T$  are the mass and thermal diffusion coefficients of the progress variable. Note that this equation has assumed that the effects of  $\nabla W/W$  are small;

this assumption follows from similar arguments made in this chapter (see, for example, Fig. 5.4). This progress variable equation is in an identical form to that proposed by Regele et al. [102] with the addition of non-constant Lewis numbers and thermal diffusion. Deriving a transport equation for the mixture fraction (the second tabulation variable) is the primary goal of the following sections.

### 5.1.1 Derivation of the mixture fraction transport equation

The overall procedure in this section follows closely the methodology outlined in Regele et al. [102]. By deriving a transport equation for a second tabulation variable which is free of chemical source terms, implementation of the proposed tabulated chemistry model in Large Eddy Simulations will be easier as fewer terms will need to be closed. In an effort to derive a second transported scalar without chemistry effects, the one-step chemistry approximation is briefly considered. The global reaction equation for a one-step irreversible chemical reaction (OSIR) is given as



where  $\nu_F$  and  $\nu_O$  represent the stoichiometric coefficients for the fuel ( $F$ ) and oxidizer ( $O$ ), respectively, and  $P$  represents the products. Under the OSIR approximation, there are two key relations:

- $\nu \dot{\omega}_F - \dot{\omega}_O = 0$ , where  $\nu$  is the stoichiometric mass ratio given by [125]

$$\nu = \frac{\nu_O W_O}{\nu_F W_F}, \quad (5.5)$$

$\dot{\omega}_F$  is the fuel source term, and  $\dot{\omega}_O$  is the oxidizer source term.

- The fuel and oxidizer mass fractions are related to the product mass fraction through [75]

$$\frac{Y_{F,u} - Y_F}{\nu_F W_F} = \frac{Y_{O,u} - Y_O}{\nu_O W_O} = \frac{Y_P - Y_{P,u}}{\nu_P W_P}, \quad (5.6)$$

where the subscript  $u$  represents unburnt conditions.

The first relation suggests a simple way to remove chemical source terms from some new scalar transport equation: if a given chemical process (e.g., the combustion of lean hydrogen–air mixtures) is closely approximated by one-step chemistry, then multiplying the fuel transport equation by  $\nu$  and subtracting the oxidizer transport equation should result in a near-zero chemical source term. The development of the mixture fraction thus begins with the expression

$$\frac{\partial \rho (\nu Y_F - Y_O)}{\partial t} + \nabla \cdot [\rho \mathbf{u} (\nu Y_F - Y_O)] = -\nabla \cdot (\nu \mathbf{j}_F - \mathbf{j}_O) + \rho (\nu \dot{\omega}_F - \dot{\omega}_O). \quad (5.7)$$

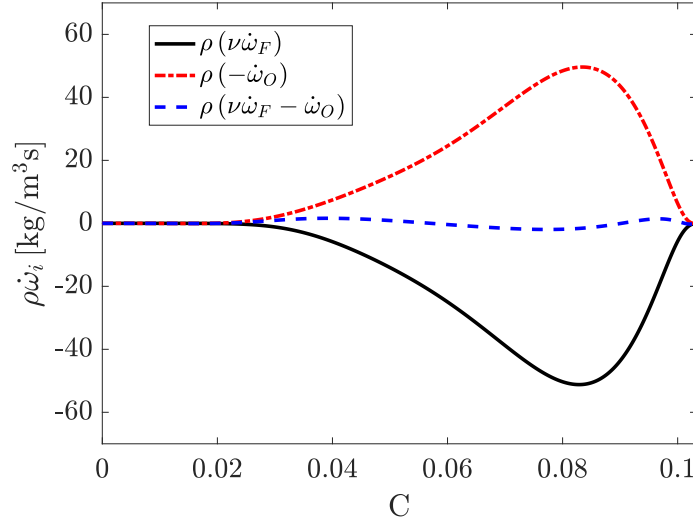


Figure 5.1: Magnitudes of the chemical source terms for the fuel (solid black), oxidizer (dot-dashed red), and the one-step chemistry approximation (dashed blue) as functions of  $C$  for a one-dimensional solution of  $\text{H}_2$ -air at  $\phi = 0.4$ .

Figure 5.1 shows the profiles of  $\nu\dot{\omega}_F$ ,  $\dot{\omega}_O$ , and their difference, as functions of  $C$  for a one-dimensional unstretched lean hydrogen-air mixture at an equivalence ratio of  $\phi = 0.4$  using the finite-rate chemistry mechanism of Hong et al. [59, 60, 72]. If the governing chemistry for this mixture was accurately predicted using OSIR, one would expect to find that  $(\nu\dot{\omega}_F - \dot{\omega}_O) \equiv 0$ . It is clear that the difference in source terms is small compared to the individual fuel and oxidizer source terms, with the difference constituting only 3.7% of  $\max(|\nu\dot{\omega}_F|, |\dot{\omega}_O|)$ . However, it is not sufficient to show that  $\nu\dot{\omega}_F - \dot{\omega}_O \approx 0$ , as the magnitude of this difference may still be on the order of the remaining terms in Eq. 5.7. Thus, Fig. 5.2 shows the magnitude of each term in Eq. 5.7 for a one-dimensional unstretched flame at steady state. This figure indicates that indeed  $\nu\dot{\omega}_F - \dot{\omega}_O \approx 0$  and is small in magnitude compared to the remaining terms. Therefore, the chemical source terms will be dropped from Eq. 5.7.

Equation 5.7 introduces a term,  $(\nu Y_F - Y_O)$ , similar to the traditional mixture fraction in non-premixed flames under the assumption of OSIR [125],

$$\mathcal{Z} = \frac{\nu Y_F - Y_O + Y_{O,2}}{\nu Y_{F,1} + Y_{O,2}}, \quad (5.8)$$

where  $Y_{F,1}$  is the fuel mass fraction in the fuel stream and  $Y_{O,2}$  is the oxidizer mass fraction in the oxidizer stream. Both  $Y_{F,1}$  and  $Y_{O,2}$  are constant. In diffusion flames,  $\mathcal{Z}$  represents the relative amounts of fuel and oxidizer at a given point in the mixture. In fuel-rich conditions,  $\mathcal{Z}$  is large ( $\mathcal{Z} = 1$  in the fuel stream), while  $\mathcal{Z}$  decreases

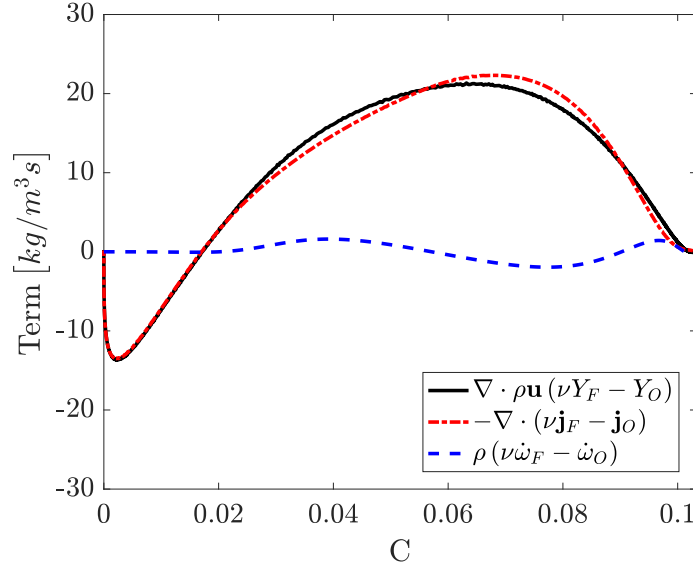


Figure 5.2: Magnitudes of the contributions to Eq. 5.7, including the convective (solid black), diffusive (dot-dashed red), and one-step chemistry approximation (dashed blue) as functions of  $C$  for a one-dimensional solution of  $\text{H}_2$ -air at  $\phi = 0.4$

as the mixture becomes lean ( $\mathcal{Z} = 0$  in the oxidizer stream) [125]. In the case of premixed mixtures, it is considered that the “fuel stream” would consist of only fuel, and thus  $Y_{F,1} = 1$  for the lean hydrogen-air premixed flames considered in this work. Similarly, the “oxidizer stream” is air, and thus  $Y_{O,2}$  is the mass fraction of  $\text{O}_2$  in air. However, the model development will be kept general, and both  $Y_{O,2}$  and  $Y_{F,1}$  will remain as arbitrary values until the model is implemented later in this chapter.

Equation 5.7 is now made to include a mixture fraction-like variable,  $Z$ , leading to an equation of the form

$$\frac{\partial \rho (\nu Y_F - Y_O + Y_{O,2})}{\partial t} + \nabla \cdot [\rho \mathbf{u} (\nu Y_F - Y_O + Y_{O,2})] = -\nabla \cdot (\nu \mathbf{j}_F - \mathbf{j}_O). \quad (5.9)$$

Then, division of Eq. 5.9 by  $(\nu Y_{F,1} + Y_{O,2})$  yields

$$\frac{\partial (\rho Z)}{\partial t} + \nabla \cdot (\rho \mathbf{u} Z) = -\nabla \cdot \mathbf{j}_Z, \quad (5.10)$$

where  $\mathbf{j}_Z = (\nu \mathbf{j}_F - \mathbf{j}_O) / (\nu Y_{F,1} + Y_{O,2})$  is a diffusion flux for the mixture fraction given by Eq. 5.8. Note that  $\mathcal{Z}$  and  $Z$  are fundamentally different quantities.  $Z$  is the solution to the transport equation Eq. 5.10 (and, as will be shown later, is a non-conserved scalar) where no assumption of one-step chemistry have been made. However,  $\mathcal{Z}$  requires an assumption of one-step chemistry, and takes the form given by Eq. 5.8. [125].

The inclusion of  $\mathbf{j}_Z$  presents a challenge in solving the transport equations for  $Z$  and  $C$ , as  $\mathbf{j}_Z$  contains mass fractions of various species. Substitution of the fuel and oxidizer diffusion fluxes, given by Eq. 5.2, into Eq. 5.10 yields

$$\mathbf{j}_Z = \left( \frac{\rho}{vY_{F,1} + Y_{O,2}} \right) \left[ -v \left( D_F \nabla Y_F + D_F Y_F \frac{\nabla W}{W} + \frac{D_F^T}{\rho} \frac{\nabla T}{T} - Y_F \mathbf{u}_c^D \right) + \left( D_O \nabla Y_O + D_O Y_O \frac{\nabla W}{W} + \frac{D_O^T}{\rho} \frac{\nabla T}{T} - Y_O \mathbf{u}_c^D \right) \right]. \quad (5.11)$$

Unfortunately,  $\mathbf{u}_c$  contains information on all of the species in the chemical model (see Eq. 2.9; note that the thermal diffusion coefficients have been corrected using  $\mathbf{u}_c^T$ , such that  $\sum_i D_i^T = 0$ ). The correction velocity can be expanded as

$$\begin{aligned} \mathbf{u}_c &= \sum_i D_i \nabla Y_i + \frac{\nabla W}{W} \sum_i D_i Y_i \\ &= D_F \nabla Y_F + D_O \nabla Y_O + D_C \nabla C + \sum_{i \neq (F,O,C)} D_i \nabla Y_i \\ &\quad + \frac{\nabla W}{W} \left[ D_F Y_F + D_O Y_O + D_C C + \sum_{i \neq (F,O,C)} D_i Y_i \right]. \end{aligned} \quad (5.12)$$

As shown in Fig. 5.3, all species (except H and H<sub>2</sub>) have similar mass diffusion coefficients close to  $\alpha$  (i.e.,  $Le_i \approx 1$  for these species). As  $D_C$  is necessarily included in the chemistry table to solve Eq. 5.3, it is retained explicitly in Eq. 5.12. The remaining diffusion coefficients in Eq. 5.12 will be approximated using  $D_{N_2}$ . Thus, the correction velocity can be simplified to

$$\begin{aligned} \mathbf{u}_c^D &= D_F \nabla Y_F + D_O \nabla Y_O + D_C \nabla C + D_{N_2} [\nabla (1 - Y_F - Y_O - C)] \\ &\quad + \frac{\nabla W}{W} [D_F Y_F + D_O Y_O + D_C C + D_{N_2} (1 - Y_F - Y_O - C)]. \end{aligned} \quad (5.13)$$

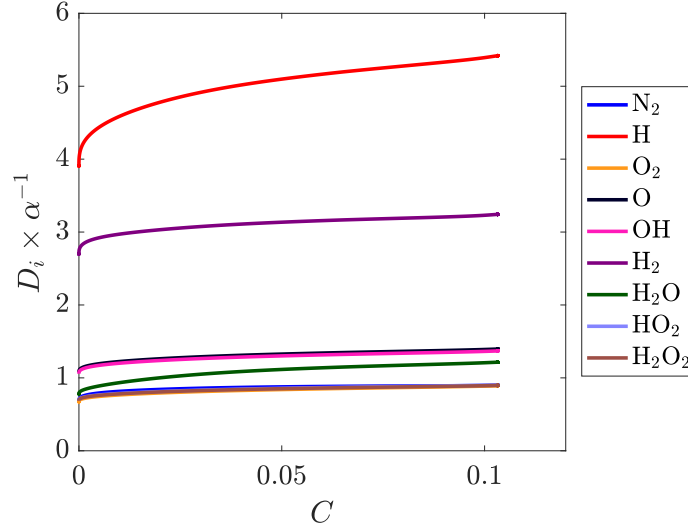


Figure 5.3: Diffusion coefficients of all species in the H<sub>2</sub>–air chemical mechanism, normalized by the thermal diffusivity  $\alpha$ , as functions of  $C$  for a one-dimensional solution of H<sub>2</sub>–air at  $\phi = 0.4$ .

Substitution of  $\mathbf{u}_c^D$  into Eq. 5.11 and collecting gradient terms yields

$$\begin{aligned}
 \left(\frac{1}{\rho}\right) \mathbf{j}_Z = & \nabla Y_F \left[ \frac{-\nu D_F}{\nu Y_{F,1} + Y_{O,2}} + \Delta_F Z^* \right] \\
 & + \nabla Y_O \left[ \frac{D_O}{\nu Y_{F,1} + Y_{O,2}} + \Delta_O Z^* \right] \\
 & + \nabla C [\Delta_C Z^*] \\
 & - \frac{\nabla W}{W} \frac{D_W}{\nu Y_{F,1} + Y_{O,2}} \\
 & - \frac{\nabla T}{T} \frac{1}{\rho} \left[ \frac{\nu D_F^T - D_O^T}{\nu Y_{F,1} + Y_{O,2}} \right],
 \end{aligned} \tag{5.14}$$

where

$$Z^* = \frac{\nu Y_F - Y_O}{\nu Y_{F,1} + Y_{O,2}} \tag{5.15}$$

is used for convenience and  $\Delta_\psi = D_\psi - D_{N_2}$  is the difference in diffusion coefficients between species  $\psi = (F, O, C)$  and N<sub>2</sub>. The diffusion term associated with  $\nabla W/W$  is

$$\begin{aligned}
 D_W = & \nu D_F Y_F - D_O Y_O - (\nu Y_F - Y_O) \\
 & \times [D_F Y_F + D_O Y_O + D_C C + D_{N_2} (1 - Y_F - Y_O - C)].
 \end{aligned} \tag{5.16}$$

Figure 5.4 shows the magnitudes of each term in the expression of  $\mathbf{j}_Z$  for a lean hydrogen–air flame at  $\phi = 0.4$ . It is clear that terms contributed by  $\nabla W/W$  and  $\nabla C$

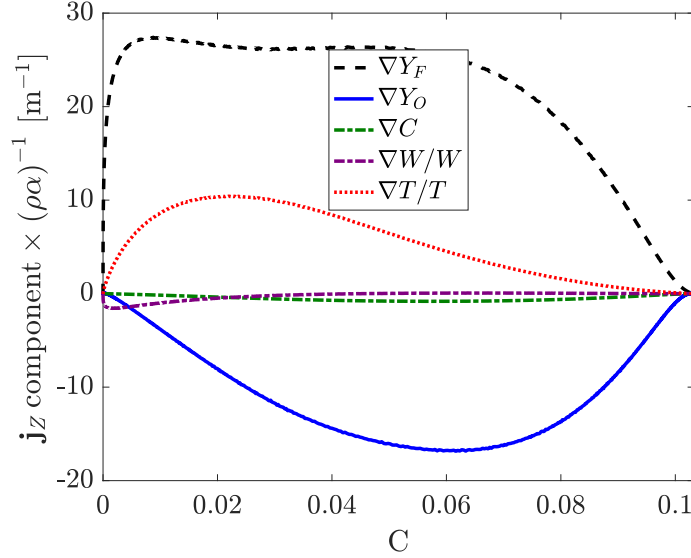


Figure 5.4: Magnitudes of the components of  $\mathbf{j}_Z$ , given by Eq. 5.14, normalized by the thermal diffusivity, as functions of  $C$  for a one-dimensional solution of  $\text{H}_2$ -air at  $\phi = 0.4$ .

are minor compared to the remaining terms. Because of this result, the contribution of the molecular weight term will be neglected moving forward (including in the progress variable equation, Eq. 5.3). While a similar argument can be made for the progress variable term, its inclusion in the chemistry table is trivial as all required thermo-chemical properties are necessary for the solution of the progress variable transport equation. The contributions due to  $\nabla C$  thus remain at this time.

The diffusion flux of  $Z$ , however, still contains mass fractions of the fuel and oxidizer. These terms can be removed by again considering the approximation of OSIR. Using Eq. 5.6, the mass fractions of the fuel and oxidizer can be related to the mass fraction of the products via

$$Y_F = Y_{F,u} - Y_P \frac{\nu_F W_F}{\nu_P W_P}, \quad Y_O = Y_{O,u} - Y_P \frac{\nu_O W_O}{\nu_P W_P}. \quad (5.17)$$

Then, under pure mixing conditions (where the fuel and oxidizer streams are allowed to mix prior to combustion), the unburnt fuel and oxidizer mass fractions are directly related to the OSIR mixture fraction through [125]

$$Y_{F,u} = Y_{F,1} \mathcal{Z}, \quad Y_{O,u} = Y_{O,2} (1 - \mathcal{Z}). \quad (5.18)$$

Substitution of Eq. 5.18 and Eq. 5.5 into Eq. 5.17 — and recognizing that  $Y_P = C$  — yields

$$Y_F = Y_{F,1} \mathcal{Z} - \frac{1}{\nu + 1} C, \quad Y_O = Y_{O,2} (1 - \mathcal{Z}) - \frac{\nu}{\nu + 1} C, \quad (5.19)$$

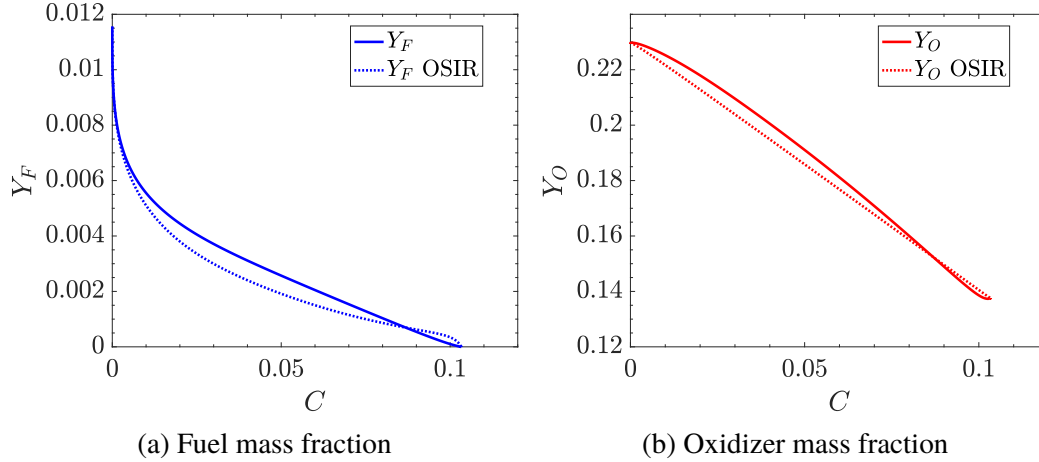


Figure 5.5: Comparison of the finite-rate chemistry mass fraction profiles and mass fraction profiles under the OSIR assumption.

and thus

$$\nabla Y_F = Y_{F,1} \nabla \mathcal{Z} - \frac{1}{\nu + 1} \nabla C, \quad \nabla Y_O = -Y_{O,2} \nabla \mathcal{Z} - \frac{\nu}{\nu + 1} \nabla C. \quad (5.20)$$

While Eqs. 5.19 and 5.20 rely on an assumption of OSIR, the tabulated chemistry model is desired to predict finite-rate chemistry results. Before these expressions for the fuel and oxidizer mass fractions are implemented into  $\mathbf{j}_Z$ , their applicability must be investigated. Figure 5.5 shows the fuel and oxidizer mass fractions from a finite-rate chemistry simulation of a one-dimensional unstretched flame with a lean hydrogen–air mixture at  $\phi = 0.4$ . The expected values of  $Y_F$ , computed using Eq. 5.19 are also shown. Note that  $C$  and the species profiles for  $\mathcal{Z}$  are from finite-rate chemistry. From these two figures, the OSIR approximation for  $\mathcal{Z}$  predicts mass fractions of the two reactant species to within a maximum error of 6.2% and 2.5%, relative to the maximum mass fraction of  $Y_F$  and  $Y_O$ , respectively. As  $\mathcal{Z}$  reproduces closely the fuel and oxidizer profiles, it is assumed that  $Z$  and  $\mathcal{Z}$  are in good agreement (this assumption will be verified in Section 5.1.2, after the model development is complete).

After substitution of Eq. 5.20 into Eq. 5.14 (under the approximation of OSIR), the diffusion flux for  $Z$  can be written as

$$\left(\frac{1}{\rho}\right) \mathbf{j}_Z = -(D_Z - Z_1) \nabla Z + (D_Z^* - C_1) \nabla C - \frac{1}{\rho} \left( \frac{\nu D_F^T - D_O^T}{\nu Y_{F,1} + Y_{O,2}} \right) \frac{\nabla T}{T}, \quad (5.21)$$

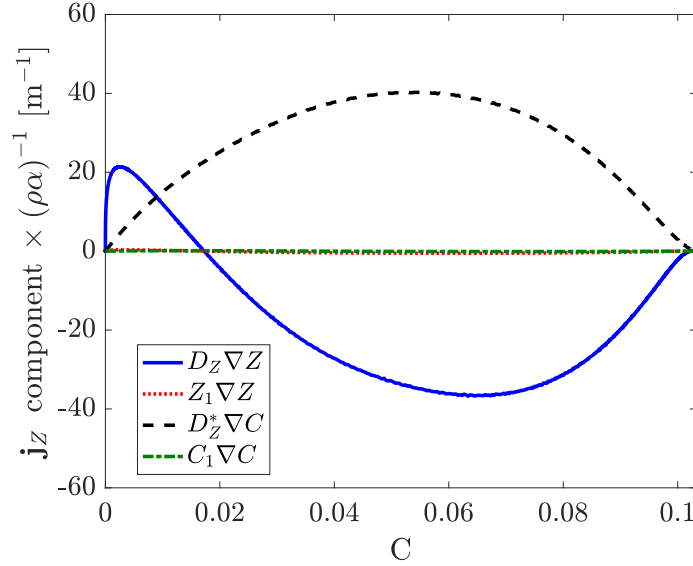


Figure 5.6: Magnitudes of the four terms in Eq. 5.21 for a one-dimensional solution of  $\text{H}_2$ -air at  $\phi = 0.4$ .

where the four terms of  $\nabla Z$  and  $\nabla C$  are

$$\begin{aligned}
 D_Z &= \left( \frac{\nu Y_{F,1} D_F + Y_{O,2} D_O}{\nu Y_{F,1} + Y_{O,2}} \right) \\
 Z_1 &= Z^* [Y_{F,1} \Delta_F - Y_{O,2} \Delta_O] \\
 D_Z^* &= \frac{\nu}{\nu + 1} \left( \frac{D_F - D_O}{\nu Y_{F,1} + Y_{O,2}} \right) \\
 C_1 &= \frac{Z^*}{\nu + 1} [\Delta_F + \nu \Delta_O - (\nu + 1) \Delta_C] .
 \end{aligned} \tag{5.22}$$

Figure 5.6 shows a comparison of the magnitudes of each term in Eq. 5.21. From this figure,  $Z_1$  and  $C_1$  (i.e., the terms composed of  $Z^*$  as given in Eq. 5.15), have significantly reduced magnitudes compared to  $D_Z$  and  $D_Z^*$ . By neglecting  $Z_1$  and  $C_1$ , the transport equation of  $Z$  can be re-expressed as

$$\begin{aligned}
 \frac{\partial (\rho Z)}{\partial t} + \nabla \cdot (\rho \mathbf{u} Z) \\
 = \nabla \cdot (\rho D_Z \nabla Z) - \nabla \cdot (\rho D_Z^* \nabla C) + \nabla \cdot \left( \rho D_Z^T \frac{\nabla T}{T} \right) ,
 \end{aligned} \tag{5.23}$$

where the temperature is a function of the two transported variables (i.e.,  $T = T(C, Z)$ ), and  $D_Z^T$  is

$$D_Z^T = \frac{1}{\rho} \left( \frac{\nu D_F^T - D_O^T}{\nu Y_{F,1} + Y_{O,2}} \right) . \tag{5.24}$$

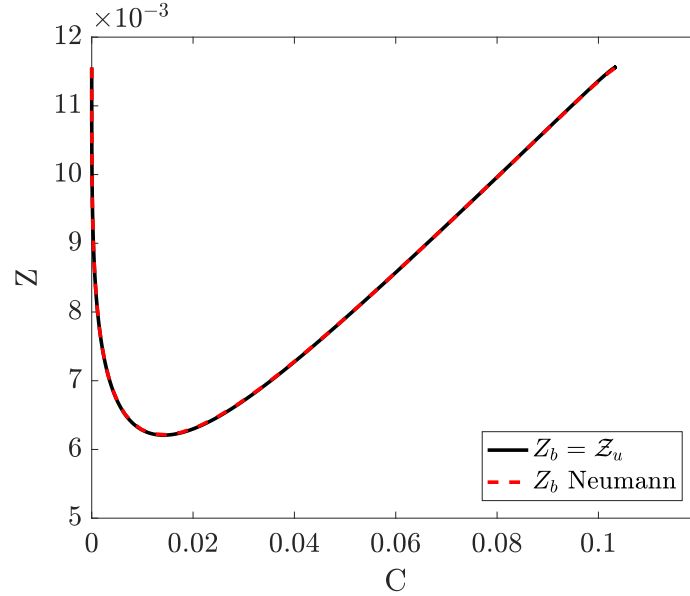


Figure 5.7: Comparison of the outlet boundary condition for  $Z$  as a function of  $C$  for a one-dimensional unstretched premixed hydrogen–air flame at  $\phi = 0.4$ .

Equation 5.23 is the proposed mixture fraction transport model which will be used to solve for  $Z$  in the remainder of this work.  $C$  and  $Z$  will be transported using Eqs. 5.3 and 5.23, respectively, during the simulations described in Chapter 6. While only these two variables are transported, the underlying chemistry of the one-dimensional flames (e.g.,  $Y_i$ ,  $D_i$ ,  $D_i^T$ ,  $\dot{\omega}_i$ ) is included in the chemistry table described in Section 5.2.1.

### 5.1.2 Analysis of the proposed mixture fraction equation

Two boundary conditions are required for the steady-state solution of Eq. 5.23. The boundary value for the unburnt mixture,  $Z_u$ , is determined by solving for  $\mathcal{Z}$  using the unburnt mixture properties, i.e.,

$$Z_u = \mathcal{Z}_u = \frac{\nu Y_{\text{H}_2,u} - Y_{\text{O}_2,u} + Y_{\text{O}_2}}{\nu + Y_{\text{O}_2}}, \quad (5.25)$$

where the subscript  $u$  denotes unburnt conditions and  $Y_{\text{O}_2} = 0.232$ . Two possible boundary conditions exist for the mixture fraction in the burnt mixture,  $Z_b$ . First, substitution of the mixture properties from finite-rate chemistry into Eq. 5.8 results in  $Z_b = \mathcal{Z}_u$ . Alternatively, one could use a Neumann boundary condition in the fully burnt mixture. Figure 5.7 shows the resulting  $Z$  profile for each of these boundary conditions; no discernable difference is found and thus  $Z_b = Z_u$  is chosen.

Figure 5.8 shows a comparison of  $Z$  (the solution to Eq. 5.23) and  $\mathcal{Z}$  for a one-

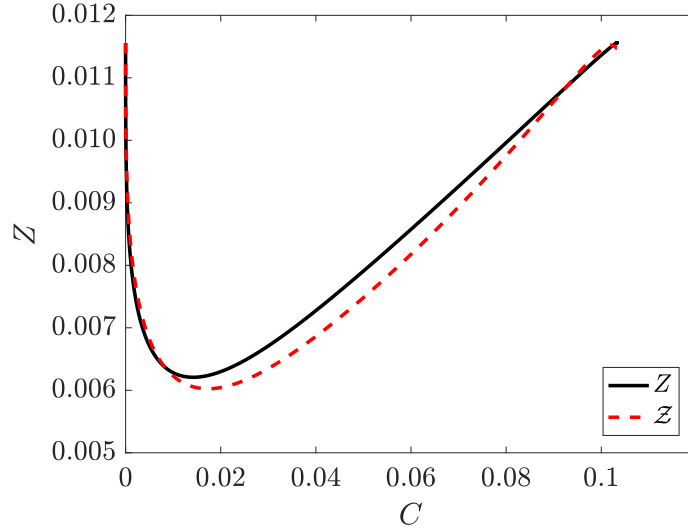


Figure 5.8: Comparison of  $Z$  (solid black, computed using Eq. 5.23) and  $\mathcal{Z}$  (dashed red, computed using Eq. 5.8 with a nine-species finite-rate chemistry model) as a function of  $C$  for a one-dimensional unstretched premixed hydrogen–air flame at  $\phi = 0.4$ .

dimensional unstretched flame at  $\phi = 0.4$ . Note that  $\mathcal{Z}$  is computed using  $Y_{\text{H}_2}$  and  $Y_{\text{O}_2}$  profiles from the finite-rate chemistry simulation with nine species and 54 reactions [59]. As expected from previous comparisons of the OSIR approximation and finite-rate chemistry (e.g., Figs. 5.1 and 5.5), the comparison between  $Z$  and  $\mathcal{Z}$  is quite good with a maximum percent deviation between the two profiles of 6%. This agreement is similar to the results of Regele et al. [102], which showed that lean hydrogen–air mixtures were well characterized by the OSIR approximation.

Further insight into  $Z$  can be gained by decomposing the cross-diffusion term (containing  $\nabla C$ ) in Eq. 5.23. Following Xuan et al. [126] and Savard and Blanquart [110], the second term on the right-hand side of Eq. 5.23 can be expanded to

$$\nabla \cdot (\rho D_Z^* \nabla C) = -\rho D_Z^* |\nabla C| \kappa + \mathbf{n} \cdot \nabla (\rho D_Z^* |\nabla C|), \quad (5.26)$$

where the curvature,  $\kappa$ , is defined as

$$\kappa = -\nabla \cdot \mathbf{n} = -\nabla \cdot \left( \frac{\nabla C}{|\nabla C|} \right). \quad (5.27)$$

This expansion shows that curvature effects of the flame surface (defined as an isosurface of  $C$ ) are present in this model through the use of a cross-diffusivity,  $D_Z^*$  (i.e., diffusion of  $Z$  due to gradients of  $C$ ), which is derived naturally from the fuel and oxidizer transport equations. This observation makes clear a critical aspect

of the chemistry tabulation: using one-dimensional flat flames and the proposed  $Z$  equation allows flame surface curvature effects to be included in the governing transport equations.

## 5.2 Implementation of the mixture fraction transport equation into NGA

### 5.2.1 Chemistry tabulation

The chemistry table can now be created. This process begins by importing a single FlameMaster [100] solution for the one-dimensional, unstretched, premixed hydrogen–air flame at a given equivalence ratio. This solution includes species mass fractions, mass diffusion coefficients, and thermal diffusion coefficients. When creating the chemistry table, the transport equation for  $Z$  (Eq. 5.23) is discretized using a second-order finite difference scheme and solved by inverting the resulting linear system. The  $Z$  profile is stored along with all necessary thermo-chemical properties. The chemistry table includes  $\rho$ ,  $T$ ,  $D_C$ ,  $D_C^T$ ,  $D_Z$ ,  $D_Z^*$ ,  $D_Z^T$ , and  $\dot{\omega}_C$ . Figure 5.9a shows the profile of  $Z$  as a function of  $C$  for the  $\phi = 0.4$  flame.

Next, the bounds of the chemistry table are prescribed. In this work, all six of the flame configurations detailed in Section 2.6 are lean premixed hydrogen–air flames; thus, the lower limit of the chemistry table is determined based on the convergence capabilities of the one-dimensional flame solver, FlameMaster [100]. The upper limit of the chemistry table is set arbitrarily, above the expected values of local equivalence ratio enrichment (this limit should be confirmed a posteriori, and is done in the  $Z$ – $C$  scatter plots given in Chapter 6 for each flame configuration). Figure 5.9b shows the bounds of the chemistry table ( $\phi \in [0.25, 1.3]$ ), along with the original  $\phi = 0.4$  flame solution.

Then, the range of  $\phi$  is spanned; these flame solutions are shown in Fig. 5.9c. For the chemistry tables used in this chapter, the equivalence ratios are concentrated near  $\phi = 0.4$  to reduce interpolation errors near the nominal equivalence ratio of many of the flame configurations. The one-dimensional flame solutions are manually inspected to verify every pair of  $Z$ – $C$  values are unique. These flame solutions now include the requisite information to solve the  $C$  and  $Z$  transport equations; a plot of the flame profiles, colored by their progress variable source term,  $\dot{\omega}_C$ , is shown in Fig. 5.9d.

Finally, the chemistry table is created by interpolating the thermo-chemical data of the flame solutions onto a structured manifold consisting of 500 points in the  $C$  and  $Z$  directions. These points are equally spaced in  $0 \leq Z \leq \max(Z)$ . The  $C$  direction

contains values of  $0 \leq C \leq 0.25$  with the first 10 points spaced logarithmically (due to the large  $dZ/dC$  at low values of  $C$ ); the remaining points are equally spaced.

Once the one-dimensional flame solutions have been loaded, the required thermo-chemical properties are mapped to the mixture fraction/progress variable space of the chemistry table. After this bilinear interpolation, the structured  $Z$ - $C$  space contains tabulated data of the one-dimensional flame solutions. Figure 5.9e shows three one-dimensional flamelet solutions (in white) computed using Eqs. 5.3 and 5.23, as well as a contour plot of  $\dot{\omega}_C$ . The one-dimensional flames shown have equivalence ratios of  $\phi = 0.25$  (lower),  $\phi = 0.4$  (middle), and 1.3 (upper), representing the lower and upper bounds of the current chemistry table and the equivalence ratio used for many of the upcoming cases.

### 5.2.2 Treatment of regions outside the chemistry table

In addition to the progress variable source term for the entire constructed chemistry table, Fig. 5.9e shows the extent of the thermodynamic equilibrium conditions (dashed white line) for each of the flame solutions which construct the chemistry table. This “thermodynamic equilibrium line” simply connects the fully burnt value, in  $Z$ - $C$  space, of all of the one-dimensional flames.

There are three regions of the chemistry table which lie outside of the one-dimensional flame solutions used in the chemistry table construction. These regions are labeled “1”, “2”, and “3” in Fig. 5.9e. Region 1 represents mixture conditions which are near the extinction limit of the one-dimensional flame solutions and over which FlameMaster has difficulties finding a flame solution. Note that this is a similar lower limit as was found throughout literature for planar hydrogen-air mixtures at  $T_u = 298$  K and  $p_o = 1$  atm [107]. A linear interpolation in the  $Z$  direction is used between the lowest one-dimensional flame solution and the thermodynamic equilibrium line for table look-ups in this region. Region 2 consists of  $Z$ - $C$  space which extends beyond the thermodynamic equilibrium conditions of the one-dimensional flames. This region is un-physical as no data should exist past the thermodynamic equilibrium line. However, due to numerical errors, values in this region may be accessed. Tabulated data in this region is set equal to values found on the equilibrium line at the same value of  $Z$ . Put simply, thermo-chemical data in region 2 are copied from the thermodynamic equilibrium line to larger values of  $C$ . Finally, Region 3 is the portion of  $Z$ - $C$  space the user has determined is outside the scope of the current simulation; this region is more fuel-rich than is expected in the flame configurations

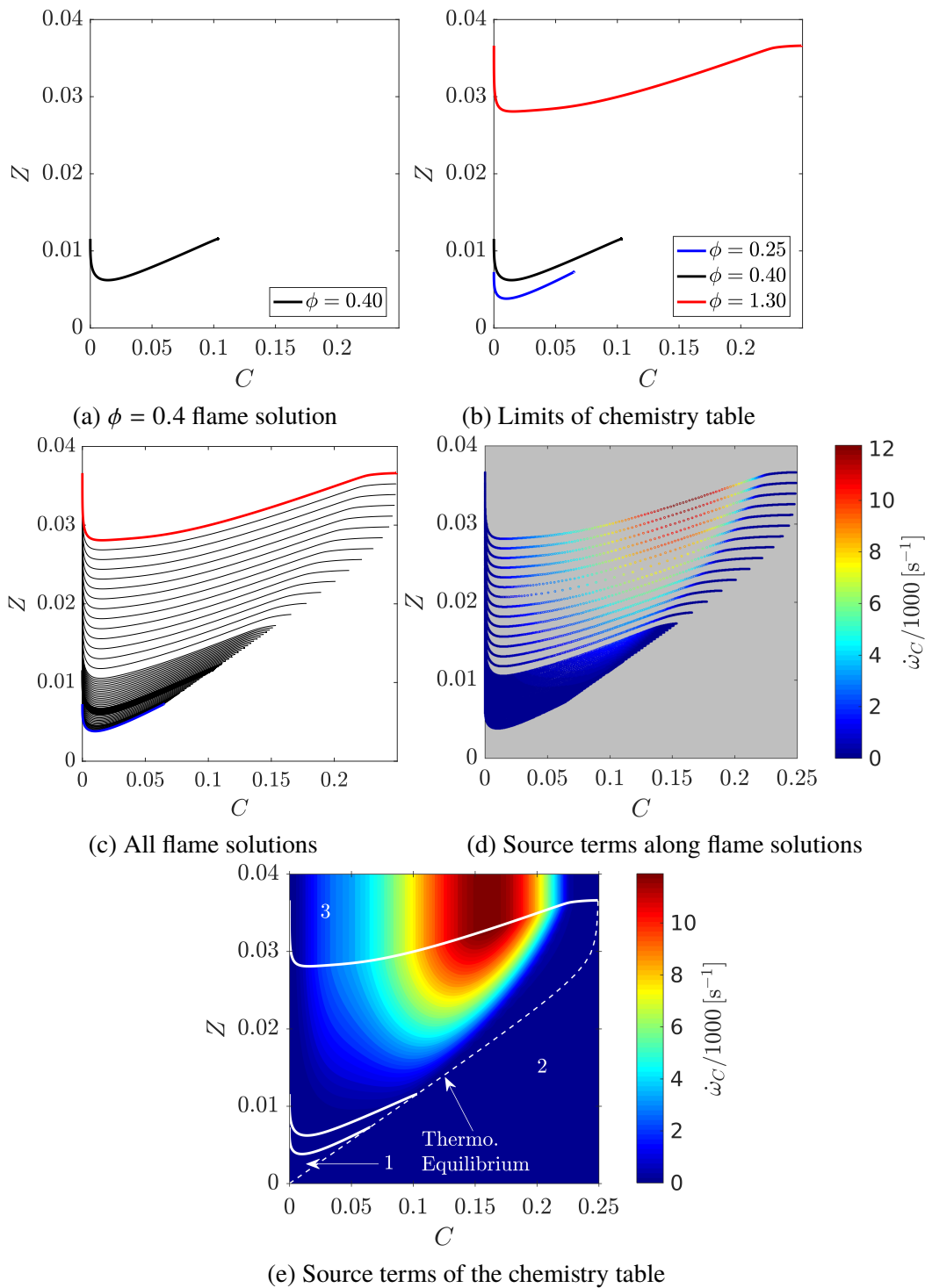


Figure 5.9: Progression of the chemistry table creation, showing (a) a single flame solution at  $\phi = 0.4$ , (b) the bounds of the chemistry table, (c) all flame solutions in the chemistry table, (d) all flame solutions colored by their corresponding progress variable source term, and (e) the complete chemistry table with specific regions described in Section 5.2.2.

of interest. Similar to region 2, thermo-chemical properties in this region are found by matching the desired value of  $C$  for the most fuel-rich flame solution.

A scatter plot of data in  $Z$ – $C$  space will be provided for each flame configuration investigated in Chapter 6. These figures will indicate the range of  $Z$  and  $C$  found for each configuration and give an indication of the number of data points that lie outside the one-dimensional flame solutions.

### 5.3 Verification of the tabulated chemistry model

Prior to, and after, the tabulated chemistry model is implemented in NGA, a number of verification cases are considered. First, two mathematical formulations indicate that the newly-developed mixture-fraction equation is in agreement with previous methodologies. Then, one-dimensional unstretched flames are computed using tabulated chemistry, and the flame structure and global quantities are compared.

#### 5.3.1 Analytical verification of the mixture fraction transport equation

In Chapter 6, a constant Lewis number tabulation is considered. The Lewis number describes the relative diffusion of species and temperature, and constant values have historically been implemented in computational studies to reduce the costs of computing transport properties. Recall, the Lewis number of species  $i$ ,  $Le_i$ , is defined as

$$Le_i = \frac{\alpha}{D_{i,m}}. \quad (5.28)$$

To determine  $Le_i$  for the chemistry table creation, one-dimensional unstretched flames are solved using mixture-averaged mass diffusion. The Lewis number is computed throughout the flame structure using Eq. 5.28. For the constant Lewis number cases considered, the value of  $Le_i$  is found at the maximum temperature of the one-dimensional unstretched flame; thus,  $D_i^{Le} = \alpha/Le_i$ . Burali et al. found that selecting Lewis numbers at either the location of maximum temperature or maximum mass fraction of each individual species resulted in nearly identical flame structures [20].

The first verification assumes constant, unity Lewis numbers (i.e.,  $\alpha = D_i$ ) and neglects thermal diffusion. Under these assumptions, the diffusion coefficients in  $\mathbf{j}_Z$

(Eq. 5.21) are greatly simplified:

$$\begin{aligned}
 D_Z &= \alpha, \\
 Z_1 &= 0, \\
 D_Z^* &= 0, \\
 C_1 &= 0, \\
 D_Z^T &= 0.
 \end{aligned} \tag{5.29}$$

These coefficients indicate that no fluctuations in mixture fraction, due to flame front curvature, are possible ( $D_Z^* = 0$  in Eq. 5.26). This agrees with the observations of Knudsen and Pitsch [69], and thus curvature effects would not be present in simulations under these assumptions.

Next, one can consider that all Lewis numbers are unity, except for that of the fuel, and that thermal diffusion is negligible. These assumptions are identical to those of Regele et al. [102]. Now, Eq. 5.21 can be rewritten as

$$\begin{aligned}
 \left(\frac{1}{\rho}\right) \mathbf{j}_Z &= -\nabla Z \left[ D \left( \frac{\nu Y_{F,1} \frac{1}{Le_F} + Y_{O,2}}{\nu Y_{F,1} + Y_{O,2}} \right) - DZ^* Y_{F,1} \left( \frac{1}{Le_F} - 1 \right) \right] \\
 &+ \nabla C \left[ \left( \frac{\nu}{\nu + 1} \right) D \left( \frac{\frac{1}{Le_F} - 1}{\nu Y_{F,1} + Y_{O,2}} \right) - DZ^* \left( \frac{1}{\nu + 1} \right) \left( \frac{1}{Le_F} - 1 \right) \right],
 \end{aligned} \tag{5.30}$$

where  $Le_F$  is the fuel Lewis number and  $D = \alpha$  is the diffusion coefficient of all species (except the fuel). In the constant Lewis number cases considered in Chapter 6,  $Le_F = 0.3$ .

Equation 5.30 can be further simplified, assuming that  $Y_{F,1} = 1$  (as is the case for all configurations in this work). Then

$$\begin{aligned}
 \left(\frac{1}{\rho}\right) \mathbf{j}_Z &= -\nabla Z \left\{ D \left[ 1 + \left( \frac{1}{Le_F} - 1 \right) (1 - Z) \right] \right\} \\
 &+ \nabla C \left[ D \left( \frac{1}{\nu + 1} \right) \left( \frac{1}{Le_F} - 1 \right) (1 - Z) \right],
 \end{aligned} \tag{5.31}$$

where  $Z$  has been approximated using OSIR (i.e., Eq. 5.8). This expression is identical to Eqs. 18 and 19 given in Regele et al. [102]. Thus, the present formulation of the  $Z$  and  $C$  equations are consistent with, yet more general than, previous formulations.

### 5.3.2 Comparison with optimal estimations from detailed chemistry

By transporting  $Z$  during a finite-rate chemistry simulation, it is possible to compare the predicted values of  $\dot{\omega}_C$  from tabulated chemistry (denoted  $\dot{\omega}_C^{\text{Tab.}}$ ) with  $\dot{\omega}_C$

from detailed chemistry (denoted  $\dot{\omega}_C^{\text{Det.}}$ ). The two-dimensional unsteady and three-dimensional turbulent flames are used to transport  $Z$  during a finite-rate chemistry solution. All diffusion coefficients and the source term for  $\text{H}_2\text{O}$  for the  $Z$  equation are determined using mixture-averaged mass and thermal diffusion and finite-rate chemistry.

From these results, values of  $\dot{\omega}_{\text{H}_2\text{O}}^{\text{Det.}}$  may be compared to the tabulated source term. One comparison technique is to consider a function (called the optimal estimator),  $f(C, Z)$ , which minimizes the error of the predicted tabulated source term [88] given as

$$\epsilon_f = \sqrt{\frac{\int_V (f(C, Z) - \dot{\omega}_C^{\text{Det.}})^2 dV}{\int_V (\dot{\omega}_C^{\text{Det.}})^2 dV}}. \quad (5.32)$$

Moreau et al. [88] showed that the optimal estimator  $f$  must be equivalent to the conditional mean, i.e., the conditional mean  $\langle \dot{\omega}_C^{\text{Det.}} | C, Z \rangle$  is the function of  $C$  and  $Z$  that would give the closest approximation to the true finite-rate chemistry source term for  $\text{H}_2\text{O}$ . Thus, comparisons of  $\dot{\omega}_C^{\text{Tab.}}$  to the conditional mean of  $\dot{\omega}_C^{\text{Det.}}$  will provide insight to the applicability of the chosen tabulated chemistry model.

Figure 5.10 shows the conditional mean of  $\dot{\omega}_C^{\text{Det.}}$ , conditioned on  $C$  and  $Z$ , for the two-dimensional unsteady and three-dimensional turbulent finite-rate chemistry simulations. At first glance, the conditional means have similar profiles to the chemistry table shown in Fig. 5.9e. A more quantitative comparison is given in Fig. 5.11, showing the conditional mean of  $\dot{\omega}_C^{\text{Det.}}$  at  $C_{\text{peak}}$  for the two configurations (represented by the vertical dashed lines in Fig. 5.10). The agreement is excellent for the two-dimensional flame, and remains good for the three-dimensional flame (within 25%) up to  $Z/Z_{\text{peak}} = 1.4$ . The table is able to capture increased source terms over six times the peak source term from the one-dimensional flame. Further, a single chemistry table is able to predict the source terms of the two limiting cases considered: a laminar flame with moderate curvature and extinction and a turbulent flame with large high flame curvature. Finally, if only a single tabulation variable (i.e.,  $C$ ) was used, all data in Fig. 5.11 would reduce to a single data point at  $Z/Z_{\text{peak}} = 1$  and  $\dot{\omega}_C/\dot{\omega}_C^{\text{1D}} = 1$ , eliminating all fluctuations in the source term due to differential diffusion.

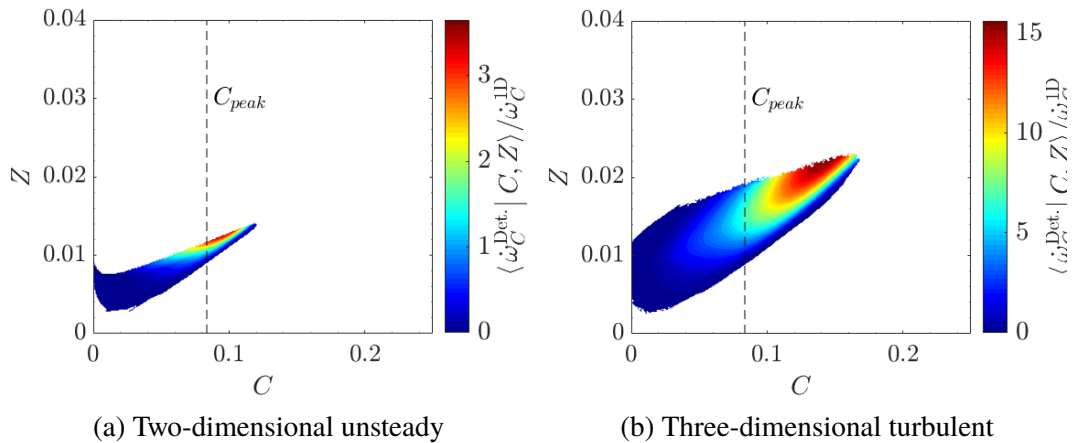


Figure 5.10: Conditional mean of  $\omega_{\text{H}_2\text{O}}$ , conditioned on  $C$  and  $Z$  for the (a) two-dimensional unsteady and (b) three-dimensional turbulent flame configurations, computed using finite-rate chemistry. The vertical dashed lines represent  $C_{peak}$ . Note that the range of the colorbar changes.

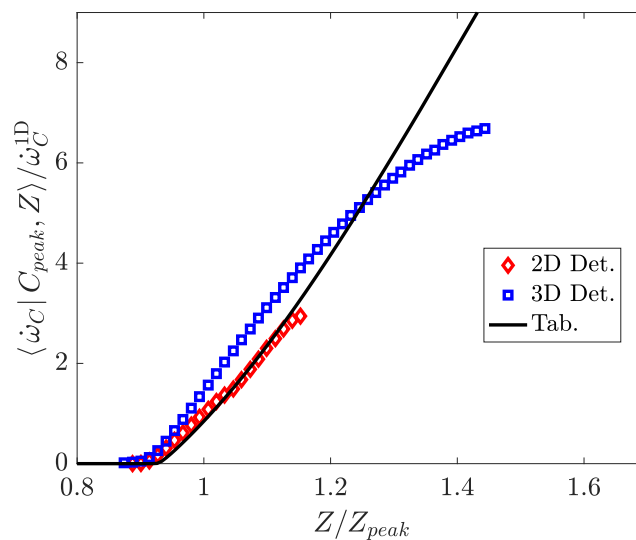


Figure 5.11: Conditional mean of  $\omega_C$ , conditioned on  $C_{peak}$  and  $Z$  for the two-dimensional unsteady (red diamonds) and three-dimensional turbulent flame configurations (blue squares).

## VALIDATION OF THE TABULATED CHEMISTRY MODEL INCLUDING CURVATURE EFFECTS

- [1] J. Schlup and G. Blanquart. “Reproducing curvature effects due to differential diffusion in tabulated chemistry”. In: *Proc. Combust. Inst.* (Under review).

In this chapter, the mixture fraction model developed in Chapter 5 is applied to one-dimensional curved flames, two-dimensional tubular and unsteady flames, and three-dimensional turbulent flames, to investigate the predictive capabilities of the  $Z$ - $C$  tabulation. All detailed chemistry simulations, abbreviated “Det.”, implement the MA-MA transport model for comparison. Tabulated chemistry simulations were performed with both the newly-developed tabulation (including thermal diffusion) and the constant Lewis number approach of Regele et al. [102]. The constant Lewis number cases are considered to provide a measure of improvement using the proposed tabulation approach; these results are compared in Section 6.6. Additionally, except for the one-dimensional cases in Section 6.1 and the two-dimensional tubular case in Section 6.3, all mixtures considered have unburnt conditions of  $\phi = 0.4$ ,  $T_u = 298$  K, and  $p_0 = 1$  atm. All computational grids match the configurations detailed in Table 2.2 and explored in Chapter 3.

Before transporting  $Z$  using Eq. 5.23, or performing any tabulated chemistry simulations, both initial and boundary conditions are required for the transient flame configurations considered. The initial profile for any tabulated chemistry simulation in this chapter begins with a finite-rate chemistry solution. From the detailed chemistry scalar fields, values of  $C = Y_{\text{H}_2\text{O}}$  are extracted. Then, the initial  $Z$  field is constructed using  $Y_{\text{H}_2}$  and  $Y_{\text{O}_2}$  in Eq. 5.8. Because  $Z \neq \mathcal{Z}$ , there exists an initial transient in any of the tabulated chemistry simulations. The initial transients are removed prior to analyzing flame structures or collecting flame statistics. The inlet boundary condition for  $Z$  is set using Eq. 5.25 above.

### 6.1 One-dimensional unstretched flames

For simulations of the underlying one-dimensional flat flames which construct the chemistry table, the proposed chemistry tabulation should recover exactly the finite-

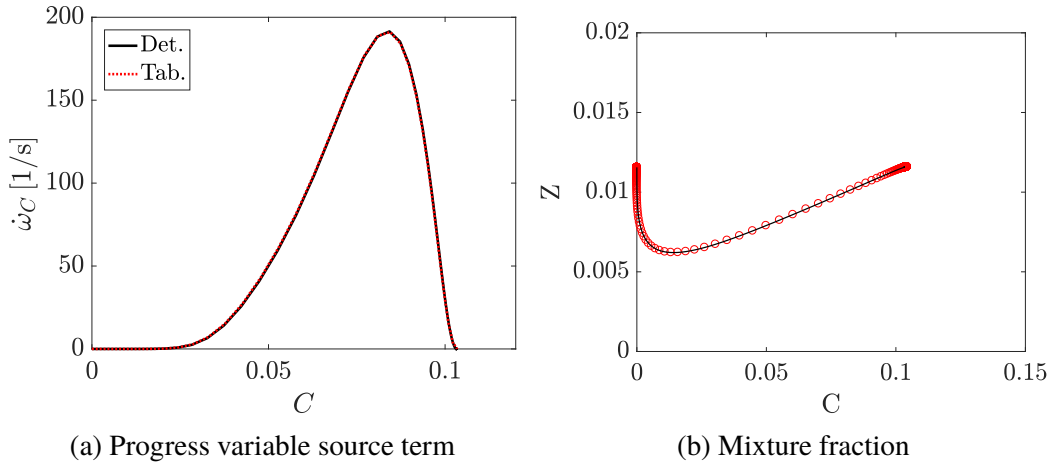


Figure 6.1: Comparison of (a) progress variable source term and (b) mixture fraction as functions of progress variable for the one-dimensional unstretched flame at  $\phi = 0.4$ . Detailed chemistry (solid black line) and tabulated chemistry (dotted red line) profiles agree very well.

rate chemistry results. This is performed using one-dimensional unstretched flames at a variety of equivalence ratios, from  $\phi = 0.35$  to 1.0. For the tabulated chemistry simulations, flame speeds relative to the unburnt mixture are computed using a form identical to Eq. 2.73, i.e.,

$$S_L = \frac{\int \rho \dot{\omega}_C dV}{\rho_u C_b A}, \quad (6.1)$$

where  $C_b$  is the progress variable in the burnt mixture. Figure 6.1a shows a comparison of progress variable source term as a function of progress variable using finite-rate chemistry and tabulated chemistry for a  $\phi = 0.4$  flame. As expected, the tabulated chemistry simulation recovers the underlying one-dimensional unstretched flame contained in the chemistry table. Further evaluation is provided via a plot of  $Z$  as a function of  $C$  in Fig. 6.1b. The two profiles overlap over the entire range of  $C$ .

Quantitative comparisons of the flame structure can be made using the laminar flame speed; these results are shown in Fig. 6.2a across the entire range of equivalence ratios. The corresponding  $S_L^o$  are in agreement to within 0.75% of results from finite-rate chemistry, computed using

$$\epsilon_{S_L}^d = \left| \frac{S_L^{o, \text{Det.}} - S_L^{\text{Tab.}}}{S_L^{o, \text{Det.}}} \right|. \quad (6.2)$$

Differences are likely due to chemistry table interpolation.

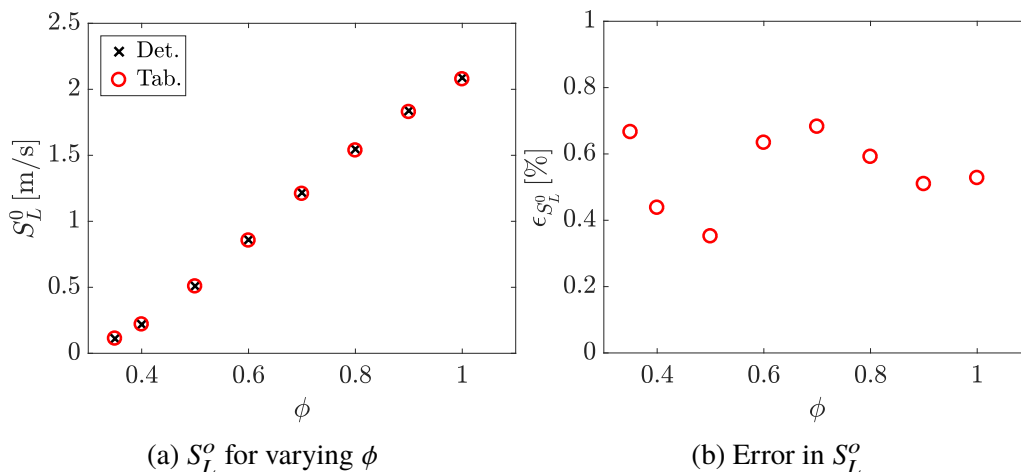


Figure 6.2: (a) Comparison of the unstretched laminar flame speeds and (b) percent error in the computed flame speeds, computed using finite-rate chemistry (black crosses) and tabulated chemistry (red circles) for a range of equivalence ratios.

## 6.2 Cylindrical, outwardly-propagating flame

The one-dimensional, cylindrically expanding flame is now considered. In order to generate initial data files for this configuration, a set of one-dimensional tubular flame simulations were performed. The initial outwardly propagating flame profile, with curvature  $\kappa_{cyl} = 1/r_F$ , is set by using the tubular flame solution with  $\kappa_{cyl}l_F \approx 0.35$ .

Figure 6.3 shows the flame speed of the outwardly propagating flame, normalized by its unstretched flame speed.  $S_L$  is computed using Eq. 6.1, with the area  $A_{ref}$  determined by the surface area of a cylinder with radius  $r_F$ . Differential diffusion effects increase the flame speed significantly above the unstretched flame speed,  $S_L^o$ . As the flame propagates outwardly, the flame surface curvature decreases, and the effects of both differential diffusion and thermal diffusion become less significant; this agrees with the observations from previous work [102] and the results from Chapter 3. Ultimately, the one-dimensional unstretched flame is recovered as the curvature approaches zero.

A number of critical results are present in Fig. 6.3. First, the results from the detailed chemistry simulations are predicted accurately using the Z–C tabulation method, with a deviation at maximum curvature of 3%. Second, the inclusion of thermal diffusion in the tabulated chemistry model also agrees well with detailed chemistry, and enhances the effects of differential diffusion. The use of the constant Lewis number approximation (as was done in Regele et al. [102]), underpredicts the normalized flame speed in regions of high curvature by 10%, compared to the

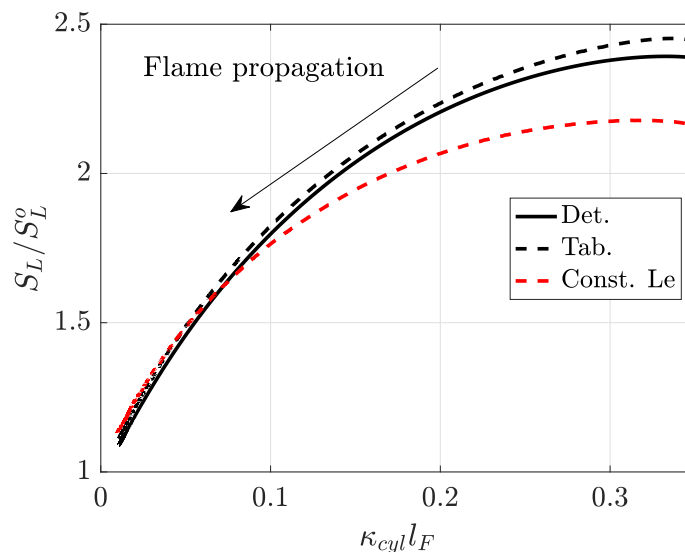


Figure 6.3: Flame speed of outwardly propagating flames, normalized by their corresponding one-dimensional unstretched laminar flame speed, as a function of normalized curvature. Detailed chemistry results (solid black) are shown along with tabulated chemistry results (dashed). The constant Lewis number tabulated chemistry model [102] is in red.

detailed chemistry case. As a point of comparison, the tabulated chemistry result overpredicts the finite-rate chemistry result by only 2.5%. The constant Lewis number approximation recovers fairly well the finite-rate and tabulated chemistry results at low flame curvature.

Figure 6.4 shows a scatter plot of  $Z$  and  $C$  for the flame at  $\kappa l_F = 0.06$ . As expected, the values of  $Z$  and  $C$  lie above the corresponding one-dimensional flat flame due to differential diffusion causing local fuel enrichment. The fully burnt conditions near the axis of the cylindrically expanding flame have a larger value of  $C$  due to the fuel enrichment and follow the thermodynamic equilibrium line. The values of  $C$  and  $Z$  from tabulated chemistry closely match those of the finite-rate chemistry solution, with a small offset in the  $Z$  direction arising from a slightly different flame curvature between the two data files.

It is important to reiterate that the chemistry table is constructed solely of one-dimensional flat flames. Yet it is evident from the results of this section that curvature effects — introduced through the cross-diffusivity  $D_Z^*$  of the mixture fraction — are well predicted using this flat flame-based chemistry table.

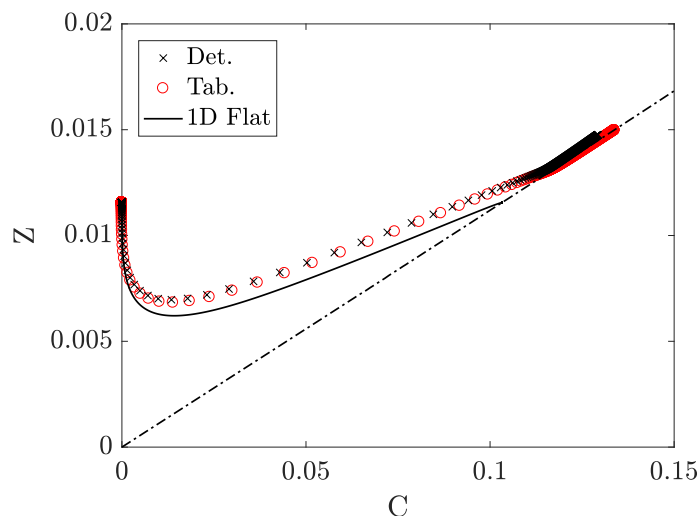


Figure 6.4: Scatter plot of the mixture fraction as a function of progress variable using tabulated chemistry with thermal diffusion for the one-dimensional outwardly-propagating cylindrical flame (red circles) at  $\kappa l_F = 0.06$ . An a priori case (finite-rate chemistry transporting  $Z$ ) is also shown (black crosses). The thermodynamic equilibrium line is also shown (black dot-dashed line).

### 6.3 Two-dimensional cellular tubular flame

The tubular flame configuration described in Section 2.6.3 is now investigated. Boundary conditions identical to the detailed chemistry simulation are used for the tabulated chemistry case. The inlet mixture has an equivalence ratio of  $\phi = 0.25$ , resulting in an inlet unburnt mixture fraction of  $Z_u = 0.00726$ .

Figure 6.5 shows contour plots of the progress variable source term for finite-rate chemistry and tabulated chemistry. Results for cases with thermal diffusion and the constant Lewis number approximation are shown. The contour plots indicate qualitative agreement between the finite-rate and tabulated chemistry results; by including thermal diffusion, the flame has a larger flame radius and a wider azimuthal span. Additionally, the flame experiences more pronounced localized extinction near the boundaries of the cellular instability. As was done for the previous cases, Fig. 6.6 shows the location of all data in  $Z$ - $C$  space for the steady-state solution. Despite the unburnt equivalence ratio matching the lowest flame contained in the chemistry table, all data lies within the given chemistry table due to the increase in local equivalence ratio [53].

Similar to the quantitative comparisons for the tubular flame configuration in Chapter 3, Fig. 6.7 shows azimuthal profiles of the maximum progress variable source term, and the radial location of this maximum value. The tabulated chemistry method

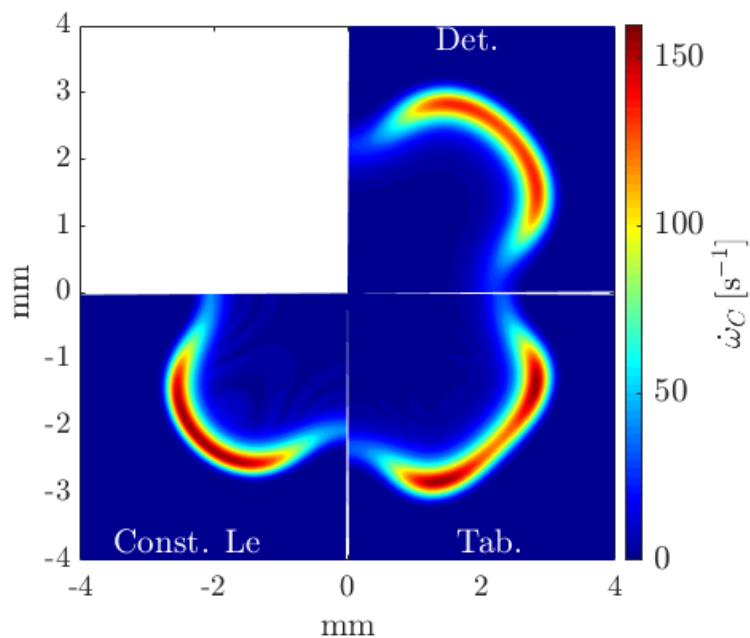


Figure 6.5: Contours of the progress variable source term for the (clockwise from top right) detailed chemistry, tabulated chemistry with thermal diffusion, and tabulated chemistry assuming constant Lewis numbers.

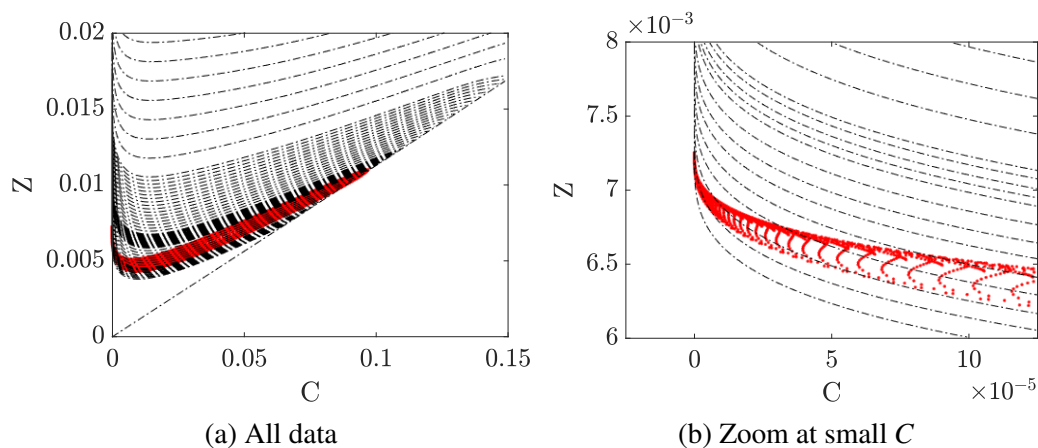
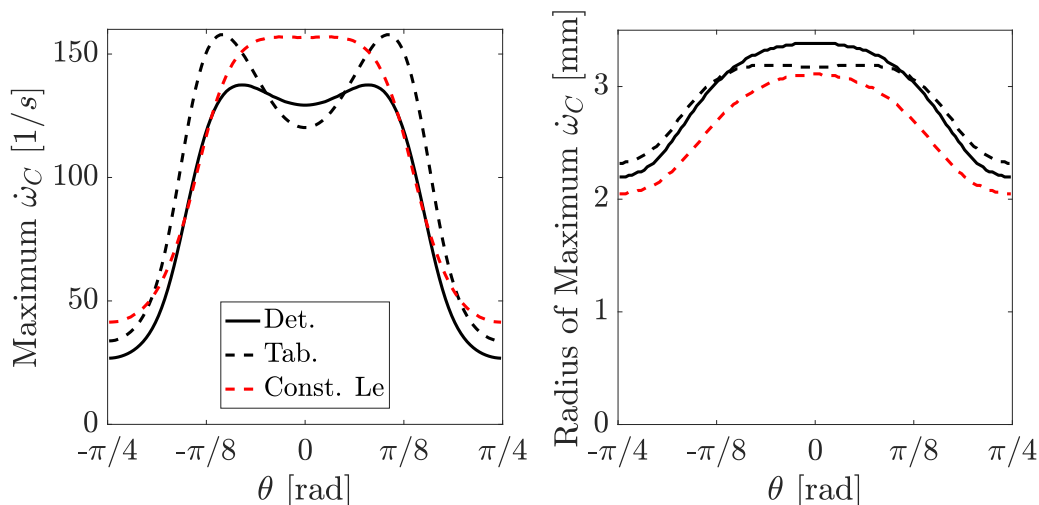


Figure 6.6: Scatter plot of the mixture fraction as a function of progress variable for (a) all data and (b) data at small  $C$  using tabulated chemistry with thermal diffusion for the two-dimensional tubular flame (red points). The one-dimensional flames contained in the chemistry table, and the thermodynamic equilibrium line, are also shown (black).



(a) Maximum progress variable source term (b) Radius of maximum progress variable source term

Figure 6.7: Profiles of the (a) maximum  $\dot{\omega}_C$  and (b) radial location of maximum  $\dot{\omega}_C$  as functions of the azimuthal coordinate. Cases with mixture-averaged diffusion and thermal diffusion (black) and constant Lewis number diffusion (red) are shown, using finite-rate chemistry (solid lines) and tabulated chemistry (dashed lines).

with thermal diffusion predicts higher source term values at the edge of the cellular instabilities than the finite-rate chemistry results, with similar source terms at the center of the instability. The extinction regions between instabilities ( $\theta = \pm\pi/4$ ) exhibit more pronounced extinction when including thermal diffusion, matching the results from finite-rate chemistry. Figure 6.7a also indicates that the maximum source term for the tabulated chemistry case with thermal diffusion is overpredicted through the entire flame region; this overprediction is most pronounced at the edges of the instability (near  $\theta = \pm\pi/8$ ), while the instability center experiences reduced source terms compared to finite-rate chemistry. This reduction in source term is caused by the flat instability profile seen in Fig. 6.5 reducing the fuel focusing effect of differential diffusion.

Figure 6.7b shows that using tabulated chemistry with thermal diffusion predicts the flame position within 6% at the center of the extinction zone, and within 5% at the center of the cellular instability. The slight disagreement is indicative of a different cellular instability shape, as shown in the contour plots of Fig. 6.5. The results using constant Lewis numbers underpredict the flame position throughout the instability, likely due to the neglect of thermal diffusion.

Despite the overprediction in source term and differences in flame position, the

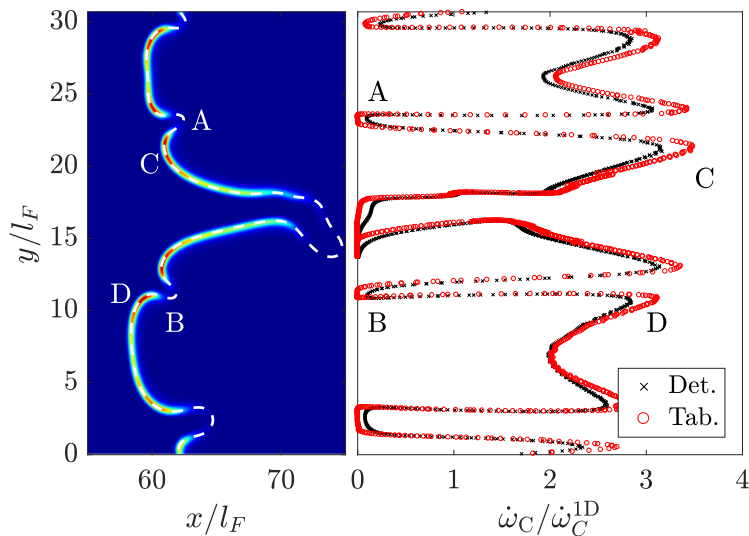


Figure 6.8: (Left) Contour plot of the progress variable source term with isosurface of  $C_{peak}$  (dashed line) and (right) normalized progress variable source term on  $C_{peak}$  isosurface for the detailed chemistry (black crosses) and  $Z$ - $C$  tabulation (red circles). The  $y$ -axis is identical for both figures.

agreement between finite-rate chemistry and tabulated chemistry appears quite good, especially considering the chemistry table is constructed solely using flat, unstretched one-dimensional flames. The resulting chemistry table appears to qualitatively and quantitatively reproduce flame statistics in this steady flame configuration, even under the influence of localized extinction and enhanced burning.

## 6.4 Two-dimensional freely propagating flame

Next, the two-dimensional, freely propagating, unstable laminar flame is considered. First, an a priori analysis of the effects of  $Z$  are presented (transported during a finite-rate chemistry simulation), followed by investigations of flame statistics using an a posteriori implementation of the tabulated chemistry.

### 6.4.1 A priori analysis

The progress variable chemical source term from detailed chemistry is compared to that predicted by the  $Z$ - $C$  tabulation.  $Z$  was transported using Eq. 5.23 during the detailed chemistry solution. Then, the  $Z$  and  $C$  fields from the detailed chemistry simulation are used to interpolate  $\dot{\omega}_C^{Tab.}$  from the chemistry table. This source term is now compared to  $\dot{\omega}_C^{Det.}$ .

Figure 6.8 shows a contour plot of the progress variable source term, along with an isosurface (dashed white line) of the progress variable at its peak source term in a

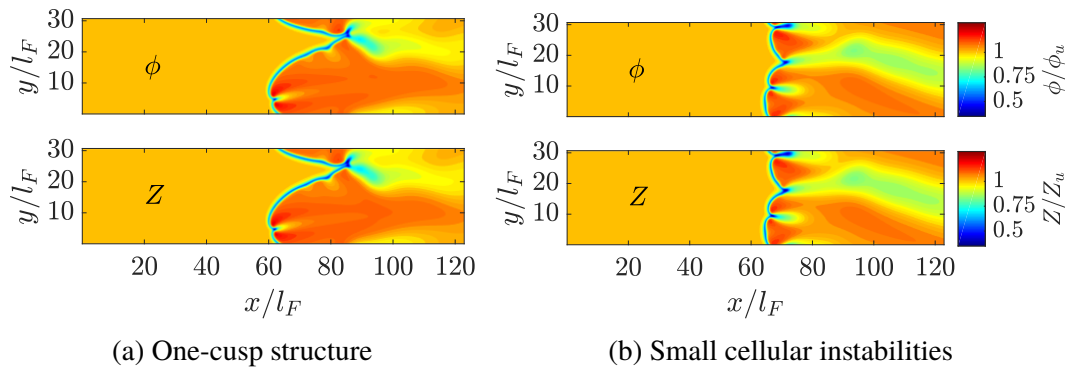


Figure 6.9: Contour plots of the local equivalence ratio (top) and mixture fraction (bottom), transported in a finite-rate chemistry simulation, for two time instances of the two-dimensional freely propagating flame. Both parameters are normalized by their respective inlet values.

one-dimensional flat flamelet at  $\phi = 0.4$  ( $C_{peak} = 0.0835$ ). Next to the contour plot is a figure showing  $\dot{\omega}_C$  along the flame isosurface. At multiple locations along the flame surface (e.g., A and B), the flame appears to extinguish, and the source term is close to zero. Other areas (e.g., C and D) indicate significant burning enhancement with source terms up to three times the peak one-dimensional source term. The agreement between detailed chemistry and the  $Z$ – $C$  tabulation is quite good over the entire flame surface; this includes regions of flame extinction being captured well by a chemistry table constructed of only burning flames. It should be noted that without differential diffusion effects in the chemistry tabulation, no local variations in equivalence ratio are possible and the peak progress variable would be a constant at  $\dot{\omega}_C^{1D}$ . The proposed  $Z$ – $C$  tabulation permits, and indeed accurately captures, the fluctuations due to differential diffusion, albeit with slight overprediction of the source term extremes.

#### 6.4.2 A posteriori analysis

Now, a set of a posteriori analyses are performed using tabulated chemistry. The tabulated chemistry simulations are initialized using a data file from the finite-rate chemistry simulations, with  $Z$  computed using Eq. 5.8. The initial transient is eliminated from the subsequent analysis by removing the first  $10 \tau_F$ , where  $\tau_F$  is the flame time scale,  $\tau_F = l_F/S_L^o$ ; this corresponds to approximately 30 flame flow-through times. Approximately  $150 \tau_F$  are collected for analysis. The analyses for the tabulated chemistry model mirror those performed in Chapter 3 on the evaluation of the thermal diffusion model.

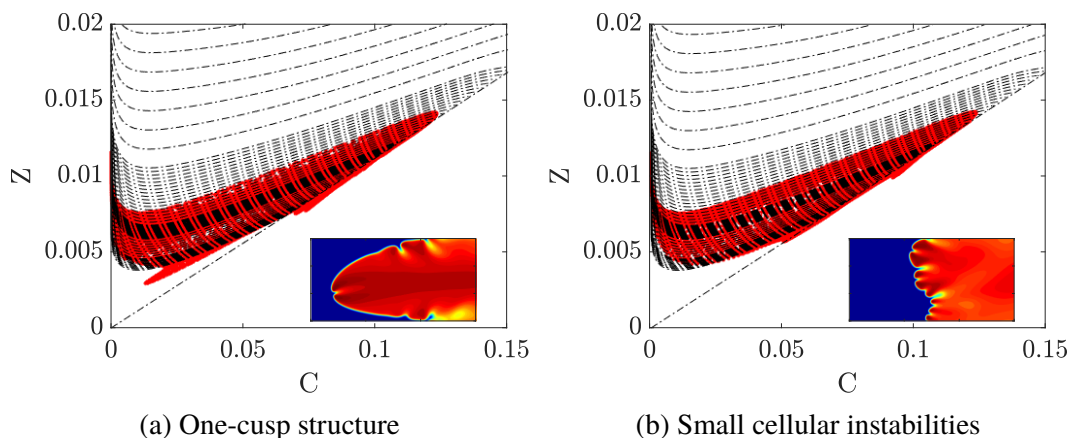


Figure 6.10: Scatter plot of the mixture fraction as a function of progress variable using tabulated chemistry with thermal diffusion for the two-dimensional freely propagating flame (red points). The one-dimensional flames contained in the chemistry table, and the thermodynamic equilibrium line, are also shown (black).

First, as a demonstration of the local enrichment due to differential diffusion and the physical meaning of  $Z$ , Fig. 6.9 shows an example pair of contour plots: the top contour plots indicate local equivalence ratio, normalized by the inlet equivalence ratio, from a finite-rate chemistry simulation for two time steps. The local equivalence ratio is computed as  $\phi = 0.5X_H/X_O$  where  $X_i$  are the elemental mole fractions of element  $i$  at the given location in the computational domain. The bottom contour plots show  $Z$ , transported during the finite-rate chemistry simulation and normalized by the inlet value of  $Z$ , at the same time instances as the equivalence ratio contours. From these figures, the effects of differential diffusion in the chemistry tabulation, i.e., fluctuations in  $Z$  corresponding to the equivalence ratio fluctuations found in finite-rate chemistry, are readily visible. The excellent agreement between the normalized values of  $\phi$  and  $Z$  reinforces the choice of mixture fraction as a transported variable to determine local fuel enrichment or flame extinction.

A scatter plot of  $Z$  and  $C$  values from tabulated chemistry is shown in Fig. 6.10 for two data files with similar flame structure as Fig. 6.9. Local enrichment and extinction is shown by the significant scatter of data. Points beyond the thermodynamic equilibrium line are indicative of numerical errors.

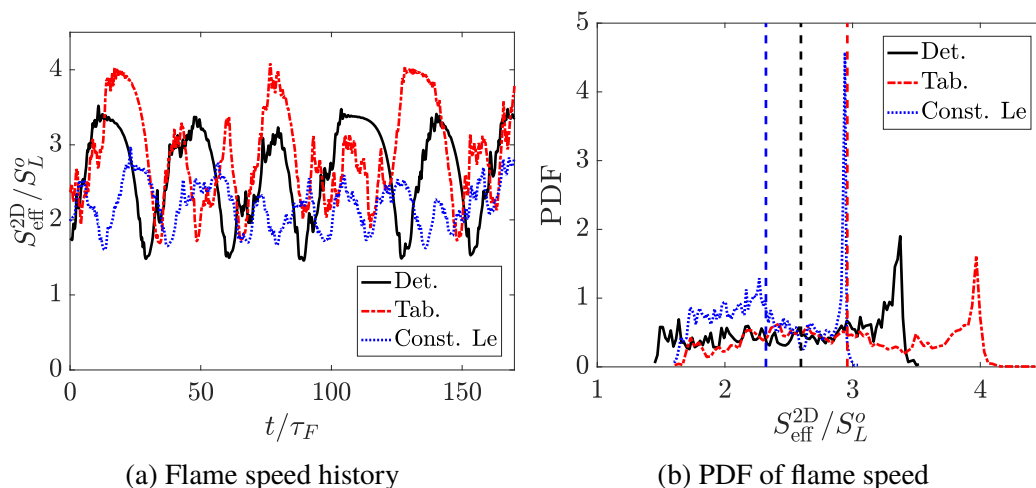


Figure 6.11: Flame speed history (left) and PDF of normalized flame speed (right) for detailed chemistry (solid black), tabulated chemistry with thermal diffusion (dot-dashed red), and tabulated chemistry assuming constant Lewis numbers [102] (dotted blue). The vertical dashed lines represent the temporal mean of the corresponding flame speeds.

### Global flame statistics

Flame speed time histories using detailed chemistry, the proposed tabulated chemistry model, and the constant Lewis number tabulated chemistry model of Regele et al. [102] are shown in Fig. 6.11. The time histories indicate that tabulated chemistry still reproduces the periodic flame speed found in finite-rate chemistry simulations. The proposed tabulated chemistry method, however, predicts larger flame speeds relative to the detailed chemistry results. The overprediction can be quantified by investigating the PDF of the flame speed, shown in Fig. 6.11b. Here, the mean flame speeds, indicated by the vertical dashed lines, show that the proposed tabulated chemistry model overpredicts  $S_{\text{eff}}^{2D}$  of the detailed chemistry model by 14%.

A similar set of conclusions are shown in the PDF of the flame surface area in Fig. 6.12a. The flame area statistics also reveal an increase in flame surface area by implementing the proposed tabulated chemistry methodology, relative to the detailed chemistry results. The percent increase is found to be approximately 24%.

### Local flame statistics

Both  $S_{\text{eff}}^{2D}$  and  $A_{\text{FP}}^{2D}$  represent global quantities; local measurements show the applicability of tabulated chemistry in regions of enhanced burning and localized extinction

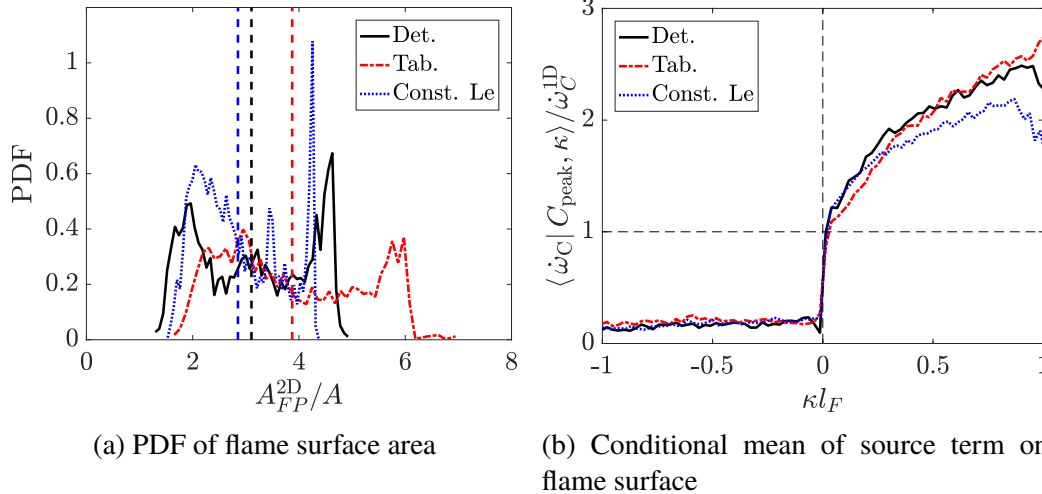


Figure 6.12: PDF of flame surface area normalized by domain cross-sectional area (left) and normalized product source term as a function of normalized local flame curvature (right) for detailed chemistry (solid black), tabulated chemistry with thermal diffusion (dot-dashed red), and tabulated chemistry assuming constant Lewis numbers [102] (dotted blue). The vertical dashed lines on the left figure represent the temporal mean of the flame area.

along the flame surface. An averaged measure of the localized effects of the flame considers the mean of  $\dot{\omega}_C$  along the flame surface defined by  $C_{peak}$ , conditioned on the flame curvature. The conditional mean is shown in Fig. 6.12b. The  $Z$ - $C$  tabulation model accurately predicts the progress variable source term, in both regions of positive curvature (convex to the unburnt mixture) and negative curvature (concave to the unburnt mixture), despite the slight disagreement in global quantities. In regions of positive curvature, the progress variable source term increases dramatically over the peak laminar value,  $\dot{\omega}_C^{1D}$ , while local flame extinction is found in regions of negative curvature. This indicates that the proposed  $Z$ - $C$  tabulation developed in Section 5.1 accurately predicts local fluctuations of  $\dot{\omega}_C$  (at a given value of  $C$ ) due to curvature, made possible by the new mixture fraction diffusion flux (Eq. 5.23).

### 6.5 Three-dimensional turbulent flame

The analyses in Sections 6.2 - 6.4 considered only laminar flames. The addition of turbulence, especially at high Karlovitz number,  $Ka$ , introduces turbulence-induced curvature which may affect the flame structure, in addition to instability-induced curvature.

The Karlovitz and turbulent Reynolds numbers, based on unburnt properties, match those of the finite-rate chemistry simulation presented in Chapter 3:  $Ka_u = \tau_F / \tau_\eta =$

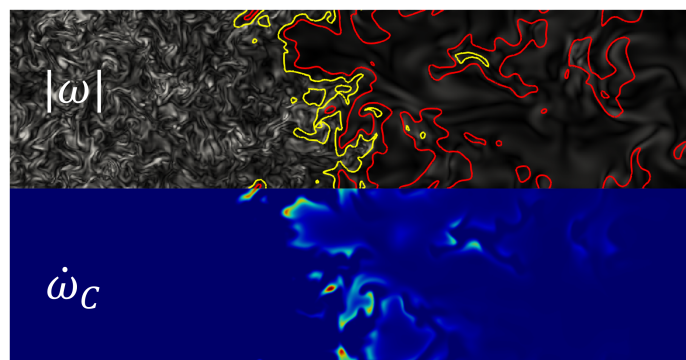


Figure 6.13: Two-dimensional slice of the vorticity magnitude (with isolines representing  $C_{peak}/10$  (yellow) and  $C_{peak}$  (red)) and progress variable source term.

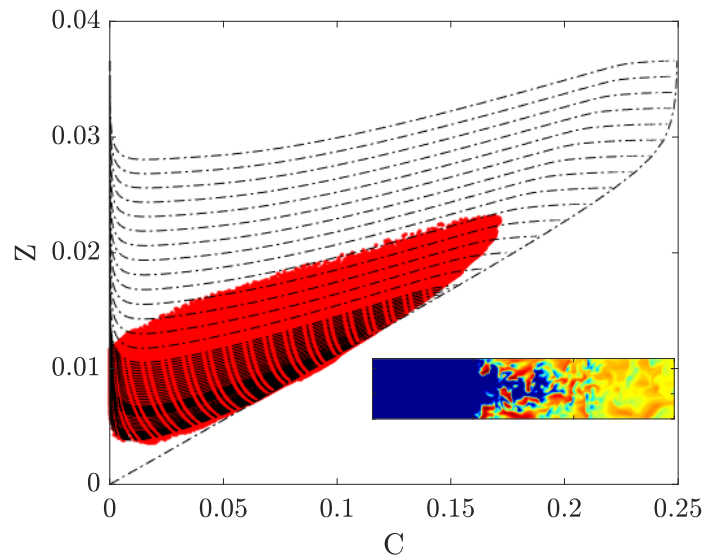


Figure 6.14: Scatter plot of the mixture fraction as a function of progress variable using tabulated chemistry with thermal diffusion for the three-dimensional turbulent flame (red points). The one-dimensional flames contained in the chemistry table, and the thermodynamic equilibrium line, are also shown (black).

149, and  $Re_t = u'l/\nu = 289$ . The initial data field is a fully-turbulent result from the finite-rate chemistry simulation.  $Z$  is again initialized using Eq. 5.8. As mentioned in the model development and the previous simulation sections, an initial transient must be removed as  $Z$  is transported following Eq. 5.23. Statistics are collected over 25 eddy turnover times after this initial transient has been removed. Figure 6.13 shows a two-dimensional slice of the turbulent flow. Isosurfaces of  $C_{peak}/10$  (yellow) and  $C_{peak}$  (red) indicate an approximation of the flame brush. The vorticity magnitude (shown in the top contour plot) significantly changes through the flame, due to increased viscosity in the burnt mixture [4, 111]. The isosurfaces also reveal pockets of unburnt mixture in the burnt region of the flame. An additional contour plot, showing the progress variable source term, qualitatively presents the fluctuating product source term along the flame surface.

The scatter plot in Fig. 6.14 indicate that a significant amount of fuel enrichment and local extinction is present in the turbulent flame. Further, the amount of enrichment is much larger than that found in the two-dimensional freely-propagating flame (note the different axis scales in Fig. 6.10). Few points exist below the lowest flame solution, and the thermodynamic equilibrium line continues to provide a limit on the maximum value of  $C$  at a given  $Z$  (i.e., equivalence ratio).

### Global flame statistics

Figure 6.15a shows a time history of turbulent flame speeds for the detailed chemistry, tabulated chemistry with thermal diffusion, and the constant Lewis number tabulated chemistry model of Regele et al. [102]. Similar to the two-dimensional freely propagating flame, the tabulated chemistry model overpredicts the turbulent flame speed. This overprediction is quantified in Fig. 6.15b, which shows that the use of tabulated chemistry with thermal diffusion results in an increase of approximately 14% over the detailed chemistry model. Compared to the finite-rate chemistry results shown in Section 3.6, the overprediction is less than the discrepancy incurred by neglecting thermal diffusion. Similar to the two-dimensional unsteady flame, the flame surface area is increased due to differential diffusion as well as turbulent mixing. However, the tabulated chemistry method continues to overpredict the turbulent flame area by 16%, a similar increase as was found for the turbulent flame speed.

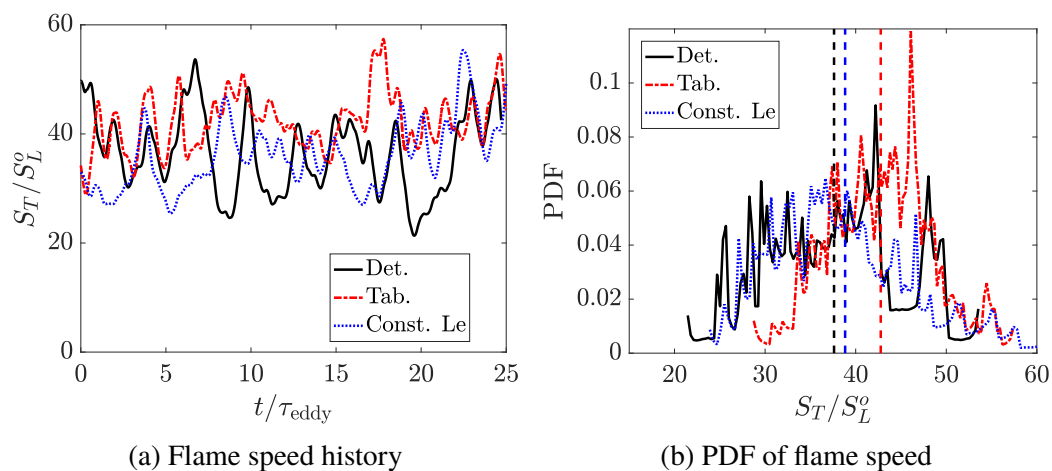


Figure 6.15: Flame speed history (left) and PDF of normalized flame speed (right) for detailed chemistry (solid black), tabulated chemistry with thermal diffusion (dot-dashed red), and tabulated chemistry assuming constant Lewis numbers [102] (dotted blue). The dashed lines represent the temporal mean of the flame speeds.

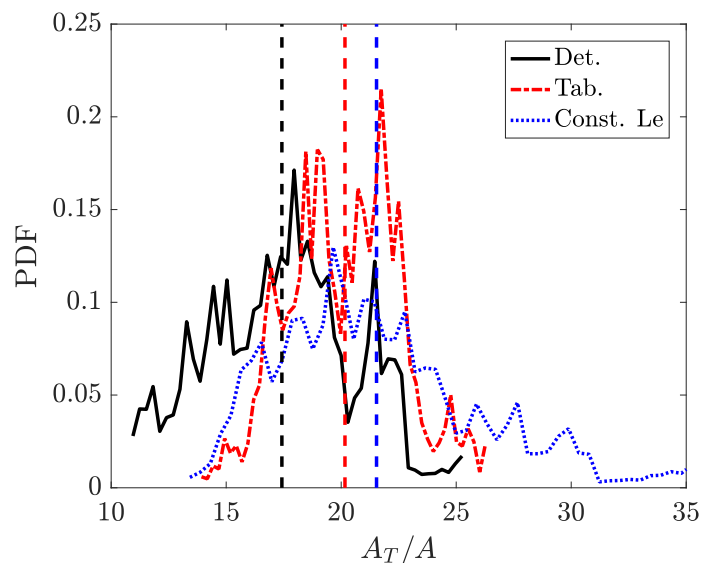


Figure 6.16: PDF of turbulent three-dimensional flame surface area normalized by domain cross-sectional area for detailed chemistry (solid black), tabulated chemistry with thermal diffusion (dot-dashed red), and tabulated chemistry assuming constant Lewis numbers [102] (dotted blue). The vertical dashed lines on the left figure represent the temporal mean of the flame area.

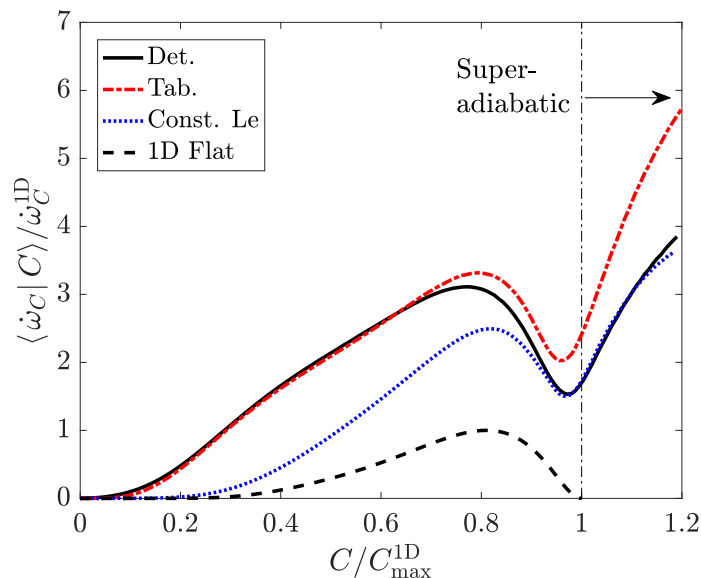


Figure 6.17: Conditional mean of the normalized progress variable source term for the detailed chemistry (black), proposed tabulated chemistry (red), and constant Lewis number tabulated chemistry (blue) models. A one-dimensional flame profile is shown for reference (dashed black line).

### Local flame statistics

The curvature-induced acceleration of the flame propagation is once again investigated through the mean of  $\dot{\omega}_C$ , conditioned on  $C$  throughout the domain, as shown in Fig. 6.17. Data spanning 95% of the range of  $C$  is presented. The first observation is that  $\langle \dot{\omega}_C | C \rangle$  in this turbulent flame is much greater than that of a laminar unstretched flame due to differential diffusion. This increase in source term corresponds to an increase in turbulent flame speed. The tabulated and detailed chemistry conditional means show excellent agreement up to the maximum progress variable found in a one-dimensional unstretched flame, indicated by the vertical dot-dashed line in Fig. 6.17.

Fig. 6.17 also shows regions which exceed the adiabatic fully-burnt properties of the inlet mixture. These regions are often referred to as “super-adiabatic” or hot spots [7, 8, 33]. The general trend of the detailed chemistry model is captured qualitatively in the hot-spot region by the proposed  $Z$ – $C$  tabulation (albeit at a larger magnitude), despite the chemistry table containing only adiabatic flames.

Figure 6.18 shows the conditional mean of  $\dot{\omega}_C$  along the flame surface, conditioned on the flame curvature. Data spanning 95% of the range of  $\kappa$  is provided. This figure indicates good agreement between detailed and tabulated chemistry in regions of

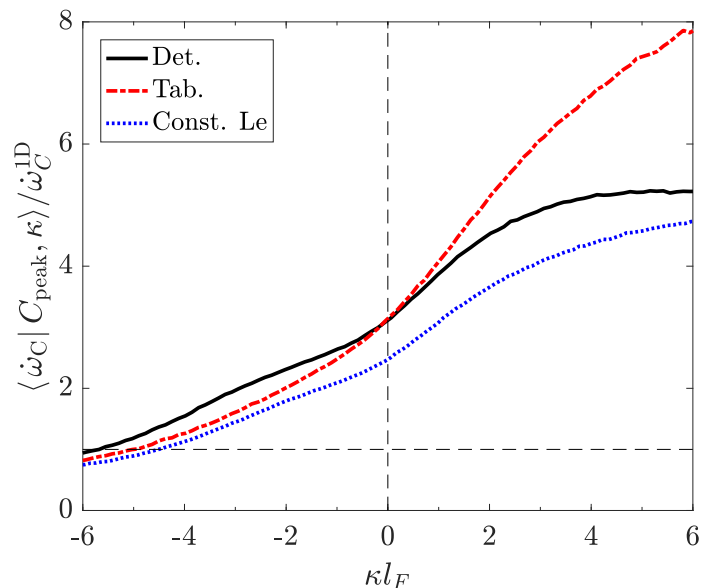


Figure 6.18: Conditional mean of the progress variable source term as a function of normalized local flame curvature for detailed chemistry (black), tabulated chemistry with thermal diffusion (red), and tabulated chemistry assuming constant Lewis numbers [102] (blue).

high negative curvature and up to  $\kappa l_F \approx 1$ . At high curvature (exceeding the laminar flame thickness), Fig. 6.18 shows that the mean progress variable source term overpredicts the finite-rate chemistry results.

## 6.6 Summary of results

The above results focused primarily on the comparison between finite-rate chemistry and the proposed tabulated chemistry model. It is instructive to also consider the improvement found by the proposed tabulated chemistry model through comparisons with the constant Lewis number model.

Both the proposed tabulated chemistry model with thermal diffusion, and the constant Lewis number chemistry table, struggle to predict unsteady global flame statistics; however, there are important distinctions to be made between the results of the two tabulation methods. It is common practice to relate the turbulent flame speed and surface area. For example, Bray [17] and Candel and Poinso [21] suggested that the turbulent flame speed and flame area are correlated through

$$\frac{S_T}{S_L} = \frac{A_T}{A} I_0. \quad (6.3)$$

Here,  $I_0$  is the burning efficiency, which is a measure of local flame structure.

Recently, a closure for  $I_0$  has been proposed as [73, 109]

$$I_0 \approx \frac{\langle \dot{\omega}_F / |\nabla T| | T_{peak}^{turb} \rangle}{\dot{\omega}_{F,lam}^{1D} / |\nabla T_{lam}^{1D}|}, \quad (6.4)$$

which was found to be nearly constant across a range of fuels (hydrogen was not considered), chemistry models, diffusion models, and turbulence intensities. In this expression,  $T_{peak}^{1D}$  represents the temperature of peak source term in a laminar flame, while  $T_{peak}^{turb}$  corresponds to the temperature of peak mean chemical source term in the turbulent flame. A detailed analysis of the burning efficiency in lean premixed hydrogen–air flames is beyond the scope of this work, but is suggested as an avenue of future investigation. Instead, the relationship given in Eq. 6.3 will be used to investigate the tabulation methods.

The constant Lewis number chemistry table predicts larger turbulent flame areas compared to the detailed chemistry results (Fig. 6.16). However, the source term of  $C$  is underpredicted, relative to the finite-rate chemistry results, through a majority of the flame (Fig. 6.17). These two observations, in conjunction with Eq. 6.3, suggest some manner of error cancellation; an increase in  $A_T/A$  of 24%, coupled with a decrease of the chemical source term of approximately 20% (disagreement of  $I_0$  with detailed chemistry) results in a flame speed which closely matches finite-rate chemistry (an increase of 3%) (Fig. 6.15b).

A similar analysis using the proposed tabulation methodology results in different conclusions. The new tabulation method overpredicts the detailed chemistry  $A_T/A$  by 15%, while closely matching the chemistry source term over nearly the entire flame structure. As a result, the tabulated chemistry turbulent flame speed overpredicts the detailed chemistry results by 14%, indicating an accurate prediction of  $I_0$  by tabulated chemistry.

Put simply, comparisons of solely the turbulent flame speed are insufficient to determine the applicability of the tabulation method. The constant Lewis number approach appears to predict  $S_T$  well, yet this may be an artifact of the coupled interaction of the flame area and local effects. However, while the proposed tabulation model overpredicts  $S_T/S_L$ , the overprediction is consistent with  $A_T/A$  while the local source terms are very well approximated using the new chemistry tabulation. These results suggest that, by improving the agreement on the turbulent flame area, the turbulent flame speed agreement between detailed and tabulated chemistry would also be improved. This improvement should be achieved through future developments of the tabulated chemistry approach.

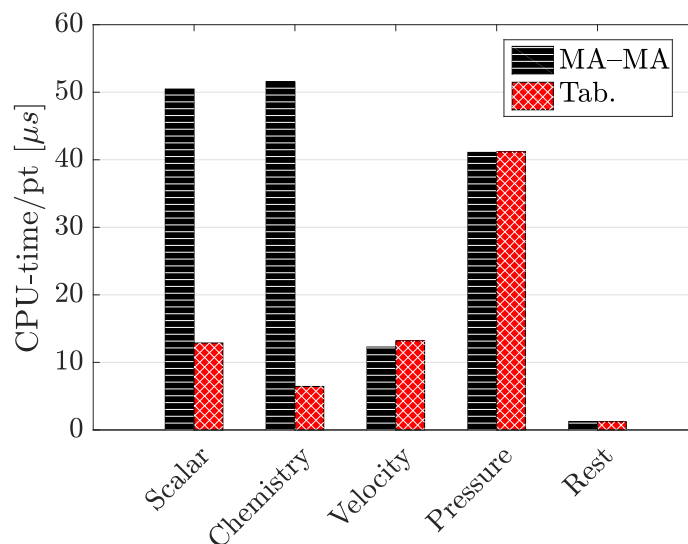


Figure 6.19: Computational time per grid point for each part of NGA for the three-dimensional turbulent configuration. The detailed chemistry (black) and proposed tabulated chemistry model (red) are shown. “Chemistry” includes the cost of computing diffusion coefficients (for detailed chemistry) and all chemistry table interpolation (for tabulated).

## 6.7 Reduction in computational cost

The proposed Z–C tabulation model provides accurate descriptions of the local flame structure for a wide range of flame configurations. One of the primary benefits of this chemistry modeling technique is its reduced computational cost compared to detailed finite-rate chemistry simulations. A comparison of the computational cost of these two techniques is thus of significant interest.

### 6.7.1 Wall time reduction

Figure 6.19 shows the computational time for each part of the finite-rate chemistry procedure (using mixture-averaged diffusion models) and tabulated chemistry. Only the three-dimensional turbulent flame configuration is included in this comparison. An identical computational grid and domain decomposition is used. A total of 20 iterations are run for each case, and averaged timings are reported. These two turbulent simulations were performed on the National Energy Research Scientific Computing (NERSC) Center’s Cori system [29], using 24 compute nodes, each with 32 Haswell cores.

As can be seen from Fig. 6.19, there is a significant cost reduction in using tabulated chemistry compared to finite-rate chemistry. This cost reduction results from two factors: a reduced number of transported scalars and simplified thermo-chemical

property computations. The finite-rate chemistry model transports a total of  $N$  species and temperature. Recall that the lean hydrogen–air chemistry model used throughout this work consists of nine species and 54 reactions. The tabulated chemistry procedure only requires transporting two scalar quantities ( $Z$  and  $C$ ), as these two scalars create the low-dimensional manifold on which all other required properties may be found. This reduction in transported scalars results in a 75% reduction in the cost of scalar transport which, in turn, reduces the overall cost of scalar transport from 33% to 17% of the total simulation cost. It should be noted that this is a “best case” scenario for finite-rate chemistry (or “worst case” for tabulated chemistry); if more species were included in the full chemical model, the scalar transport cost for detailed chemistry would increase linearly, while the tabulated chemistry cost would remain fixed.

In addition, a significant reduction is found in the cost of chemistry. Here, chemistry cost refers to the determination of all thermo-chemical properties and required chemical source terms. In the detailed chemistry model, this cost primarily consists of computing mass and thermal diffusion coefficients, viscosity, and species chemical source terms. The “chemistry” cost for tabulated chemistry consists of the table look-ups for various properties (e.g.,  $D_Z$  and  $\dot{\omega}_C$ ). By using tabulated chemistry, the cost associated with chemistry calculations is reduced by nearly 90%. This reduction results in the chemistry cost being reduced from 33% to only 8% of the total simulation cost. Again, the number of chemical species considered in detailed chemistry will significantly affect the finite-rate chemistry timings. The result of both scalar and combustion cost reductions is a simulation 53% less expensive than the detailed chemistry simulation.

### 6.7.2 Stiff chemistry removal

A reduction in the wall time of a simulation is not the only cost-benefit found by utilizing tabulated chemistry. The tabulation of one-dimensional flame solutions also reduces the effect of stiff chemistry source terms, i.e., chemical reactions involving both short lived radicals and small length scales. The only remaining chemistry source term in tabulated chemistry is the production of  $\text{H}_2\text{O}$ , which suggests that a larger  $\Delta t$  and  $\Delta x$  may be permissible while maintaining solution accuracy.

These claims are investigated by considering the one-dimensional unstretched flame at  $\phi = 0.4$ . The flame is allowed to propagate upstream in the domain. This

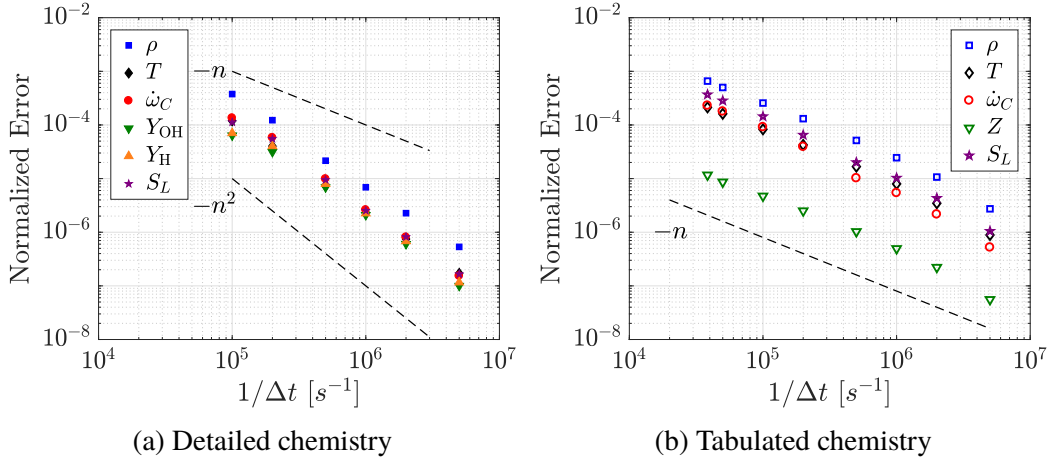


Figure 6.20: Errors of various parameters for (a) detailed chemistry and (b) tabulated chemistry for a range of simulation time step, normalized by  $\psi_V^{\text{fine}}$  at  $\Delta t = 0.1 \mu\text{s}$ , with a fixed  $\Delta x = l_F/20$ .

procedure first investigates a variety of time steps at a fixed grid spacing. Then, a fixed time step is used while altering the grid spacing. The chosen nominal values are  $\Delta t = 1 \times 10^{-6} \text{ s}$  and  $\Delta x = l_F/20$ . The error measurement considered in this work is the volume integral of various parameters,  $\psi_V = \int_V \psi dV$ . Each value of  $\psi_V$  is compared to the volume integral of the most refined case, and the error is computed as

$$\epsilon_V = \left| \frac{\psi_V - \psi_V^{\text{fine}}}{\psi_V^{\text{fine}}} \right|. \quad (6.5)$$

Data are saved at intervals of approximately  $3 \tau_F$ , and a total of  $30 \tau_F$  are investigated. The error is computed for each data file, and errors across the  $30 \tau_F$  for a given  $(\Delta t, \Delta x)$  are averaged.

The considered time steps range from  $0.1 \mu\text{s} < \Delta t < 25 \mu\text{s}$ , and grid spacings range from  $80 < l_F/\Delta x < 2$ . The maximum time step was limited by the CFL condition at the given nominal grid spacing. It should be noted that detailed chemistry time steps greater than  $10 \mu\text{s}$  were found to be unstable and are not considered.

First, Fig. 6.20 shows the normalized errors of thermo-chemical parameters and the flame speed as a function of  $\Delta t$  at a fixed  $\Delta x$ . The errors for detailed chemistry converge nearly quadratically, while tabulated chemistry experiences linear convergence. The potential cost saving of using tabulated chemistry is found by comparing the normalized error of a given quantity (e.g., temperature) for both chemistry models. The normalized error of temperature is shown in Fig. 6.21. It is found that tabulated chemistry is stable for time steps larger than finite-rate chemistry – up to

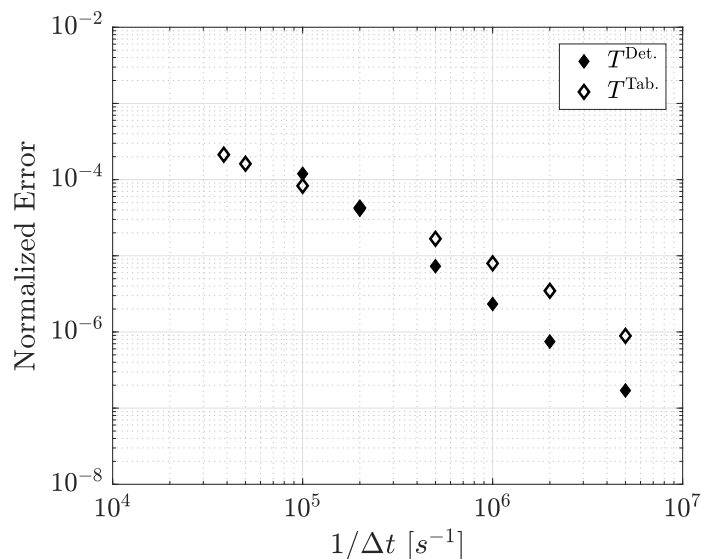


Figure 6.21: Comparison of the error in the volume integral of the temperature for detailed chemistry (black diamonds) and tabulated chemistry (red circles), normalized by  $\psi_V^{\text{fine}}$  at  $\Delta t = 0.1 \mu\text{s}$ , as a function of time step.

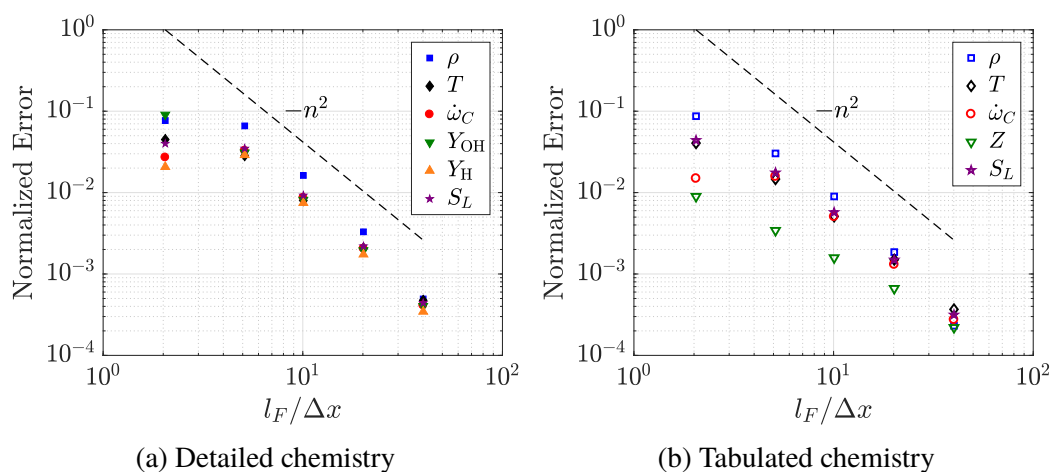


Figure 6.22: Errors of various parameters for (a) detailed chemistry and (b) tabulated chemistry for a range of grid spacing, normalized by  $\psi_V^{\text{fine}}$  at  $l_F/\Delta x = 80$ , with a fixed  $\Delta t = 1 \mu\text{s}$ .

2.5 times larger (limited by the CFL constraint) in the present example. These results show that tabulated chemistry may be run using  $\Delta t = 25 \mu\text{s}$  with a normalized error of  $2 \times 10^{-4}$ .

A similar set of analyses can be performed by varying  $\Delta x$ . Figure 6.22 shows normalized errors for detailed and tabulated chemistry at a fixed  $\Delta t$ . These normalized errors also decay quadratically. Investigating the normalized error in  $T$  (shown in Fig. 6.23) shows that a tabulated chemistry grid spacing of  $l_F/\Delta x = 15$  can be used

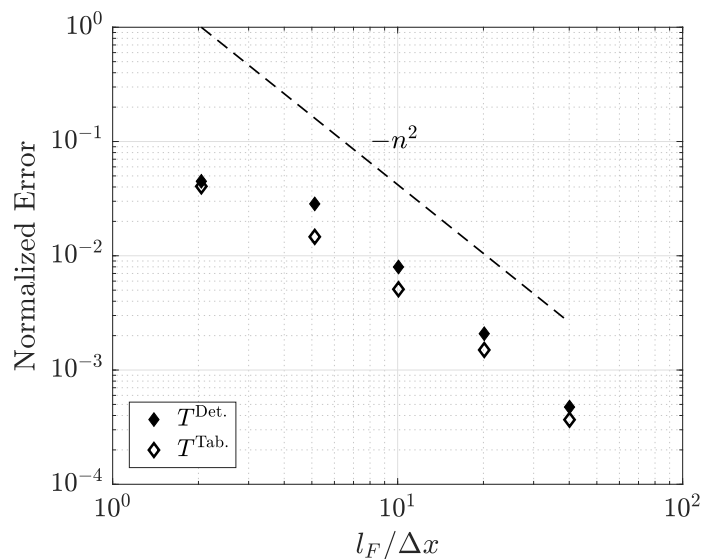


Figure 6.23: Comparison of the error in the volume integral of the temperature for detailed chemistry (filled symbols) and tabulated chemistry (open symbols), normalized by  $\psi_V^{\text{fine}}$  at  $l_F / \Delta x = 80$ , as a function of grid spacing.

to retain a similar accuracy of detailed chemistry with  $l_F / \Delta x = 20$ . This results in a 25% reduction in the number of computational grid points. Additional computational cost savings could be achieved by leveraging the CFL condition relation between time step and grid size.

### 6.7.3 Summary of computational cost reductions

Three cost-reductions have been discussed for tabulated chemistry. By using an identical computational grid and time step for both tabulated and detailed chemistry, the wall-time savings were found to reduce computational costs by 50%. Further cost improvements could also be leveraged. By removing stiff chemical source terms, the time step and grid spacing can also be relaxed. For example, the time step can be increased 2.5 times the maximum stable time step for finite-rate chemistry. This results in 60% fewer time steps for tabulated chemistry. Finally, similar accuracy as the detailed chemistry cases can be found by reducing the number of grid points by 25%. When considering a 25% increase in grid size could lead to an additional increase in the allowable time step, the use of tabulated chemistry will result in simulations nearly 10 times faster than the finite-rate chemistry methods.

*Chapter 7*

## CONCLUSION

Lean premixed hydrogen–air flames were investigated using direct numerical simulations in order to evaluate and develop new transport property and chemistry models. A thermal diffusion model given by Chapman and Cowling [24] was systematically evaluated across a range of flame configurations. This model was used as a basis for a novel thermal diffusion model which substantially reduced computational costs. Finally, differential diffusion and thermal diffusion were incorporated into a new tabulated chemistry framework, which was evaluated using similar flame configurations.

**7.1 Mixture-averaged thermal diffusion**

The mixture-averaged thermal diffusion model (MA–MA) originally proposed by Chapman and Cowling [24] was implemented and evaluated against the multicomponent thermal diffusion model (MA–MC).

The MA–MA model was first evaluated using a set of multicomponent transport simulations. It was found that the inclusion of thermal diffusion, using either MA or MC thermal diffusion, altered the laminar flame speed of one-dimensional lean premixed hydrogen flames by up to 5%. The mixture-averaged thermal diffusion model was then shown to predict both experimental results and results using multicomponent thermal diffusion. Further, thermal diffusion was found to enhance cellular instabilities, increase flame propagation speeds and surface areas (global effects), and increase product source terms and flame surface curvature (local effects) in two-dimensional unsteady flames. These effects were also identified in three-dimensional configurations for both laminar and turbulent flames. The comparison between the MA–MA and MA–MC models was excellent across all cases considered. Further, Chapman and Cowling’s thermal diffusion model reduced the computational cost of including the Soret and Dufour effects compared to the more expensive multicomponent approach. The results found throughout this work indicate that thermal diffusion must be included in simulations of lean hydrogen flames to capture the flame properties, and that thermal diffusion can be implemented in a cost-efficient manner for three-dimensional flames.

## 7.2 Development of a reduced thermal diffusion model

To further reduce the computational cost of including thermal diffusion, a reduced thermal diffusion model (RM), derived from Chapman and Cowling's thermal diffusion model [24], was developed and evaluated. This reduced model simplified the mixture-averaged approach by using various relationships between transport properties and molecular weights. Assuming that the molecular weight of the species of interest is significantly less than that of the mixture, the model performs very well with a scaling parameter determined using several unburnt mixtures. Mixtures of hydrogen/air/diluent and hydrocarbon/air/diluent at a variety of unburnt temperatures and pressures were all investigated. More precisely, the unstretched laminar flame speeds using the RM model agree with the multicomponent model, showing a maximum relative error of 1.5% across all cases, with errors less than 0.5% for nearly all considered mixtures. Additionally, this reduced model, which was shown to predict accurate thermal diffusion coefficients in mixtures where the thermal diffusion of H and H<sub>2</sub> is critical, can be applied to many fuel/air mixtures. For combustion mixtures where thermal diffusion is not as important (e.g., rich H<sub>2</sub>/air or light to medium hydrocarbon fuels) the RM implementation will still predict accurate flame speeds, even if the thermal diffusion fluxes have a moderate error relative to the multicomponent method. This is simply due to the fact that thermal diffusion has little influence on these mixtures.

An a priori comparison in a turbulent flame simulation also shows excellent agreement between the RM and MC models. Not only were the mean trends of  $D_i^T$  captured, but the super-adiabatic regions and fluctuations due to turbulent transport were also reproduced by the RM method. Finally, the RM method has a fixed cost for chemical models up to 100 species, which significantly reduces the computational time of including thermal diffusion effects in reacting flow simulations.

## 7.3 Incorporating differential and thermal diffusion in tabulated chemistry

By relaxing the unity Lewis number (apart from the fuel) and no thermal diffusion approximations suggested by Regele et al. [102], a new chemistry tabulation model was derived using a mixture fraction-like variable and a progress variable. The tabulated chemistry model was applied to multiple flame configurations: one-dimensional unstretched and stretched, two-dimensional steady and unsteady, and three-dimensional turbulent flames.

It was found that the newly proposed tabulated chemistry model accurately captures

both local properties (e.g., progress variable source terms) as well as global properties (e.g., flame speeds) of the considered flames. This result is entirely reliant on the cross-diffusivity,  $D_Z^*$ , of the mixture fraction, which permits information about the flame curvature and differential diffusion effects to be included in the  $Z$ - $C$  model. By using one-dimensional, flat, burning flames in the chemistry table, this model is able to capture both flame curvature and flame extinction effects. Additionally, the adiabatic flames which construct the chemistry table were able to predict the formation of “hot spots” in a turbulent flame. The proposed  $Z$ - $C$  model allows for a simple representation of a complex chemical process. Using this model, further investigations into turbulent flames, hydrocarbon fuels, and the implementation of  $Z$  and  $C$  in large eddy simulations should be considered, where computational cost reductions will be larger.

#### 7.4 Future Work

The models presented in this thesis have been thoroughly evaluated for a wide range of lean premixed hydrogen–air flame configurations. The benefits found by using a reduced thermal diffusion model and tabulated chemistry suggest that these models be explored in other flame configurations and with hydrocarbon fuels.

Thermal diffusion has an influence on other fuel/oxidizer mixtures which were not considered in this work. In particular, high-hydrogen content syngas has been investigated recently using multicomponent thermal diffusion [101]. As this fuel contains carbon-based species, and potentially large hydrocarbon molecules, the governing chemical model could have hundreds of species and thousands of reactions. Additionally, other heavy hydrocarbon mixtures, e.g., rich iso-octane [16], exhibit thermo-diffusive instabilities which may also require thermal diffusion to fully investigate. Other unstable flame configurations, such as lean high pressure hydrogen and rich high pressure acetylene, propane, and iso-octane flames, have shown flame surface cracking leading to cellular instability formation [16, 64]. These flame fronts enhance the focusing effects of non-unity Lewis number mixtures, and thermal diffusion could increase these effects further. Using the reduced thermal diffusion model developed in Chapter 4, especially for hydrocarbon combustion, would negligibly increase computational costs.

For fuel/air mixtures not considered in Chapter 4, the reduced thermal diffusion model should be reevaluated to verify the governing assumptions still hold, and that the scaling parameters do not change appreciably. For example, a fuel whose molec-

ular weight is similar to that of the mixture may not satisfy the assumptions given in the model development. While this evaluation should ideally be performed for each additional fuel/air mixture, the scaling parameter analysis outlined in Chapter 4 is straightforward, requiring only one-dimensional flames with multicomponent thermal diffusion.

Tabulated chemistry presents a different set of future analyses. The next set of studies should focus on methods to increase the agreement between finite-rate chemistry and tabulated chemistry. Currently, linear interpolation is performed in the chemistry table look-up procedure. Alternative interpolation methods (perhaps based on the shape of the chemistry table, e.g., Fig. 5.11 at  $C_{peak}$ ), may present a more accurate interpolation without increasing the number of underlying flame solutions or increasing the resolution of the chemistry table. The treatment of extinction points below the lowest flame solution in the chemistry table should also be investigated, as this region may be interrogated more frequently in flames with high probability of extinction. Finally, the addition of a new tabulation variable, or perhaps the inclusion of additional scalars in the definition of  $Z$  (for example,  $H$ ), may improve the agreement between the chemistry table and the optimal estimator.

As described in Section 6.6, the disagreement of mean global flame statistics presents a challenge: how are the mean local statistics captured along the flame surface, while the flame speed and surface area are over-predicted? One possible tool to investigate the interplay of global and local effects is the burning efficiency introduced in Eqs. 6.3 and 6.4. These two expressions relate global effects with localized effects along the flame surface. In the case of tabulated chemistry, where the fuel source term and temperature are not readily available, one may consider  $\dot{\omega}_C$  and  $C$ , instead of measurements on the fuel and temperature. Additionally, as the two-dimensional and three-dimensional laminar freely propagating flames have increased flame speed and surface area (similar to the turbulent case), this style of investigation may also be applicable to more tractable flame configurations. The results of these analyses should be compared to those of Lapointe and Blanquart [73], to provide an additional measure of the burning efficiency in a thermo-diffusive mixture at a range of Karlovitz numbers.

Finally, the mathematical development of the chemistry tabulation is fuel agnostic. While the current model was evaluated using hydrogen–air mixtures only, it may prove valuable for hydrocarbon combustion. This was briefly explored in Regele et al. for their chemistry tabulation approach using rich propane mixtures [102].

The benefits of tabulated chemistry, especially wall-time reduction due to orders-of-magnitude fewer transported scalars, would be significantly more pronounced than the values reported in this thesis. A similar set of analyses investigating the interaction of flame surface curvature and differential diffusion effects in rich mixtures of heavy hydrocarbon fuels which are thermo-diffusively unstable should be investigated.

## Appendix A

### SPECIES PROPERTY FITS

#### A.1 Collision integral fits

The collision integrals are expressed as rational functions of the form

$$\chi = \frac{\sum_m c_m (T_i^*)^m}{\sum_m d_m (T_i^*)^m}, \quad (\text{A.1})$$

where  $\chi = [\Omega_i^{(1,1)*}, \Omega_i^{(2,2)*}, C_{ij}^*]$  with coefficients from Table A.1 [100]. Figure A.1 shows the rational function fit for tabulated data from Monchick and Mason [87]. The reduced temperature range covers all conditions for the reacting flow simulations considered in this thesis.

#### A.2 Species property fits

Fits for the species collision diameters and Lennard-Jones parameters for species  $i$  are presented here. These fits have been used in FlameMaster [100] and are documented here, for completeness. The collision diameter may be replaced with a fit based on molecular weights given as,

$$\sigma_i = 1.234W_i^{0.33}. \quad (\text{A.2})$$

Additionally,  $\epsilon_i$ , the potential well depth of species  $i$ , is well approximated as a function of molecular weights,

$$\frac{\epsilon_i}{k_B} = 37.15W_i^{0.58}. \quad (\text{A.3})$$

Table A.1: Coefficients of the rational functions fitting  $\Omega_i^{(2,2)*}$  and  $C_{ij}^*$ .

Variable	Coefficient	$m = 0$	$m = 1$	$m = 2$	$m = 3$	$m = 4$
$\Omega_i^{(1,1)*}$	$c_m$	6.87283	9.41223	7.74424	0.23425	—
	$d_m$	1.45338	5.22698	9.71085	0.46540	0.00042
$\Omega_i^{(2,2)*}$	$c_m$	3.35306	2.53272	2.90242	0.11186	—
	$d_m$	0.86623	1.39139	3.15849	0.18973	0.00018
$C_{ij}^*$	$c_m$	0.73680	-0.16258	0.70953	1.39801	0.06796
	$d_m$	0.81695	-0.06989	1.01867	1.45230	0.07200

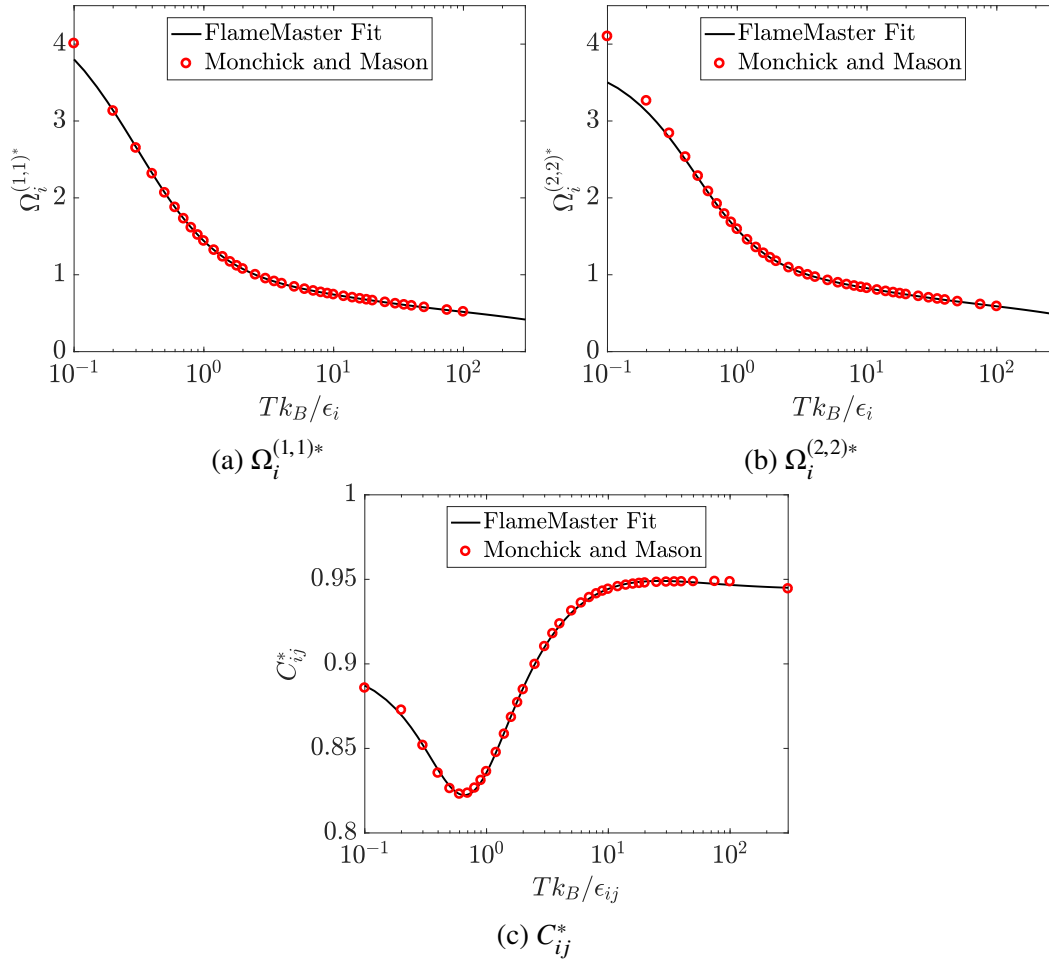


Figure A.1: Rational function fits of (a)  $\Omega_i^{(1,1)*}$ , (b)  $\Omega_i^{(2,2)*}$  and (c)  $C_{ij}^*$  (black lines), using coefficients from FlameMaster [100] and tabulated data (red circles) from Monchick and Mason [87].

Figure A.2 shows these two fits for species present in CaltechMech [14]. The transport property data in Fig. A.2 are aggregated from multiple references [14].

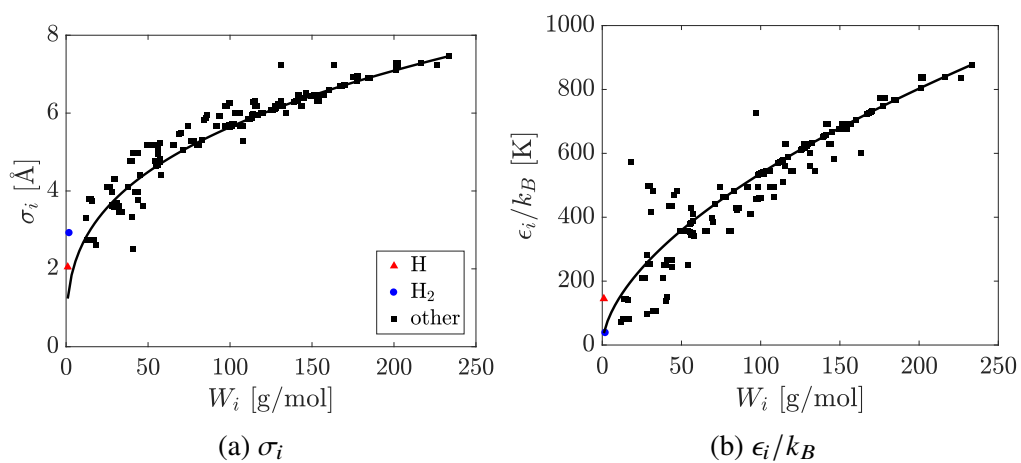


Figure A.2: Power law fits (black lines) of (a)  $\sigma_i$  using Eq. 4.13 and (b)  $\epsilon_i/k_B$  using Eq. 4.15 as functions of  $W_i$ . The fit coefficients are from FlameMaster [100] and the transport property data (symbols) are from multiple references [14]. H is the red triangle and H<sub>2</sub> is the blue circle.

## Appendix B

# SENSITIVITY ANALYSIS OF FLAME INSTABILITY LENGTH SCALES

### Introduction<sup>1</sup>

The cellular instability characteristic lengths have not been investigated to any great detail, with the cellular structure surface area receiving the most attention [33]. This appendix aims to provide a methodology for extracting the length scales in the two-dimensional, freely propagating flame configuration. The instability length scales from simulations using various diffusion models are investigated and statistics of the flame length scales are extracted.

This appendix is organized as follows: first, the proposed methodology is presented in Section B.1. Then, a sensitivity analysis is presented in Section B.2. This method was applied to numerical data using different diffusion models, and the results were discussed in Section 3.7.1.

### B.1 Methodology

The data analyzed is that of the two-dimensional unsteady freely-propagating flame, whose results were discussed in Section 3.4. Data from each of the three diffusion models (MA-xx, MA-MA, and MA-MC) are analyzed using the same methodology, outlined below and detailed in the following paragraphs:

1. Identify and extract the flame surface.
2. Post-process the flame surface to remove closed contours (i.e., unburnt reactants surrounded by burnt products).
3. Calculate the species source term and the flame curvature along flame surface.
4. Determine locations of cellular structures and extinction zones.
5. Calculate the cellular instability arc lengths,  $l_c$ , and extinction zone lengths,  $l_e$ .

---

<sup>1</sup>The original length scale detection methodology was first developed as part of a Caltech Senior thesis by Morgan Hill (BS '16). This methodology was greatly expanded, and the sensitivity analysis conducted, in Schlup and Blanquart, Extracting length scales of a thermo-diffusively unstable laminar flame, 10th U.S. National Combustion Meeting (2017).

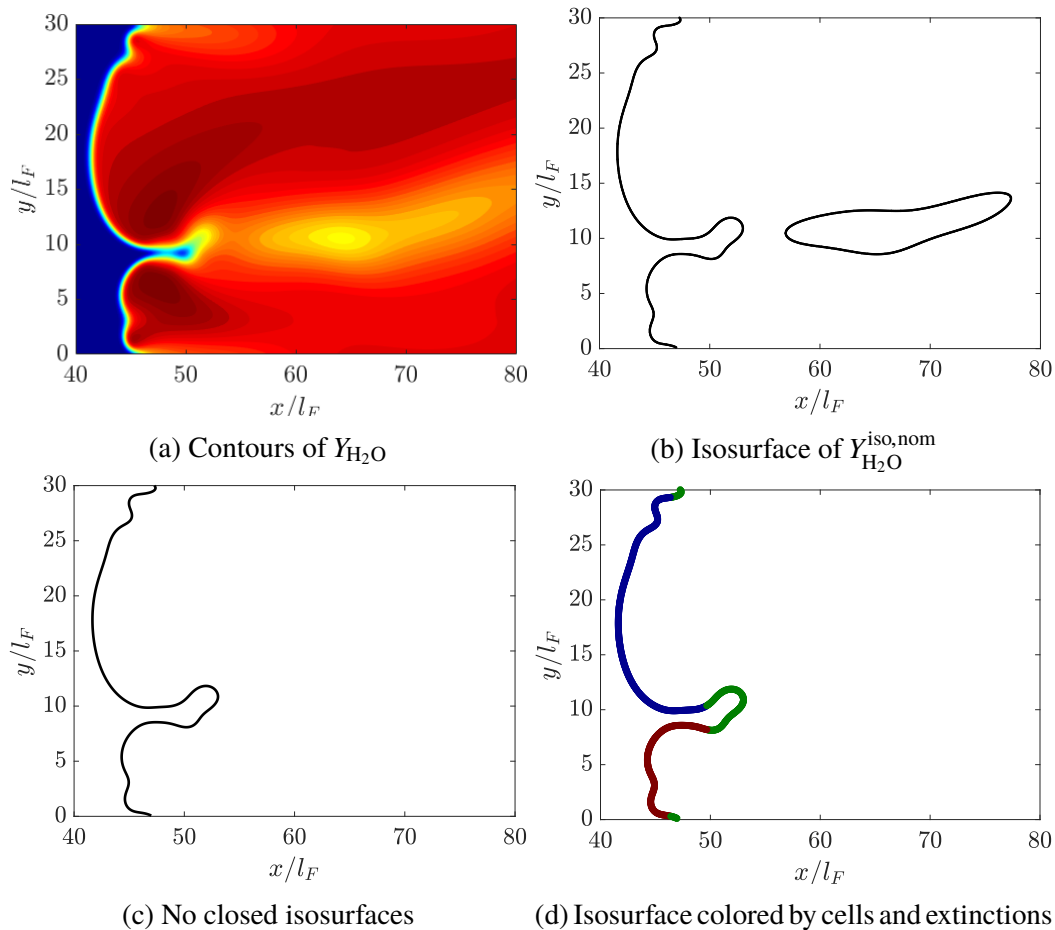


Figure B.1: Method of extracting cellular structures: (a) filled contour plot of  $Y_{H_2O}$ , (b) isosurface of  $Y_{H_2O}^{iso,nom}$  with detached pocket, (c) isosurface with pocket removed, and (d) isosurface with two cells indicated (blue and red segments), and the extinction regions between adjacent cells (green segments).

The first step of this procedure is identifying the flame surface. The flame surface is defined using an isosurface of  $Y_{H_2O}^{iso}$  (or  $T^{iso}$  when performing the sensitivity analyses in Section B.2.2). Nominal values of the flame isosurface are chosen to be  $Y_{H_2O}^{iso,nom} = Y_{H_2O}^{peak}$  and  $T^{iso,nom} = T^{peak}$ , where the superscript peak indicates the value of  $Y_{H_2O}$  or  $T$  corresponding to the maximum source term of  $H_2O$  in a one-dimensional hydrogen-air flame with identical inlet properties. Contours of  $Y_{H_2O}$  (Fig. B.1a), with a detected isosurface of  $Y_{H_2O}^{iso,nom}$  (Fig. B.1b), are shown. In this work, the Matlab function `contourc` is implemented to extract the isosurface.

Once the flame surface has been identified, some post-processing is performed. In this analysis, only portions of the flame surface which are not closed are considered. These pockets, one of which is depicted in Fig. B.1b, are not considered part of the

cellular instabilities and are thus not of current interest. These closed contours are removed from the detected isosurface such that a single, continuous isoline defines the flame front (Fig. B.1c).

After the flame surface is extracted from the data, the curvature and chemical source terms along the isosurface are computed. The flame curvature is defined using Eq. 3.2, where the surface normal is computed using the isosurface variable (either  $Y_{\text{H}_2\text{O}}$  or  $T$ ). This definition of the flame surface yields positive curvature when the surface is convex to the unburnt mixture and negative curvature when concave to the unburnt mixture.

The flame surface is then split into regions, termed “cells” (i.e., the cellular instabilities) and “extinction zones”. This classification is made by determining a threshold value for either the  $\text{H}_2\text{O}$  source term along the flame surface or the curvature of the flame surface. An example of identified cellular structures is given in Fig. B.1d, where two identified cells are colored blue and red, and extinction regions along the flame surface are colored green. Previous work has defined extinction as regions along the flame surface where the product source term is reduced below a certain percentage of the peak value in a one-dimensional flame,  $\dot{\omega}_{\text{H}_2\text{O}}^{\text{1D}}$  [33, 74]. Figure 6.12b gives two possible definitions of extinction based on the conditional mean,  $\langle \dot{\omega}_{\text{H}_2\text{O}} | Y_{\text{H}_2\text{O}}^{\text{peak}}, \kappa \rangle$ : first, there appears to be a mean lower bound of  $\dot{\omega}_{\text{H}_2\text{O}}$  at  $0.2 \dot{\omega}_{\text{H}_2\text{O}}^{\text{1D}}$ . Second, when  $\kappa < 0$ , the mean value of  $\dot{\omega}_{\text{H}_2\text{O}}$  is nearly constant. As an initial guess, extinction thresholds of  $\dot{\omega}_{\text{H}_2\text{O}}^{\text{th}} = 0.2 \dot{\omega}_{\text{H}_2\text{O}}^{\text{1D}}$  and  $\kappa^{\text{th}} l_F = -0.65$  are chosen, where the superscript “th” represents extinction threshold values. Portions of the flame isosurface which are not considered extinction zones are classified as cellular instabilities.

After the cells and extinction zones have been identified, the flame surface length scales are calculated. The characteristic length scales for this work are defined to be the arc length of the cells and the straight-line lengths across extinction regions. Figure B.2 depicts these length scales, showing the arc-length of cellular instabilities as the arc length of the blue and red sections, and the straight-line lengths indicated by the straight green lines. The cell arc and extinction zone lengths are then stored for each data file. The straight line length is considered as the characteristic length for extinction, as it is the smallest length scale concerning the extinction zone (necessary for sub-grid scale considerations), and is significantly less sensitive to the flame isosurface (see the inset of Fig. B.9 for an example of the effects on the extinction region by varying  $Y_{\text{H}_2\text{O}}^{\text{iso}}$ ).

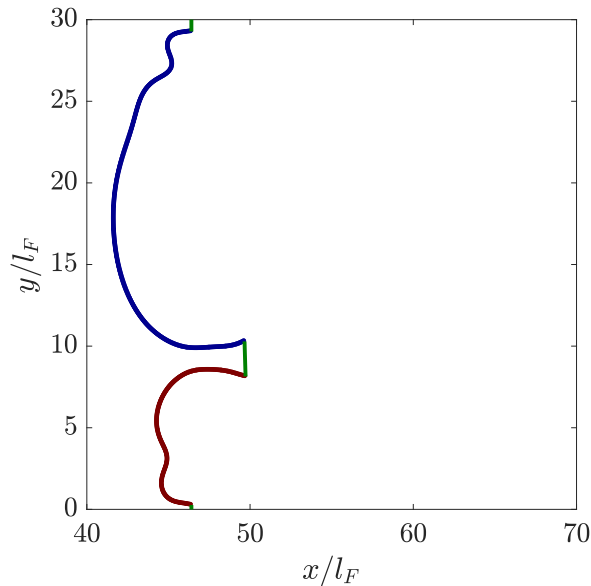


Figure B.2: Depiction of the cellular instability length scales, showing two cellular instabilities (red and blue sections), and two extinction length scales (green lines). Note that one extinction region exists across the periodic boundary.

Table B.1: Range of the sensitivity analysis variables. Note that the maximum considered  $Y_{\text{H}_2\text{O}}^{\text{iso}}$  and  $T^{\text{iso}}$  is dependent on isosurfaces remaining inside the computational domain.

Variable	Minimum	Maximum
$Y_{\text{H}_2\text{O}}^{\text{iso}}/Y_{\text{H}_2\text{O}}^{\text{peak}}$	0.75	1.00
$T^{\text{iso}}/T^{\text{peak}}$	0.75	1.03
$\dot{\omega}_{\text{H}_2\text{O}}^{\text{th}}/\dot{\omega}_{\text{H}_2\text{O}}^{\text{1D}}$	0.05	0.50
$\kappa^{\text{th}}l_F$	-2.60	0.00

## B.2 Sensitivity analyses

A sensitivity analysis is performed on all available data to determine the influence of the independent parameters,  $Y_{\text{H}_2\text{O}}^{\text{iso}}$ ,  $T^{\text{iso}}$ ,  $\dot{\omega}_{\text{H}_2\text{O}}^{\text{th}}$ , and  $\kappa^{\text{th}}$ . A “one-at-a-time” sensitivity analysis methodology is chosen, where a nominal value of each independent variable is kept constant as the remaining variable is varied. Table B.1 lists the four sensitivity analysis variables, and the range in which they are investigated. The nominal values are  $Y_{\text{H}_2\text{O}}^{\text{iso}} = Y_{\text{H}_2\text{O}}^{\text{peak}}$ ,  $T^{\text{iso}} = T^{\text{peak}}$ ,  $\dot{\omega}_{\text{H}_2\text{O}}^{\text{th}} = 0.2 \dot{\omega}_{\text{H}_2\text{O}}^{\text{1D}}$ , and  $\kappa^{\text{th}} = -0.65 l_F$ .

The isosurface range is determined by the desire to investigate regions with large source terms near the flame front. Thus, a range is selected which encompasses the value of  $Y_{\text{H}_2\text{O}}$  and  $T$  at peak product source term. The maximum isosurface value

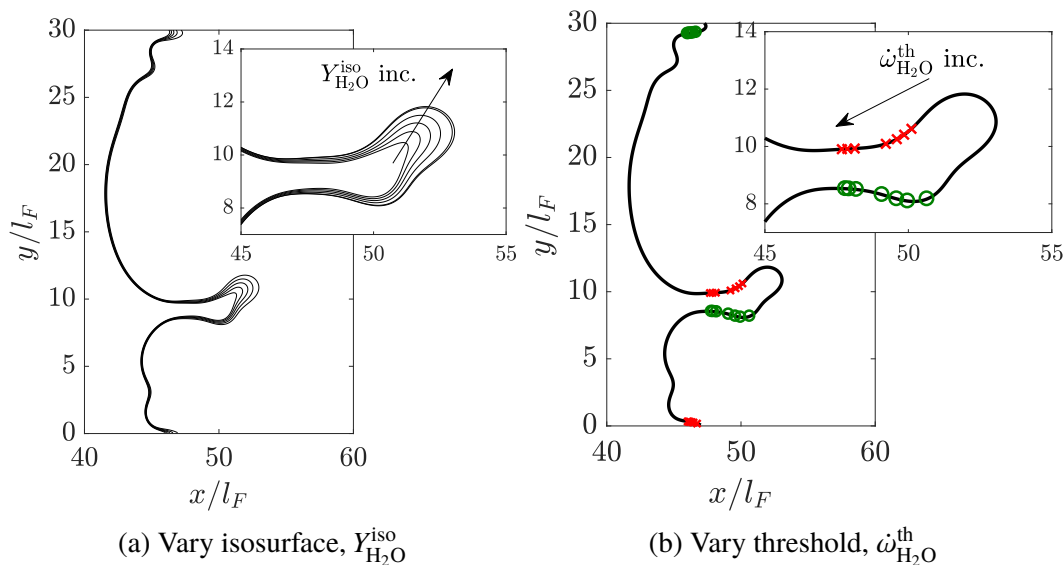


Figure B.3: Varying (a)  $Y_{\text{H}_2\text{O}}^{\text{iso}}$  and (b)  $\dot{\omega}_{\text{H}_2\text{O}}^{\text{th}}$  for a single data file. Arrows indicate direction of increasing sensitivity variable.

is constrained by the length of the computational domain. In many of the data files, increasing the isosurface further caused the isosurface to exit the domain. With this condition, it is impossible to identify accurately both instabilities and extinction zones. The range of extinction threshold values is based on the conditional means of product source term (e.g., Fig. 6.12b). This figure indicates that the mean source term in highly negative regions of the flame surface is near  $0.2 \dot{\omega}_{\text{H}_2\text{O}}^{\text{1D}}$ . Thus, the threshold source term spans from 5% to 50% of  $\dot{\omega}_{\text{H}_2\text{O}}^{\text{1D}}$ . A similar argument is made for the flame curvature; the maximum flame curvature for extinction threshold is 0, as the conditional mean of the product source term rapidly rises for larger curvatures.

### B.2.1 Sensitivity analysis of $Y_{\text{H}_2\text{O}}^{\text{iso}}$ and $\dot{\omega}_{\text{H}_2\text{O}}^{\text{th}}$

Figure B.3a depicts a range of isosurfaces for various  $Y_{\text{H}_2\text{O}}^{\text{iso}}$ . It is clear that the flame surface in regions of positive curvature (associated with the cellular instabilities) does not change significantly with a varying flame isosurface value, as the gradients of  $Y_{\text{H}_2\text{O}}$  are large. In regions of high negative curvature, the flame isosurface elongates appreciably. For a fixed value of  $Y_{\text{H}_2\text{O}}^{\text{iso}}$ , increasing  $\dot{\omega}_{\text{H}_2\text{O}}^{\text{th}}$  causes the location of the extinction points to shift along the flame surface, naturally changing the cellular instability lengths (see Fig. B.3b).

Figures B.4 and B.5 give an example of the sensitivity analysis procedure. Figure B.4 shows the PDF of cell arc length over all collected data for the MA–MA diffusion model, using  $Y_{\text{H}_2\text{O}}^{\text{iso,nom}}$  and  $\dot{\omega}_{\text{H}_2\text{O}}^{\text{th,nom}}$ . Then, a range of  $Y_{\text{H}_2\text{O}}^{\text{iso}}$  (while maintaining  $\dot{\omega}_{\text{H}_2\text{O}}^{\text{th,nom}}$ )

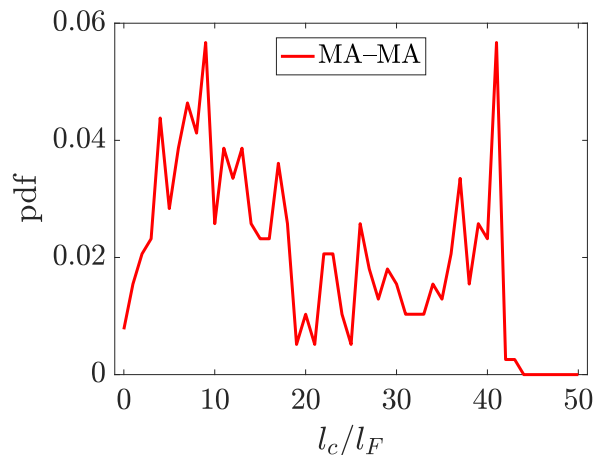


Figure B.4: PDF of the cell length for an isosurface of  $Y_{\text{H}_2\text{O}}^{\text{iso,nom}}$  and source term threshold  $\dot{\omega}_{\text{H}_2\text{O}}^{\text{th,nom}}$  for the MA-MA diffusion model.

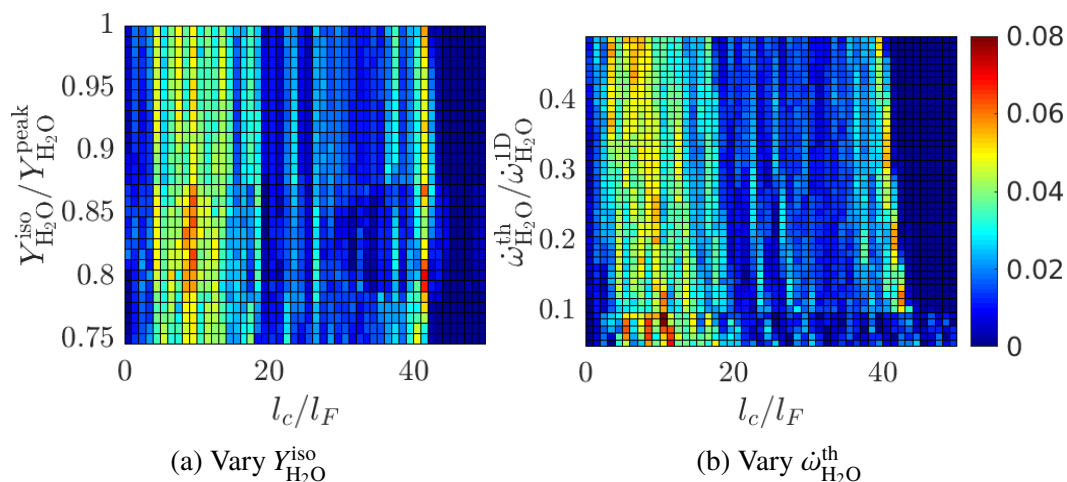


Figure B.5: Cellular instability length sensitivity maps, varying (a)  $Y_{\text{H}_2\text{O}}^{\text{iso}}$  and (b)  $\dot{\omega}_{\text{H}_2\text{O}}^{\text{th}}$ . Colors indicate values of the PDF.

is analyzed.

PDFs of the length scales at all given pairs of independent variables are generated. These PDFs are visualized in Fig. B.5a, where the probability densities are represented by the colorbar as functions of the chosen isosurface. An identical set of analyses on the cellular instability arc length can then be performed by varying  $\dot{\omega}_{\text{H}_2\text{O}}^{\text{th}}$  while maintaining  $Y_{\text{H}_2\text{O}}^{\text{iso,nom}}$ . The sensitivity of the cellular instability length due to changes in  $\dot{\omega}_{\text{H}_2\text{O}}^{\text{th}}$  is shown in Fig. B.5b. Finally, this sensitivity analysis procedure may be performed on the extinction zone length scales (shown in Fig. B.6).

From Fig. B.5, a number of trends are visible. First, there is a wide distribution of

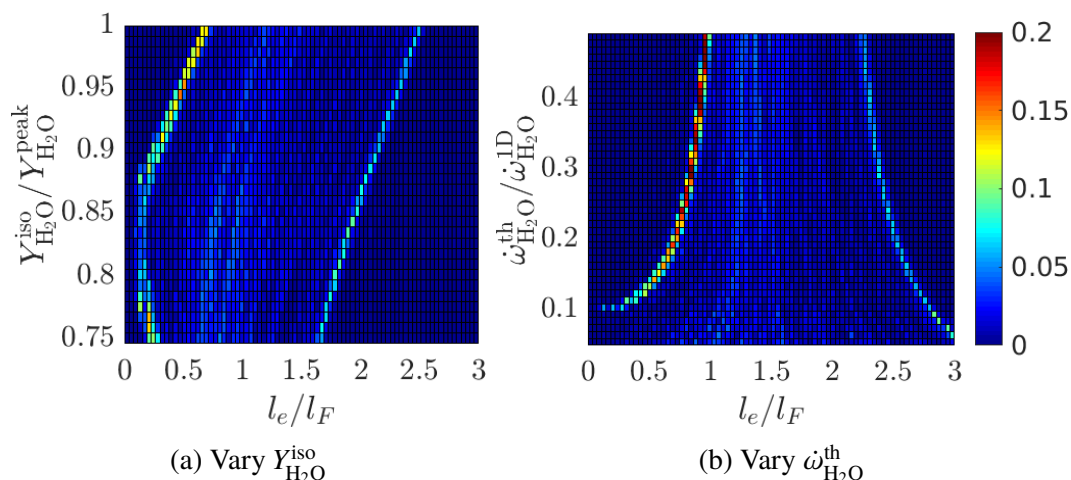


Figure B.6: Extinction zone length sensitivity maps, varying (a)  $Y_{H_2O}^{iso}$  and (b)  $\dot{\omega}_{H_2O}^{th}$ . Colors indicate values of the PDF.

cellular instability lengths for all investigated values of  $Y_{H_2O}^{iso}$  and  $\dot{\omega}_{H_2O}^{th}$ . Additionally, there exists a large concentration of cellular structures with sizes near  $10 l_c/l_F$ , and a second concentration of larger instabilities near  $40 l_c/l_F$ . These two sizes correspond to the smaller instabilities and large lobe-like structures. Figure B.7 shows the growth of the smaller instabilities across the surface of the large lobe structures. Further, there is a maximum cell size near  $43 l_c/l_F$ , and a minimum size of approximately  $3 l_c/l_F$ . While the minimum cellular instability size is largely independent of the domain size, the domain height may control the maximum cellular size. The effect of domain size is investigated in Section 3.7.1.

There is no clear trend in the cellular instability size as  $Y_{H_2O}^{iso}$  is varied, indicating the size of the cellular structures is insensitive to the chosen values of  $Y_{H_2O}^{iso}$ . This can be seen by the nearly uniform regions of high probability as the analysis variables are changed. A slight decrease in the cellular instability length is found as  $\dot{\omega}_{H_2O}^{th}$  increases; this is expected as the extinction points simply translate along the fixed isosurface as shown in Fig. B.3b. However, the decrease in cell arc length is small (roughly 5%) over the investigated range of  $\dot{\omega}_{H_2O}^{th}$ .

The extinction zone length sensitivity analyses (Fig. B.6) show a different set of trends. For analyses on both  $Y_{H_2O}^{iso}$  and  $\dot{\omega}_{H_2O}^{th}$ , there are two distinct peak values of the PDF of the extinction zone length. These peaks correspond to two different extinction regions along the flame surface; Figure B.8 indicates the smaller ( $l_e/l_F < 1$ ) and larger ( $l_e/l_F > 1$ ) extinction zones which manifest in the PDFs.

These two extinction zone types are quite sensitive to both  $Y_{H_2O}^{iso}$  and  $\dot{\omega}_{H_2O}^{th}$ . As the

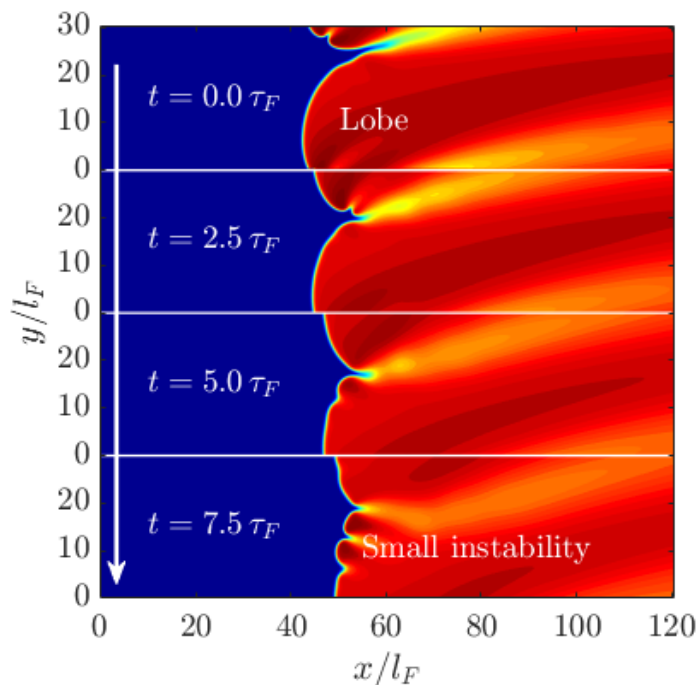


Figure B.7:  $Y_{\text{H}_2\text{O}}$  contour plots showing the time history of a larger lobe breaking down into smaller cellular instabilities.

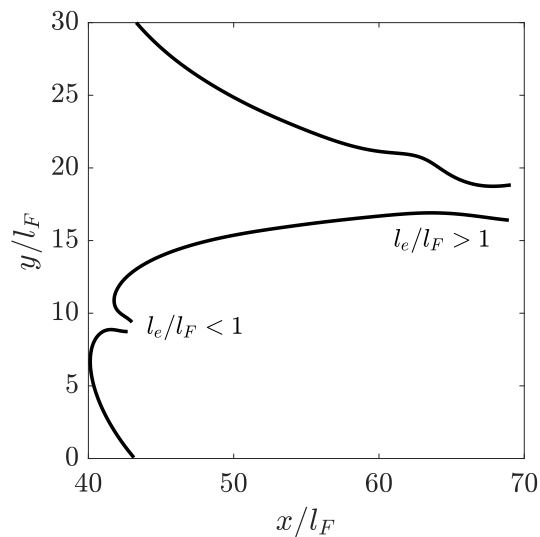


Figure B.8: Flame isosurface (showing only burning regions) with two extinction zones visible: one at  $l_e/l_F < 1$  and one at  $l_e/l_F > 1$ .

isosurface value increases, the two extinction zone sizes become larger. This can be seen most easily for the extinction zones larger than  $l_F$ , shown in Fig. B.9. The large extinction zone moves toward the burnt mixture as  $Y_{\text{H}_2\text{O}}^{\text{iso}}$  increases and the extinction locations on the isosurface diverge.

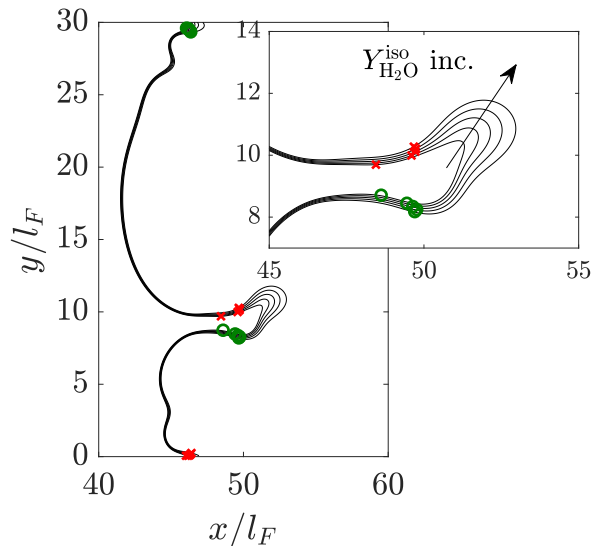


Figure B.9: Fixed  $\omega_{\text{H}_2\text{O}}^{\text{th,nom}}$  for a range of  $Y_{\text{H}_2\text{O}}^{\text{iso}}$ , showing the variation in extinction length scales between two cellular structures.

As the extinction threshold changes, the extinction length scales also change appreciably. For low values of  $\omega_{\text{H}_2\text{O}}^{\text{th}}$ , the extinction length scales diverge from one another. For the smaller extinction length scales, present in the cusps at the leading edge of large lobe formations, the increase of  $\omega_{\text{H}_2\text{O}}^{\text{th}}$  cause the two extinction locations on the isosurface to diverge away from the negative curvature cusp (Fig. B.10). For the larger extinction lengths, appearing in the regions between large lobe structures (e.g., Fig. B.3b), an increasing extinction threshold results in the extinction points on the isosurface to advance toward the unburnt mixture. Often, this results in the extinction points converging, as shown in Fig. B.3b.

### B.2.2 Sensitivity analysis of $T^{\text{iso}}$ and $\kappa^{\text{th}}$

Similar to the discussion of the length scale sensitivities due to  $Y_{\text{H}_2\text{O}}^{\text{iso}}$  and  $\omega_{\text{H}_2\text{O}}^{\text{th}}$ , a sensitivity analysis is also performed using temperature isosurfaces,  $T^{\text{iso}}$ , and curvature thresholds,  $\kappa^{\text{th}}$ , to define the cellular structures.

First, Fig. B.11 shows the sensitivity of the cellular length scale as  $T^{\text{iso}}$  and  $\kappa^{\text{th}}$  are varied. Figure B.11a shows the larger cellular instability lengths are very sensitive to the chosen value of  $T^{\text{iso}}$ , increasing by 50% over the chosen range of  $T^{\text{iso}}$ . Further, the probability densities of cell lengths become more spread as  $\kappa^{\text{th}}$  decreases. The distribution of smaller cell lengths remain relatively uniform over  $T^{\text{iso}}$ .

Next, Fig. B.12 shows sensitivity analyses of the extinction length scales as  $T^{\text{iso}}$  and  $\kappa^{\text{th}}$  change. Figure B.12a shows only one peak extinction length which increases

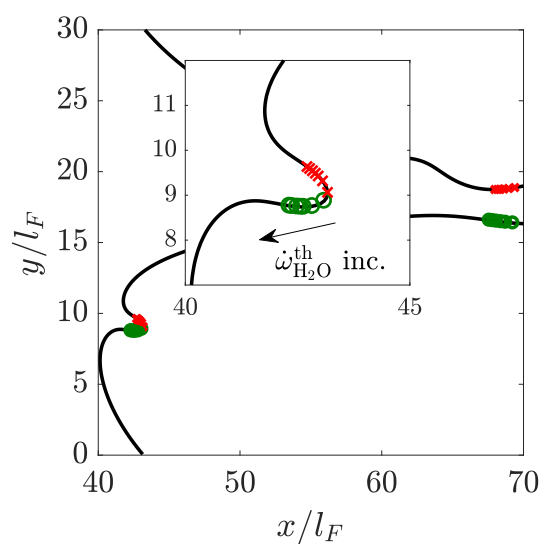


Figure B.10: Fixed  $Y_{\text{H}_2\text{O}}^{\text{iso}}$  for a range of  $\omega_{\text{H}_2\text{O}}^{\text{th}}$ , showing the movement of extinction points (red crosses and green circles) near a highly-negative curvature cusp.

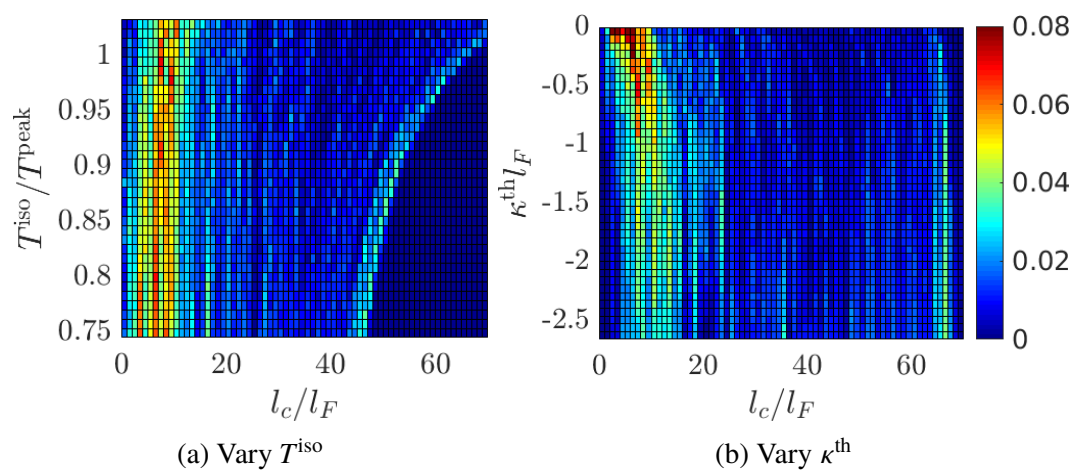


Figure B.11: Cellular instability length sensitivity maps, varying (a)  $T^{\text{iso}}$  and (b)  $\kappa^{\text{th}}$ . Colors indicate values of the PDF.

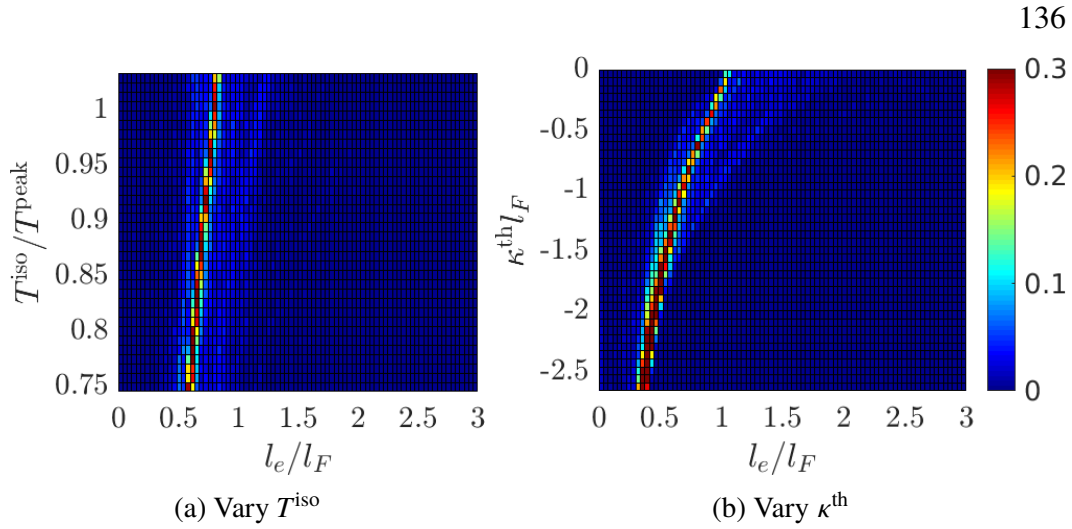


Figure B.12: Extinction zone length sensitivity maps, varying (a)  $T^{\text{iso}}$  and (b)  $\kappa^{\text{th}}$ . Colors indicate values of the PDF.

in size as  $T^{\text{iso}}$  increases (yet staying near  $l_e/l_F = 1$ ). This is contrary to the two peak extinction lengths found using  $Y_{\text{H}_2\text{O}}^{\text{iso}}$  and  $\dot{\omega}_{\text{H}_2\text{O}}^{\text{th}}$ . Similarly, only one peak extinction length scale is found while varying  $\kappa^{\text{th}}$ . However, the extinction length scale decreases by nearly a factor of three while decreasing  $\kappa^{\text{th}}$ .

### B.2.3 Sensitivity analysis conclusions

A number of conclusions can be drawn from the preceding sensitivity analyses. First, there is little variation of the cellular instability length scale for a wide range of  $Y_{\text{H}_2\text{O}}^{\text{iso}}$  and  $\dot{\omega}_{\text{H}_2\text{O}}^{\text{th}}$ . Indeed, the cell arc length scales at  $Y_{\text{H}_2\text{O}}^{\text{iso,nom}}$  and  $\dot{\omega}_{\text{H}_2\text{O}}^{\text{iso,nom}}$  are nearly uniform with respect to small deviations of these values.

The extinction length scales show some dependence on the chosen isosurface and extinction threshold values. The sensitivity analysis on  $Y_{\text{H}_2\text{O}}^{\text{iso}}$  and  $\dot{\omega}_{\text{H}_2\text{O}}^{\text{th}}$  shows two distinct extinction length scales ( $l_e < l_F$  and  $l_e > l_F$ ). The values of  $l_e$  generally increase as  $Y_{\text{H}_2\text{O}}^{\text{iso}}$  increases (except for  $l_e < l_F$  at low values of  $Y_{\text{H}_2\text{O}}^{\text{iso}}$ ). As the extinction threshold  $\dot{\omega}_{\text{H}_2\text{O}}^{\text{th}}$  increases, two separate trends are found; for small  $l_e$  (extinction zones existing in the large lobes), the extinction length scale increases. This phenomenon is seen in Fig. B.10 as the extinction points along the flame surface diverge at the negatively-curved cusps of these cellular structures. For large  $l_e$  (found deep in the domain, between large structures), an increasing value of  $\dot{\omega}_{\text{H}_2\text{O}}^{\text{th}}$  is indicative of unburnt reactants becoming isolated pockets; the increasing extinction threshold moves the extinction points toward the unburnt mixture, where the pocket begins to close (shown in Fig. B.3b). The analyses using  $T^{\text{iso}}$  and  $\kappa^{\text{th}}$  indicate only one extinction length scale,  $l_e < l_F$ , which grows as both sensitivity

values increase.

It appears appropriate to consider the nominal values of  $Y_{\text{H}_2\text{O}}^{\text{iso}}$  and  $\dot{\omega}_{\text{H}_2\text{O}}^{\text{th}}$ , as the cellular instability length scale is insensitive to changes around these values, and the extinction length scales remain of the order of the flame thickness. The cellular instability and extinction length scales are quite sensitive to the selection of  $T^{\text{iso}}$  and  $\kappa^{\text{th}}$ . For these reasons,  $T^{\text{iso}}$  and  $\kappa^{\text{th}}$  detection mechanisms will not be considered further.

While this analysis provides only a cursory investigation of the length scales in an unsteady two-dimensional freely propagating flame, the methodology to extract characteristic length scales has been demonstrated to yield quantitative data necessary for future work. The methodology presented here indicates that sensitivity analyses of the controlling variables identifies appropriate analysis parameters,  $Y_{\text{H}_2\text{O}}^{\text{iso}}$  and  $\dot{\omega}_{\text{H}_2\text{O}}^{\text{th}}$ , which have direct relations to flame structure statistics. The identified extinction zone length scales are often smaller than the laminar flame thickness, and thus future simulations using LES should consider the effects of flame extinction in the sub-grid scale model formulation.

## BIBLIOGRAPHY

- [1] U.S. Energy Information Administration. *Annual Energy Outlook 2018 with projections to 2050*. Tech. rep. Office of Energy Analysis, U.S. Department of Energy, Washington, DC, 2018.
- [2] U.S. Environmental Protection Agency. *Stationary Gas Turbines and Stationary Combustion Turbines, subparts GG & KKKK*. Tech. rep. Federal Register, 2011.
- [3] C. Altantzis et al. “Numerical simulation of propagating circular and cylindrical lean premixed hydrogen/air flames”. In: *Proc. Combust. Inst.* 34.1 (2013), pp. 1109–1115.
- [4] A. J. Aspden. “A numerical study of diffusive effects in turbulent lean premixed hydrogen flames”. In: *Proceedings of the Combustion Institute* 36.2 (2017), pp. 1997–2004. ISSN: 1540-7489. DOI: [10.1016/j.proci.2016.07.053](https://doi.org/10.1016/j.proci.2016.07.053).
- [5] A. J. Aspden, M. S. Day, and J. B. Bell. “Characterization of low Lewis number flames”. In: *Proc. Combust. Inst.* 33.1 (2011), pp. 1463–1471. ISSN: 1540-7489.
- [6] A. J. Aspden, M. S. Day, and J. B. Bell. “Lewis number effects in distributed flames”. In: *Proc. Combust. Inst.* 33.1 (2011), pp. 1473–1480. ISSN: 1540-7489.
- [7] A. J. Aspden, M. S. Day, and J. B. Bell. “Turbulence-chemistry interaction in lean premixed hydrogen combustion”. In: *Proc. Combust. Inst.* 35.2 (2015), pp. 1321–1329. ISSN: 1540-7489.
- [8] A. J. Aspden, M. S. Day, and J. B. Bell. “Turbulence-flame interactions in lean premixed hydrogen: Transition to the distributed burning regime”. In: *J. Fluid Mech.* 680 (Aug. 2011), pp. 287–320. ISSN: 1469-7645.
- [9] R. Bastiaans and A. W. Vreman. “Numerical simulation of instabilities in lean premixed hydrogen combustion”. In: *Int. J. Numer. Method. Heat Fluid Fl.* 22.1 (2012), pp. 112–128.
- [10] J. K. Bechtold and M. Matalon. “Hydrodynamic and diffusion effects on the stability of spherically expanding flames”. In: *Combust. Flame* 67.1 (1987), pp. 77–90. ISSN: 0010-2180.
- [11] J. B. Bell et al. “Interaction of turbulence and chemistry in a low-swirl burner”. In: *J. Phys. Conf. Ser.* Vol. 125. IOP Publishing, 2008, p. 012027.
- [12] R. B. Bird, W. E. Stewart, and E. N. Lightfoot. *Transport Phenomena*. New York: Wiley, 1960.

- [13] F. Bisetti et al. “On the formation and early evolution of soot in turbulent nonpremixed flames”. In: *Combust. Flame* 159.1 (2012), pp. 317–335.
- [14] G. Blanquart. *CaltechMech Version 2.4*. <http://www.theforce.caltech.edu/CaltechMech>. 2017.
- [15] H. Bongers and L. P. H. De Goey. “The effect of simplified transport modeling on the burning velocity of laminar premixed flames”. In: *Combust. Sci. Technol.* 175.10 (2003), pp. 1915–1928.
- [16] D. Bradley et al. “The development and structure of flame instabilities and cellularity at low Markstein numbers in explosions”. In: *Combust. Flame* 122.1 (2000), pp. 195–209. DOI: [10.1016/S0010-2180\(00\)00113-9](https://doi.org/10.1016/S0010-2180(00)00113-9).
- [17] K. N. C. Bray. “Studies of the turbulent burning velocity”. In: *Proc. R. Soc. Lond.* 431.1882 (1990), pp. 315–335. DOI: [10.1098/rspa.1990.0133](https://doi.org/10.1098/rspa.1990.0133).
- [18] B. Bregeon, A. S. Gordon, and F. A. Williams. “Near-limit downward propagation of hydrogen and methane flames in oxygen-nitrogen mixtures”. In: *Combust. Flame* 33 (1978), pp. 33–45. ISSN: 0010-2180.
- [19] C. Bruno et al. “Impact of multi-component diffusion in turbulent combustion using direct numerical simulations”. In: *Combust. Flame* 162.11 (2015), pp. 4313–4330. ISSN: 0010-2180.
- [20] N. Burali et al. “Assessment of the constant non-unity Lewis number assumption in chemically-reacting flows”. In: *Combust. Theor. Model.* (2016), pp. 1–26.
- [21] S. M. Candel and T. J. Poinso. “Flame Stretch and the Balance Equation for the Flame Area”. In: *Combust. Sci. Technol.* 70.1-3 (1990), pp. 1–15. DOI: [10.1080/00102209008951608](https://doi.org/10.1080/00102209008951608).
- [22] P. L. Carroll and G. Blanquart. “A proposed modification to Lundgren’s physical space velocity forcing method for isotropic turbulence”. In: *Phys. Fluids* 25.10 (2013), p. 105114.
- [23] D. Cecere et al. “Direct numerical simulation of a turbulent lean premixed CH<sub>4</sub>/H<sub>2</sub>-Air slot flame”. In: *Combust. Flame* 165 (2016), pp. 384–401.
- [24] S. Chapman and T.G. Cowling. *The mathematical theory of non-uniform gases: An account of the kinetic theory of viscosity, thermal conduction and diffusion in gases*. Cambridge University Press, 1970.
- [25] R. K. Cheng and D. Littlejohn. “Laboratory Study of Premixed H<sub>2</sub>-Air and H<sub>2</sub>-N<sub>2</sub>-Air Flames in a Low-Swirl Injector for Ultra-Low Emissions Gas Turbines”. In: *J. Eng. Gas Turbine Power* 130 (2008), pp. 31503–31511.
- [26] R. K. Cheng et al. “Laboratory investigations of a low-swirl injector with H<sub>2</sub> and CH<sub>4</sub> at gas turbine conditions”. In: *Proc. Combust. Inst.* 32.2 (2009), pp. 3001–3009.

- [27] P. Clavin and F. A. Williams. “Effects of molecular diffusion and of thermal expansion on the structure and dynamics of premixed flames in turbulent flows of large scale and low intensity”. In: *J. Fluid Mech.* 116 (Mar. 1982), pp. 251–282.
- [28] T. P. Coffee and J. M. Heimerl. “Transport algorithms for premixed, laminar steady-state flames”. In: *Combust. Flame* 43 (1981), pp. 273–289.
- [29] Cori. <http://www.nersc.gov/users/computational-systems/cori/>. Accessed: 2018-04-18.
- [30] S. G. Davis et al. “An optimized kinetic model of H<sub>2</sub>/CO combustion”. In: *Proc. Combust. Inst.* 30.1 (2005), pp. 1283–1292. doi: [10.1016/j.proci.2004.08.252](https://doi.org/10.1016/j.proci.2004.08.252).
- [31] M. S. Day and J. B. Bell. “Numerical simulation of laminar reacting flows with complex chemistry”. In: *Combust. Theor. Model.* 4.4 (2000), pp. 535–556. doi: [10.1088/1364-7830/4/4/309](https://doi.org/10.1088/1364-7830/4/4/309).
- [32] M. S. Day et al. “Cellular burning in lean premixed turbulent hydrogen-air flames: Coupling experimental and computational analysis at the laboratory scale”. In: *J. Phys. Conf. Ser.* 180.1 (2009), p. 012031.
- [33] M. S. Day et al. “Turbulence effects on cellular burning structures in lean premixed hydrogen flames”. In: *Combust. Flame* 156.5 (2009), pp. 1035–1045. issn: 0010-2180.
- [34] M.S. Day et al. “A combined computational and experimental characterization of lean premixed turbulent low swirl laboratory flames II. Hydrogen flames”. In: *Combust. Flame* 162.5 (2015), pp. 2148–2165.
- [35] B. Decourt et al. *Hydrogen-based energy conversion*. Tech. rep. SBC Energy Institute, 2014.
- [36] O. Desjardins et al. “High order conservative finite difference scheme for variable density low Mach number turbulent flows”. In: *J. Comput. Phys.* 227.15 (2008), pp. 7125–7159. issn: 0021-9991.
- [37] G. Dixon-Lewis. “Flame structure and flame reaction kinetics. II. Transport phenomena in multicomponent systems”. In: *Proc. R. Soc. London, Ser. A*. Vol. 307. The Royal Society, 1968, pp. 111–135.
- [38] A. Ern and V. Giovangigli. “Fast and accurate multicomponent transport property evaluation”. In: *J. Comput. Phys.* 120.1 (1995), pp. 105–116.
- [39] A. Ern and V. Giovangigli. “Impact of Detailed Multicomponent Transport on Planar and Counterflow Hydrogen/Air and Methane/Air Flames”. In: *Combust. Sci. Technol.* 149.1-6 (1999), pp. 157–181.
- [40] A. Ern and V. Giovangigli. *Multicomponent transport algorithms*. Vol. 24. Springer-Verlag, 1994.

- [41] A. Ern and V. Giovangigli. “Thermal diffusion effects in hydrogen-air and methane-air flames”. In: *Combust. Theor. Model.* 2.4 (1998), pp. 349–372.
- [42] J. H. Ferziger and H. G. Kaper. *Mathematical theory of transport processes in gases*. North Holland, 1972.
- [43] A. J. Fillo et al. “Assessing the importance of multicomponent transport properties using direct numerical simulations of premixed, turbulent flames”. In: *Proceedings of the 10th US Combustion Meeting*. College Park, MD: Combust. Inst., 2017. DOI: [AbstractID:2TF-0272](https://doi.org/10.2514/6.2017-1000).
- [44] B. Fiorina, D. Veynante, and S. Candel. “Modeling Combustion Chemistry in Large Eddy Simulation of Turbulent Flames”. In: *Flow Turb. Combust.* 94.1 (Jan. 2015), pp. 3–42.
- [45] R. M. Fristrom and L. Monchick. “Two simple approximations to the thermal diffusion factor and their applications to flame studies”. In: *Combust. Flame* 71.1 (1988), pp. 89–99.
- [46] C. E. Frouzakis et al. “Numerical study of unstable hydrogen/air flames: Shape and propagation speed”. In: *Proc. Combust. Inst.* 35.1 (2015), pp. 1087–1095. ISSN: 1540-7489.
- [47] G. Gahleitner. “Hydrogen from renewable electricity: An international review of power-to-gas pilot plants for stationary applications”. In: *Int. J. Hydrog. Energ.* 38.5 (2013), pp. 2039–2061. DOI: [10.1016/j.ijhydene.2012.12.010](https://doi.org/10.1016/j.ijhydene.2012.12.010).
- [48] P. García-Ybarra, C. Nicoli, and P. Clavin. “Soret and dilution effects on premixed flames”. In: *Combust. Sci. Technol.* 42.1-2 (1984), pp. 87–109.
- [49] O. Gicquel, N. Darabiha, and D. Thévenin. “Laminar premixed hydrogen/air counterflow flame simulations using flame prolongation of ILDM with differential diffusion”. In: *Proc. Combust. Inst.* 28.2 (2000), pp. 1901–1908.
- [50] V. Giovangigli. “Multicomponent transport in laminar flames”. In: *Proc. Combust. Inst.* 35.1 (2015), pp. 625–637. DOI: <https://doi.org/10.1016/j.proci.2014.08.011>.
- [51] J. F. Grcar, J. B. Bell, and M. S. Day. “The Soret effect in naturally propagating, premixed, lean, hydrogen–air flames”. In: *Proc. Combust. Inst.* 32.1 (2009), pp. 1173–1180.
- [52] C. A. Hall and R. W. Pitz. “A structural study of premixed hydrogen-air cellular tubular flames”. In: *Proc. Combust. Inst.* 34.1 (2013), pp. 973–980.
- [53] C. A. Hall and R. W. Pitz. “Numerical simulation of premixed H<sub>2</sub>-air cellular tubular flames”. In: *Combust. Theor. Model.* 20.2 (2016), pp. 328–348.
- [54] C. A. Hall et al. “Minor-species structure of premixed cellular tubular flames”. In: *Proc. Combust. Inst.* 35.1 (2015), pp. 1107–1114.

- [55] E. R. Hawkes et al. “Scalar mixing in direct numerical simulations of temporally evolving plane jet flames with skeletal CO/H<sub>2</sub> kinetics”. In: *Proc. Combust. Inst.* 31.1 (2007), pp. 1633–1640. doi: [10.1016/j.proci.2006.08.079](https://doi.org/10.1016/j.proci.2006.08.079).
- [56] Nuclear Emergency Response Headquarters. *Report of Japanese Government to the IAEA Ministerial Conference on Nuclear Safety - The Accident at TEPCO’s Fukushima Nuclear Power Stations*. Tech. rep. Government of Japan, 2011.
- [57] M. Herrmann, G. Blanquart, and V. Raman. “Flux corrected finite volume scheme for preserving scalar boundedness in reacting large-eddy simulations”. In: *AIAA J.* 44.12 (2006), pp. 2879–2886.
- [58] J. O. Hirschfelder, C. F. Curtiss, and R. B. Bird. *Molecular theory of gases and liquids*. New York: Wiley, 1964.
- [59] Z. Hong, D. F. Davidson, and R. K. Hanson. “An improved H<sub>2</sub>/O<sub>2</sub> mechanism based on recent shock tube/laser absorption measurements”. In: *Combust. Flame* 158.4 (2011), pp. 633–644.
- [60] Z. Hong et al. “On the rate constants of OH + HO<sub>2</sub> and HO<sub>2</sub> + HO<sub>2</sub>: Comprehensive study of H<sub>2</sub>O<sub>2</sub> thermal decomposition using multi-species laser absorption”. In: *Proc. Combust. Inst.* 34.1 (2013), pp. 565–571. ISSN: 1540-7489.
- [61] *HYPRE: Scalable Linear Solvers and Multigrid Methods*. <http://www.llnl.gov/CASC/hypre>. Accessed: 2018-04-05.
- [62] H. G. Im and J. H. Chen. “Preferential diffusion effects on the burning rate of interacting turbulent premixed hydrogen-air flames”. In: *Combust. Flame* 131.3 (2002), pp. 246–258. ISSN: 0010-2180.
- [63] S. Ishizuka and D. Dunn-Rankin. *Tubular combustion*. Momentum Press, 2013.
- [64] G. Jomaas, C. K. Law, and J. K. Bechtold. “On transition to cellularity in expanding spherical flames”. In: *J. Fluid Mech.* 583 (2007), pp. 1–26.
- [65] R. J. Kee, M. E. Coltrin, and P. Glarborg. *Chemically reacting flow: Theory and practice*. New Jersey: Wiley, 2003.
- [66] R. J. Kee, F. M. Rupley, and J. A. Miller. *Chemkin-II: A Fortran chemical kinetics package for the analysis of gas-phase chemical kinetics*. Tech. rep. Sandia National Labs., Livermore, CA (USA), 1989.
- [67] S. O. Kim et al. “A DNS study of the ignition of lean PRF/air mixtures with temperature inhomogeneities under high pressure and intermediate temperature”. In: *Combust. Flame* 162.3 (2015), pp. 717–726.

- [68] E. Knudsen and H. Pitsch. “A general flamelet transformation useful for distinguishing between premixed and non-premixed modes of combustion”. In: *Combust. Flame* 156.3 (2009), pp. 678–696.
- [69] E. Knudsen and H. Pitsch. “Capabilities and limitations of multi-regime flamelet combustion models”. In: *Combust. Flame* 159.1 (2012), pp. 242–264.
- [70] A. Körner. *Technology roadmap: Hydrogen and fuel cells*. Tech. rep. International Energy Agency Energy Technology Policy Division, 2015.
- [71] J. Kurtz et al. *Performance of existing hydrogen stations*. Tech. rep. National Renewable Energy Laboratory, 2017.
- [72] K.-Y. Lam, D. F. Davidson, and R. K. Hanson. “A Shock Tube Study of  $\text{H}_2 + \text{OH} \rightarrow \text{H}_2\text{O} + \text{H}$  Using OH Laser Absorption”. In: *Int. J. Chem. Kinet.* 45.6 (2013), pp. 363–373.
- [73] S. Lapointe and G. Blanquart. “Fuel and chemistry effects in high Karlovitz premixed turbulent flames”. In: *Combust. Flame* 167 (2016), pp. 294–307. ISSN: 0010-2180.
- [74] S. Lapointe, B. Savard, and G. Blanquart. “Differential diffusion effects, distributed burning, and local extinctions in high Karlovitz premixed flames”. In: *Combust. Flame* 162.9 (2015), pp. 3341–3355. ISSN: 0010-2180.
- [75] C. K. Law. *Combustion physics*. Cambridge University Press, 2010.
- [76] C. K. Law, G. Jomaas, and J. K. Bechtold. “Cellular instabilities of expanding hydrogen/propane spherical flames at elevated pressures: Theory and experiment”. In: *Proc. Combust. Inst.* 30.1 (2005), pp. 159–167. ISSN: 1540-7489.
- [77] B. P. Leonard. “A stable and accurate convective modelling procedure based on quadratic upstream interpolation”. In: *Comput. Method. Appl. Mech. Eng.* 19.1 (1979), pp. 59–98.
- [78] D. Littlejohn and R. K. Cheng. “Fuel effects on a low-swirl injector for lean premixed gas turbines”. In: *Proc. Combust. Inst.* 31.2 (2007), pp. 3155–3162. ISSN: 1540-7489.
- [79] T. S. Lundgren. “Linearly forced isotropic turbulence”. In: *Annual Research Briefs*. Center for Turbulence Research, Stanford University, 2003, pp. 461–473.
- [80] U. Maas and S.B. Pope. “Simplifying chemical kinetics: Intrinsic low-dimensional manifolds in composition space”. In: *Combust. Flame* 88.3 (1992), pp. 239–264.
- [81] A. Majda and J. Sethian. “The Derivation and Numerical Solution of the Equations for Zero Mach Number Combustion”. In: *Combust. Sci. Technol.* 42.3-4 (1985), pp. 185–205. DOI: [10.1080/00102208508960376](https://doi.org/10.1080/00102208508960376).

- [82] E. A. Mason and S. C. Saxena. “Approximate formula for the thermal conductivity of gas mixtures”. In: *Phys. Fluids* 1.5 (1958), pp. 361–369.
- [83] M. Matalon. “Intrinsic Flame Instabilities in Premixed and Nonpremixed Combustion”. In: *Ann. Rev. Fluid Mech.* 39.1 (2007), pp. 163–191.
- [84] S. Mathur, P.K. Tondon, and S.C. Saxena. “Thermal conductivity of binary, ternary and quaternary mixtures of rare gases”. In: *Mol. Phys.* 12.6 (1967), pp. 569–579. eprint:<http://dx.doi.org/10.1080/00268976700100731>.
- [85] J. R. Maughan et al. “Reducing Gas Turbine Emissions Through Hydrogen-Enhanced, Steam-Injected Combustion”. In: *J. Eng. Gas Turbines Power* 118.1 (1996), pp. 78–85. doi: [10.1115/1.2816553](https://doi.org/10.1115/1.2816553).
- [86] T. Mitani and F.A. Williams. “Studies of cellular flames in hydrogen-oxygen-nitrogen mixtures”. In: *Combust. Flame* 39.2 (1980), pp. 169–190. ISSN: 0010-2180.
- [87] L. Monchick and E. A. Mason. “Transport Properties of Polar Gases”. In: *J. Chem. Phys.* 35.5 (1961), pp. 1676–1697.
- [88] A. Moreau, O. Teytaud, and J.-P. Bertoglio. “Optimal estimation for large-eddy simulation of turbulence and application to the analysis of subgrid models”. In: *Phys. Fluids* 18.10 (2006), p. 105101.
- [89] J. A. van Oijen, R. J. M. Bastiaans, and L. P. H. de Goey. “Low-dimensional manifolds in direct numerical simulations of premixed turbulent flames”. In: *Pro. Combust. Inst.* 31.1 (2007), pp. 1377–1384.
- [90] J. A. van Oijen and L. P. H. de Goey. “Modelling of Premixed Laminar Flames using Flamelet-Generated Manifolds”. In: *Combust. Sci. Technol.* 161.1 (2000), pp. 113–137.
- [91] J. A. van Oijen et al. “Direct Numerical Simulations of Premixed Turbulent Flames with Reduced Chemistry: Validation and Flamelet Analysis”. In: *Flow Turb. Combust.* 75.1 (2005), pp. 67–84.
- [92] J. A. van Oijen et al. “State-of-the-art in premixed combustion modeling using flamelet generated manifolds”. In: *Prog. Ener. Combust. Sci.* 57 (2016), pp. 30–74. doi: <https://doi.org/10.1016/j.pecs.2016.07.001>.
- [93] E. S. Oran and J. P. Boris. “Detailed modelling of combustion systems”. In: *Prog. Energy Combust. Sci.* 7.1 (1981), pp. 1–72.
- [94] G. Patnaik et al. “Detailed numerical simulations of cellular flames”. In: *Symp. (Int.) Combust.* 22.1 (1989), pp. 1517–1526. ISSN: 0082-0784.
- [95] P. Paul and J. Warnatz. “A re-evaluation of the means used to calculate transport properties of reacting flows”. In: *Symp. (Int.) Combust.* 27.1 (1998), pp. 495–504.

- [96] P. Pelce and P. Clavin. “Influence of hydrodynamics and diffusion upon the stability limits of laminar premixed flames”. In: *J. Fluid Mech.* 124 (1982), pp. 219–237.
- [97] N. Peters. *Turbulent Combustion*. Cambridge University Press, 2000.
- [98] C. D. Pierce. “Progress-variable approach for large-eddy simulation of turbulent combustion”. PhD thesis. Stanford University, 2001.
- [99] C. D. Pierce and P. Moin. “Progress-variable approach for large-eddy simulation of non-premixed turbulent combustion”. In: *J. Fluid Mech.* 504 (2004), pp. 73–97.
- [100] H. Pitsch. *A C++ computer program for 0D combustion and 1D laminar flame calculations*. Tech. rep. Aachen, Germany: RWTH Aachen University, 1998.
- [101] K. K. J. Ranga Dinesh et al. “High hydrogen content syngas fuel burning in lean premixed spherical flames at elevated pressures: Effects of preferential diffusion”. In: *Int. J. Hydrog. Energ.* 41.40 (2016), pp. 18231–18249.
- [102] J. D. Regele et al. “A two-equation model for non-unity Lewis number differential diffusion in lean premixed laminar flames”. In: *Combust. Flame* 160.2 (2013), pp. 240–250.
- [103] E. S. Richardson and J. H. Chen. “Application of PDF mixing models to premixed flames with differential diffusion”. In: *Combust. Flame* 159.7 (2012), pp. 2398–2414.
- [104] C. Rosales and C. Meneveau. “Linear forcing in numerical simulations of isotropic turbulence: Physical space implementations and convergence properties”. In: *Phys. Fluids* 17.9 (2005), p. 095106.
- [105] D. E. Rosner. *Transport processes in chemically reacting flow systems*. Butterworth Publishers, Stoneham, MA, 1986.
- [106] J. W. Ruge and K. Stüben. “Algebraic Multigrid”. In: *Frontiers in Applied Mathematics: Multigrid Methods*. Ed. by S. F. McCormick. Chap. 4, pp. 73–130. DOI: [10.1137/1.9781611971057.ch4](https://doi.org/10.1137/1.9781611971057.ch4).
- [107] A. L. Sánchez and F. A. Williams. “Recent advances in understanding of flammability characteristics of hydrogen”. In: *Prog. Energy Combust. Sci.* 41 (2014), pp. 1–55.
- [108] B. Savard and G. Blanquart. “An a priori model for the effective species Lewis numbers in premixed turbulent flames”. In: *Combust. Flame* 161.6 (2014), pp. 1547–1557. ISSN: 0010-2180.
- [109] B. Savard and G. Blanquart. “Broken reaction zone and differential diffusion effects in high Karlovitz n-C7H16 premixed turbulent flames”. In: *Combust. Flame* 162.5 (2015), pp. 2020–2033. DOI: [10.1016/j.combustflame.2014.12.020](https://doi.org/10.1016/j.combustflame.2014.12.020).

- [110] B. Savard and G. Blanquart. “Effects of dissipation rate and diffusion rate of the progress variable on local fuel burning rate in premixed turbulent flames”. In: *Combust. Flame* 180 (2017), pp. 77–87.
- [111] B. Savard, B. Bobbitt, and G. Blanquart. “Structure of a high Karlovitz n-C7H16 premixed turbulent flame”. In: *Proceedings of the Combustion Institute* 35.2 (2015), pp. 1377–1384. DOI: [10.1016/j.proci.2014.06.133](https://doi.org/10.1016/j.proci.2014.06.133).
- [112] B. Savard et al. “A computationally-efficient, semi-implicit, iterative method for the time-integration of reacting flows with stiff chemistry”. In: *J. Comput. Phys.* 295 (2015), pp. 740–769. ISSN: 0021-9991.
- [113] J. Schlup and G. Blanquart. “A reduced thermal diffusion model for H and H<sub>2</sub>”. In: *Combust. Flame* 191 (2018), pp. 1–8. DOI: [10.1016/j.combustflame.2017.12.022](https://doi.org/10.1016/j.combustflame.2017.12.022).
- [114] J. Schlup and G. Blanquart. “Validation of a mixture-averaged thermal diffusion model for premixed lean hydrogen flames”. In: *Combust. Theor. Model.* 22.2 (2018), pp. 264–290. DOI: [10.1080/13647830.2017.1398350](https://doi.org/10.1080/13647830.2017.1398350).
- [115] G. I. Sivashinsky. “Instabilities, pattern formation, and turbulence in flames”. In: *Annu. Rev. Fluid Mech.* 15.1 (1983), pp. 179–199.
- [116] G. P. Smith et al. *GRI-Mech 3.0*. <http://combustion.berkeley.edu/gri-mech/>. 1999.
- [117] M. D. Smooke and V. Giovangigli. “Extinction of tubular premixed laminar flames with complex chemistry”. In: *Symp. (Int.) Combust.* Vol. 23. Elsevier, 1991, pp. 447–454.
- [118] C. Y. TerMaath et al. “Emissions reduction benefits from hydrogen addition to midsize gas turbine feedstocks”. In: *Int. J. Hydrog. Energ.* 31.9 (2006), pp. 1147–1158. DOI: [10.1016/j.ijhydene.2005.10.002](https://doi.org/10.1016/j.ijhydene.2005.10.002).
- [119] G. C. Tiekstra and F. P. Koopman. “The NATURALHY project: first step in assessing the potential of the existing natural gas network for hydrogen delivery”. In: *IGRC2008*. 2008, pp. 1–10. URL: <https://refman.energytransitionmodel.com/publications/1799>.
- [120] J. Towns et al. “XSEDE: Accelerating Scientific Discovery”. In: *Comput. Sci. Eng.* 16.5 (2014), pp. 62–74. ISSN: 1521-9615.
- [121] H. A. van der Vorst. “Bi-CGSTAB: A Fast and Smoothly Converging Variant of Bi-CG for the Solution of Nonsymmetric Linear Systems”. In: *SIAM J. Sci. Comput.* 13.2 (1992), pp. 631–644. DOI: [10.1137/0913035](https://doi.org/10.1137/0913035).
- [122] A. W. Vreman, R. J. M. Bastiaans, and B. J. Geurts. “A Similarity Subgrid Model for Premixed Turbulent Combustion”. In: *Flow Turb. Combust.* 82.2 (Mar. 2009), pp. 233–248.

- [123] J. Warnatz. “Influence of Transport Models and Boundary Conditions on Flame Structure”. In: *Numerical Methods in Laminar Flame Propagation: A GAMM-Workshop*. Ed. by N. Peters and J. Warnatz. Wiesbaden: Vieweg+Teubner Verlag, 1982, pp. 87–111.
- [124] A. Wehrfritz et al. “Large Eddy Simulation of n-dodecane spray flames using Flamelet Generated Manifolds”. In: *Combust. Flame* 167 (2016), pp. 113–131.
- [125] F. A. Williams. *Combustion Theory*. Benjamin/Cummings, 1985.
- [126] Y. Xuan, G. Blanquart, and M. E. Mueller. “Modeling curvature effects in diffusion flames using a laminar flamelet model”. In: *Combust. Flame* 161.5 (2014), pp. 1294–1309.
- [127] J. Yanez, M. Kuznetsov, and A. Souto-Iglesias. “An analysis of the hydrogen explosion in the Fukushima-Daiichi accident”. In: *Int. J. Hydrog. Ener.* 40.25 (2015), pp. 8261–8280. DOI: [10.1016/j.ijhydene.2015.03.154](https://doi.org/10.1016/j.ijhydene.2015.03.154).
- [128] F. Yang et al. “A mechanistic study of Soret diffusion in hydrogen–air flames”. In: *Combust. Flame* 157.1 (2010), pp. 192–200.
- [129] J. Yuan, Y. Ju, and C. K. Law. “Coupled hydrodynamic and diffusional-thermal instabilities in flame propagation at subunity Lewis numbers”. In: *Phys. Fluids* 17.7 (2005), p. 074106.
- [130] L. Zimmer et al. “Investigation of mass and energy coupling between soot particles and gas species in modelling ethylene counterflow diffusion flames”. In: *Combust. Theor. Model.* 21.2 (2017), pp. 358–379.